Development of Advanced Technology for Photocatalytic Degradation of Organic Pollutants in Wastewater

A THESIS SUMITTED TO THE MIE UNIVERSITY FOR THE DEGREE OF DOCTOR OF PHILOSOPHY IN THE GRADUATE SCHOOL OF ENGINEERING

By

Md. Ashraful Islam Molla

ANALYTICAL & ENVIRONMENTAL CHEMISTRY LABORATORY
DEPARTMENT OF CHEMISTRY FOR MATERIALS
GRADUATE SCHOOL OF ENGINEERING
MIE UNIVERSITY
MIE, JAPAN

2018

ACKNOWLEDGEMENTS

All praise is to almighty ALLAH the first and the last that facilitates my task and gave me the patience to complete my research journey safely. At this moment I belive the opportunity has come to express my gratitude for all people who provided me with the necessary supports and made this journey smooth and enjoyable.

On this occasion, I would like to express my heartfelt gratitude and regards to my esteemed guide Professor Dr. Satoshi Kaneco, whose continuous, untiring guidance and supervision, valuable suggestions, constructive criticism, constant support, kind treatment and immediate response for all necessities during the period of this research enabled me to learn in–depth of my research field and to overcome my limitations in pursuit with innovative concepts. I am grateful to him for being so generous to assist me in my personal matters beyond academic affairs. There are no suitable words to express my gratitude.

I am extremely grateful to Associate Professor Dr. Hideyuki Katsumata for explaining many aspects of my research and giving proper advising and valuable suggestions. My profound thanks are due to his constant support, kind treatment and immediate response to carry out this work.

I would also like to thank my examiners Professor Dr. Nobuyuki Imanishi and Professor Dr. Atsushi Ishihara for their advice regarding corrections which I feel improved not only the thesis, but will also assist me greatly in my future endeavors.

I express my special thanks to Associate Professor Dr. Tohru Suzuki and Assistant Professor Ms. Mai Furukawa for their constant support. I also convey my thanks to our research group members for their kind help. I acknowledge with deep sense of gratitude and sincere thanks to Mr. Shoji Nakamura and Ms. Yukiko Fujita for helping me with instrumental analysis of the samples.

I would like to acknowledge the Ministry of Education, Culture, Sports, Science and Technology (MEXT), Japan for giving me a three and half year's scholarship. I also highly thankful to this organization for providing research grant.

Finally, family was the driving force for me to achieve this goal. I am extremely grateful to my parents for their valuable support and continuous encouragement. I am lucky to have the passionate care from my lovely wife Mst. Meherun Nesa. I want to thank my two little angels Muhammad Ruwayfe Ashraf and Tasfyah Ashraf Aishah for making our lives cheerful and enjoyable. I would like to express my sincere thanks to other family members for paying much attention to me.

Mie Md. Ashraful Islam Molla

27.02.2018

TABLE OF CONTENTS

LIST OF FIGURES

LIST OF TABLES

LIST OF ABBREVIATIONS/ACRONYMS/SYMBOLS

Å	Angstrom
$\boldsymbol{\beta}$	Full width at half–maximum
$\boldsymbol{\varepsilon}$	Strain
$\boldsymbol{\eta}$	Slope
$\boldsymbol{\theta}$	Bragg diffraction angle
$\boldsymbol{\lambda}$	Wavelength
$\boldsymbol{\lambda_{max}}$	Wavelength of maximum absorbance
$\boldsymbol{\chi}$	Electronegativity of the semiconductor
°C	Degree Celsius
$\boldsymbol{A/A_0}$	Absorbance at any time/Absorbance at 0 time
AA	Ascorbic acid
Ag	Silver
AO	*Di*–ammonium oxalate monohydrate
AOP	Advanced oxidation process
AR88	Acid red 88
BET	Brunauer–Emmett–Teller
b.p.	Boiling point
BPB	Bromophenol blue
$\boldsymbol{C/C_0}$	Concentration at any time/Concentration at 0 time
CB	Conduction band
COD	Chemical oxygen demand
$\boldsymbol{D}$	Average crystallite size
DRS	Diffuse reflectance spectra

e^-	Electron from electron–hole pair
e.g.	For example
E_a	Activation energy
E_g	Band–gap energy
EPMA	Electron probe micro–analyzer
et al.	And others
etc.	Et cetera
FMT	Famotidine
FWHM	Full width at half maximum
GC–MS	Gas Chromatography tandem Mass Spectrometry
h	Hour
h^+	Positive hole from electron–hole pair
Hg–Xe lamp	Mercury–Xenon lamp
HOMO	Highest occupied molecule orbital
HPLC	High–performance liquid chromatography
$h\nu$	Photon energy
i.d.	Internal diameter
LED	light–emitting diode
L–H	Langmuir–Hinshelwood
LUMO	Lower unoccupied molecule orbital
M.W.	Molecular weight
m/z	Mass to Charge ratio
MF	Microfiltration
min	Minute
MO	Methyl orange

MS	Mass spectrometry
NF	Nanofiltration
NHE	Normal hydrogen electrode
OII	Orange II
PL	Photoluminescence
POPs	Persistent organic pollutants
ppm	Parts per million
PZC	Point zero charge
q_e	Adsorbed quantity at equilibrium
R^2	Coefficient constant
Ref.	Reference
RhB	Rhodamine B
RO	Reverse osmosis
SEM	Scanning electron microscope
T	Temperature in Kelvin
$t_{1/2}$	Half–life
TBA	*Tert*–butyl alcohol
TEM	Transmission electron microscope
TiO_2	Titanium dioxide
TOC	Total organic carbon
UF	Ultrafiltration
UV	Ultra violet (Light)
UV–vis	Ultra violet and visible (Light)
V	Volume of the unit cell of hexagonal
V/V	Volume per volume

VB	Valence band
W–H	Williamson–Hall
wt.%	Percent by weight
XPS	X–ray diffractometer
XRD	X–ray photoelectron spectroscopy
ZnO	Zinc oxide

CHAPTER 1

LITERATURE REVIEW

1.1. INTRODUCTION

The presence of organic pollutants (OPs) in humans has become subject of intense research for human exposure and health risk assessment [1]. This is the reason that, over the years, instruments to regulate and control environmental pollutants to protect human health and environment have been created by the international community. The most ambitious plan is the Stockholm Convention (2013), which aim is to eliminate and, when it is not possible, regulate emissions and discharges of persistent organic pollutants (POPs).

OPs can be defined as a set of highly toxic synthetic organic compounds, which have a long persistence in the environment. All this is because they are resistant to degradation and are bio–accumulative; therefore, they are incorporated in the tissues of living organisms and can increase their concentration through the food chain, and have the potential to be transported over long distances reaching areas where they had never occurred. All this makes them a threat to human health and the environment across the globe. OPs are manufactured either for a specific purpose (e.g. pesticides or flame–retardants) or produced as byproducts (e.g. of incinerated waste). They lead to chronic diseases such as male reproductive problems, pregnancy complications, certain cancers, obesity and affect brain development. Persistent organic pollutants (POPs) are toxic substances composed of organic (carbon–based) chemical compounds and mixtures. POPs possess a particular combination of physical and chemical properties [2], since they:

- remain intact for long periods of time (many years);
- become widely distributed throughout the environment as a result of natural processes involving soil, water and air;
- are resisting normal processes that break down contaminants;

- accumulate in the fatty tissue of living organisms and are found at higher concentrations at higher levels in the food chain; and
- are toxic to both humans and wildlife.

As a result of releases to the environment over the past several decades due especially to human activities, POPs are now widely distributed over large regions (including those where POPs have never been used) and, in some cases; they are found around the globe. This extensive contamination of environmental media and living organisms includes many foodstuffs and has resulted in the sustained exposure of many species, including humans, for periods of time that span generations, resulting in both acute and chronic toxic effects. Even small quantities of POPs can cause nervous system damage, diseases of the immune system, reproductive and developmental disorders, and cancers.

Organic pollution occurs when large quantities of organic compounds, which act as substrates for microorganisms, are released into watercourses. During the decomposition process the dissolved oxygen in the receiving water may be used up at a greater rate than it can be replenished, causing oxygen depletion and having severe consequences for the stream biota. Organic effluents also frequently contain large quantities of suspended solids which reduce the light available to photosynthetic organisms and, on settling out, alter the characteristics of the river bed, rendering it an unsuitable habitat for many invertebrates. Toxic ammonia is often present.

An immense array of organic compounds is currently widely used, and many of these are potent contaminants when they are released into freshwater ecosystems.

In a great majority of industrial processes water is used as a solvent, reaction or transport medium, therefore it is not surprising that many efforts in the last two decades have been made for the abatement of pollutants from industrial aqueous waste streams. Industrial plants generate increasing amounts of wastewater, contaminated with toxic and hazardous organic compounds, which cause severe problems for the environment. Wastewaters produced in many industrial processes often contain organic compounds that are toxic and not amenable to direct biological treatment. These industrial wastewaters must be treated in order to meet the specifications for discharge or for recycling in the process [3].

One of the main current worldwide concerns is the growth of water pollution by organic compounds arising from many industrial, agricultural and urban human activities. The vast majority of these compounds are persistent organic pollutants, owing to their resistance to conventional chemical, biological and photolytic processes. As a result, they have been detected in rivers, lakes, oceans and even drinking water all over the world. This constitutes a serious environmental health problem mainly due to their toxicity and potential hazardous health effects (carcinogenicity, mutagenicity and bactericidality) on living organisms, including human beings [4–7]. Water is the most important natural resource for life on our planet, and it is usually contaminated with materials including organic pollutants. A shortage of clean water can lead to serious problems and diseases. [8]. Dyes, chemicals, agricultural wastes and pharmaceuticals are some of the most common recalcitrant organic pollutants [9,10]. Most of these pollutants have characteristic features, such as low water solubility, high lipid solubility, semivolatility and high molecular masses, which enable their prevalence in air, land and water sources for a long time period [11].

1.2. DYES IN THE ENVIRONMENT

Many industries including textile, cosmetic, paper, leather, light–harvesting, arrays, agricultural research, photoelectrochemical cells, pharmaceutical and food produce large volumes of wastewater polluted with high concentration of dyes and other components. As a result, about 280,000 tons of textile dyes are currently discharged in effluents every year and introduced in the aquatic environment [12]. Moreover, 0.5–20% of dyes are lost in the dyeing process, the wastewater would be high in coloring, chemical oxidation demand (COD), alkalinity, toxicity and treatment difficulty [13]. Azo dyes are the largest group of synthetic colorants used in the textile industry [14] constituting 60–70% of all dyestuffs produced [15]. A dye is used to impart color to a material, of which it becomes an integral part. An aromatic ring associated with a side chain usually required for resonance and thus to impart color. Characterization of dyes is based on their chemical structure and application. They are composed of the atoms responsible for the dye color called chromophores as well as an electron withdrawing or donating substituent that causes or intensifies the color of chromophores, called auxochrome [16]. Usual chromophores are –C=C– (ethenyl), –C=O (carbonyl), –C=N– (imino), –CH=S (thiocarbonyl), –N=N– (azo), –N–O (nitroso), $–NO_2$ (nitro) and usual auxochromes are $–NH_2$ (amino), –COOH (carboxylic), $–SO_3H$ (sulphonyl) and –OH (hydroxyl) [17]. They have one or more azo groups (R1–N=N–R2) having aromatic rings mostly substituted by sulfonate group ($–SO_3$) and hydroxyl group (–OH), etc. [18]. Dyes often contain the complex aromatic molecular structure and are chemically stable against natural degradation [19].

1.3. EFFECTS OF DYE WASTEWATER

Textile wastewaters generated from different stages of textile processing contains huge amount of pollutants that are very harmful to the environment if released without proper treatment. The release of textile wastewater to the environment causes aesthetic problems as the changed color of the water bodies such as lakes and rivers, after releasing of wastewater from the industry, cannot be tolerated by the local people. For popular organic colorants in the Color Index, azo dyes are used the most (60–70% of the total) with potential toxic or carcinogenic products [20]. The accumulation of color hinders sunlight penetration, disturbs the ecosystem of receiving water and resists photochemical and biological attack [21]. Ground water systems are also get affected by these pollutants due to leaching through the soil [22]. Harmful direct and indirect effects of textile wastewater have been summarized in Figure 1.1.

Apart from this, several dyes and their decomposition derivatives have proved toxic to aquatic life (aquatic plants, microorganisms, fish and mammals) [23]. Additionally, fairly intensive studies has inferred that such colored allergens may undergo chemical and biological assimilations, cause eutrophication, consume dissolved oxygen, prevent reoxygenation in receiving streams and have a tendency to sequester metal ions accelerating genotoxicity and microtoxicity [24]. In a wider sense, sporadic and excessive exposure to colored effluents is susceptible to a broad spectrum of immune suppression, respiratory, circulatory, central nervous and neurobehavioral disorders presage as allergy, autoimmune diseases, multiple myeloma, leukemia, vomiting, hyperventilation, insomnia, profuse diarrhea, salivation, cyanosis, jaundice, quadriplegia, tissue necrosis, eye (or skin) infections, irritation to even lung edema [25]. Hence, to protect fragile ecosystems, it is

required that these dyes must undergo thorough elimination prior to their release.

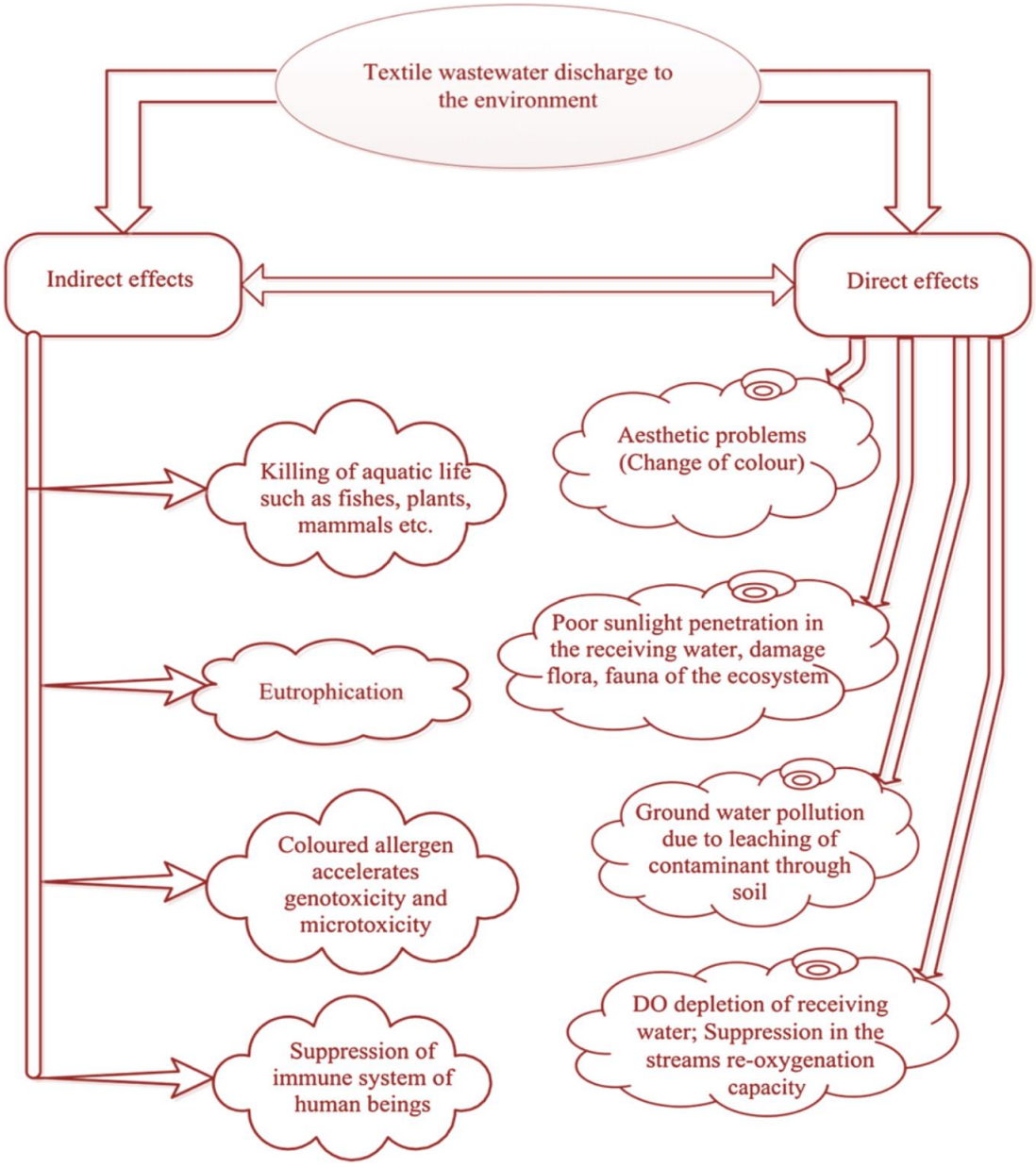

Figure 1.1. Schematic representation of the effect of textile wastewater into the environment (Reproduced from [26] with permission from Elsevier).

1.4. HERBICIDES IN THE ENVIRONMENT

Herbicides are included in a broad range of organic micro–pollutants with ecological impact. Distinct herbicide categories have different types of effects on living organisms, hampering generalization. Although herbicides have a soil impact, water pollution from herbicide runoff is the main pathway causing ecological effects [27]. In an effort to maximize crop yields, the application of pesticides has become commonplace. Recently, the widespread use of pesticides has come under scrutiny. For example, amitrole and atrazine are two such pesticides that have been detected in drinking water supplies and groundwater [28]. The main sources of water pollution by herbicides are agricultural activities, the cleaning of herbicide containers and equipment, and wastewaters from agricultural industries and herbicide manufacturing plants. The toxicity and persistence of herbicides means that they pose a severe environmental challenge [29]. Herbicides have widely variable toxicity. The acute toxicity due to exposure had led to long–term problems and a range of health effect from skin rashes to death [30]. World health organization estimated that at least 3 million cases of acute poisoning and 20,000 deaths occurs annually due to exposure to pesticide [31]. Figure 1.2 illustrates the main impacts of herbicides on environment.

Amitrole is a nonflammable, colorless–to–white, crystalline solid that is odorless when pure. It is a well–known herbicide which is often used in combination with other active agents for weed control in agriculture and along roadsides and railways [32,33]. It is also used as a chemical reagent in the photographic industry and as a hardening agent in chemical resins. Good solubility of amitrole leads to its penetration into surface and ground waters. Amitrole content in drinking water has been monitored at a regulatory level of 0.1 μg/L in European countries [34]. It

is non–selective and largely employed to substitute some banned herbicides. Associated symptoms in humans include skin rash, vomiting, diarrhea and nose bleeds can be caused by amitrole. It has also been reported as endocrine and thyroid gland disruptors as well as possible carcinogens [35]. Amitrole is one of the herbicides resistant to conventional treatment techniques, which raises the question of development of alternative methods for herbicide removal from the natural environment. Therefore, increasingly strict environmental restrictions in the presence of amitrole in effluents and natural systems require treatment technologies that minimize environmental risks at a reasonable cost.

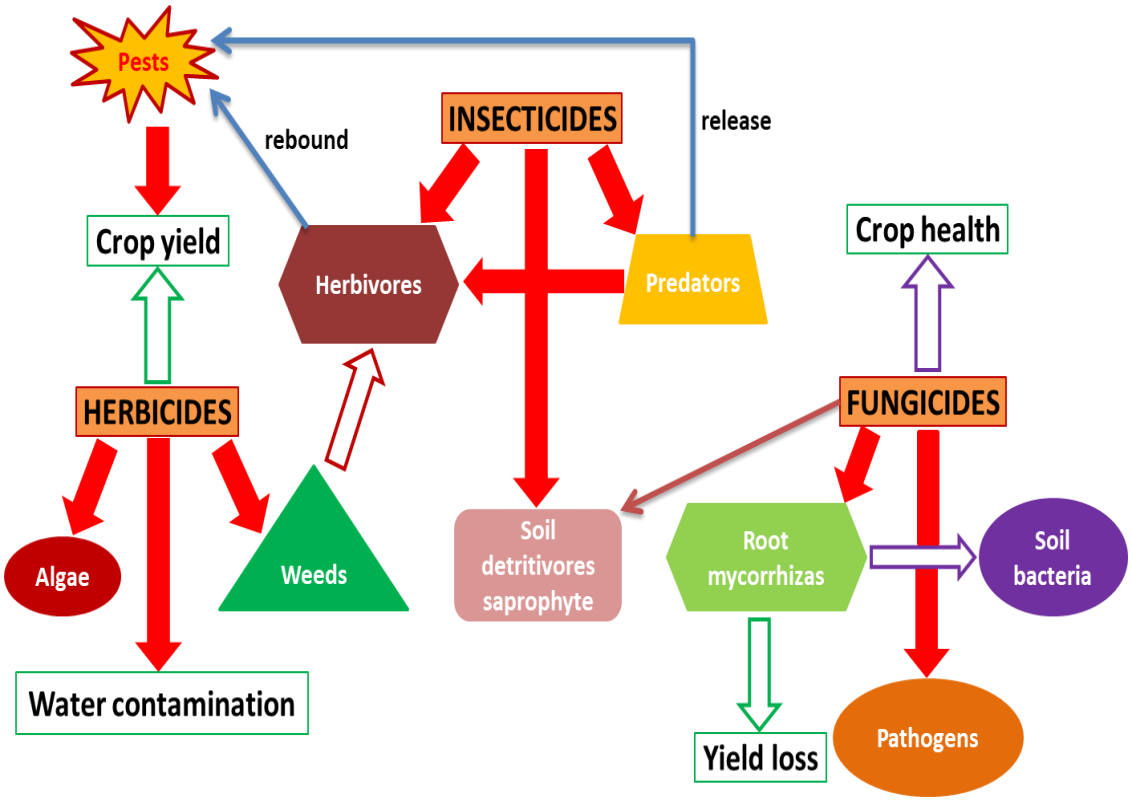

Figure 1.2. Schematic diagram showing the main impacts of herbicides on soil, plant and arthropod communities. Red arrows indicate decreases and blue arrows indicate increases; empty arrows indicate indirect effects.

1.5. PHARMACEUTICALS IN THE ENVIRONMENT

In recent years, the presence of pharmaceuticals in the environment has become a serious cause for concern and the problem is continuing to grow with the on–going development of more potent and more metabolically resistant drugs [36]. There are many classes of pharmaceuticals which include analgesics, anti–depressants, contraceptives, antibiotics and also veterinary medicines and pesticides used in agriculture. Endocrine disrupting chemicals (EDCs) are another class of compounds causing further alarm and these chemicals include not only hormones and contraceptive drugs but also a number of phenolic compounds, dioxins and polychlorobiphenyls (PCBs) amongst others [37,38]. All of these chemicals through various sources end up eventually in our environment and the effects of these bioactive molecules are, as of yet, still unknown. There are a number of point–sources for the entry of drugs to the environment [39]. At home, routes of entry include direct flushing of unused/out–of–date pharmaceuticals down the toilet. In the majority of cases, while on drug therapy, pharmaceuticals pass through our bodies. These drugs can undergo transformations in the body such as oxidation, reduction etc. or end up in a conjugated form of the original drug. In some cases though, drugs can be mostly un–metabolized and thus, entry through human waste (urine and faeces) is another route of entry to the environment [40,41]. Drugs that are discarded in household rubbish will inevitably end up in landfill and can leach into soil.

Famotidine (FMT) is a histamine H2–receptor antagonist, has been used by mixing with various drugs [42,43]. This compound is extensively used for treating a variety of stomach and duodenum sicknesses, connected with an excessive secretion of H^+ ions. It is potently inhibiting gastric acid secretion and is generally

used in the treatment and prevention of gastric and duodenal ulcers, gastroesophageal reflux disease and Zollinger–Ellison syndrome [44,45]. FMT is useful in promoting the healing of stomach and duodenal ulcers and reducing ulcer pain [46]. It is also used for treatment of Alzheimer's [47] and Parkinson's diseases [48]. In 2010, Famotidine was the 3rd (Pepcid Complete) and 4th (Pepcid AC) most popular antacid with sales of over $105 million [49]. In patients that use FMT, it has been documented that 65–70% of the drug is recovered unchanged in the urine, thereby rendering this drug as one of the many that is released into the environment on a day–to–day basis [50]. It is also discharged from the pharmaceutical industry and partially degraded during conventional water treatment [51]. Due to its common use, it is systematically found in wastewaters at low, but detectable concentrations [52]. It has been reported that average concentrations of FMT include 25 ng/L in drug production facilities, 94 ng/L in hospitals and 14 ng/L in regional wastewater discharges [53]. Its frequent presence in wastewaters underscores the need to study its fate in environmental conditions.

From a chemical point of view, FMT belongs to the thiazole derivative group of compounds. FMT is sparingly soluble in organic solvents such as chloroform, methanol and ether. It shows hydrophilic property ($\log K_{ow}$ = –0.64) [54]. This compound, due to the presence of an amine, thiazole and thioether groups in its structure, displays excellent complexing properties [55]. FMT slowly hydrolyzes in aqueous solutions (pK_a in aqueous solutions 6.7) [56]. The rate of hydrolysis depends on the pH and temperature of the solution [57]. The DT_{50} of FMT in solution at 25 °C has been assayed to be 43 days at pH 6.9 [58]. Taking the above into account, FMT could be considered as a persistent contaminant in an aqueous

environment.

Over 4000 pharmaceuticals are used across the globe for medical and veterinary healthcare, as well as growth promotion of livestock [59]. When most medications are consumed, parent compounds and metabolites are excreted into the wastewater system or directly into the environment [60] (Figure 1.3). Depending on their physico–chemical properties, compounds can be degraded, partition to water or solid phases including biosolids (such as sewage sludge) enter the aquatic or terrestrial environment. Ironically, some policies designed to improve the quality of aquatic environments and sustainability of water resources might contribute to the contamination of terrestrial ecosystems. For example, biosolids previously dumped in the ocean are now sent to landfills, incinerated or applied to agricultural land as fertilizer. Figure 1.3 illustrates the sources of pharmaceuticals in the environment, dispersion into the environment and the fate of pharmaceuticals in environments.

Aqueous sewage effluent is being used increasingly for irrigation, particularly in water–stressed regions of the world [61]. Agricultural applications of sewage derived biosolids containing human pharmaceuticals are currently dwarfed by the use of livestock manure (dung and urine) containing veterinary drugs, as fertilizer [62]. Veterinary drugs also may be released into the environment both directly (e.g. anthelmintic 'worming' treatments excreted in dung and antibiotics from the aquaculture industry) and indirectly via predation or scavenging of medicated animals [63] (Figure 1.3). Recycled raw sewage, municipal wastewater and biosolids are also being applied increasingly to urban green spaces such as parks and golf courses, which is likely to result in increased environmental exposure to

organisms occurring across a range of habitats [64]. Pharmaceuticals also have been detected at high concentrations near drug production facilities, particularly in countries with developing economies [65].

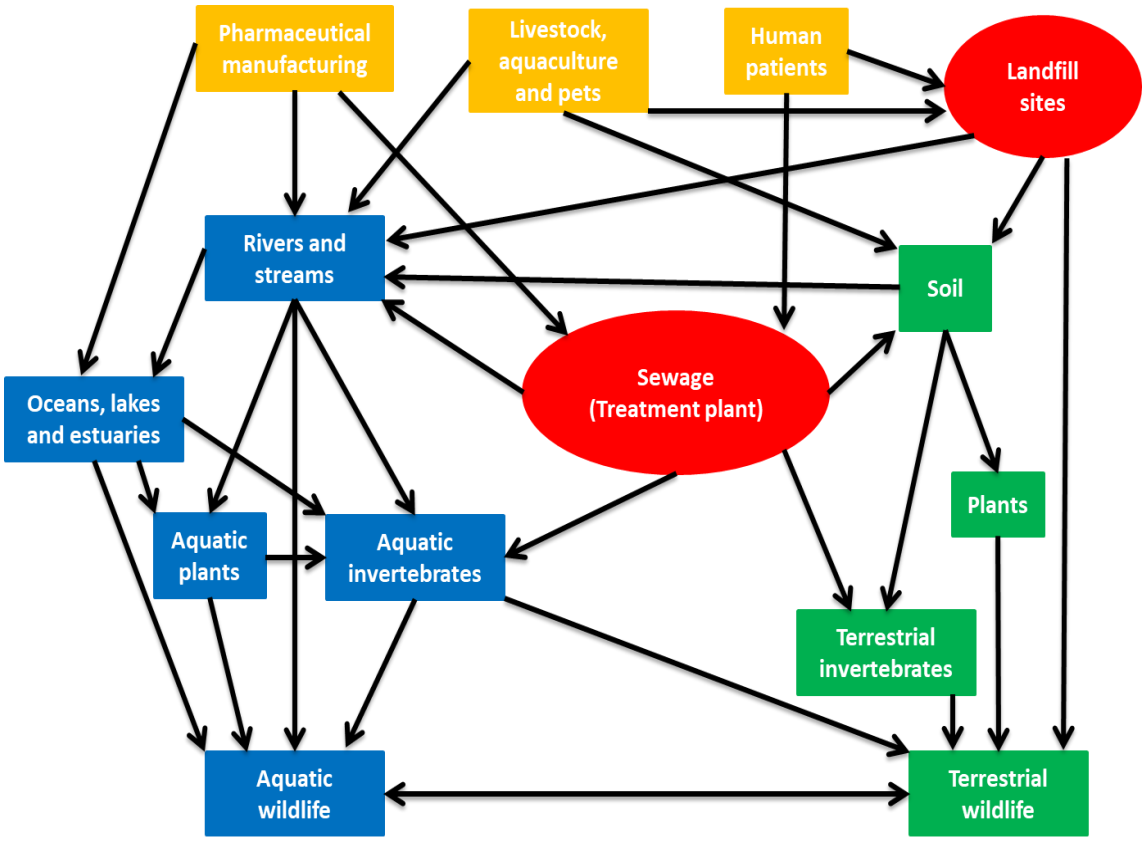

Figure 1.3. Pharmaceuticals can disperse through the environment via multiple and potentially complex pathways some of which are shown here. Sources of pharmaceuticals in the environment (yellow boxes) include pharmaceutical manufacturing, livestock, aquaculture and pets, and human patients. Pharmaceuticals can then disperse directly into the environment or via sewage treatment plants and landfill (red ovals). The fate of pharmaceuticals in aquatic (blue boxes) and terrestrial (green boxes) environments can result in uptake of pharmaceuticals into wildlife.

1.6. ORGANIC POLLUTANTS REMOVAL TECHNIQUES

Water sustainable supplies are vital for agriculture, industry, recreation, energy production and domestic consumption. The removal of organic pollutants is becoming an important environmental issue and a serious threat to the long term development of human society [66]. Among the various types of pollution, organic wastewater has attracted the attention of some researchers. The main sources of water contamination include the industrialization (textile, rubber, leather, paper, plastics, coal, food, petrochemical, pharmaceutical, dye industries, etc.), agricultural activities (the use of pesticides in agriculture, forestry, as well as veterinary and aquaculture drugs), municipal wastewater, other environmental and global changes [67,68]. A few hundred organic pollutants have been found to contaminate water resources [69]. These contaminations are very dangerous due to their various side effects and embryotoxicity, mutagenicity, teratogenicity and carcinogenicity as well as health disorders to human beings, such as the dysfunction of kidney, reproductive system, liver, brain, and central nervous system [70,71]. Hence, it is necessary to provide an effective treatment for organic wastewater. The elimination of OPs from wastes has been an important subject of many studies in order to protect the environment and water resources. Currently, several treatment technologies are employed to remove organic pollutants from wastewater which include coagulation–flocculation [72], biological treatment [73], membrane technologies [74], adsorption [75,76], advanced oxidation processes (AOPs) [77,78], photo–Fenton treatment [79], chemical oxidation [80], electrochemical oxidation/degradation [81], photocatalytic oxidation/degradation [82] and combined methods. Figure 1.4 represents the various techniques used for the removal of organic pollutants.

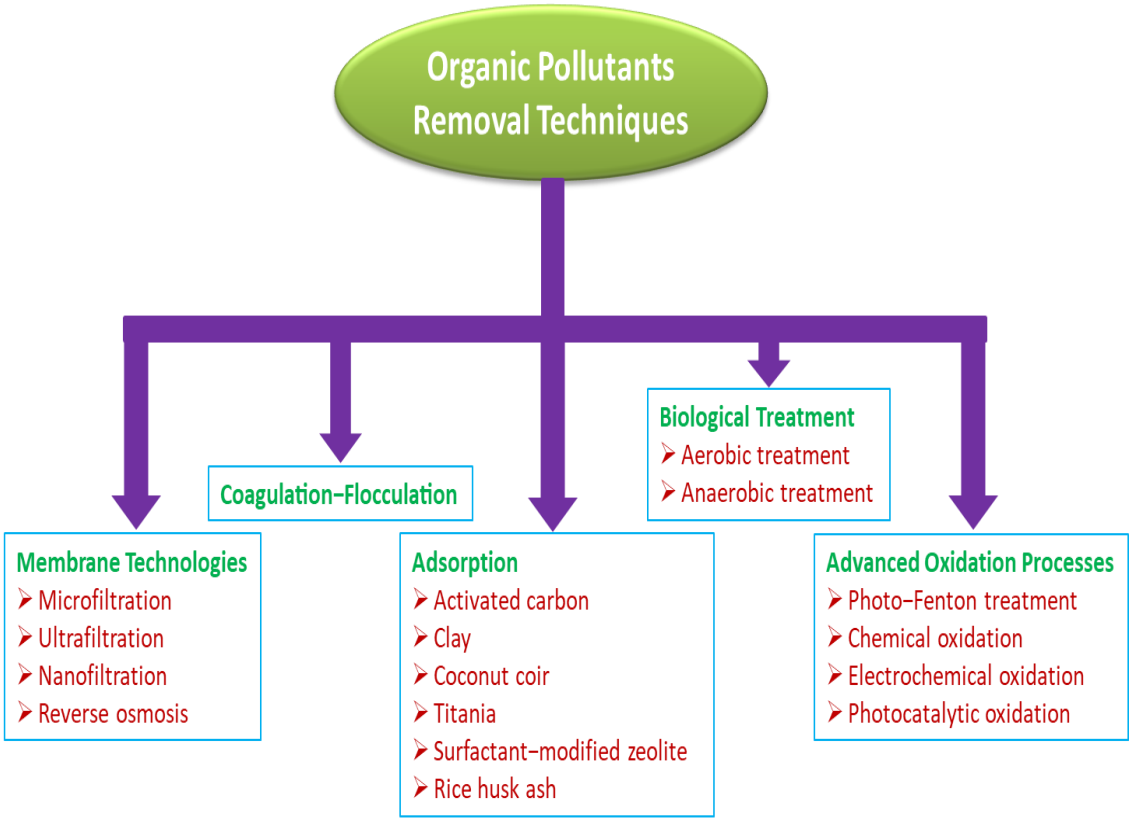

Figure 1.4. Schematic diagram showing various techniques used for the removal of organic pollutants.

1.6.1. Coagulation–Flocculation

The coagulation–flocculation process is one of the widely used methods for purification of urban and industrial wastewaters [83,84]. It was reported that the Egyptians were using aluminum sulfate (alum) to cause suspended particles to settle in water as early as 1500 BC [85]. Although the early Romans were also familiar with alum, it was not until 77 AD that its utilization as a coagulant in water treatment was mentioned [86]. Today, the coagulation–flocculation of water is implemented with the aim to agglomerate fine particles and colloids into larger particles for reducing turbidity, natural organic matter as well as other soluble organic and inorganic pollutants in the wastewater [85]. This process comprises two distinct stages: (i) rapid mixing of dispersed coagulant into water/wastewater

to be treated via violent agitation and (ii) flocculation for agglomeration of small particles into well–defined flocs via gentle agitation [87]. Finally, the flocs are allowed to settle and then removed as sludge while the treated water/wastewater (supernatant) is transferred into subsequent treatment process or for discharge into a watercourse. Owing to its easy operation, relatively simple design, and low energy consumption, coagulation–flocculation has been successfully employed in different types of industries [88,89]. Moreover, coagulation–flocculation can be used as a pretreatment, posttreatment, or even as the main treatment of wastewater because of the versatility of the treatment process [90]. Coagulation–flocculation is effective for removing high concentration organic pollutants in water and wastewater [91]. Coagulation of dye–containing wastewater has been used for many years as main treatment or pretreatment due to its low capital cost [92]. However, the major limitation of this process is the generation of sludge and ineffective decolorization of some soluble dyes [93].

1.6.2. Biological Treatment

Biological treatment is the most common and widespread technique used in dye wastewater treatment [94,95]. A large number of species have been used for decolouration and mineralization of various dyes. The methodology offers considerable advantages like being relatively inexpensive, having low running costs and the end products of complete mineralization not being toxic. The process can be aerobic (in presence of oxygen), anaerobic (without oxygen) or combined aerobic–anaerobic.

1.6.2.1. Aerobic treatment: Bacteria and fungi are the two microorganism groups that have been most widely studied for their ability to treat dye wastewaters. In

aerobic conditions, enzymes secreted by bacteria present in the wastewater break down the organic **c**ompounds. Aerobic wastewater treatment processes include treatments such as activated sludge, oxidation ditches, trickling filter, lagoon–based treatments and aerobic digestion. Equipment may include diffused aeration systems or mechanical surface aerators, in order to maximize oxygen transfer and minimize odors as the wastewater is treated. Aeration is one of the first stages in the process since bacteria and other organisms require oxygen to break down organic substances in the wastewater being treated. Activated sludge process is a proven biological wastewater treatment widely used for the secondary treatment of both domestic and industrial wastewater. It is particularly well suited for treating waste streams high in organic or biodegradable content. Biological filtration uses particular families of nonpathogenic microorganisms for aerobic treatment. Filters of this type contain media such as plastic balls or open–profile bio media, which have massive surface areas for the beneficial bacteria to adhere to and colonize. It can be used on challenging chemicals such as biodegradable organic compounds. However, biological treatment systems such as activated sludge and biological trickling filters are unable to remove a wide range of emerging contaminants and most of these compounds remain soluble in the effluent [96,97].

1.6.2.2. Anaerobic treatment: The potential of anaerobic treatment applications for the degradation of a wide variety of synthetic dyes has been well demonstrated and established [98]. Anaerobic treatment is a process that uses bacteria to break down organic material in an oxygen–free environment. Lagoons and septic tanks are example implementations of these types of anaerobic treatment methods. Typically, this treatment involves the degradation of organic matter anaerobically.

Azo dyes are generally persistent under aerobic conditions [99]. However, under anaerobic conditions, they undergo facile reductive fission, yielding colorless aromatic amine compounds [100]. Azo dyes require an anaerobic and an aerobic phase for their complete biodegradation. Combined anaerobic aerobic treatment is therefore the most logical strategy for the complete removal of azo dyes from wastewater.

1.6.3. Membrane Technologies

Membrane technologies which is classified into microfiltration (MF), ultrafiltration (UF), nanofiltration (NF) and reverse osmosis (RO) is a pressure–driven process in which the membrane acts as a selective barrier to restrict the passage of pollutants and allows relatively clear water to pass through [101,102]. These are considered as some new highly effective processes and as alternative methods of removing huge amounts of organic micropollutants [103,104]. Water/wastewater treatment by membrane techniques is cost–effective and technically feasible and can be better alternatives for the traditional treatment systems since their high efficiency in removal of pollutants meets the high environmental standards [105].

MF refers to membranes that have pore diameters from 0.1 to 10 μm [106] and is the membrane with the largest pores. It can be used to filter suspended particulates, large colloids, bacteria and organics. The MF is also used as pretreatment for NF and RO. UF refers to membranes that have pore diameters from 0.001 to 0.02 microns. UF generally used for the separation of colloids up to a range of 0.001 to 0.1 microns. It enables the concentration, purification and fractionation of macromolecules such as proteins, dyes, and other polymeric materials. UF is also used as a pretreatment to NF and RO processes. NF has

membrane pore size in the range between UF and RO. Simpson et al. [107] has defined NF as charged UF and is sometimes refers to as a low pressure RO. The NF has the advantage of low operating pressure compared to RO, and has a high rejection of organics compared to UF. Although NF based membrane processes are quite effective in removing huge loads of micropollutants [108], advanced materials and treatment methods are required to treat newly emerging micropollutants. RO was the first membrane process to be widely commercialized. It is a reversal of the natural process of osmosis. In RO, an external pressure greater than osmotic pressure is applied so that the water from concentrated solution passes into dilute solution. RO have proved to be quite effective filtration technologies for removal of micropollutants [109]. Membrane filtration have been considered as a promising technology for dissolve organic matter removal, however, membrane fouling is still one of the major challenges for its application on a large scale [110]. Furthermore, NF and RO membranes are not effective to treat complex and complicated polluted waters [111].

1.6.4. Adsorption

Adsorption is a surface phenomenon with common mechanism for organic and inorganic pollutants removal. When a solution containing absorbable solute comes into contact with a solid with a highly porous surface structure, liquid–solid intermolecular forces of attraction cause some of the solute molecules from the solution to be concentrated or deposited at the solid surface. The solute retained (on the solid surface) in adsorption processes is called adsorbate, whereas, the solid on which it is retained is called as an adsorbent. This surface accumulation of adsorbate on adsorbent is called adsorption. This creation of an adsorbed phase

having a composition different from that of the bulk fluid phase forms the basis of separation by adsorption technology.

In a bulk material, all the bonding requirements (be they ionic, covalent, or metallic) of the constituent atoms of the material are filled by other atoms in the material. However, atoms on the surface of the adsorbent are not wholly surrounded by other adsorbent atoms and therefore can attract adsorbates. The exact nature of the bonding depends on the details of the species involved, but the adsorption process is generally classified as physicsorption (characteristic of weak Van Der Waals forces) or chemisorption (characteristic of covalent bonding). It may also occur due to electrostatic attraction. As the adsorption progress, an equilibrium of adsorption of the solute between the solution and adsorbent is attained (where the adsorption of solute is from the bulk onto the adsorbent is minimum). The adsorption amount (q_e, mmol/g) of the molecules at the equilibrium step was determined according to the following Eq. (1.1) [112]:

$$q_e = V(C_o - C_e)/M \quad (1.1)$$

where V is the solution volume (L), M is the mass of monolithic adsorbents (g), and C_o and C_e are the initial and equilibrium adsorbate concentrations, respectively.

Other definition of adsorption is a mass transfer process by which a substance is transferred from the liquid phase to the surface of a solid, and becomes bound by physical and/or chemical interactions. Large surface area leads to high adsorption capacity and surface reactivity [113]. Adsorption is one of the most effective processes of advanced wastewater treatment which industries employ to reduce hazardous organic pollutants present in the effluent [114]. Due to validity, simplicity, inexpensiveness, ease of operation, flexibility, insensitivity to toxic

pollutants, as well as high efficiency and effectiveness, the adsorption is considered to be an attractive method for organic pollution purification [115]. Moreover, adsorption can also remove soluble and insoluble organic pollutants without the generation of hazardous by–products [116]. Various adsorbents have been developed for the removal of organic pollutants (e.g., dyes, pesticides, pharmaceuticals/drugs and phenols) from water [117,118]. In recent years, several materials and their activated carbon like clay [119], tree leaves [120], coconut coir [121], titania [122], surfactant–modified zeolite [123], rice husk ash [124], wheat straw [125] etc. have been evaluated as adsorbents for the removal of dyes and other pollutants from wastewaters. Among them, activated carbon is one of the most popular adsorbents used widely in different types of industries for removal of toxic pollutants, ions, non–biodegradable wastewaters regarding its excellent adsorption capacity and lower cost [126]. However, it has certain shortcomings that include limited availability, low adsorption capacity and difficult recovery.

1.6.5. Advanced Oxidation Processes (AOPs)

The concept of "advanced oxidation processes" was established by Glaze et co–workers in 1987 [127]. Advanced oxidation processes (AOPs) have following advantages (i) complete mineralization, (ii) no waste disposal problem, (iii) no expensive oxidants needed, (iv) low cost and (v) only mild temperature and pressure are necessary [128]. AOPs are one of the most promising ways for the effective degradation of many organic pollutants [129]. AOPs are found to be the most effective in the treatment of wastewater from different industries such as textiles [130], colour and pigments [131], dyes [132], pharmaceutical [133] and petroleum [134]. AOPs involve the generation of the hydroxyl radical (•OH), which

is a strong oxidizing agent (standard oxidation potential of 2.8 V) and can completely mineralize pollutants to CO_2, H_2O and oxides of inorganic compounds. Depending on the nature of the organic species, the generated hydroxyl radical can attack the organic compound by radical addition, hydrogen abstraction, electron transfer and radical combination [135]. However, their success depends upon the rate of production of hydroxyl radicals and the effective utilization of these radicals for mineralization. The various factors affecting the performance of AOPs include: types and concentration of contaminants, mechanism of production of oxidizing agents and their concentration, initial pH of the wastewater, temperature and pressure [136]. Four different methods are employed in Advanced Oxidation Processes (AOPs) to generate hydroxyl radicals and treat wastewater, namely (i) ozone treatment, (ii) electrochemical processes, (iii) direct decomposition of water and (iv) photocatalysis [137]. Figure 1.5 displays the advanced oxidation technologies for hydroxyl radical generation.

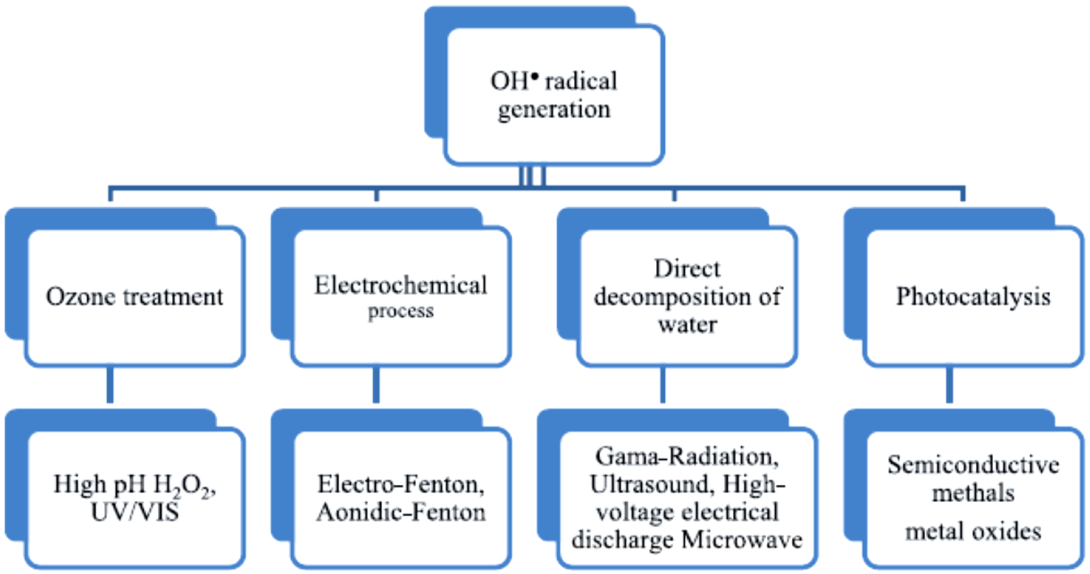

Figure 1.5. Advanced oxidation technologies for hydroxyl radical generations (Reproduced from [137] with permission from Elsevier).

1.6.6. Photo–Fenton Treatment

The Fenton process is cost effective, environmentally friendly, and increasingly used for wastewater treatment [138]. The oxidation power of Fenton reagent is due to the generation of hydroxyl radical (•OH) during the iron catalyzed decomposition of hydrogen peroxide in acid medium. This process involves a simple reaction between H_2O_2 and ferrous salts in an aqueous solution at ambient conditions to generate •OH radicals [139]:

$$Fe^{2+} + H_2O_2 \rightarrow Fe^{3+} + OH^- + {}^{\bullet}OH \qquad (1.2)$$

Hydroxyl radical with a high oxidation potential (2.8 eV) attacks and completely destroys the pollutants in Fenton process. The Fe species can be recycled via Eq. (1.3):

$$Fe^{3+} + H_2O_2 \rightarrow Fe^{2+} + HO_2^- + H^+ \qquad (1.3)$$

Despite being a chemically efficient process for the removal of organic pollutants, the Fenton reaction slows appreciably due to the slow conversion of ferric ions to ferrous salts (Eq. 1.2). The degradation of pollutants can be considerably improved by using UV–radiation. This is due to the generation of additional hydroxyl radicals [140].

The combination of Fenton reaction in UV light, the so–called photo–Fenton reaction, had been shown to enhance the efficiency of the Fenton process [141]. Photo–Fenton processes are reported to be effective in removing several classes of contaminants, such as pesticides [142], dyes [143], insecticides [144], pharmaceuticals [145], nitrobenzene [146], chlorophenols [147] and polychlorinated biphenyls [148]. Furthermore, the possibility of employing solar energy in photo–Fenton processes helps improving their economic and environmental sustainability. However, the application of such processes implies

some drawbacks including the need to operate in a narrow pH range (2.8–3.5). A strict pH control is substantially required to ensure that Fe(II) and Fe(III) species exert their catalytic role, thus avoiding any precipitation of inactive iron oxyhydroxides and maximizing the concentration of photoactive species. To this purpose, real applications include addition of acidifying reagents and final neutralization with relevant environmental and economic disadvantages [149]. Furthermore, the Fenton reaction produces substantial amounts of iron sludge due to the loss of iron ions and hydroxyl radicals are consumed by hydrogen peroxide due to the radical scavenging of hydrogen peroxide, limiting its application for wastewater treatment [150,151].

1.6.7. Chemical Oxidation

Chemical oxidation is one half of a redox reaction, which results in the loss of electrons. One of the reactants in the reaction becomes oxidized, or loses electrons, while the other reactant becomes reduced, or gains electrons. Oxidizing compounds that give electrons away to other compounds in a reaction are used to change the contaminants into harmless compounds. Chemical oxidation is a process involving the transfer of electrons from an oxidizing reagent to the chemical species being oxidized. Chemical oxidation has been effectively applied for several decades for the remediation of groundwater and aquifers [152]. Recently, it has become a popular technology for the remediation of organic contaminants in water and wastewater systems. Various kinds of oxidizing agents such as permanganate, ozone (O_3), hydrogen peroxide (H_2O_2), persulfate alone or in combination with other oxidants have been used for degradation of organic compounds [153,154]. H_2O_2 is the most commonly used oxidant for the selective degradation of organic contaminants in wastewater systems. Similarly, persulfate

and $SO_4^{\bullet-}$ radicals have been applied in the degradation of organic compounds and wastewater treatment [155].

1.6.8. Electrochemical Oxidation/Degradation

In electrochemical techniques, the main reagent is the electron, called the "Clean Reagent," which degrades all the organics present in the effluent without generating any secondary pollutant or by–product/sludge. The electrochemical technique offers high removal efficiencies and has lower temperature requirements compared to nonelectrochemical treatment. [156]. Electrochemical oxidation has been considered a promising method for biorefractory organic pollutants pollution control due to its environmental friendly, high energy efficiency, removal efficiency and strong controllability [137,158]. It has been applied in kinds of wastewater treatment, including pharmaceutical wastewater [159], printing and dyeing wastewater [160] and pesticide wastewater [161]. In the electrochemical oxidation process, the solutions are decontaminated through the direct reaction of pollutants with $^{\bullet}OH$ radicals formed at the anode surface [162] during the electrolysis process.

$$M + H_2O \rightarrow M(^{\bullet}OH) + H^+ + e^- \quad (1.4)$$

The electrode material, as a key part of electrolysis process, plays an important role in the electrochemical oxidation of pollutants [163]. Many electrode materials, such as Pt, graphite, SnO_2, IrO_2, PbO_2 and boron–doped diamond (BDD) electrodes [164,165], have been employed to the electrochemical degradation of different pollutants. Among the electrode materials, BDD is the best known material for electrochemical oxidation due to its excellent physical and chemical properties, which include high wide potential window, high stability in various solution and

extraordinarily well resistance to corrosion. Especially, the superior features of high oxygen evolution potential and high stability endow the BDD electrode with potential widely electrochemical application in wastewater treatment, and the degradation of different pollutants has been studied on BDD electrodes including phenols, surfactants, antibiotics and medical intermediate, pesticides, pigment and dyes, and so on [166]. The PbO_2 electrode has also been successfully used in wastewater treatment processes for its low cost and good electrochemical stability [167]. Nevertheless, the main drawbacks of electrochemical techniques are high electricity cost and sludge production and also pollution from chlorinated organics, heavy metals due to indirect oxidation.

1.6.9. Photocatalytic Oxidation/Degradation

The term photocatalysis consists of the combination of photochemistry and catalysis [168]. It implies that light and a catalyst are necessary to bring about or to accelerate a chemical transformation. In other words, photocatalysis can be defined as “acceleration of a photoreaction in the presence of a catalyst”. Photocatalysis involved a photochemical reaction at a metal oxide semiconductor's surface, which must be at least two reactions occurring simultaneously, the first reaction involving oxidation, from photo–induced positive holes, and the second reaction involving reduction, from photo–induced negative electrons [169]. In a heterogeneous photocatalysis system, photoinduced molecular transformations or reactions take place at the surface of a catalyst. This photocatalysis system has attracted great interest from science community as the most promising way to solve the environmental problems such as air purification, water disinfection, hazardous waste remediation and water purification [170,171]. In recent years, interest in photocatalysis has focused on the use of semiconductor materials as

photocatalysts for the removal of organic pollutants from water. Such semiconductors are increasingly used for oxidation or degradation of organic dyes and other contaminants particularly in industrial wastewater. The basic mechanism for this remediation is primarily based on the oxygen defects on the surface of the semiconducting materials which when activated by photon irradiation are used to destroy the organic contaminants [172]. Semiconductor photocatalysts have wide range of advantages for water treatment such as: [173–177].

- Capable of complete removal of pollutants
- Possible treatment for Non–biodegradable waste water
- Expensive chemicals are not required
- Low operational and installation cost
- No sludge treatment cost
- Unprofessional and unmanned operation
- Simple pre–processing
- Recycle and reuse of photocatalyst
- Small amount of catalyst can treat large amount of water
- Potential to utilize solar energy
- Negligible toxicity

Semiconductor photocatalysts are capable candidates to provide a sustainable solution for environmental pollution, through efficient degradation of pollutants [178]. Semiconductor photocatalysts play an important role in the process of the photodegradation of organic pollutants with light illumination (visible or UV light) [179,180]. The common semiconductors used in photocatalyst process are shown in Table 1.1.

Table 1.1

Common semiconductors used in photocatalysis processes [181].

Semiconductor	**Band gap (eV)**	**Wavelength (nm)**	**Light absorption**	**Valence band (V vs NHE)**	**Conduction band (V vs NHE)**
TiO_2	3.2	387	UV	+3.1	−0.1
ZnO	3.2	387	UV	+3.0	−0.2
SnO_2	3.8	318	UV	+4.1	+0.3
ZnS	3.7	335	UV	+1.4	−2.3
WO_3	2.8	443	Visible	+3.0	+0.4
CdS	2.5	496	Visible	+2.1	−0.4
CdSe	2.5	729	Visible	+1.6	−0.1

1.7. TITANIUM DIOXIDE (TiO_2)

Among various types of semiconductors, the traditional semiconductor titanium dioxide (TiO_2) has been widely studied for the degradation of various organic compounds because it is nontoxic, highly efficient, stable, environmentally friendly, and inexpensive [182–184]. TiO_2 exists as three natural allotropes: brookite (orthorhombic, 3.2 eV), anatase (tetragonal, 3.2 eV) and rutile (tetragonal, 3.0 eV). Anatase and rutile have been proven as the most effective photocatalysts, with anatase showing higher photocatalytic efficiency over rutile [185]. Degussa (Evonik) P25, Aeroxide TiO_2 P25, is a titania photocatalyst that is used widely because of its relatively high levels of activity in many photocatalytic reaction systems. It is well known that P25 is composed of anatase and rutile crystallites, the reported ratio being typically 70:30 or 80:20. The co–presence of anatase and rutile crystallites in P25 induces the high level of photocatalytic activity; transfer of photoexcited electrons and positive holes between interconnecting anatase and rutile particles may enhance charge separation and hence improve the efficiency of utilization of electron–hole pairs [186]. Titanium dioxide (TiO_2), has been extensively used on environmental applications, self–cleaning, deodorizing and sterilizing applications owing to its abundant resource, excellent photocatalytic performance, high refractive index, resistance to photocorrosion and high chemical stability against photodegradation (Figure 1.6). As an excellent catalyst, it has been proven to be a promising catalyst for water and air pollutant remedy or purification. Its excellent performance in pollutants destruction is mainly ascribed to the strong oxidation potential of the photogenerated valence band holes in TiO_2 (E_{VB} = +2.7 V vs. NHE at pH 7) [187,188].

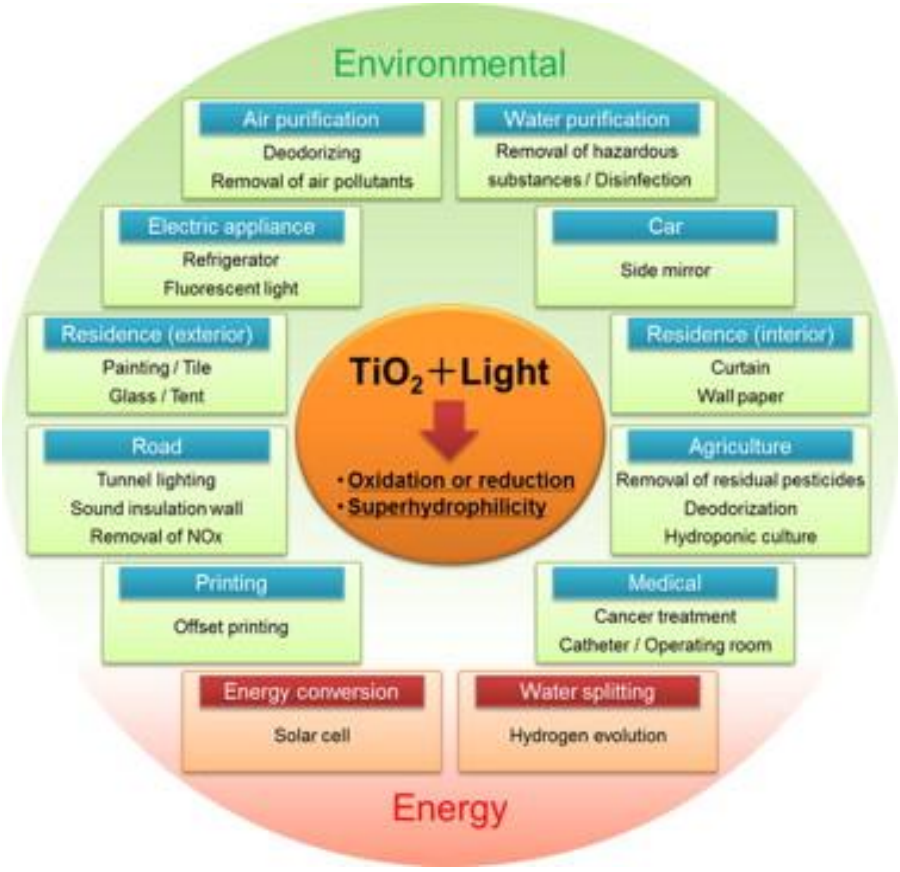

Figure 1.6. Applications of TiO_2 photocatalysis (Reproduced from [189] with permission from Elsevier).

1.8. ZINC OXIDE (ZnO)

In the field of photocatalysis today, ZnO has emerged as the leading candidate as an efficient and promising candidate in green environmental management system because of its unique characteristics, such as direct and wide band gap in the near–UV spectral region, strong oxidation ability and good photocatalytic property [190]. ZnO has received much attention in the degradation and complete mineralization of environmental pollutants [191]. ZnO has well–defined crystal structures which are commonly in rocksalt, wurtzite or cubic (zinc blende) structure. A rocksalt structure of ZnO can be yielded under high pressure thus ZnO in this structure is quite rare. The ZnO wurtzite structure has the highest thermodynamic stability among the three structures. It is the most common structure of ZnO [192]. The wurtzite structure comprises of two interpenetrating face–centered cubic (fcc) lattices of zinc and oxygen [193]. ZnO has large exciton binding energy of 60 meV and transparency in the visible region [194]. This fascinating property of ZnO has made it a potential material in the field of photocatalysis [195]. Since ZnO has almost the same band gap energy as TiO_2 (3.2 eV), its photocatalytic capability is anticipated to be similar to that of TiO_2. Moreover, ZnO is relatively cheaper compared to TiO_2 whereby the usages of TiO_2 are uneconomic for large scale water treatment operations [196]. The greatest advantage of ZnO is the ability to absorb a wide range of solar spectrum and more light quanta than some semiconducting metaloxides [197]. ZnO is one of the many naturally occurring oxygen deficient metal oxides that decomposes complex organic molecules in the presence of solar/UV illumination [198,199].

Titanium oxide (TiO_2) and zinc oxide (ZnO) have been considered to be of greater importance as they have the capacity to remove organic contaminants due to their physical and chemical properties, environmental friendliness and stability. However, their photocatalytic activity is triggered only by UV irradiation. This is a major setback to carry out the degradation of industrial effluent under natural solar light. The solar spectrum consists of only 5–7% of UV region and 45% of visible region. Achieving photocatalytic process in the visible region has greater significance in the minimization of the environmental issues [200]. Many efforts have been made in the last two decades in order to overcome this limitation. Several methods have been investigated to modify photocatalysts surface in order to extend the photo response range to visible spectral region. These include band gap modification, surface modifications and use of composite materials. Band gap modification can be done by doping with metal cations, nonmetal ions, nonmetal, transition metal, noble metal and metalloid [201,202]. Surface modification can be done via coupling organic materials and semiconductors e.g. by dye–sensitization; surface–complex assisted sensitization; polymer sensitization; and semiconductor coupling with co–catalysts, dye–sensitization and capping of photocatalysts etc. Among them, the two main approaches are dye–sensitization [203] and doping with impurities [204].

1.9. DYE–SENSITIZATION

The dye–sensitization technique has been reported as an innovative technology that could play an important role in developing efficient and cost–effective semiconductor photocatalyst in the near future [205]. It can extend the light absorption range, enhance photon harvesting efficiency, provide extra excited electron pairs from a dye and accelerate charge transfer, leading to a high efficiency of photoelectric conversion [206]. Dye–sensitized TiO_2 has been widely and successfully applied to the degradation of pollutants. The photocatalytic activity of TiO_2 under visible light could be enhanced by coupling of organic and inorganic dyes to TiO_2 surface [207]. Besides, the photochemical properties of dyes and the interfacial transfers of electrons between dyes and TiO_2 are very important parameters to ensure high photocatalytic efficiency [208]. The physical adsorption of dyes occurs through the weak van der Waals interaction between dye molecule and the TiO_2 surface. The extent of dye adsorption depends on the initial concentration of dye, the nature of dye, the surface of the photocatalyst and the pH of the solution [209]. The photochemical process is initiated by photoexcitation of dye molecules upon illumination by visible light, followed by the transfer of the electrons from the excited dye to the conduction band of TiO_2. Subsequently, in the presence of suitable electron donors (e.g. EDTA, organic acids, water, alcohols, etc.), the oxidized dye is regenerated. The injection of electron into the conduction band of TiO_2 is favorable due to the more negative potential of the lowest unoccupied molecular orbital (LUMO) of the dye molecules as compared to the potential of the TiO_2 conduction band [207]. The electrons injected by dye molecules to the surface of titania are scavenged by molecules of oxygen to promote the generation of superoxide radical $^{\bullet}O_2^-$ and hydrogen peroxide radical $^{\bullet}OOH$. These radicals attack the aromatic rings of organic pollutants forming intermediates and mineralizing

them to carbon dioxide and water. Figure 1.7 illustrates the principle of dye–sensitized TiO_2 under visible light illumination.

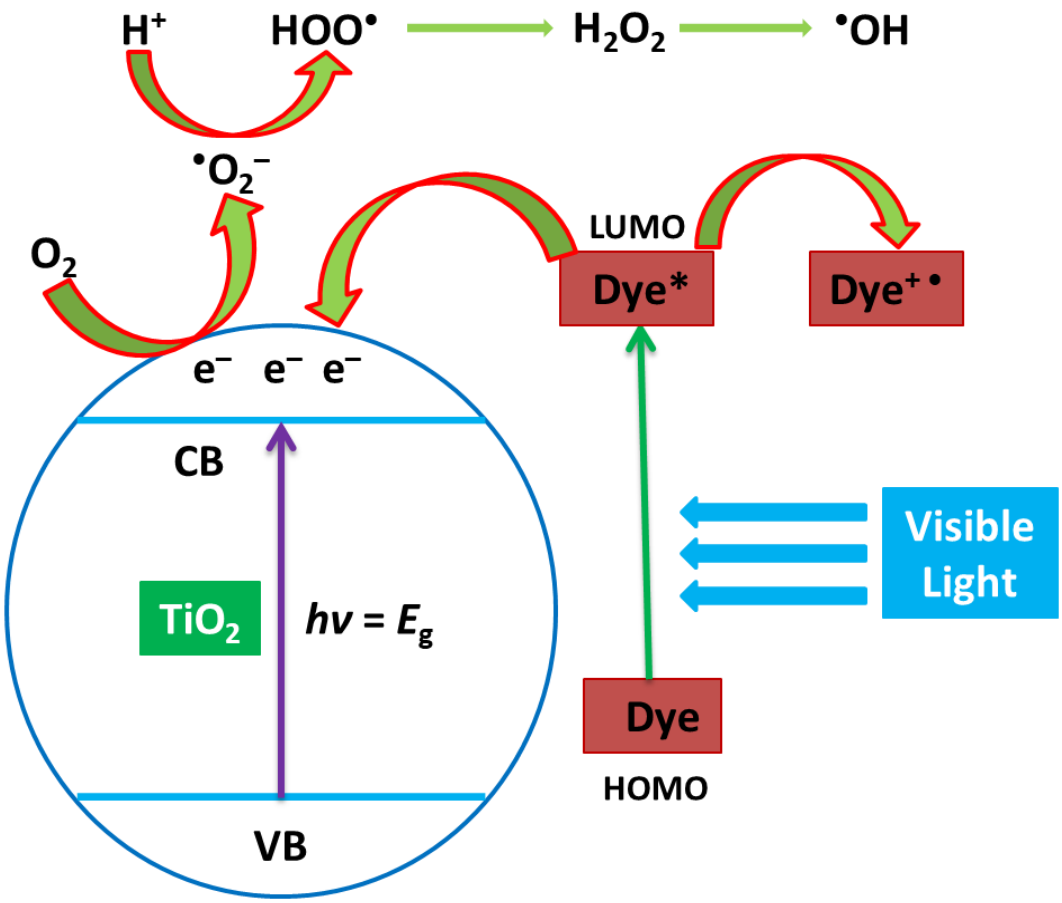

Figure 1.7. Schematic diagram illustrating the dye–sensitized TiO_2 pathway under visible light illumination.

1.10. DOPING PROCESSES

In doping processes, the rapid charge recombination is retarded and visible light absorption is enabled by defect states created in the band gap. In the first case, recombination is inhibited and the interfacial charge transfer is enhanced by the trapping of VB holes or CB electrons in the defect sites. In the second case, electronic transitions from the defect states to the CB or from the VB to the defect states are allowed under sub–band gap irradiation. Metal ions (transition metals and noble metals) and non–metal ions are the two main categories of dopants. [210]. The doping process shifts the optical absorption of ZnO into the visible region, expanding the excitation wavelength of the semiconductor as such increasing applications areas and improving its photocatalytic activity [211]. Different elements as Sn [212], Al [213], Mn [214], Mg [215], Ag [216], S [217] and N [218] are used in doping ZnO. Doped ZnO particles show remarkable characteristics compared to undoped ZnO such as reduced bandgap energy due to inter band formation between the CB and VB. Doping of Ag metal into the ZnO lattice can lead to changes in the electrical, optical and magnetic properties of ZnO. Besides, it reduces band gap energy of ZnO, improves charge separation between electron and hole by forming electron traps and, enhances photocatalytic activity of ZnO [219]. Especially Ag can trap the photogenerated electrons from the semiconductor and allow the holes to react with the surface–bound H_2O or OH^- to produce hydroxyl radicals ($^{\bullet}OH$) that result in the degradation reaction of organic species present [220]. Additionally, Ag also has the highest electrical and thermal conductivity among all metals, which makes it an ideal component for electrical interconnection [221]. As shown in Table 1.2, several researches have focused on photocatalytic activity by Ag modified ZnO under UV light irradiation and a few under visible and solar light irradiation using model organic pollutants.

Table 1.2

List of recently investigated photocatalytic activity of Ag/ZnO system.

Samples	Organic pollutants	Light source	Ref.
Ag–loaded ZnO	Phenol	Simulated solar light	[222]
Ag/ZnO	Methyl orange	UV light	[223]
Ag/ZnO	Methylene blue	Visible light	[224]
ZnO/Ag	Metamitron	UV light	[225]
	Metribuzin		
Ag/ZnO	Reactive Black GR	Sunlight	[226]
	Metronidazole	Visible light	
Ag/ZnO	Methyl Orange	UV light	[227]
	Phenol	Visible light	
ZnO–Ag	Rhodamine B	UV light	[228]
		Solar light	
		Visible light	
Ag–doped ZnO	Methyl violet	UV light	[229]
Ag–doped ZnO	Bisphenol A	UV light	[230]
	Nonylphenol		
Ag–ZnO	Methyl orange	UV light	[231]
Ag/ZnO	Methylene blue	UV light	[232]
Ag/ZnO	Rhodamine 6G	UV light	[233]
		Visible light	
Ag/ZnO	Rhodamine B	UV light	[234]
Ag/ZnO	Methyl orange	UV light	[235]

1.11. PHOTOCATALYTIC DEGRADATION MECHANISMS

1.11.1. Photocatalytic Oxidation

Removal of contaminants from water by heterogeneous photocatalysis has attracted constant research since its beginning as a great number of excellent reviews and books devoted by many researchers [236,237]. Although there are many types of photocatalysts and various applications, the basic principle in photocatalysis is mostly similar. Two or more phases are typically involved in a photocatalytic reaction: (a) a light source and (b) a semiconductor material are used to initiate the photoreaction while the catalyst system can simultaneously carry out oxidation and reduction reactions using UV light as well as sunlight. Under light illumination, photons with energies greater than the band–gap energy (ΔE) can result in the excitation of valence band (VB) electrons which leads to the promotion of electron from valence band to conduction band causing the formation of positive hole in the valence band and negative electron in the conduction band [238]. Figure 1.8 illustrates the mechanism of the photocatalytic oxidation of organic compounds under UV light [239]. The reactions for the photocatalytic process are as follows [240–243]:

$TiO_2 + h\nu\ (UV) \rightarrow TiO_2\ (e_{CB}^- + h_{VB}^+)$ (1.5)

$TiO_2\ (e_{CB}^- + h_{VB}^+) \rightarrow TiO_2 + heat$ (1.6)

$TiO_2\ (h_{VB}^+) + H_2O \rightarrow TiO_2 + H^+ + {}^\bullet OH$ (1.7)

$TiO_2\ (h_{VB}^+) + OH^- \rightarrow TiO_2 + {}^\bullet OH$ (1.8)

$TiO_2\ (e_{CB}^-) + O_2 \rightarrow TiO_2 + {}^\bullet O_2^-$ (1.9)

${}^\bullet O_2^- + H^+ \rightarrow HO_2^\bullet$ (1.10)

$HO_2^\bullet + HO_2^\bullet \rightarrow H_2O_2 + O_2$ (1.11)

$TiO_2\ (e_{CB}^-) + H_2O_2 \rightarrow {}^\bullet OH + OH^-$ (1.12)

$H_2O_2 + {}^{\bullet}O_2^- \rightarrow {}^{\bullet}OH + OH^- + O_2$ (1.13)

Organic compound + $^{\bullet}OH \rightarrow$ degradation products (1.14)

Organic compound + TiO_2 (h_{VB}^+) $\rightarrow$ oxidation products (1.15)

Organic compound + TiO_2 (e_{CB}^-) $\rightarrow$ reduction products (1.16)

The charges carriers, h_{VB}^+ and e_{CB}^-, can recombine, or h_{VB}^+ can be scavenged by oxidizing species (e.g., H_2O, OH^-, organic compound), and e_{CB}^-, by reducing species (e.g., O_2) in the solution. These combinations lead mainly to the formation of hydroxyl radicals ($^{\bullet}OH$) as well as superoxide radical anions ($^{\bullet}O_2^-$) and hydroperoxyl radicals ($HOO^{\bullet}$) on the surface of TiO_2, which are able to destroy a large variety of organic compounds (toxic and non–toxic) and biological agents [244–246].

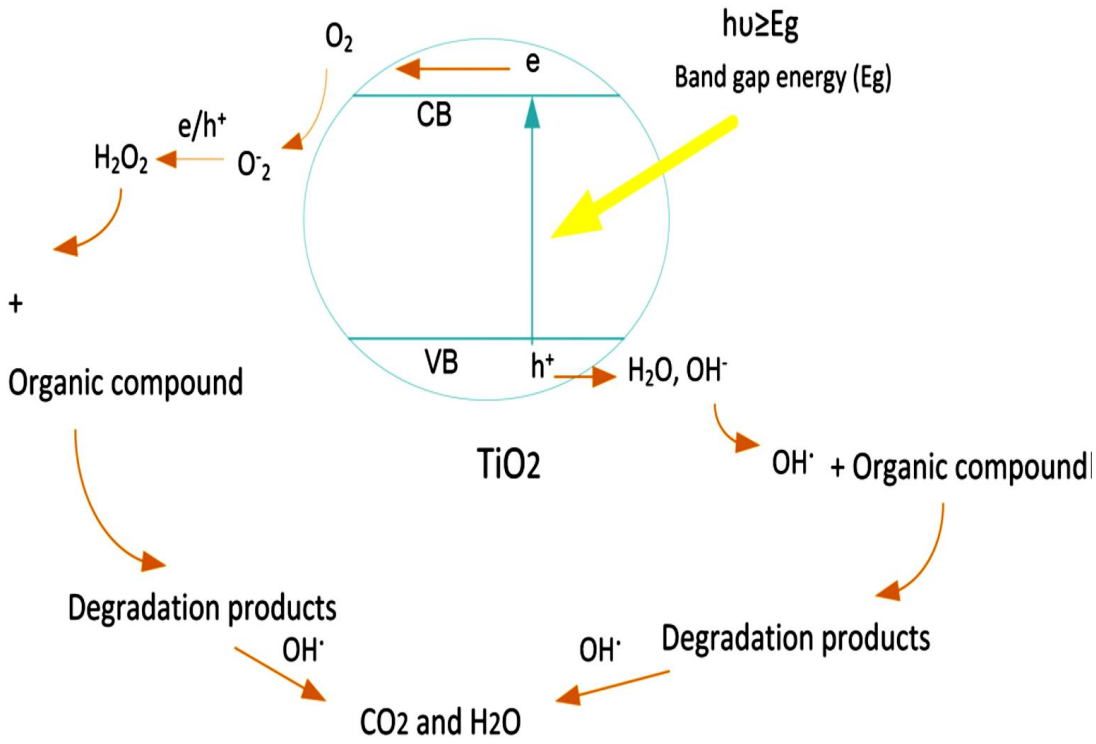

Figure 1.8. Schematic diagram illustrating the principle of TiO_2 photocatalysis (Reproduced from [239] with permission from Elsevier).

1.11.2. Photosensitized Oxidation

The mechanism of photosensitized oxidation (called also photo–assisted degradation) by visible radiation (λ > 420 nm) is different from the pathway implicated under UV light radiation. The mechanism suggests that excitation of the adsorbed dye takes place by visible light to appropriate singlet or triplet states, subsequently followed by electron injection from the excited dye molecule onto the conduction band of the TiO_2 particles, whereas the dye is converted to the cationic dye radicals ($Dye^{\bullet+}$) that undergoes degradation to yield products as follows [247–252]:

$$Dye + h\nu\ (VIS) \rightarrow {}^1Dye^* \text{ or } {}^3Dye^* \quad (1.17)$$

$${}^1Dye^* \text{ or } {}^3Dye^* + TiO_2 \rightarrow Dye^{\bullet+} + TiO_2\ (e_{CB}^-) \quad (1.18)$$

$$TiO_2\ (e_{CB}^-) + O_2 \rightarrow {}^{\bullet}O_2^- + TiO_2 \quad (1.19)$$

$$Dye^{\bullet+} \rightarrow \text{degradation products} \quad (1.20)$$

The cationic dye radicals readily react with hydroxyl ions undergoing oxidation via reactions 1.21 and 1.22 or interacts effectively with ${}^{\bullet}O_2^-$, $HO_2^{\bullet}$ or $HO^{\bullet}$ species to generate intermediates that ultimately lead to CO_2 (Eqs. 1.23–1.27).

$$Dye^{\bullet+} + OH^- \rightarrow Dye + {}^{\bullet}OH \quad (1.21)$$

$$Dye + 2\ {}^{\bullet}OH \rightarrow H_2O + \text{oxidation products} \quad (1.22)$$

$${}^{\bullet}O_2^- + H^+ \rightarrow HO_2^{\bullet} \quad (1.23)$$

$$HO_2^{\bullet} + H^+ + TiO_2\ (e_{CB}^-) \rightarrow H_2O_2 + TiO_2 \quad (1.24)$$

$$H_2O_2 + TiO_2\ (e_{CB}^-) \rightarrow {}^{\bullet}OH + HO^- + TiO_2 \quad (1.25)$$

$$Dye^{\bullet+} + {}^{\bullet}O_2^- \rightarrow DO_2 \rightarrow \text{degradation products} \quad (1.26)$$

$$Dye^{\bullet+} + HO_2^{\bullet} \text{ (or } {}^{\bullet}OH) \rightarrow \text{degradation products} \quad (1.27)$$

In experiments that are carried out using sunlight or simulated sunlight (laboratory experiments) it is suggested that both photooxidation and photosensitizing mechanism occurred during the irradiation, and both TiO_2 and the light source are necessary for the reaction to occur. In the photocatalytic oxidation, TiO_2 has to be irradiated and excited in near–UV energy to induce charge separation. On the other hand, dyes rather TiO_2 are excited by visible light followed by electron injection onto TiO_2 conduction band, which leads to photosensitized oxidation. It is difficult to conclude whether the photocatalytic oxidation is superior to the photosensitizing oxidation mechanism, but the photosensitizing mechanism will help to improve the overall efficiency and make the photobleaching of dyes using solar light more feasible [253].

1.12. OBJECTIVES OF THIS RESEARCH

Although extensive research works have been conducted for the removal of organic pollutants from wastewater using various techniques as discussed before, an efficient and cost effective treatment technique is yet to be established. Therefore, continued research is going on in this area. In this circumstance, this study has focused on the photocatalyst for the removal of organic pollutants from contaminated water in order to develop more efficient, economical and appropriate technique with the following main objectives:

- To investigate the optimization of solar photocatalytic degradation conditions of aqueous amitrole solution using TiO_2 and the mineralization of amitrole.
- To study the photocatalytic degradation and reaction mechanism of dye in water with self–dye–sensitized TiO_2 and ZnO under visible light irradiation.
- To evaluate the photocatalytic activity and reaction mechanism of dye–sensitized TiO_2 in the degradation of Famotidine under visible light irradiation.
- To study the photocatalytic degradation of Famotidine with Ag–doped ZnO under UV light irradiation and the optimum Ag–doping amount, calcination temperature and time.

1.13. REFERENCES

[1] A. Covaci, C. Hura, A. Gheorghe, H. Neels, A.C. Dirtu, Organochlorine contaminants in hair of adolescents from Iassy, Romania, Chemosphere 72 (2008) 16–20.

[2] S. Convention, Stockholm Convention, 2008, http://chm.pops.int/Home/tabid/2121/Default.aspx.

[3] J. Levec, A. Pintar, Catalytic wet–air oxidation processes: A review, Catal. Today 124 (2007) 172–184.

[4] H. Zollinger, Color Chemistry: Syntheses, Properties, and Applications of Organic Dyes and Pigments, 3rd ed., VHCA and Wiley–VCH, Zurich, 2003.

[5] K.P. Sharma, S. Sharma, S. Sharma, P.K. Singh, S. Kumar, R. Grover, P.K. Sharma, A comparative study on characterization of textile wastewaters (untreated and treated) toxicity by chemical and biological tests, Chemosphere 69 (2007) 48–54.

[6] K. Kümmerer, The presence of pharmaceuticals in the environment due to human use–Present knowledge and future challenges. J. Environ. Manage. 90 (2009) 2354–2366.

[7] C.A. Damalas, I.G. Eleftherohorinos, Pesticide exposure safety issues, and risk assessment indicators, Int. J. Environ. Res. Public Health 8 (2011) 1402–1419.

[8] E.S. Baeissa, Novel Pd/$CaSn(OH)_6$ nanocomposite prepared by modified sonochemical method for photocatalytic degradation of methylene blue dye, J. Alloy Compd. 590 (2014) 303–308.

[9] H. Lachheb, E. Puzenat, A. Houas, M. Ksibi, E. Elaloui, C. Guillard, J.–M. Herrmann, Photocatalytic degradation of various types of dyes (Alizarin S,

Crocein Orange G, Methyl Red, Congo Red, Methylene Blue) in water by UV–irradiated titania, Appl. Catal. B 39 (2002) 75–90.

[10] D. Sud, P. Kaur, Heterogeneous photocatalytic degradation of selected organophosphate pesticides: a review, Crit. Rev. Environ. Sci. Technol. 42 (2011) 2365–2407.

[11] S. Rasalingam, C.–M. Wu, R.T. Koodali, Modulation of pore sizes of titanium dioxide photocatalysts by a facile template free hydrothermal synthesis method: implications for photocatalytic degradation of rhodamine B, ACS Appl. Mater. Interfaces 7 (2015) 4368–4380.

[12] E. Brillas, C.A. Martinez–Huitle, Decontamination of wastewaters containing synthetic organic dyes by electrochemical methods. An updated review, Appl. Catal. B: Environ. 166–167 (2015) 603–643.

[13] C. Bauer, P. Jacques, A. Kalt, Photooxidation of an azo dye induced by visible light incident on the surface of TiO_2, J. Photochem. Photobiol. A Chem. 140 (2001) 87–92.

[14] S. Meric, D. Kaptan, T. Olmez, Color and COD removal from wastewater containing Reactive Black 5 using Fenton's oxidation process, Chemosphere 54 (2004) 435–441.

[15] K. M. Kodam, I. Soojhawon, P.D. Lokhande, K.R. Gawai, Microbial decolourization of a reactive azo dye under anaerobic conditions, World J. Microbiol. Biotechnol. 21 (2005) 367–370.

[16] R. Christie, Color Chemistry, The Royal Society of Chemistry, Cambridge, UK, 2001.

[17] F.P. Van der Zee, Anaerobic azo dye reduction, PhD Dissertation, Wageningen University, Wageningen, The Netherlands, 2002.

[18] P. Rajaguru, K. Kalaiselvi, M. Palanivel, V. Subburam, Biodegradation of azo dyes in a sequential anaerobic–aerobic system, Appl. Microbiol. Biotechnol. 54 (2000) 268–273.

[19] M.A. Ahmed, E.E. El–Katori, Z.H. Gharni, Photocatalytic degradation of methylene blue dye using Fe_2O_3/TiO_2 nanoparticles prepared by sol–gel method, J. Alloys Compd. 553 (2013) 19–29

[20] A. Houas, H. Lachheb, M. Ksibi, E. Elaloui, C. Guillard, J.M. Hermann, Photocat–alytic degradation pathway of methylene blue in water, Appl. Catal. B Environ. 31 (2001) 145–157.

[21] B. Merzouk, K. Madani, A. Sekki, Using electrocoagulation–electroflotation technology to treat synthetic solution and textile wastewater, two case studies, Desalination 250 (2010) 573–577.

[22] A. Khaled, A. El–Nemr, A. El–Sikaily, O. Abdelwahab, Treatment of artificial textile dye effluent containing direct yellow 12 by orange peel carbon, Desalination 238 (2009) 210–232.

[23] G.E. Ustun, S.K.A. Solmaz, A. Birgul, Regeneration of industrial district wastewater using a combination of Fenton process and ion exchange–A case study, Resour. Conserv. Recycl. 52 (2007) 425–440.

[24] K.Y. Foo, B.H. Hameed, Decontamination of textile wastewater via TiO_2/ activated carbon composite materials, Adv. Colloid Interface Sci. 159 (2010) 130–143.

[25] R. Anliker, In: Richardson, M. (Ed.), Toxic hazard assessment of chemicals, The Royal Society of Chemistry, London, 1986.

[26] A.K. Verma, R.R. Dash, P. Bhunia, A review on chemical coagulation/flocculation technologies for removal of colour from textile wastewaters, J. Environ. Manage. 93 (2012) 154–168.

[27] F. Orellana–Garcı´a, M.A. A´lvarez, M.V. Lo´pez–Ramo´n, J. Rivera–Utrilla, M. Sa´nchez–Polo, Effect of $HO^{\bullet}$, SO_4^{-} and CO_3^{-}/HCO_3^{-} radicals on the photodegradation of the herbicide amitrole by UV radiation in aqueous solution, Chem. Eng. J. 267 (2015) 182–190.

[28] J. Andersen, M.l Pelaez, L. Guay, Z. Zhang, K. O'Shea, D.D. Dionysiou, NF–TiO_2 photocatalysis of amitrole and atrazine with addition of oxidants under simulated solar light: Emerging synergies, degradation intermediates, and reusable attributes, J. Hazard. Mater. 260 (2013) 569–575.

[29] F. Orellana–Garcı´a, M.A. A´lvarez, V. Lo´pez–Ramo´n, J. Rivera–Utrilla, M. Sa´nchez–Polo, A.J. Mota, Photodegradation of herbicides with different chemical natures in aqueous solution by ultraviolet radiation. Effects of operational variables and solution chemistry, Chem. Eng. J. 255 (2014) 307–315.

[30] D. Mada, N. Duniya, I.G. Adams, Effect of continuous application of herbicide on soil and environment with crop protection machinery in southern adamawa state, Inter. Ref. J. Eng. Sci. 2 (2013) 4–9.

[31] P. Orhii, Sensitization Workshop on Safe and Responsible use of Agro chemical, National Agency for food and Drug Administration and Control Abuja, Nigeria, 2010, 2–6.

[32] M. Ersoz, H.J. Duncan, M. Lale, H.I. Ucan, Herbicide penetration through isolated periderm and cuticular membranes. Environ. Tech. 17 (1996) 87–93.

[33] L. Agnolucci, F.D. Vecchia, R. Barbato, V. Tassani, G. Casadoro, N. Rascio, Amitrole effects on chloroplasts of barley plants grown at different temperatures, J. plant physiol. 147 (1996) 493–502.

[34] A. Da Pozzo, C. I. Merli, Sirés, J. A. Garrido, R.M. Rodríguez, E. Brillas, Removal of the herbicide amitrole from water by anodic oxidation and electro–Fenton, Environ. Chem. Lett. 3 (2005) 7–11.

[35] C. Chen, S. Yang, Y. Gao, C. Sun, B. Gu, C. Xu, Photolytic destruction of endocrine disruptor atrazine in aqueous solution under UV irradiation: products and pathways, J. Hazard. Mater. 172 (2009) 675–684.

[36] S.K. Khetan, T.J. Collins, Human pharmaceuticals in the aquatic environment: a challenge to green chemistry, Chem. Rev. 107 (2007) 2319–2364.

[37] Z. Liu, Y. Kanjo, S. Mizutani, Removal mechanisms for Endocrine Disrupting Compounds (EDCs) in wastewater treatment–physical means, biodegradation, and chemical advanced oxidation: a review, Sci. Total Environ. 407 (2009) 731–748.

[38] http://ec.europa.eu/environment/water/water-framework/priority_substances.htm (accessed: 06–12–2012).

[39] K. Kummerer, Pharmaceuticals in the Environment: Sources, Fate, Effects and Risks, Springer Publications, 2005.

[40] K. Kakinoki, K. Yamane, R. Teraoka, M. Otsuka, Y. Matsuda, Effect of relative humidity on the photocatalytic activity of titanium dioxide and photostability of famotidine, J. Pharm. Sci. 93 (2004) 582–589.

[41] M. Maniscalco, D. Singh–Franco, W.R. Wolowich, R. Torres–Colón, Solifenacin succinate for the treatment of symptoms of overactive bladder, Clin. Ther. 28 (2006) 1247–1272.

[42] M.H. Torosian, Stability and compatibility issues, In Nutrition for the hospitalized patient: Basic science and principles of practice, New York, Marcel Dekker, 1995.

[43] X. Keyi, N. Gagnon, C. Bisson, M, Desmarais, M. LeBel, Stability of famotidine in polyvinyl chloride minibags and polypropylene syringes and compatibility of famotidine with selected drugs, Ann. Pharmacother. 27 (1993) 422–426.

[44] C.W. Howden, G.N. Tytgat, The tolerability and safety profile of famotidine, Clin. Ther. 18 (1996) 36–41.

[45] H.D. Langtry, S.M. Grant, K.L. Goa, Famotidine, and updated review of its pharmacodynamic and pharmacokinetic properties, and therapeutic use in peptic ulcer disease and other allied diseases, Drug 38 (1989) 551–557.

[46] J.G. Hardman, L.E. Limbird, P.B. Molinoff, R.W. Ruddon, A.G. Goodman, (eds.), Goodman and Gilman's The Pharmacological Basis of Therapeutics, 9th ed., McGraw Hill, New York, 1996.

[47] J.C. Breitner, K.A. Welsh, M.J. Helms, P.C. Gaskell, B.A. Gau, A.D. Roses, M.A. Pericak–Vance, A.M. Saunders, Delayedonsetof Alzheimer's diseasewith nonsteroidal anti–inflammatory and histamine H_2 blocking drugs, Neurobiol. Aging 16 (1995) 523–527.

[48] S.P. Molinary, R. Aminski, A.D. Rocco, M.D. Yahr, The use of famotidine in treatment of Parkinson's disease: a pilot study, J. Neural Transm. 9 (1995) 243–248.

[49] Data sourced from SymphonyIRI Group Inc.

[50] K.W. Lee, S.R. Kayser, R.H. Hongo, Z.H. Tseng, M.M. Scheinman, Famotidine and long QT syndrome, Am. J. Cardiol. 93 (2004) 1325–1327.

[51] J. Radjenovic´, M. Petrovic´, D. Barcelo´, Fate and distribution of pharmaceuticals in wastewater and sewage sludge of the conventional activated sludge (CAS) and advanced membrane bioreactor (MBR) treatment, Water Res. 43 (2009) 831–841.

[52] S. Terzic´, I. Senta, M. Ahel, M. Gros, M. Petrovic´, D. Barcelo, J. Muller, T. Knepper, J. Marti, F. Ventura, P. Jovanc´ic´, D. Jabuc´ar, Occurrence and fate of emerging wastewater contaminants in Western Balkan region, Sci. Total Environ. 399 (2008) 66–77.

[53] A.Y.–Ch. Lin, T.–H. Yu, Ch.–F. Lin, Pharmaceutical contamination in residential, industrial, and agricultural waste streams: Risk to environments in Taiwan, Chemosphere 74 (2008) 131–41.

[54] M. Gross, M. Petrovic´, D. Barcelo, Development of a multi–residue analytical methodology based on liquid chromatography–tandem mass spectrophotometry (LC–MS/MS) for screening and trace level determination of pharmaceuticals in surface and wastewaters, Talanta 70 (2006) 678–90.

[55] S. Murphy, C. Saurel, A. Morrissey, J. Tobin, M. Oelgemoller, K. Nolan, Photocatalytic activity of a porphyrin/TiO_2 composite in the degradation of pharmaceuticals, Appl. Catal. B: Environ. 119–120 (2012) 156–165.

[56] G.L. Patrick, Chemia medyczna, Warszawa: WNTed, 2003.

[57] Y. Wu, R. Fassihi, Stability of metronidazole, tetracycline HCl and famotidine alone and in combination, Int. J. Pharm. 290 (2005) 1–13.

[58] G.H. Junnarkar, S. Stavchansky, Isothermal and nonisothermal decomposition of famotidine in aqueous solution, Pharm. Res. 2 (1995) 599–604.

[59] Boxall ABA et al. Pharmaceuticals and personal care products in the environment: what are the big questions? Environ. Health Perspect. 120 (2012) 1221–1229.

[60] S.C. Monteiro, A.B.A. Boxall, Occurrence and fate of human pharmaceuticals in the environment, Rev. Environ. Contam. Toxicol. 202 (2010) 53–154.

[61] G. Gielen, M.R. van den Heuvel, P.W. Clinton, L.G. Greenfield, Factors impacting on pharmaceutical leaching following sewage application to land, Chemosphere 74 (2009) 537–542.

[62] Topp E et al. Runoff of pharmaceuticals and personal care products following application of biosolids to an agricultural field, Sci. Total Environ. 396 (2008) 52–59.

[63] K.J. Park, C.T. Muller, S. Markman, O. Swinscow–Hall, D. Pascoe, K.L. Buchanan, Detection of endocrine disrupting chemicals in aerial invertebrates at sewage treatment works, Chemosphere 77 (2009) 1459–1464.

[64] D. Fatta–Kassinos, I.K. Kalavrouziotis, P.N. Koukoulakis, M.I. Vasquez, The risks associated with wastewater reuse and xenobiotics in the agroecological environment, Sci. Total Environ. 409 (2011) 3555–3563.

[65] D.G.J. Larsson, Pollution from drug manufacturing: review and perspectives, Phil. Trans. R. Soc. B 369 (2014) 20130571.

[66] S. Horikoshi, F. Hojo, H. Hidaka, N. Serpone, Environmental remediation by an integrated microwave/UV illumination technique. 8. Fate of Carboxylic acids, aldehydes, alkoxycarbonyl and phenolic substrates in a microwave radiation field in the presence of TiO_2 particles under UV irradiation, Environ. Sci. Technol. 38 (2004) 2198–2208.

[67] V.O. Njoku, M.A. Islam, M. Asif, B.H. Hameed, Utilization of sky fruit husk agricultural waste to produce high quality activated carbon for the herbicide bentazon adsorption, Chem. Eng. J. 251 (2014) 183–191.

[68] C. Djilani, R. Zaghdoudi, A. Modarressi, M. Rogalski, F. Djazi, A. Lallam, Elimination of organic micropollutants by adsorption on activated carbon prepared from agricultural waste, Chem. Eng. J. 189–190 (2012) 203–212.

[69] I. Ali, M. Asim, T.A. Khan, Low cost adsorbents for the removal of organic pollutants from wastewater, J. Environ. Manag. 113 (2012) 170–183.

[70] A.S. Costa, L.P.C. Romão, B.R. Araújo, S.C.O. Lucas, S.T.A. Maciel, A. Wisniewski Jr., M.R. Alexandre, Environmental strategies to remove volatile aromatic fractions (BTEX) from petroleum industry wastewater using biomass, Bioresour. Technol. 105 (2012) 31–39.

[71] M.P. Tavlieva, S.D. Genieva, V.G. Georgieva, L.T. Vlaev, Kinetic study of brilliant green adsorption for aqueous solution onto white rice husk ash, J. Colloid Interface Sci. 49 (2013) 112–122.

[72] S.W. Won, S.B. Choi, B.W. Chung, D. Park, J.M. Park, Y.S. Yun, Biosorptive decolorization of reactive orange 16 using the waste biomass of corynebacterium glutamicum, Ind. Eng. Chem. Res. 43 (2004) 7865–7869.

[73] R. Ahmad, P.K. Mondal, S.Q. Usmani, Hybrid UASFB aerobic bioreactor for biodegradation of acid yellow–36 in wastewater, Bioresour. Technol. 101 (2010) 3787–3790.

[74] Y. Xu, R.E. Lebrun, P.–J. Gallo, P. Blond, Treatment of textile dye plant effluent by nanofiltration membrane, Sep. Sci. Technol. 34 (1999) 2501–2519.

[75] Y.L. Dong, B. Lu, S.Y. Zang, J.X. Zhao, X.G. Wang, Q.H. Cai, Removal of methylene blue from coloured effluents by adsorption onto SBA–15, J. Chem. Technol. Biotechnol. 86 (2011) 616–619.

[76] P.V. Messina, P.C. Schulz, Adsorption of reactive dyes on titania–silica mesoporous materials, J. Colloid Interface Sci. 299 (2006) 305–320.

[77] W. Guo, X. Liu, P. Huo, X. Gao, D. Wu, Z. Lu, Y. Yan, Hydrothermal synthesis spherical TiO_2 and its photo–degradation property on salicylic acid, Appl. Surf. Sci. 258 (2012) 6891–6896.

[78] Z. He, C. Sun, S. Yang, Y. Ding, H. He, Z. Wang, Photocatalytic Degradation of rhodamine B by Bi_2WO_6 with electron accepting agent under microwave irradiation: mechanism and pathway, J. Hazard. Mater. 162 (2009) 1477–1486.

[79] J.M. Salman, V.O. Njoku, B.H. Hameed, Adsorption of pesticides from aqueous solution onto banana stalk activated carbon, Chem. Eng. J. 174 (2011) 41–48.

[80] M. Ahmaruzzaman, S.L. Gayatri, Activated tea waste as a potential low–cost adsorbent for the removal of p–nitrophenol from wastewater, J. Chem. Eng. Data 55 (2010) 4614–4623.

[81] M.J.K. Ahmed, M. Ahmaruzzaman, R.A. Reza, Lignocellulosic–derived modified agricultural waste: development, characterisation and implementation in sequestering pyridine from aqueous solutions, J. Colloid Interface Sci. 428 (2014) 222–234.

[82] J.M. Salman, B.H. Hameed, Effect of preparation conditions of oil palm fronds activated carbon on adsorption of bentazon from aqueous solutions, J. Hazard. Mater. 175 (2010) 133–137.

[83] T. Pavón–Silva, V. Pacheco–Salazar, J. Carlos Sánchez–Meza, G. Roa–Morales, A. Colín–Cruz, Physicochemical and biological combined treatment applied to a food industry wastewater for reuse, J. Environ. Sci. Health, Part A: Toxic/Hazard. Subst. Environ. Eng. 44 (2009) 108–115.

[84] A.C. Rodrigues, M. Boroski, N.S. Shimada, J.C. Garcia, J. Nozaki, N. Hioka, Treatment of paper pulp and paper mill wastewater by coagulation–flocculation followed by heterogeneous photocatalysis, J. Photochem. Photobiol. A 194 (2008) 1–10.

[85] S. Parson, B. Jefferson, Introduction to Potable Water Treatment Processes, Blackwell Publishing Ltd., UK, 2006.

[86] J. Bratby, Coagulation and Flocculation in Water and Wastewater Treatment, IWA Publishing, UK, 2006.

[87] F.R. Spellman, Mathematic Manual for Water and Wastewater Treatment Plant Operators, CRC Press, Boca Raton, FL, 2004.

[88] F. Almubaddal, K. Alrumaihi, A. Ajbar, Performance optimization of coagulation/flocculation in the treatment of wastewater from a polyvinyl chloride plant, J. Hazard. Mater. 161 (2009) 431–438.

[89] L.G. Torres, C. Belloc, M. Vaca, R. Iturbe, E.R. Bandala, Coagulation–flocculation process applied to wastewaters generated in hydrocarbon–contaminated soil washing: Interactions among coagulant and flocculant concentrations and pH value, J. Environ. Sci. Health Part A: Toxic/Hazard. Subst. Environ. Eng. 44 (2009) 1449–1456.

[90] A. Szyguła, E. Guibal, M. Ariño Palacín, M. Ruiz, A.M. Sastre, Removal of an anionic dye (Acid Blue 92) by coagulation–flocculation using chitosan, J. Environ. Manage. 90 (2009) 2979–2986.

[91] Z. Daud, H. Awang, N. Nasir, M.B. Ridzuan, Z. Ahmad, Suspended solid, color, COD and oil and grease removal from biodiesel wastewater by coagulation and flocculation processes, Procedia–Social Behavioral Sci. 195 (2015) 2407–2411.

[92] Y. Anjaneyulu, N.S. Chary, D.S.S. Raj, Decolourization of industrial effluents available methods and emerging technologies–a review, Rev. Environ. Sci. Biotechnol. 4 (2005) 245–273.

[93] F.I. Hai, K. Yamamoto, K. Fukushi, Hybrid treatment systems for dye wastewater, Crit. Rev. Environ. Sci. Technol. 37 (2007) 315–377.

[94] A.B. dos Santos, F.J. Cervantes, J.B. van Lier, Review paper on current technologies for decolourisation of textile wastewaters: perspectives for anaerobic biotechnology, Bioresour. Technol. 98 (2007) 2369–2385.

[95] C.T.M.J. Frijters, R.H. Vos, G. Scheffer, R. Mulder, Decolorizing and detoxifying textile wastewater, containing both soluble and insoluble dyes, in a full scale combined anaerobic/aerobic system, Water Res. 40 (2006) 1249–1257.

[96] M.R. Servos, D.T. Bennie, B.K. Burnison et al., Distribution of estrogens, 17β–estradiol and estrone, in Canadian municipal wastewater treatment plants, Sci. Total Environ. 336 (2005)155–170.

[97] T. Urase and T. Kikuta, Separate estimation of adsorption and degradation of pharmaceutical substances and estrogens in the activated sludge process, Water Res. 39 (2005) 1289–1300.

[98] H.S. Rai, M.S. Bhattacharyya, J. Singh, T.K. Bansal, P. Vats, U.C. Banerjee, Removal of dyes from the effluent of textile and dyestuff manufacturing industry: a review of emerging techniques with reference to biological treatment, Crit. Rev. Environ. Sci. Technol. 35 (2005) 219–238.

[99] M. Isık, D.T. Sponza, Effects of alkalinity and co–substrate on the performance of an upflow anaerobic sludge blanket (UASB) reactor through decolorization of Congo red azo dye, Bioresource Technol. 96 (2005) 633–643.

[100] A. Stolz, Basic and applied aspects in the microbial degradation of azo dyes, Appl. Microbiol. Biotechnol. 56 (2001) 69–80.

[101] A.L. Ahmad, B.S. Ooi, A.W. Mohammad, J.P. Choudhury, Development of a highly hydrophilic nanofiltration membrane for desalination and water treatment, Desalination, 168(2004) 215–221.

[102] J.–J. Qin, M.H. Oo, K.A. Kekre, Nanofiltration for recovering wastewater from a specific dyeing facility, Sep. Purif. Technol. 56 (2007) 199–203.

[103]K. Walha, R.B. Amar, L. Firdaous, F. Quem´ eneur, P. Jaouen´, Brackish groundwater treatment by nanofiltration, reverse osmosis and electrodialysis in Tunisia: performance and cost comparison, Desalination 207 (2007) 95–106.

[104]M. Bodzek, M. Dudziak, K. Luks–Betlej, Application of membrane techniques to water purification. Removal of phthalates, Desalination 162 (2004) 121–128.

[105]G. Owen, M. Bandi, J.A. Howell, S.J. Churchouse, Economic assessment of membrane processes for water and waste water treatment, J. Membrane Sci. 102 (1995) 77–91.

[106]M. Cheryan, Ultrafiltration and Microfiltration Handbook, Technomic Publishing Co., Lancaster, PA, 1998.

[107]A.E. Simpson, C.A. Kerr, C.A. Buckley, The effect of pH on the nanofiltration of the carbonate system in solution, Desalination 64 (1987) 305–319.

[108]N. Bolong, A.F. Ismail, M.R. Salim, T. Matsuura, A review of the effects of emerging contaminants in wastewater and options for their removal, Desalination 238 (2009) 229–246.

[109]Y. Yoon, P. Westerhoff, S.A. Snyder, E.C. Wert, Nanofiltration and ultrafiltration of endocrine disrupting compounds, pharmaceuticals and personal care products, J. Membrane Sci. 270 (2006) 88–100.

[110]J.F. Li, J. Wu, H.F. Sun, F.Q. Cheng, Y. Liu, Advanced treatment of biologically treated coking wastewater by membrane distillation coupled with precoagulation, Desalination 380 (2016) 43–51.

[111]M.T. Amin, A.A. Alazba, U. Manzoor, A review of removal of pollutants from water/wastewater using different types of nanomaterials, Adv, Mater, Sci. Eng. 2014 (2014) 825910; http://dx.doi.org/10.1155/2014/825910.

[112]M.N. Rashed, Organic pollutants–monitoring, risk and treatment, in: M.N. Rashed, Adsorption Technique for the Removal of Organic Pollutants from Water and Wastewater, InTech, Egypt, 2013, pp. 167–194.

[113]T. A. Kurniawan, W.H. Lo, Removal of refractory compounds from stabilized landfill leachate using an integrated H_2O_2 oxidation and granular activated carbon (GAC) adsorption treatment, Water Res. 43 (2009) 4079–4091.

[114]R. Kant, Adsorption of dye eosin from an aqueous solution on two different samples of activated carbon by static batch method, J. Water Resour. Prot. 4 (2012) 93–98.

[115]Y.B. Sun, C.L. Chen, D.D. Shao, J.X. Li, X.L. Tan, G.X. Zhao, et al. Enhanced adsorption of ionizable aromatic compounds on humic acid–coated carbonaceous adsorbents, RSC Adv. 2 (2012) 10359–10364.

[116]I. Ali, M. Asim, T.A. Khan, Low cost adsorbents for the removal of organic pollutants from wastewater. J. Environ. Manag. 113 (2012) 170–183.

[117]J.T. Alexander, F.I. Hai, T.M. Al–aboud, Chemical coagulation–based processes for trace organic contaminant removal: current state and future potential, J. Environ. Manage 111 (2012) 195–207.

[118]W.V. Atul, G.S. Gaikwad, M.G. Dhonde, N.T. Khaty, S.R. Thakare, Removal of organic pollutant from water by heterogenous photocatalysis: a review, Res. J. Chem. Environ. 17 (2013) 84–94.

[119]Y. El Mouzdahir, A. Elmchaouri, R. Mahboub, A. Gil, S. A. Korili, Adsorption of methylene blue from aqueous solutions on a moroccan clay, J. Chem. Eng. Data 52 (2007) 1621–1625.

[120]J. Zolgharnein, A. Shahmoradi, Adsorption of Cr(VI) onto elaeagnus tree leaves: statistical optimization, equilibrium modeling, and kinetic studies, J. Chem. Eng. Data 55 (2010) 3428–3437.

[121]Y.C. Sharma, Uma, A.S.K. Sinha, S.N. Upadhyay, Characterization and adsorption studies of *Cocos nucifera L.* activated carbon for the removal of methylene blue from aqueous solutions, J. Chem. Eng. Data 55 (2010) 2662–2667.

[122]M.L. Fetterolf, H.V. Patel, J.M. Jennings, Adsorption of methylene blue and acid blue 40 on titania from aqueous solution, J. Chem. Eng. Data 48 (2003) 831–835.

[123]D. Karadag, M. Turan, E. Akgul, S. Tok, A. Faki, Adsorption equilibrium and kinetics of reactive black 5 and reactive red 239 in aqueous solution onto surfactant–modified zeolite, J. Chem. Eng. Data 52 (2007) 1615–1620.

[124]V.C. Srivastava, I.D. Mall, I.M. Mishra, Equilibrium modeling of ternary adsorption of metal ions onto rice husk ash, J. Chem. Eng. Data 54 (2009) 705–711.

[125]Y. Wu, L. Zhang, C. Gao, J. Ma, X. Ma, R. Han, Adsorption of copper ions and methylene blue in a single and binary system on wheat straw, J. Chem. Eng. Data 54 (2009) 3229–3234.

[126]B. Balci, O. Keskinkan, M. Avci, Use of BDST and an ANN model for prediction of dye adsorption efficiency of Eucalyptus camaldulensis barks in fixed–bed system, Expert System with Applications, 38 (2011) 949–956.

[127]W.H. Glaze, J.W. Kang, D.H. Chapin, The chemistry of water treatment involving ozone, hydrogen peroxide and ultraviolet radiation, Ozone Sci. Eng. 9 (1987) 335–342.

[128]D. Rajamanickam, M. Shanthi, Photocatalytic degradation of an organic pollutant by zinc oxide–solar process, Arabian J. Chem. 9 (2016) S1858–S1868.

[129]S. Devipriya, S. Yesodharan, Photocatalytic degradation of pesticide contaminants in water, Sol. Energy Mater, Sol. Cells 86 (2005) 309–348.

[130]M. Perez, F. Torrades, X. Domenech, J. Peral, Fenton and photo–Fenton oxidation of textile effluents, Water Res. 36 (2002) 2703–2710.

[131]T.J. Park, K.H. Lee, E.J. Jung, C.W. Kim, Removal of refractory organics and color in pigment wastewater with fenton oxidation, Water Sci. Technol. 39 (1999) 189–192.

[132]S. Chakma, V.S. Moholkar, Mechanistic analysis of hybrid sono–photo–ferrioxalate system for decolorization of azo dye, J. Taiwan Inst. Chem. Eng. 60 (2016) 469–478.

[133]H. Tekin, O. Bilkay, S.S. Ataberk, T.H. Balta, I.H. Ceribasi, F.D. Sanin, F.B. Dilek, U. Yetis, Use of Fenton oxidation to improve the biodegradability of a pharmaceutical wastewater, J. Hazard. Mater. 136 (2006) 258–265.

[134]D.A. Aljuboury, P. Palaniandy, H.B.A. Aziz, S. Feroz, Treatment of petroleum wastewater using combination of solar photo–two catalyst TiO_2 and photo–Fenton process, J. Environ. Chem. Eng. 3 (2015) 1117–1124.

[135]R. Munter, Advanced oxidation processes–current status and prospects, Proc. Eston. Acad. Sci. Chem. 50 (2001) 59–80.

[136]Y.W. Kang, K.–Y. Hwang, Effects of reaction conditions on the oxidation efficiency in the Fenton process, Water Res. 34 (2000) 2786–2790.

[137]M.R.D. Khaki, M.S. Shafeeyan, A.A.A. Raman, W.M.A. Wan Daud, Application of doped photocatalysts for organic pollutant degradation–A review, J. Environ. Manage. 198 (2017) 78–94.

[138]P.V. Nidheesh, Heterogeneous Fenton catalysts for the abatement of organic pollutants from aqueous solution: a review, RSC Adv. 5 (2015) 40552–40577.

[139]J.J. Pignatello, E. Oliveros, A. MacKay, Advanced oxidation processes for organic contaminant destruction based on the fenton reaction and related chemistry, Crit. Rev. Environ. Sci. Technol. 36 (2006) 1–84.

[140]S.F. Kang, C.H. Liao, S.T. Po, Decolorization of textile wastewater by photo–Fenton oxidation technology, Chemosphere 41 (2000) 1287–1297.

[141]E.R. Bandala, M.A. Pelaez, A.J. Garcia–Lopez, M.d.J. Salgado, G. Moeller, Photocatalytic decolourisation of synthetic and real textile wastewater containing benzidine–based azo dyes, Chem. Eng. Process. 47 (2008) 169–176.

[142]P.L. Huston, J.J. Pignatello, Degradation of selected pesticide active ingredients and commercial formulations in water by the photo–assisted Fenton reaction, Water Res. 33 (1999) 1238–1246.

[143]T. Maezono, M. Tokumura, M. Sekine, Y. Kawase, Hydroxyl radical concentration profile in photo–Fenton oxidation process: generation and consumption of hydroxyl radicals during the discoloration of azo–dye Orange II, Chemosphere 82 (2011) 1422–1430.

[144]E. Evgenidou, I. Konstantinou, K. Fytianos, I. Poulios, Oxidation of two organophosphorus insecticides by the photo–assisted Fenton reaction, Water Res. 41 (2007) 2015–2027.

[145]M.G. Alalm, A. Tawfik, S. Ookawara, Degradation of four pharmaceuticals by solar photo–Fenton process: kinetics and costs estimation, J. Environ. Chem. Eng. 3 (2015) 46–51.

[146]R.G. Zepp, B.C. Faust, J. Hoigné, Hydroxyl radical formation in aqueous reactions (pH 3–8) of iron(II) with hydrogen peroxide: the photo–Fenton reaction, Environ. Sci. Technol. 26 (1992) 313–319.

[147]G. Ruppert, R. Bauer, G.J. Heisler, The photo–Fenton reaction–an effective photochemical wastewater treatment process, Photochem. Photobiol. 73 (1993) 75–78.

[148]J.J. Pignatello, G. Chapa, Degradation of PCBs by ferric ion, hydrogen peroxide and UV light, Environ. Toxicol. Chem. 13 (1994) 423–427.

[149]A. De Luca, R.F. Dantas, S. Esplugas, Assessment of iron chelates efficiency for photo–Fenton at neutral pH, Water Res. 61 (2014) 232–242.

[150]H.S. El–Desoky, M.M. Ghoneim, R. El–Sheikh, N.M. Zidan, Oxidation of Levafix CA reactive azo–dyes in industrial wastewater of textile dyeing by electro–generated Fenton's reagent, J. Hazard. Mater. 175 (2010) 858–865.

[151]S. Wang, A comparative study of Fenton and Fenton–like reaction kinetics in decolourisation of wastewater, Dyes Pigments 76 (2008) 714–720.

[152]A. Tsitonaki, B. Petri, M. Crimi, H. Mossbaek, R.L. Siegrist, P.L. Bjerg, In situ chemical oxidation of contaminated soil and groundwater using persulfate: a review, Crit. Rev. Environ. Sci. Technol. 40 (2010) 55–91.

[153]Z. Miao, X. Gu, S. Lu, D.D. Dionysiou, S.R. Al–Abed, X. Zang, X. Wu, Z. Qiu, Q. Sui, M. Danish, Mechanism of PCE oxidation by percarbonate in a chelated Fe(II)–based catalyzed system, Chem. Eng. J. 275 (2015) 53–62.

[154]Y. Yang, J.J. Pignatello, J. Ma, W.A. Mitch, Effect of matrix components on UV/H_2O_2 and UV/$S_2O_8^{2-}$ advanced oxidation processes for trace organic degradation in reverse osmosis brines from municipal wastewater reuse facilities, Water Res. 89 (2016) 192–200.

[155]F. Ghanbari, M. Moradi, F. Gohari, Degradation of 2,4,6–trichlorophenol in aqueous solutions using peroxymonosulfate/activated carbon/UV process via sulfate and hydroxyl radicals, J. Water Process Eng. 9 (2016) 22–28.

[156]M.S. Morsi, A.A. Al–Sarawy, W.A. Shehab El–Dein, Electrochemical degradation of some organic dyes by electrochemical oxidation on a Pb/PbO_2 electrode, Desalin. Water Treat. 26 (2011) 301–308.

[157]J.F. Niu, H. Lin, J.L. Xu, H. Wu, Y.Y. Li, Electrochemical mineralization of perfluorocarboxylic acids (PFCAs) by Ce–doped modified porous nanocrystalline PbO_2 film electrode, Environ. Sci. Technol. 46 (2012) 10191–10198.

[158]L. Yahia Cherif, I. Yahiaoui, F. Aissani–Benissad, K. Madi, N. Benmehdi, F. Fourcade, A. Amrane, Heat attachment method for the immobilization of TiO_2 on glass plates: application to photodegradation of basic yellow dye and optimization of operating parameters, using response surface methodology, Ind. Eng. Chem. Res. 53 (2014) 3813–3819.

[159]L. Feng, E.D. van Hullebusch, M.A. Rodrigo, G. Esposito, M.A. Oturan, Removal of residual anti–inflammatory and analgesic pharmaceuticals from aqueous systems by electrochemical advanced oxidation processes: A review, Chem. Eng. J. 228 (2013) 944–964.

[160]I. Yahiaoui, F. Aissani–Benissad, F. Fourcade, A. Amrane, Combination of an electrochemical pre–treatment with a biological oxidation for the mineralization of nonbiodegradable organic dyes: basic yellow 28 dye, Environ. Prog. Sustain. Energy 1 (2014) 160–169.

[161]Y. Aamet, L. Agengui, R. Abdelhédi, Electrochemical degradation of chlorpyrifos pesticide in aqueous solutions by anodic oxidation at boron–doped diamond electrodes, Chem. Eng. J. 161 (2010) 167–172.

[162]M. Panizza, G. Cerisola, Direct and mediated anodic oxidation of organic pollutants, Chem. Rev. 109 (2009) 6541–6569.

[163]F. Sopaj, M.A. Rodrigo, N. Oturan, F.I. Podvorica, J. Pinson, M.A. Oturan, Influence of the anode materials on the electrochemical oxidation efficiency. Application to oxidative degradation of the pharmaceutical amoxicillin, Chem. Eng. J. 262 (2015) 286–294.

[164]N. Oturan, J. Wu, H. Zhang, V.K. Sharma, M.A. Oturan, Electrocatalytic destruction of the antibiotic tetracycline in aqueous medium by electrochemical advanced oxidation processes: effect of electrode materials, Appl. Catal. B: Environ. 140–141 (2013) 92–97.

[165]J.Q. Fan, G.H. Zhao, H.Y. Zhao, S.N. Chai, T.C. Cao, Fabrication and application of mesoporous Sb–doped SnO_2 electrode with high specific surface in electrochemical degradation of ketoprofen, Electrochim. Acta 94 (2013) 21–29.

[166]Y. He, W. Huang, R. Chen, W. Zhang, H. Lin, Enhanced electrochemical oxidation of organic pollutants by boron–doped diamond based on porous titanium, Sep. Purif. Technol. 149 (2015) 124–131.

[167]C.Q. Zhong, K.J. Wei, W.Q. Han, L.J. Wang, X.Y. Sun, J.S. Li, Electrochemical degradation of tricyclazole in aqueous solution using Ti/SnO_2–Sb/PbO_2 anode, J. Electroanal. Chem. 705 (2013) 68–74.

[168]N. Serpone, E. Pelizzetti, Photocatalysis: Fundamentals and Applications, first ed., Wiley–Interscience, John Wiley and Sons, Inc, New York, 1989.

[169]A. Fujishima, X.T. Zhang, D.A. Tryk, TiO_2 photocatalysis and related surface phenomena, Surf. Sci. Rep. 63 (2008) 515–582.

[170]J. Yu, X. Yu, Hydrothermal synthesis and photocatalytic activity of zinc oxide hollow spheres, Environ. Sci. Technol. 42 (2008) 4902–4907.

[171]M. Ni, M. Leung, D. Leung, K. Sumathy, A review and recent developments in photocatalytic water–splitting using TiO_2 for hydrogen production, Renew. Sustain. Energy Rev. 11 (2007) 401–425.

[172]A. Gupta, J.R. Saurav, S. Bhattacharya, Solar light based degradation of organic pollutants using ZnO nanobrushes for water filtration, RSC Adv. 5 (2015) 71472–71481.

[173]R. Venkatadri, R.W. Peters, Chemical oxidation technologies: ultraviolet light/hydrogen peroxide, Fenton's reagent, and titanium dioxide–assisted photocatalysis, Hazard. Waste Hazard. Mater. 10 (1993) 107–149.

[174]M.R. Hoffmann, S.T. Martin, W. Choi, D.W. Bahnemann, Environmental applications of semiconductor photocatalysis, Chem. Rev. 95 (1995) 69– 96.

[175]A.L. Pruden, D.F. Ollis, Photoassisted heterogeneous catalysis: the degradation of trichloroethylene in water, J. Catal. 82 (1983) 404–417.

[176]C. Kormann, D.W. Bahnemann, M.R. Hoffmann, Photolysis of chloroform and other organic molecules in aqueous titanium dioxide suspensions, Environ. Sci. Technol. 25 (1991) 494–500.

[177]J.C. Crittenden, J. Liu, D.W. Hand, D.L. Perram, Photocatalytic oxidation of chlorinated hydrocarbons in water, Water Res. 31 (1997) 429–438.

[178]D. Ravelli, D. Dondi, M. Fagnoni, A. Albini, Photocatalysis. A multi–faceted concept for green chemistry, Chem. Soc. Rev. 38 (2009) 1999–2011.

[179]Q.S. Meng, T. Wang, E.Z. Liu, X.B. Ma, Q.F. Ge, J.L. Gong, Understanding electronic and optical properties of anatase TiO_2 photocatalysts co–doped with nitrogen and transition metals, Phys. Chem. Chem. Phys. 15 (2013) 9549–9561.

[180]Z.Y. Zhang, C.L. Shao, X.H. Li, Y.Y. Sun, M.Y. Zhang, J.B. Mu, P. Zhang, Z.C. Guo, Y.C. Liu, Hierarchical assembly of ultrathin hexagonal SnS_2 nanosheets onto

electrospun TiO_2 nanofibers: Enhanced photocatalytic activity based on photoinduced interfacial charge transfer, Nanoscale 5 (2013) 606–618.

[181]R. Daghrir, P. Drogui, D. Robert, Modified TiO_2 for environmental photocatalytic applications: a review, Ind. Eng. Chem. Res. 52 (2013) 3581–3599.

[182]Z.F. Yin, L. Wu, H.G. Yang, Y.H. Su, Recent progress in biomedical applications of titanium dioxide, Phys. Chem. Chem. Phys. 15 (2013) 4844–4858.

[183]J. Virkutyte, R.S. Varma, Visible light activity of Ag–loaded and guanidine nitrate–doped nano–TiO_2: Degradation of dichlorophenol and antibacterial properties, RSC Adv. 2 (2012) 1533–1539.

[184]A.L. Linsebigle, G.Q. Lu, J.T. Yates, Photocatalysis on TiO_2 surfaces: Principles, mechanisms, and selected results, Chem. Rev. 95 (1995) 735–758.

[185]G. Pecci, R. Reyes, P. Sanhueza, J. Villase–nor, Photocatalytic degradation of pentachlorophenol on TiO_2–sol gel catalysts, Chemosphere 41 (2003) 141–146.

[186]B. Ohtani, O.O. Prieto–Mahaney, D. Li, R. Abe, What is Degussa (Evonik) P25? Crystalline composition analysis, reconstruction from isolated pure particles and photocatalytic activity test, J. Photochem. Photobiol. A: Chem. 216 (2010) 179–182.

[187]Q. Yang, Y. Liao, L. Mao, Kinetics of photocatalytic degradation of gaseous organic compounds on modified TiO_2/AC composite photocatalyst, Chin. J. Chem. Eng. 20 (2012) 572–576.

[188]P. Nguyen, C. Salim, W. Kurniawan, H. Hinode, A non–hydrolytic sol–gel synthesis of reduced graphene oxide/TiO_2 microsphere photocatalysts, Catal. Today 230 (2014) 166–173.

[189]K. Nakata, A. Fujishima, TiO_2 photocatalysis: Design and applications, J. Photochem. Photobiol. C: Photochem. Rev. 13 (2012) 169–189.

[190]A. Janotti, C.G. Van deWalle, Fundamentals of zinc oxide as a semiconductor, Rep. Prog. Phys. 72 (2009) 126501.

[191]S. Anandan, N. Ohashi, M. Miyauchi, ZnO–based visible–light photocatalyst: band–gap engineering and multi–electron reduction by co–catalyst, Appl. Catal. B Environ. 100 (2010) 502–509.

[192]S. Dubbaka, Branched Zinc Oxide Nanostructures: Synthesis and Photo Catalysis Study for Application in Dye Sensitized Solar Cells, UMI Microform, ProQuest LLC, USA, 2008.

[193]M. Yoji, W. Akio, Comparison of electronic structure of doped ZnS and ZnO calculated by a first–principle pseudopotenial method, J. Mater. Sci–Mater El 14 (2003) 149–156.

[194]M. Kumar, L. Wen, B.B. Sahu, J.G. Han, Simultaneous enhancement of carrier mobility and concentration via tailoring of Al chemical states in Al–ZnO thin films, Appl. Phys. Lett. 106 (2015) 241903.

[195]L. Wen, M. Kumar, B.B. Sahu, S.B. Jin, C. Sawangrat, K. Leksakul, J.G. Han, Advantage of dual–confined plasmas over conventional and facing–target plasmas for improving transparent–conductive properties in Al doped ZnO thin films, Surf. Coat. Technol. 284 (2015) 85–89.

[196]N. Daneshvar, S. Aber, M.S. Seyed Dorraji, A.R. Khataee, M.H. Rasoulifard, Photocatalytic degradation of the insecticide diazinon in the presence of prepared nanocrystalline ZnO powders under irradiation of UV–C light, Sep. Purif. Technol. 58 (2007) 91–98.

[197]M.A. Behnajady, N. Modirshahla, R. Hamzavi, Kinetic study on photocatalytic degradation of C.I. Acid Yellow 23 by ZnO photocatalyst, J. Hazard. Mater. 133 (2006) 226–232.

[198]N. Daneshvar, D. Salari, A.R. Khataee, Photocatalytic degradation of azo dye acid red 14 in water on ZnO as an alternative catalyst to TiO_2, J. Photochem. Photobiol. A Chem. 162 (2004) 317–322.

[199]B. Pal, M. Sharon, Enhanced photocatalytic activity of highly porous ZnO thin film, prepared by sol–gel process, Mater. Chem. Phys. 76 (2002) 82–87.

[200]R. Saravanan, N. Karthikeyan, V.K. Gupta, E. Thirumal, P. Thangadurai, V. Narayanan, A. Stephen, ZnO/Ag nanocomposite: An efficient catalyst for degradation studies of textile effluents under visible light, Mater. Sci. Eng. C 33 (2013) 2235–2244.

[201]Y. Qin, Y. Li, Z. Tian, Y. Wu, Y. Cui, Efficiently visible–light driven photoelectrocatalytic oxidation of As(III) at low positive biasing using Pt/TiO_2 nanotube electrode, Nanoscale Res. Lett. 11 (2016) 32; https://doi.org/10.1186/s11671–016–1248–5.

[202]W. Shi, W. Yang, Q. Li, S. Gao, P. Shang, J.K. Shang, The synthesis of nitrogen/sulfur co–doped TiO_2 nanocrystals with a high specific surface area and a high percentage of {001} facets and their enhanced visible–light photocatalytic performance, Nanoscale Res. Lett. 7 (2012) 590; https://doi.org/10.1186/1556–276X–7–590.

[203]M.M. Maitani, C. Zhan, D. Mochizuki, E. Suzuki, Y. Wada, Influence of co–existing alcohol on charge transfer of H_2 evolution under visible light with dye–sensitized nanocrystalline TiO_2, Appl. Catal. B: Environ. 140–141 (2013) 406–411.

[204]G. Zhang, Y.C. Zhang, M. Nadagouda, C. Han, K. O'Shea, S.M. El–Sheikh, A.A. Ismail, D.D. Dionysiou, Visible light–sensitized S, N and C co–doped polymorphic TiO_2 for photocatalytic destruction of microcystin–LR, Appl. Catal. B: Environ. 144 (2014) 614–621.

[205]M. Ni, M.K.H. Leung, D.Y.C. Leung, K. Samathy, A review and recent developments in photocatalytic water–splitting using TiO_2 for hydrogen production, Renew. Sustain. Energy Rev. 11 (2007) 401–425.

[206]M.R. Narayan, Review: Dye sensitized solar cells based on natural photosensitizers, Renew. Sustain. Energy Rev. 16 (2012) 208–215.

[207]S. Rehman, R. Ullah, A.M. Butt, N.D. Gohar, Strategies of making TiO_2 and ZnO visible light active, J. Hazard. Mater. 170 (2009) 560–569.

[208]H. Park, Y. Park, W. Kim, W. Choi, Surface modification of TiO_2 photocatalyst for environmental applications, J. Photochem. Photobiol. C 15 (2013) 1–20.

[209]S. Kaur, V. Singh, Visible light induced sonophotocatalytic degradation of reactive red dye 198 using dye sensitized TiO_2, Ultrason. Sonochem. 14 (2007) 531–537.

[210]M.R.D. Khaki, M.S. Shafeeyan, A.A.A. Raman, W.M.A.W. Daud, Application of doped photocatalysts for organic pollutant degradation–a review, J. Environ. Manage. 198 (2017) 78–94.

[211]C. Wu, Y.C. Zhang, Q. Huang, Solvolthermal synthesis of N–doped ZnO microcrystals from commercial ZnO powder with visible light–driven photocatalytic activity, Mater. Lett. 119 (2014) 104–106.

[212]T. Prakash, R. Jayaprakash, C. Espro, G. Neri, E.R. Kumar, Effect of Sn doping on microstructural and optical properties of ZnO nanoparticles synthesized by microwave irradiation method, J. Mater. Sci. 49 (2014) 1776–1784.

[213]A. Mohanta, J.G. Simmons Jr., H.O. Everitt, G. Shen, S.M. Kim, P. Kung, Effect of pressure and Al doping on structural and optical properties of ZnO nanowires synthesized by chemical vapor deposition, J. Lumin. 146 (2014) 470–474.

[214]Y.M. Hao, S.Y. Lou, S.M. Zhou, R.J. Yuan, G.Y. Zhu, N. Li, Structural, optical, and magnetic studies of manganese–doped zinc oxide hierarchical microspheres by self–assembly of nanoparticles, Nanoscale Res. Lett. 7 (2012) 100; https://doi.org/10.1186/1556-276X-7-100.

[215]C. Bundesmann, M. Schubert, D. Spemann, T. Butz, M. Lorenz, E.M. Kaidashev, M. Grundmann, N. Asheknov, H. Neumann, G. Wagner, Infrared dieletric functions and phonon modes of wurtzite $Mg_xZn_{1-x}O_{(x \leq 0.2)}$, Appl. Phys. Lett. 81 (2002) 2376–2378.

[216]A. Catellani, A. Ruini, G. Cicero, A. Calzolari, First principles description of the electronic properties of doped ZnO, Phys. Status Solids B 250 (2013) 2106–2109.

[217]N.R. Panda, B.S. Acharya, P. Nayak, Sonochemical synthesis of nitrogen doped ZnO nanorods: effect of anion on growth and optical properties, J. Mater. Sci. Mater. Lett. 24 (2013) 4043–4049.

[218]Chai, G. L.; Lin, C. S.; Wang, J. Y.; Zhang, M. Y.; Wei, J.; Cheng, W. D. Density functional theory simulations of structures and properties for Ag–doped ZnO nanotubes, J. Phys. Chem. C 115 (2011) 2907–2913.

[219]R. Shao, L. Sun, L. Tang, Z. Chen, Preparation and characterization of magnetic core–shell $ZnFe_2O_4$@ZnO nanoparticles and their application for the photodegradation of methylene blue, Chem. Eng. J. 217 (2013) 185–191.

[220]R. Kooyman, H. Kolkman, J. VanGent, J. Greve, Surface plasmon resonance immunosensors: sensitivity considerations, Anal. Chim. Acta 213 (1988) 35–45.

[221]12. M. Rycenga, C.M. Cobley, J. Zeng, W.Y. Li, C.H. Moran, Q. Zhang, D. Qin, Y.N. Xia, Controlling the synthesis and assembly of silver nanostructures for plasmonic applications, Chem. Rev. 111 (2011) 3669–3712.

[222]M.J. Sampaio, M.J. Lima, D.L. Baptista, A.M.T. Silva, C.G. Silva, J.L. Faria, Ag–loaded ZnO materials for photocatalytic water treatment, Chem. Eng. J. 318 (2017) 95–102.

[223]J. Lv, Q. Zhu, Z. Zeng, M. Zhang, J. Yang, M. Zhao, W. Wang, Y. Cheng, G. He, Z. Sun, Enhanced photocurrent and photocatalytic properties of porous ZnO thin film by Ag nanoparticles, J. Phys. Chem. Solids 111 (2017) 104–109.

[224]X. Zhang, Y, Wang, F. Hou, H. Lia, Y. Yang, X. Zhan, Y. Yang, Y. Wang, Effects of Ag loading on structural and photocatalytic properties of flower–like ZnO microspheres, Appl. Surf. Sci. 391 (2017) 476–483.

[225]Y. Xu, S. Wu, X. Li, H. Meng, X. Zhang, Z. Wang, Y. Han, Ag nanoparticle–functionalized ZnO micro–flowers for enhanced photodegradation of herbicide derivatives, Chem. Phys. Lett. 679 (2017) 119–126.

[226]X. Zhao, S. Su, G. Wu, C. Li, Z. Qin, X. Lou, J. Zhou, Facile synthesis of the flower–like ternary heterostructure of Ag/ZnO encapsulating carbon spheres with enhanced photocatalytic performance, Appl. Surf. Sci. 406 (2017) 254–264.

[227]C. Jaramillo–Páez, J.A. Navío, M.C. Hidalgo, M. Macías, High UV–photocatalytic activity of ZnO and Ag/ZnO synthesized by a facile method, Catal. Today 284 (2017) 121–128.

[228]K. Rokesh, et al., Photo–assisted advanced oxidation processes for Rhodamine B degradation using ZnO–Ag nanocomposite materials, J. Environ. Chem. Eng. (2017), http://dx.doi.org/10.1016/j.jece.2017.01.023.

[229]S.M. Hosseini, I. Abdolhosseini Sarsari, P. Kameli, H. Salamati, Effect of Ag doping on structural, optical, and photocatalytic properties of ZnO nanoparticles, J. Alloys Compd. 640 (2015) 408–415.

[230]O. Bechambi, M. Chalbi, W. Najjar, S. Sayadi, Photocatalytic activity of ZnO doped with Ag on the degradation of endocrine disrupting under UV irradiation and the investigation of its antibacterial activity, Appl. Surf. Sci. 347 (2015) 414–420.

[231]D. Zhang, X. Liu, X. Wang, Growth and photocatalytic activity of ZnO nanosheets stabilized by Ag nanoparticles, J. Alloys Compd. 509 (2011) 4972–4977.

[232]C. Ren, B. Yang, M. Wu, J. Xu, Z. Fu, Y. lv, T. Guo, Y. Zhao, C. Zhu, Synthesis of Ag/ZnO nanorods array with enhanced photocatalytic performance, J. Hazard. Mater. 182 (2010) 123–129.

[233]R. Georgekutty, M.K. Seery, S.C. Pillai, A highly efficient Ag–ZnO photocatalyst: synthesis, properties, and mechanism, J. Phys. Chem. C 112 (2008) 13563–13570.

[234]J. Xu, Y. Chang, Y. Zhang, S. Ma, Y. Qu, C. Xu, Effect of silver ions on the structure of ZnO and photocatalytic performance of Ag/ZnO composites, Appl. Surf. Sci. 255 (2008) 1996–1999.

[235]Y. Zheng, L. Zheng, Y. Zhan, X. Lin, Q. Zheng, K. Wei, Ag/ZnO heterostructure nanocrystals: synthesis, characterization, and photocatalysis, Inorg. Chem. 46 (2007) 6980–6986.

[236]S. Sakthivel, B. Neppolian, M.V. Shankar, B. Arabindoo, M. Palanichamy, V. Murugesan, Solar photocatalytic degradation of azo dye: Comparison of 53

photocatalytic efficiency of ZnO and TiO_2, Sol. Energy Mater. Sol. Cells 77 (2003) 65–82.

[237]S.H. Yoon, J.H. Lee, Oxidation mechanism of As(III) in the UV/TiO_2 system: evidence for a direct hole oxidation mechanism, Environ. Sci. Technol. 39 (2005) 9695–9701.

[238]F. Beolchini, F. Pagnanelli, I. De Michelis, F. Veglio, Treatment of concentrated arsenic(V) solutions by micellar enhanced ultrafiltration with high molecular weight cut–off membrane, J. Hazard. Mater. 148 (2007) 116–121.

[239]H. Zangeneh, A.A.L. Zinatizadeh, M. Habibi, M. Akia, M. Hasnain Isa, Photocatalytic oxidation of organic dyes and pollutants in wastewater using different modified titanium dioxides: A comparative review, J. Ind. Eng. Chem. 26 (2015) 1–36.

[240]E. Adamek, W. Baran, J. Ziemian'ska, A. Sobczak, Effect of $FeCl_3$ on sulfonamide removal and reduction of antimicrobial activity of wastewater in a photocatalytic process with TiO_2, Appl. Catal. B: Environ. 126 (2012) 29–38.

[241]S. Garcia–Segura, S. Dosta, J.M. Guilemany, E. Brillas, Solar photoelectrocatalytic degradation of Acid Orange 7 azo dye using a highly stable TiO_2 photoanode synthesized by atmospheric plasma spray, Appl. Catal. B: Environ. 132– 133 (2013) 142–150.

[242]M.C. Ortega–Lie´bana, E. Sa´nchez–Lo´pez, J. Hidalgo–Carrillo, A. Marinas, J.M. Marinas, F.J. Urbano, A comparative study of photocatalytic degradation of 3–chloropyridine under UV and solar light by homogeneous (photo–Fenton) and heterogeneous (TiO_2) photocatalysis, Appl. Catal. B: Environ. 127 (2012) 316–322.

[243]A. Alinsafi, F. Evenou, E.M. Abdulkarim, M.N. Pons, O. Zahraa, A. Benhammou, A. Yaacoubi, A. Nejmeddine, Treatment of textile industry wastewater by supported photocatalysis, Dyes and Pigments 74 (2007) 439–445.

[244]L. Lagunas–Allue´a, M.T. Martı´nez–Soriaa, J. Sanz–Asensioa, A. Salvadorb, C. Ferronatoc, J.M. Chovelon, Degradation intermediates and reaction pathway of pyraclostrobin with TiO_2 photocatalysis, Appl. Catal. B: Environ. 115–116 (2012) 285–293.

[245]E. Grabowska, J. Reszczynska, A. Zaleska, Mechanism of phenol photodegradation in the presence of pure and modified–TiO_2: A review, Water Res. 46 (2012) 5453–5471.

[246]Q. Xiang, J. Yu, P.K. Wong, Quantitative characterization of hydroxyl radicals produced by various photocatalysts, J. Colloid Interface Sci. 357 (2011) 163–167.

[247]F. Zhang, J. Zhao, T. Shen, H. Hidaka, E. Pelizzetti, N. Serpone, $Ti0_2$–assisted photodegradation of dye pollutants II. Adsorption and degradation kinetics of eosin in $Ti0_2$ dispersions under visible light irradiation, Appl. Catal. B: Environ. 15 (1998) 147–156.

[248]G. Liu, T. Wu, J. Zhao, H. Hidaka, N. Serpone, Photoassisted degradation of dye pollutants. 8. Irreversible degradation of alizarin red under visible light radiation in air–equilibrated aqueous TiO_2 dispersions, Environ. Sci. Technol. 33 (1999) 2081–2087.

[249]F. Chen, Y. Xie, J. Zhao, G. Lu, Photocatalytic degradation of dyes on a magnetically separated photocatalyst under visible and UV irradiation, Chemosphere 44 (2001) 1159–1168.

[250]J. Bandara, J.A. Mielczarski, J. Kiwi, Photosensitized Degradation of Azo Dyes on Fe, Ti, and Al Oxides. Mechanism of charge transfer during the degradation, Langmuir 15 (1999) 7680–7687.

[251]N. Daneshvar, D. Salari, A.R. Khataee, Photocatalytic degradation of azo dye acid red 14 in water: investigation of the effect of operational parameters, J. Photochem. Photobiol. A: Chem. 157 (2003) 111–116.

[252]C. Galindo, P. Jacques, A. Kalt, Photochemical and photocatalytic degradation of an indigoid dye: a case study of acid blue 74 (AB74), J. Photochem. Photobiol. A: Chem. 141 (2001) 47–56.

[253]G.A. Epling, C. Lin, Photoassisted bleaching of dyes utilizing TiO_2 and visible light, Chemosphere 46 (2002) 561–570.

CHAPTER 2

DEGRADATION, KINETICS AND MINERALIZATION IN THE SOLAR PHOTOCATALYTIC TREATMENT OF AQUEOUS AMITROLE SOLUTION WITH TiO_2

2.1. INTRODUCTION

The active use of herbicides in agriculture leads to an increase of both productivity and environmental contamination. Amitrole (3–amino–1*H*–1,2,4–triazole, M.W. = 84.08 g/mol, Figure 2.1) is a widely employed herbicide with strong estrogenic activity. Due to its low volatility (b.p. = 260 °C) and good solubility in water (280 g/L) [1], amitrole can be found in surface waters and contribute to ground–water contamination (for instance: 1.1 μg/L) via leaching [2]. Poisoning of several species by amitrole is characterized by increased intestinal peristalsis, fluid in the lungs and hemorrhages of various organs [3–5]. Hence, it is very important to urgently develop the treatment technology for high concentration amitrole solution before releasing the waste herbicide solution into the environment.

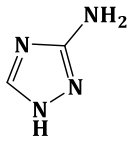

Figure 2.1. Molecular structure of amitrole.

Since absorption spectrum of amitrole does not overlap with solar emission spectrum, it is stable to photodegradation under nature relevant conditions. Direct UV–photolysis (254 nm, low pressure mercury lamp) of amitrole was shown to be ineffective, owing to its low molar absorption [6]. Catastini et al. [7] described the photochemical degradation of amitrole from aqueous solutions at pH 3.4, using iron(III) aqua complexes under solar and UV radiation, and the complete removal was achieved at 10 h of irradiation. Therefore, in the method of photo Fenton remediation, there were disadvantages because the treatment was used in only acidic area. On the other hand, the photocatalytic treatment can be applied into wide pH ranges [3,8,9]. Much attention has been focused in the past three decades on the photocatalytic degradation of organic pollutants with titanium dioxide (TiO_2) in aqueous suspension solution under UV irradiation [10]. In this process,

the TiO_2 semiconductors is excited with UV light of wavelengths less than 380 nm to form conduction band electrons (e^-) and valance band holes (h^+) which are capable of initiating the photocatalytic oxidation and reduction reactions, respectively. The photocatalytic remediation of environmental pollution on bare TiO_2 in water under sunlight irradiation by using the UV range, that is, a small fraction of solar light is possible, although it takes long time for the photocatalytic treatment.

Among the large variety of pesticides degraded by photocatalysis, the degradation of several organic compounds containing nitrogen rings has been successfully performed: Tebuconazole [11], triazolidine [12], amitrole, 3,5–diamino 1H–1,2,4 triazole, 1H–1,2,4 triazole [3], thiabendazole [13], pyridazine, pyrimidine, pyrazine [14] and Pyrimethanil [15]. A study has reported the photocatalytic degradation of amitrole using an artificial light source such as an Hg–Xe lamp [3,8,9]. The artificial lamp device is particularly expensive in the local and undeveloped areas. There is little information on the photocatalytic degradation of amitrole in water with TiO_2 under sunlight illumination. Previous research has investigated the photocatalytic remediation of amitrole in aqueous solution [16]. In the photocatalytic degradation system, amitrole could be degraded in aqueous TiO_2 dispersion under sunlight illumination.

In this chapter, the optimal conditions for photocatalytic degradation of amitrole in water with TiO_2 were studied, and the final degradation product was determined in order to evaluate the mineralization of amitrole. On the basis of the evidence of data, the kinetics and mineralization was discussed.

2.2. MATERIALS AND METHODS

The amitrole used in this study was purchased from Wako Pure Chemical Industries, Ltd. (HPLC grade > 98%, pesticide residue analysis). Amitrole aqueous solutions were prepared with ultrapure water, which was purified by an ultrapure water system (Advantec MFS, Inc., Tokyo, Japan) resulting in a resistivity >18 MΩ cm. A 30 mL aqueous solution containing 20 mg/L amitrole was put into a Pyrex reaction vessel (50 mL capacity). TiO_2 powder (anatase, purity 99.9%, diameter 230 nm, surface area 8.7 m^2/g, Wako Pure Chemical Industries, Ltd., Figure 2.2) was added to the solution to produce a concentration of 6.7 mg/mL. The pH of the solution was 9.0. The temperature was kept constant at 25 to 85 °C with a water bath. The detailed experimental conditions were shown in Table 2.2. The TiO_2 suspension containing amitrole was irradiated under sunlight illumination. In this case, the short ultraviolet radiation (λ < 300 nm) was filtered out by the vessel wall. The intensity of light was measured by a UV radio meter (UVR–400, Iuchi Co., Osaka, Japan). The variations of sunlight intensity for 60 min were less than 10%.

After illumination, the amount of amitrole in the aqueous solution was measured using a high–performance liquid chromatograph equipped with a Hitachi L–4000 UV optical detector and a separation column RSpak DE–413L (SHOWA DENKO K.K). The elution was monitored at 210 nm. The eluent used was a mixed solvent of acetonitrile and water (7/3, v/v). The flow rate of the mobile phase was 0.7 mL/min. The photodegradation system is presented in Figure 2.3.

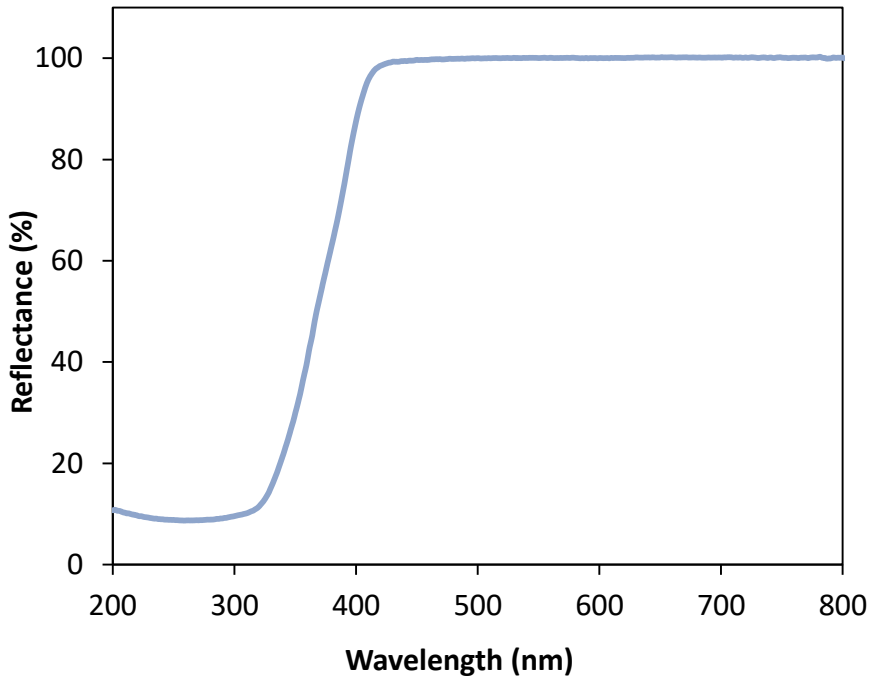

Figure 2.2. UV–Vis DRS patterns of TiO_2.

Table 2.1

Experimental conditions.

Amitrole	5–20 mg/L (volume: 30 mL)
TiO_2	0–300 mg (10 g/L)
Temperature	5–85 °C
pH	1.8–11
Light source	Sunlight
Light intensity	0–2 mW/cm^2
Illumination time	30 and 60 min

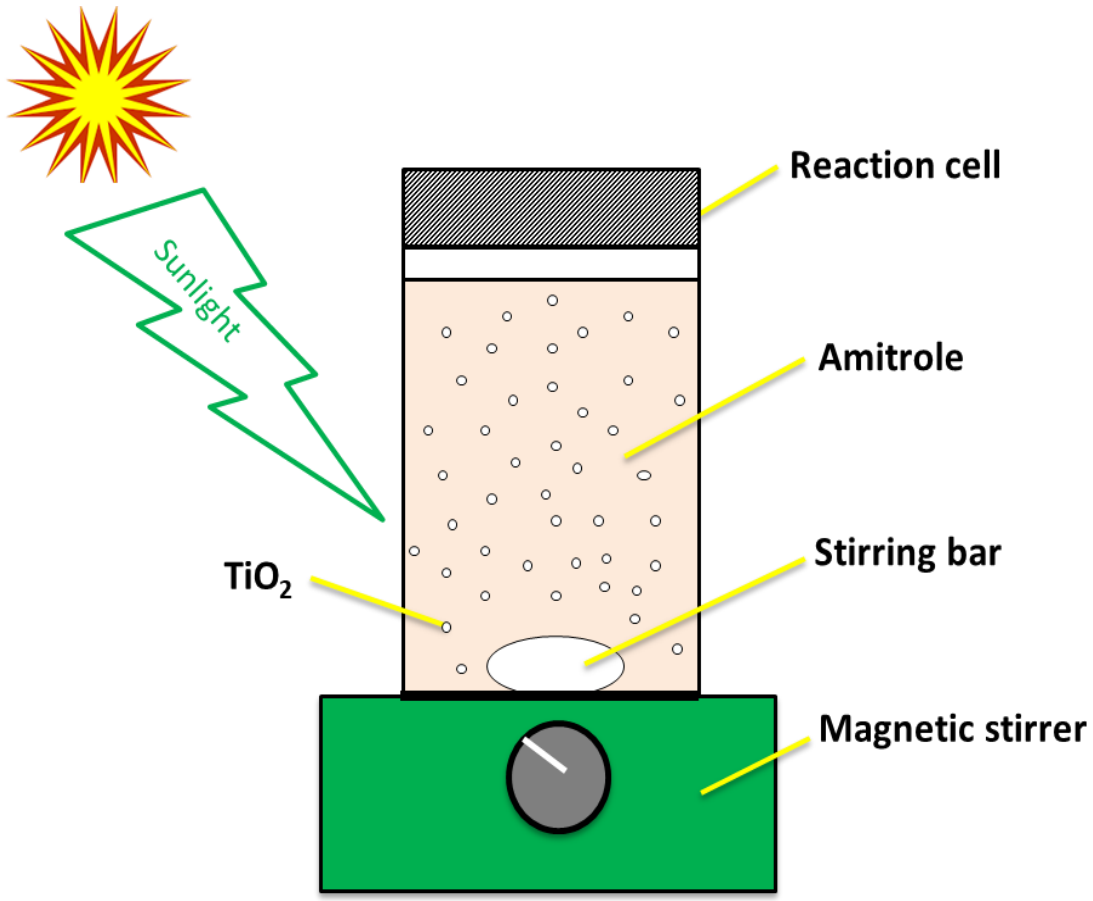

Figure 2.3. Schematic reactor for photocatalytic degradation of amitrole.

The intermediate products were extracted by means of solid–phase extraction. The extraction disk (C18 disk, 3M Empore) was placed in the conventional filtration apparatus and washed with 10 mL of solvent mixture, dichloromethane and ethyl acetate (1:1), 10 mL of methanol and 10 mL of ultrapure water. Then, the sample was percolated through the disk with a flow rate of 5 mL/min under vacuum. The compounds trapped in the disk were collected by using 4 × 5 mL of solvent mixture, dichloromethane and ethyl acetate (1:1), as eluting system. The fractions were evaporated under a gentle stream of nitrogen to 50 µL into conical vials, and 1 µL was injected into gas chromatography and mass spectrometry (GC–MS) instrument in splitless mode. For the analysis of intermediate products, a Shimadzu Gas

Chromatograph and Mass Spectrometry (GC–MS 5050A) equipped with an HP–5 capillary column (30 m × 0.25 mm i.d.) was used at the following chromatographic conditions: injector temperature 270 °C, column temperature program 40, 40–200 °C (5 °C/min), 200–210 °C (1 °C/min), 210–270 °C (20 °C/min) and 270 °C (3 min). Helium was used as the carrier gas at 1.5 mL/min. The interface was kept at 270 °C. Qualitative analyses were performed in the electron–impact (EI) mode, at 70 eV using the full scan mode.

Chemical oxygen demand (COD) in the sample solution was measured by potassium permanganate acidic method (JIS, 2003). The formation of ammonium and nitrate ions was measured by ion chromatography.

2.3. RESULTS AND DISCUSSION

In the primary experiments, the complete disappearance of amitrole was observed in <3 h, working with moderate amounts of TiO_2 (6.7 g/L) under sunlight illumination [16]. Since it was found that the solar photocatalytic purification of water containig amitrole was possible in TiO_2 aqueous suspensions, the degradation parameters were optimized in the present study.

2.3.1. Effect of Photocatalyst Dosages

The amount of catalyst is one of the main parameters for the degradation studies. In order to avoid the use of excess catalyst, it is necessary to find out the optimum loading for efficient removal of amitrole molecule. Several authors have investigated the reaction rate as a function of catalyst loading in photocatalytic degradation process [17–20]. The effect of the catalyst amount on the photocatalytic degradation has been carried out in the range of 0 to 300 mg (10 g/L) of the catalyst for 30 mL of solution. The results are shown in Figure 2.4. The degradation efficiency increased with increasing the amounts up to 200 mg (6.7 g/L), and then the efficiency was nearly flat. The increase in the efficiency seems to be due to the increase in the total surface area, namely number of active sites available for the photocatalytic reaction, as the dosage of photocatalyst increased. However, when TiO_2 was overdosed, the number of active sites on the TiO_2 surface may become almost constant because of the decreased light penetration, the increased light scattering, and the loss in surface area occasioned by agglomeration (particle–particle interactions) at high solid concentration [21]. Therefore, 200 mg (6.7 g/L) of TiO_2 was selected as the optimal amounts of photocatalyst for the sequential experiments.

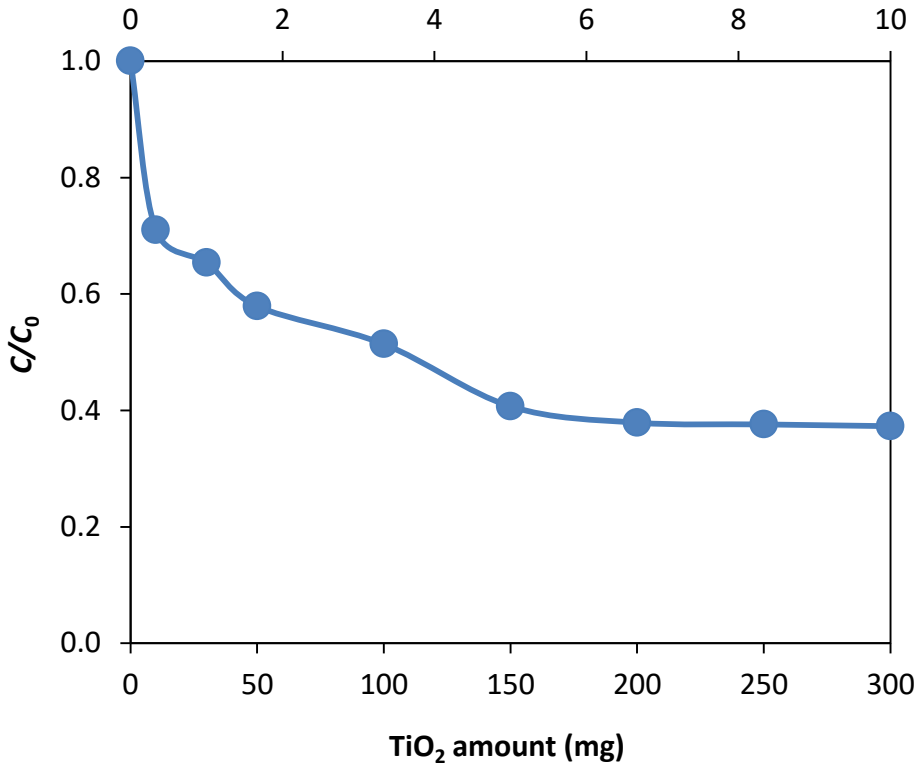

Figure 2.4. Effect of TiO_2 amount on the solar photocatalytic degradation of amitrole in water. Amitrole: 20 mg/L; illumination time: 30 min; light intensity: 1.6 mW/cm^2; temperature: 25 °C; pH: 9.

2.3.2. Effect of Initial Substrate Concentration

It is very important, from the application point of view, to study the dependence of the photocatalytic degradation on the substrate concentration. The effect of initial substrate concentrations on the solar photocatalytic decomposition using TiO_2 was investigated, and the results are given in Figure 2.5. It is found that with increasing initial substrate concentrations the degradation efficiency decreased gradually [22,23]. In this study, 20 mg/L amitrole solution was used for evaluating the solar photocatalytic degradation, in view of the practical wastewater with high concentration of amitrole.

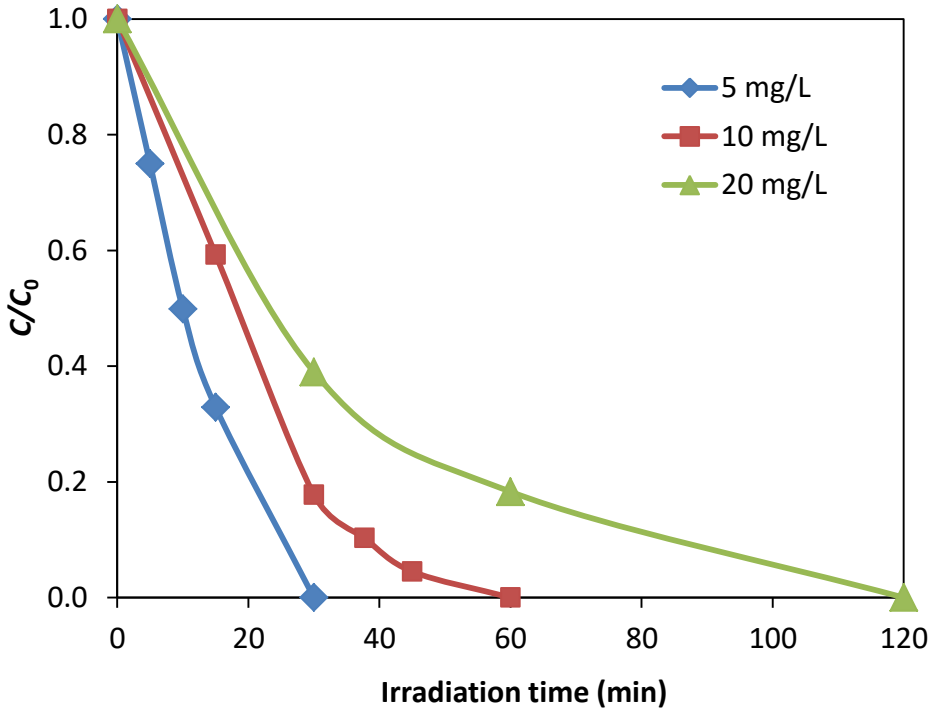

Figure 2.5. Effect of initial substrate concentration on the solar photocatalytic degradation of amitrole in water using TiO_2. TiO_2: 200 mg; amitrole: 5–20 mg/L; light intensity: 1.6 mW/cm^2; temperature: 25 °C; pH: 9.

2.3.3. Effect of Temperature

Little information on the temperature effect on the photocatalytic degradation of pollutants in water with TiO_2 has been presented [22,23]. Therefore, the effect of temperature on the solar photocatalytic degradation of amitrole in water using TiO_2 was investigated in the range of 5–85 °C. The results are shown in Figure 2.6. The degradation efficiency of amitrole gradually increased as the temperature increased. In the photocatalytic degradation of imazaquin in an aqueous suspension of titanium dioxide [24], the effect of temperature was studied in the range 20–40 °C, and the rate constants increased with increasing temperature. Ishiki et al. [25] have investigated the photocatalytic degradation of imazethapyr herbicide at TiO_2/H_2O interface. In their works, the temperature effect was studied

using a suspension between 20 and 40 °C, and the herbicide was more easily degraded at lower temperatures in the TiO_2 suspension, due to the decrease in the physisorption between the TiO_2 surface and the imazethapyr molecules. By plotting the natural logarithm of the rate constant as a function of reciprocal absolute temperature, a linear behavior was obtained in the temperatures below about 60 °C with the correlation coefficient 0.96, as drawn in the insert figure in Figure 2.6.

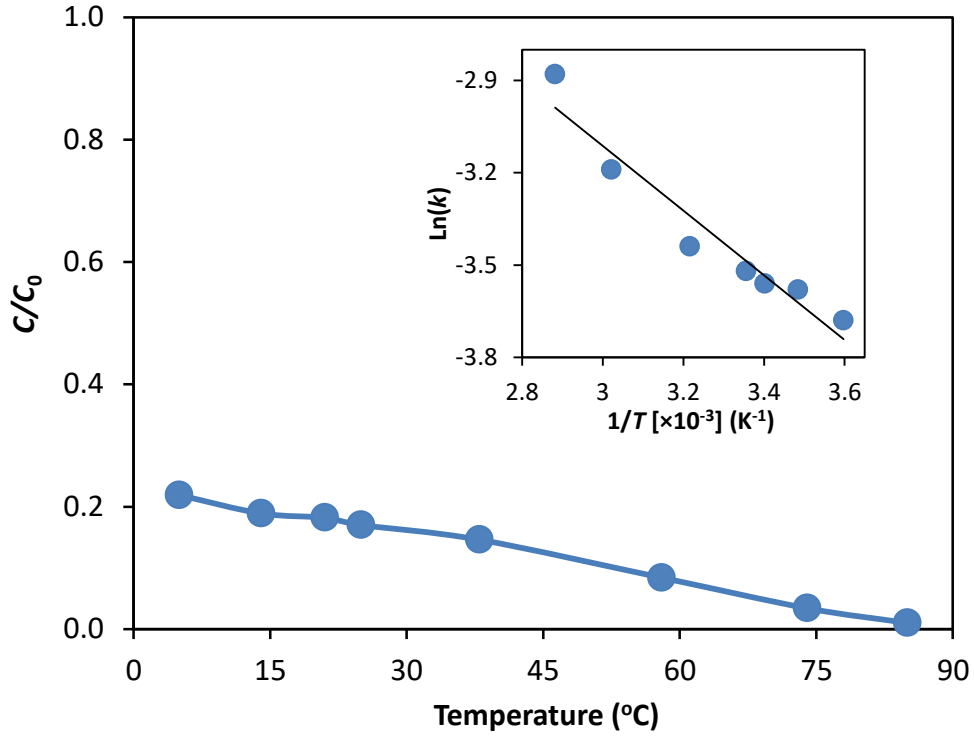

Figure 2.6. Effect of temperature on the solar photocatalytic degradation of amitrole in water using TiO_2. Inset figure: plot of Ln(k) versus $1/T$. TiO_2: 200 mg; amitrole: 20 mg/L; light intensity: 1.6 mW/cm^2; illumination time: 60 min; pH: 9.

The activation energy (E_a) was relatively low and was estimated to become 6.73 kJ/mol. It was reported in the TiO_2 photocatalytic degradation of benzene [26], naphthalene [27], imazaquin [24] and Chloramphenicol [28] that the activation energy (E_a) was 3.2, 22, 24.8 and 33 kJ/mol, respectively. Since the photoactivation process is irrelevant to thermal activation, the activation energy found is only apparent. Consequently, all subsequent illuminations were performed at 25 °C because of the operating cost for the photodegradation system.

2.3.4. Effect of Initial pH

The amphoteric behavior of most semiconductor oxides influences the surface charge of the photocatalyst. Therefore, the role of initial pH on the degradation efficiency of amitrole was investigated in the pH range 1.8–11, as shown in Figure 2.7. It is found that degradation efficiency increased with increase in pH up to 5.4. Then the degradation efficiency of amitrole gradually decreased as the pH increased. The zero–point charge (zpc) pH_{zpc} of TiO_2 particles is around 6 [29]. TiO_2 surface is positively charged in acidic media (pH < 6) whereas it is negatively charged under alkaline condition (pH > 6). Generally, the pH changes can have a non–insignificant result not only on the mode of adsorption of the amitrole substrate on TiO_2 surface, but also on the selectivity of the photodegradative reaction occurring on the particle surface since redox reactions are very sensitive to changes in the surface potential [30]. In acidic media (pH < 4) and alkaline media (pH > 10) the nonpolar amitrole may be scarcely adsorb onto the TiO_2 surface, and in neutral condition (4 < pH < 10), the adsorption can occur easily. Consequently, pH 9 was selected for the optimal experimental conditions, because of the unnecessary of chemical treatment including neutralization process.

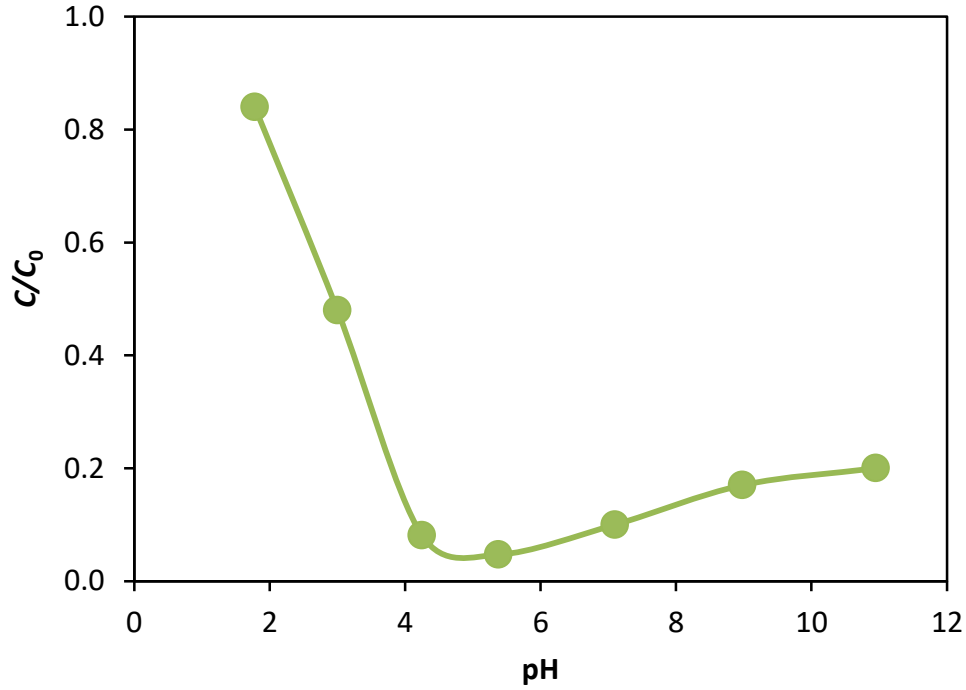

Figure 2.7. Effect of initial pH on the solar photocatalytic degradation of amitrole in water using TiO_2. TiO_2: 200 mg; amitrole: 20 mg/L; illumination time: 60 min; light intensity: 1.6 mW/cm^2; temperature: 25 °C.

2.3.5. Effect of Light Intensity

The influence of light intensity on the solar photocatalytic destruction of amitrole in water with TiO_2 was studied, as illustrated in Figure 2.8. The degradation experiments were performed during different periods of time with various light intensities on sunny and cloudy days. The degradation efficiency increased rapidly with increase in the light intensity up to 0.53 mW/cm^2 and then the efficiency increased gradually. Since the catalyst powders are suspended in a stirred solution, the light intensity will affect the degree of absorption of light by the catalyst surface. Ollis et al. [31] reviewed the effect of light intensity on the kinetics of photocatalysis and stated that (i) at low light intensities, the rate would increase linearly with increasing light intensity; (ii) at intermediate light intensities, the rate

would depend on the square root of the light intensity; and (iii) at high light intensities, the rate is independent of light intensity. Therefore, the results obtained in the solar photocatalytic degradation of amitrole in aqueous TiO_2 suspension were reasonable.

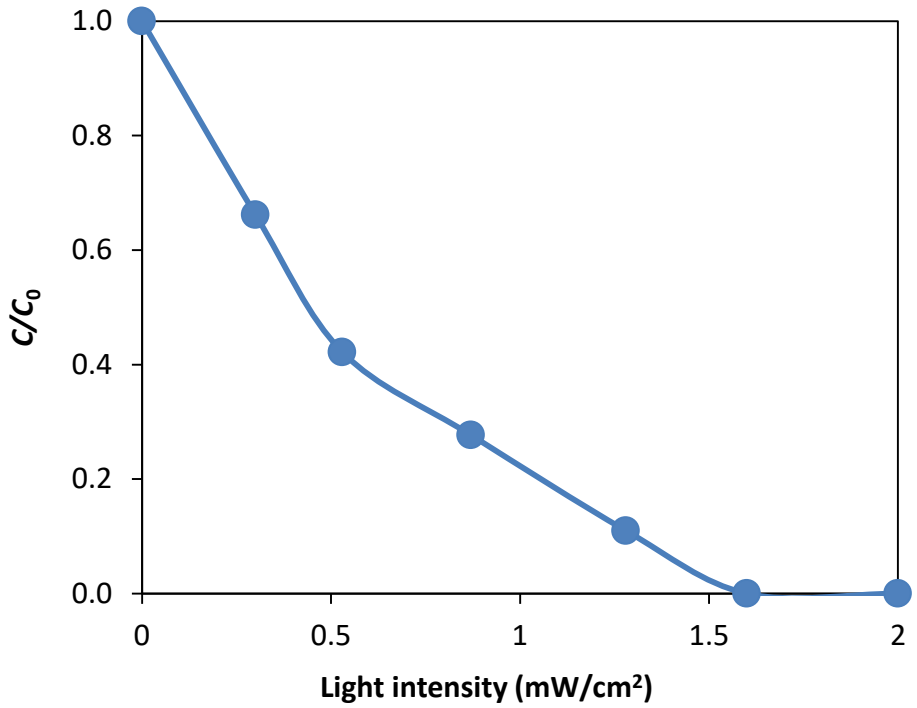

Figure 2.8. Effect of light intensity on the solar photocatalytic degradation of amitrole in water using TiO_2. TiO_2: 200 mg; amitrole: 20 mg/L; illumination time: 60 min; temperature: 25 °C; pH: 9.

2.3.6. Kinetic Analysis

The heterogeneous photocatalytic degradation of amitrole with TiO_2 obeys apparently pseudo–first–order kinetics at low initial substrate concentration, and the rate expression is given by the equation:

$$r = -\frac{dC}{dt} = kC \qquad (2.1)$$

where k is the pseudo–first–order rate constant. Amitrole is adsorbed onto TiO_2 surface and the adsorption–desorption equilibrium is reached. After the adsorption, the equilibrium concentration of amitrole solution is determined and it is taken as the initial amitrole concentration for kinetic analysis.

Integration of the above equation with the limit of $C = C_0$ at $t = 0$ with C_0 being the equilibrium concentration of the bulk solution gives the following equation:

$$\mathbf{Ln}\frac{C}{C_0} = \boldsymbol{kt} \qquad (2.2)$$

where C_0 is the equilibrium concentration of amitrole and C is the concentration at time t. The primary degradation reaction is estimated to follow a pseudo–first–order kinetic law, according to Eq. (2.2). In order to confirm the speculation, $\mathrm{Ln}(C/C_0)$ was plotted as a function of illumination time. A linear relation between amitrole concentration and irradiation time has been observed for solar light degradation as shown in Figure 2.9. The values of rate constants have been determined from the slope. As shown in Table 2.2, the rate constant values decreased with increasing the amitrole concentration, when other parameters kept unchanged. Therefore, the degradation reaction was pseudo–first–order in the tested amitrole concentration ranges. A´lvarez et al. [9] have reported the photocatalytic degradation of amitrole (25 mg/L) with TiO_2 under medium pressure mercury vapor lamp, and the rate constant values k was 0.0289 min^{-1}. In the present work, the rate constant values (0.029~0.087 min^{-1}) were the same or better compared with that obtained by A´lvarez et al. [9].

In recent years, the Langmuir–Hinshelwood (L–H) rate expression has been used successfully for heterogeneous photocatalytic degradation describing the

relationship between initial degradation rate r_0 and initial concentration C_0 [32]. A linear expression can be conveniently obtained by plotting reciprocal initial rate against reciprocal initial concentration [33].

$$\frac{1}{r_0} = \frac{1}{k} + \frac{1}{kKC_0} \quad (2.3)$$

where k is the reaction rate constant (mg/L min) and K is the adsorption coefficient of the reactant (L/mg). On the basis of the data put into Table 2.2, the reciprocal of initial rate ($1/r_0$) is plotted against reciprocal of initial concentration of amitrole ($1/C_0$) as drawn in the insert figure in Figure 2.8. According to the L–H kinetics equation shown in Eq. (2.3) and fitted in the insert figure in Figure 4.6, a straight line with an intercept of $1/k$ and a slope of $1/kK$ is obtained. The values of K and k obtained for solar light photocatalytic degradation are found to be 0.324 L/mg and 0.699 mg/L min, respectively. It was reported in the TiO_2 photocatalytic degradation of toxic dyes that K and k values of 0.024 L/mg and 7.2307 mg/L min for reactive red, 0.0136 L/mg and 8.2781 mg/L min for methylene blue, and 0.0184 L/mg and 4.7125 mg/L min for rhodamine B [34]. Kaneco et al. [22] have described that K and k values for thiram were 0.025 L/mg and 2.1 mg/L min, respectively. Kaneco et al. [23] have investigated the photocatalytic degradation of dibutyl phthalate in TiO_2, and k value was 0.152 mg/L min. From the results achieved, it was viewed that $k > K$, which suggested that a surface reaction, where the amitrole was absorbed, was the controlling step of the process.

Table 2.2

Photocatalytic degradation kinetic parameters (pseudo–first–order rate constant, correlation coefficient, substrate half–life values and initial reaction rate).

Concentration of amitrole, C_0 (mg/L)	**Rate constant, k (min^{-1})**	**Correlation coefficient, R^2**	**Half–life, $t_{1/2}$ (min^{-1})**	**Initial reaction rate, r_0 (mg/L min)**
5	0.087	0.93	7.9	0.435
10	0.057	0.96	12.1	0.570
20	0.029	0.99	23.9	0.580

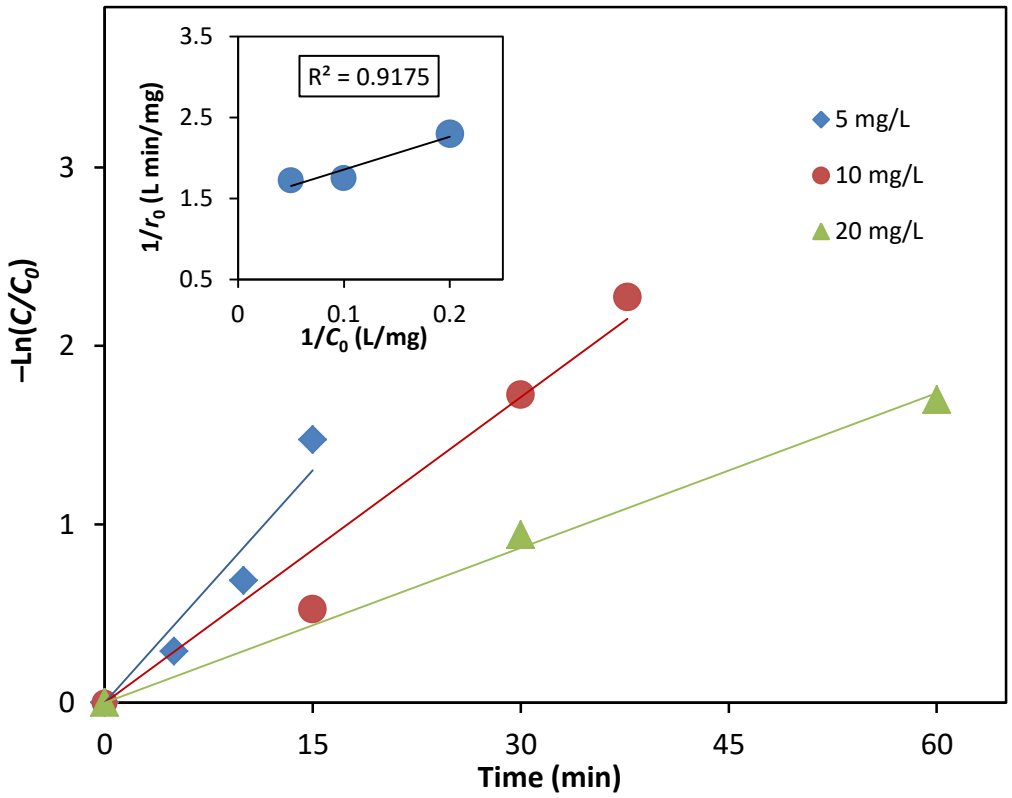

Figure 2.9. Plot of Ln(C/C_0) versus illumination time. Inset figure: plot of $1/r_0$ versus $1/C_0$. TiO_2: 200 mg; amitrole: 5–20 mg/L; light intensity: 1.6 mW/cm²; temperature: 25 °C; pH: 9.

2.3.7. Intermediate Product and Photodegradation Mechanism

The intermediate products formed in the solar photocatalytic degradation of amitrole in the aqueous TiO_2 suspension for 30 min was investigated by GC–MS analysis. One product was identified by the molecular ion and mass fragment peak. The intermediate product from amitrole exhibited a peak at m/z = 69 by the loss of the amino group, corresponding to triazole that is explained by the characteristic cleavage of the C–N bond.

In the photodegradative process with TiO_2 particulates, the absorption of light with an energy greater than 3.2 eV (wavelengths below 387 nm) generates electron/hole pairs that upon separation yield conduction band electrons and valence band holes is given by Eq. (2.4) [35]. Migration of these carriers to the surface in competition with a variety of other decay channels leads to trapping of the holes by OH^- groups or by H_2O to produce $^{\bullet}OH$ radicals which is expressed by Eq. (2.5) and trapping of the electrons by Ti^{IV} and/or by the ubiquitous oxygen molecules at the particle surface to yield the superoxide radical anion, $^{\bullet}O_2^-$, which forms the hydroperoxide radical $^{\bullet}OOH$ on protonation is shown by Eq. (2.6).

$$TiO_2 \rightarrow TiO_2\,(e_{CB}^- + h_{VB}^+) \rightarrow e_{CB}^- + h_{VB}^+ \qquad (2.4)$$

$$h_{VB}^+ + OH^-\ (\text{or } H_2O)_{surf} \rightarrow {}^{\bullet}OH + H^+ \qquad (2.5)$$

$$e_{CB}^- + O_2 \rightarrow {}^{\bullet}O_2^- + H^+ \rightarrow {}^{\bullet}OOH \qquad (2.6)$$

2.3.8. Transformation Products

The mineralization rate is a very important parameter since wastewater mineralization is the main goal of the treatment irrespectively of the configuration. Oh and Jenks [36] have recently reported that apparently cyanuric acid can be photodegraded in fluorinated–TiO_2 aqueous dispersions at low pH values and by the Fenton process. The mineralization of amitrole appeared after 25 h irradiation period is shown in Figure 2.10.

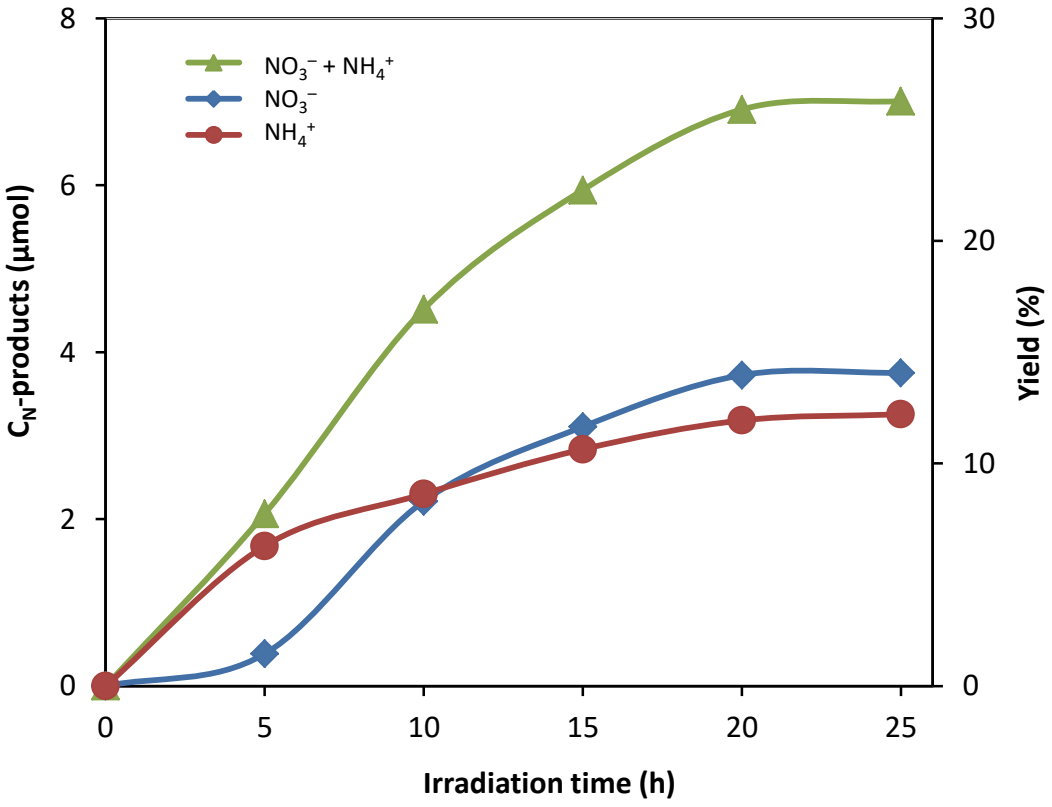

Figure 2.10. Formation of ions in the solar photocatalytic degradation of amitrole in water using TiO_2. TiO_2: 200 mg; amitrole: 20 mg/L; light intensity: 1.6 mW/cm^2; temperature: 25 °C; pH: 9.

It is found that the photocatalyzed mineralization of the endocrine disruptor amitrole in TiO_2–based photocatalysis, about 25% of the nitrogen was converted to NH_4^+ and NO_3^- ions. The remaining 75% nitrogen indicate that only NH_2 group is converted to NH_4^+ and NO_3^- ions and no cleavage happen in the amitrole ring. The remaining 75% nitrogen load remains in the nondegradable organic intermediates produced under the experimental conditions.

The formation of intermediate species triazole and 5–hydroxy–amitrole was converted to the urazole byproducts, as illustrated in Figure 2.11. The chemical oxygen demand (COD) test is widely used as an effective technique to measure the organic strength of wastewater. The test allows the measurement of waste in terms of the total quantity of oxygen required for the oxidation of organic matter to CO_2 and water [37]. In this study, the amitrole solution (30 mL) and 200 mg of TiO_2 were taken in the reactor and exposed to sunlight for 20 h. During the irradiation period the COD values of initial and treated amitrole solutions were measured. From the results, the COD was almost constant over the irradiation period. This is also confirming that the ring structure of the amitrole could not be broken. Watanabe et al. [3] have described that after cleavage of the triazole ring, the various intermediate fragments recombine to yield ring–expanded triazine intermediate, which slowly degrade to give the refractory cyanuric acid, during the photocatalyzed mineralization of amitrole at UV–irradiated TiO_2/H_2O interfaces. In the present work, cyanuric acid may be formed during the photocatalytic degradation of amitrole in water with TiO_2.

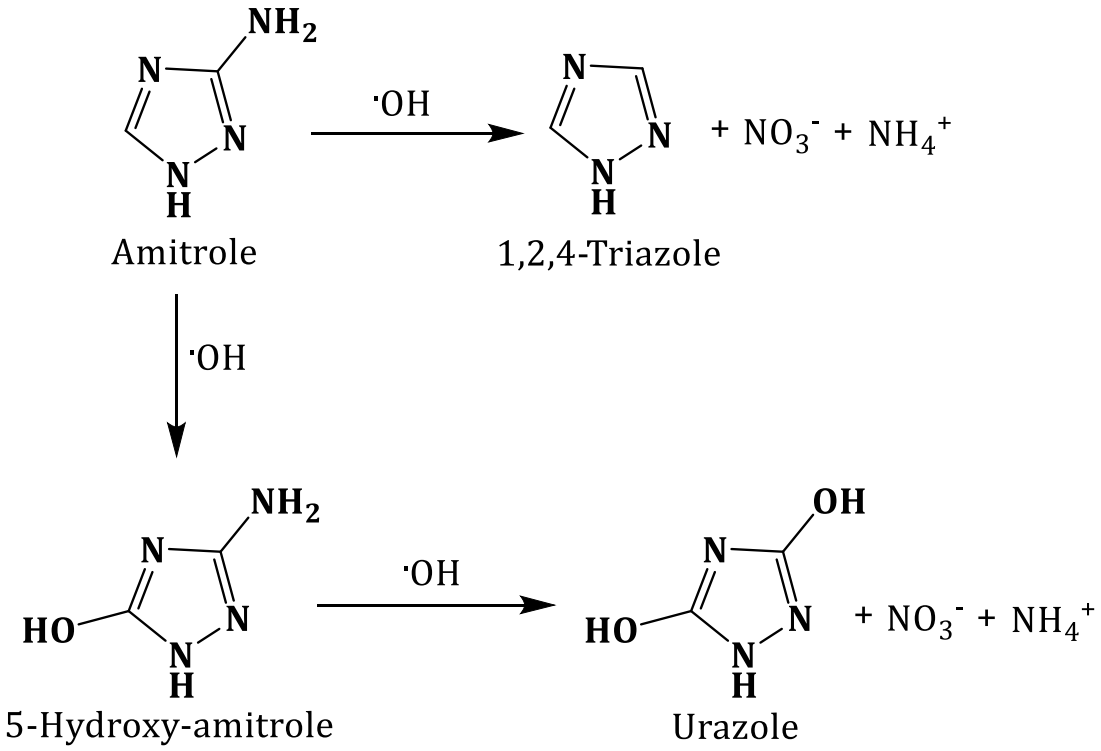

Figure 2.11. Proposed solar photocatalytic degradation pathway of amitrole.

2.4. CONCLUSIONS

The optimization of solar photocatalytic degradation conditions of amitrole in water using titanium dioxide was investigated. Typical optimum degradation conditions were as follows: photocatalyst loading: 6.7 g/L, temperature: 25 °C and pH 9. The kinetic behavior was described in terms of the Langmuir–Hinshelwood model. The activation energy (E_a) was estimated to become 6.73 kJ/mol. Nitrate (NO_3^-) and ammonium (NH_4^+) ions were detected as the end products. Triazole was identified as the intermediate products. Since the artificial lamp device for photocatalytic degradation is particularly expensive in the nonexclusive areas, the solar photocatalytic degradation technology developed may be available in those areas.

2.5. REFERENCES

[1] H. Kidd, D.R. Jones, The Agrochemicals Handbook, 3rd ed., Royal Society of Chemistry Information Services, Cambridge, UK, 1991, pp. 1–1500.

[2] I. Bobeldijk, K. Broess, P. Speksnijder, T.V. Leerdam, Determination of the herbicide amitrole in water with pre–column derivatization, liquid chromatography and tandem mass spectrometry, J. Chromatogr. A 938 (2001) 15–22.

[3] N. Watanabe, S. Horikoshi, A. Kawasaki, H. Hidaka, Formation of refractory ring–expanded triazine intermediates during the photocatalyzed mineralization of the endocrine disruptor amitrole and related triazole derivatives at UV–irradiated TiO_2/H_2O interfaces, Environ. Sci. Technol. 39 (2005) 2320–2326.

[4] I. Grcic, N. Koprivanac, D. Vujevic, S. Papic, Removal of atrazine from simulated groundwater by AOTs, J. Adv. Oxid. Technol. 11 (2008) 91–96.

[5] V. Goetz, J.P. Cambon, D. Sacco, G. Plantard, Modeling aqueous heterogeneous photocatalytic degradation of organic pollutants with immobilized TiO_2, Chem. Eng. Process. 48 (2009) 532–537.

[6] F. Orellana–Garcia, M.A. Alvarez, M.V. Lopez–Ramon, J. Rivera–Utrilla, M. Sanchez–Polo, A.J. Mota, Photodegradation of herbicides with different chemical natures in aqueous solution by ultraviolet radiation. Effects of operational variables and solution chemistry, Chem. Eng. J. 255 (2014) 307–315.

[7] C. Catastini, S. Rafqah, G. Mailhot, M. Sarakha, Degradation of amitrole by excitation of iron(III) aquacomplexes in aqueous solutions, J. Photochem. Photobiol. A: Chem. 162 (2004) 97–103.

[8] J. Andersen, M. Pelaez, L. Guay, Z. Zhang, K. O'Shea, D.D. Dionysiou, NF–TiO_2 photocatalysis of amitrole and atrazine with addition of oxidants under simulated solar light: Emerging synergies, degradation intermediates, and reusable attributes, J. Hazard. Mater. 260 (2013) 569–575.

[9] M.A. A´lvarez, F. Orellana–Garcı´a, M.V. Lo´pez–Ram´n, J. Rivera–Utrilla, M. Sa´nchez–Polo, Influence of operational parameters on photocatalytic amitrole degradation using nickel organic xerogel under UV irradiation, Arabian J. Chem. 2016; http://dx.doi.org/10.1016/j.arabjc.2016.10.005.

[10] W.J. Ong, L.L. Tan, S.P. Chai, S.T. Yong, A.R. Mohamed, Highly reactive {001} facets of TiO_2–based composites: synthesis, formation mechanism and characterization, Nanoscale 6 (2014) 1946–2008.

[11] P. Calza, S. Baudino, R. Aigotti, C. Baiocchi, P. Branca, E. Pelizzetti, High–performance liquid chromatographic/tandem mass spectrometric identification of the phototransformation products of tebuconazole on titanium dioxide, J. Mass Spec. 37 (2002) 566–576.

[12] C. Guillard, S. Horikoshi, N. Watanabe, H. Hidaka, P. Pichat, Photocatalytic degradation mechanism for heterocyclic derivatives of triazolidine and triazole, J. Photochem. Photobiol. A: Chem.149 (2002) 155–168.

[13] P. Calza, S. Baudino, R. Aigotti, C. Baiocchi, E. Pelizzetti, Ion trap tandem mass spectrometric identification of thiabendazole phototransformation products on titanium dioxide. J. Chromatogr. A 984 (2003) 59–66.

[14] S. Horikoshi, H. Hidaka, Photodegradation mechanism of heterocyclic two–nitrogen containing compounds in aqueous TiO_2 dispersions by computer simulation, J. Photochem. Photobiol. A: Chem. 141 (2001) 201–208.

[15] A. Aguera, E. Almansa, A. Tejedor, A.A. Fernandez, S. Malato, M.I. Maldonado, Photocatalytic pilot scale degradation study of pyrimethanil and of its main

degradation products in waters by means of solid–phase extraction followed by gas and liquid chromatography with mass spectrometry detection, Environ. Sci. Technol. 34 (2000) 1563–1571.

[16] S. Kaneco, K. Egusa, A.H.A. Dabwan, T. Itoh, H. Katsumata, T. Suzuki, P. Gomathisankar, Photo–electrochemistry & photo–biology for the sustainability, in: S. Kaneco, B. Viswanathan, H. Katsumata, Photocatalytic Remediation of Wastewater Contaminated with Amitorol, 1st ed., Union Press, Japan, 2012, pp. 45–57.

[17] B. Krishnakumar, M. Swaminathan, Photodegradation of Acid Violet 7 with AgBr–ZnO under highly alkaline conditions, Spectrochim. Acta A Mol. Biomol. Spectrosc. 99 (2012) 160–165.

[18] B. Subash, B. Krishnakumar, M. Swaminathan, M. Shanthi, Photocatalytic performance of WO_3 loaded Ag–ZnO for Acid Black 1 degradation by UV–A light, J. Mol. Catal. A: Chem. 366 (2013) 54–63.

[19] B. Subash, B. Krishnakumar, M. Swaminathan, M. Shanthi, Highly efficient, solar active and reusable photocatalyst, Zr loaded Ag–ZnO for Reactive Red 120 dye degradation with synergistic effect and dye sensitized mechanism, Langmuir 29 (2013) 939–949.

[20] B. Subash, B. Krishnakumar, R. Velmurugan, M. Swaminathan, M. Shanthi, Synthesis of Ce co–doped Ag–ZnO photocatalyst with excellent performance for NBB dye degradation under natural sunlight illumination, Catal. Sci. Technol. 2 (2012) 2319–2326.

[21] C.C. Wong, W. Chu, The direct photolysis and photocatalytic degradation of alachlor at different TiO_2 and UV sources, Chemosphere 50 (2003) 981–987.

[22] S. Kaneco, N. Li, K–K. Itoh, H. Katsumata, T. Suzuki, K. Ohta, Titanium dioxide mediated solar photocatalytic degradation of thiram in aqueous solution: kinetics and mineralization, Chem. Eng. J. 148 (2009) 50–56.

[23] S. Kaneco, H. Katsumata, T. Suzuki, K. Ohta, Titanium dioxide mediated photocatalytic degradation of dibutyl phthalate in aqueous solution–kinetics, mineralization and reaction mechanism, Chem. Eng. J. 125 (2006) 59–66.

[24] J.C. Garcia, K. Takashima, Photocatalytic degradation of imazaquin in an aqueous suspension of titanium dioxide, J. Photochem. Photobiol. A: Chem. 155 (2003) 215–222.

[25] R.R. Ishiki, H.M. Ishiki, K. Takashima, Photocatalytic degradation of imazethapyr herbicide at TiO_2/H_2O interface, Chemosphere 58 (2005) 1461–1469.

[26] J.–F. Wu, C.–H. Hung, C.–S. Yuan, Kinetic modeling of promotion and inhibition of temperature on photocatalytic degradation of benzene vapor, J. Photochem. Photobiol. A: Chem. 170 (2005) 299–306.

[27] A. Lair, C. Ferronato, J.–M. Chovelon, J.–M. Herrmann, Naphthalene degradation in water by heterogeneous photocatalysis: an investigation of the influence of inorganic anions, J. Photochem. Photobiol. A: Chem. 193 (2008) 193–203.

[28] A. Chatzitakis, C. Berberidou, I. Paspaltsis, G. Kyriakou, T. Sklaviadis, I. Poulios, Photocatalytic degradation and drug activity reduction of Chloramphenicol, Water Res. 42 (2008) 193–203.

[29] H.G. Yang, C.Z. Li, H.C. Gu, T.N. Fang, Rheological behavior of titanium dioxide suspensions, J. Colloid Interface Sci. 236 (2001) 96–103.

[30] S.D. Kahn, C.F. Pau, L.E. Overman, W.J. Hehre, Modeling chemical reactivity. 1. Regioselectivity of Diels–Alder cycloadditions of electron–rich dienes with electron–deficient dienophiles, J. Am. Chem. Soc. 108 (1986) 7381–7396.

[31] D.F. Ollis, Solar–assisted photocatalysis for water purification: issues, data, questions, in: E. Pelizzetti, M. Schiavello, (Eds.), Photochemical Conversion and Storage of Solar Energy, Kluwer Academic Publishers, The Netherlands, 1991, pp. 593–622.

[32] H.S. Son, S.J. Lee, K.D. Zoh, Kinetics and mechanism of TNT degradation in TiO_2 photocatalysis, Chemosphere 57 (2004) 309–317.

[33] S. Qourzal, M. Tamimi, A. Assabbane, Y. Ait–Ichou, Photodegradation of 2–naphthol using nanocrystalline TiO_2, J. Condens. Matter. 11 (2009) 55–59.

[34] M.H. Farzana, S. Meenakshi, Synergistic effect of chitosan and titanium dioxide on the removal of toxic dyes by the photodegradation technique, Ind. Eng. Chem. Res. 53 (2014) 55–63.

[35] S. Horikoshi, N. Serpone, Y. Hisamatu, H. Hidaka, Photocatalyzed degradation of polymers in aqueous semiconductor suspensions. 3. Photooxidation of a solid polymer: TiO_2–blended poly(vinyl chloride) film, Environ. Sci. Technol. 32 (1998) 4010–4016.

[36] Y.C. Oh, W.S. Jenks, Photocatalytic degradation of a cyanuric acid, a recalcitrant species, J. Photochem. Photobiol. A: Chem. 162 (2004) 323–328.

[37] R. Jain, S. Shirkarwar, Removal of hazardous dye Congo–red removal from waste material, J. Hazard. Mater. 152 (2008) 942–948.

CHAPTER 3

PHOTOCATALYTIC DEGRADATION OF DYE WITH SELF–DYE–SENSITIZATION UNDER FLUORESCENT LIGHT IRRADIATION

3.1. INTRODUCTION

Titanium dioxide (TiO_2) and zinc oxide (ZnO) have drawn great attention, because they become one of the most effective photocatalysts in the mineralization of toxic organic substances, owing its virtue of low cost, highly chemical stability and nontoxicity [1,2]. However, these catalysts can only be excited by the irradiation of UV light, due to their wide band gaps. The artificial light source, for instance an Hg–Xe lamp, is particularly expensive, whereas the fluorescent lamp is cheap, has a longer life time and use less energy. The UV region occupies only a small fraction of fluorescent lamp. This problem can be solved only by improving the light absorption capacity of photocatalysts [3,4]. The photocatalysts can be modified in order to expand their photoresponse to the visible region for pollutant degradation with several ways, including the doping with cations/anions or the coupling with another small band gap material [5]. Most of these methods, however, are time–consuming and quite expensive. Dye sensitization, on the other hand, is a simpler method that can extend catalysts activation to longer wavelengths compared with those corresponding to its band gap. Dye–sensitization begins with electron injection into the conduction band (CB) of photocatalyst from the excited dye, followed by interfacial electron transfer [6,7] (Figure 3.1).

The dye–sensitization technique has been reported as an innovative technology that could play an important role in developing efficient and cost–effective semiconductor photocatalyst in the near future [8]. It can extend the light absorption range, enhance photon harvesting efficiency, provide extra excited electron pairs from a dye and accelerate charge transfer, leading to a high efficiency of photoelectric conversion [9]. The photo–sensitized mechanism of the

dye–adsorbed TiO_2 under the visible light illumination can be simply expressed as follow: (i) the adsorbed dye is effectively excited to generate the electron/hole pair by the light illumination because of its narrower band gap in comparison with TiO_2 and (ii) the photo–excited electrons are injected from the lowest unoccupied molecular orbital (LUMO) of adsorbed dyes into the conduction band (CB) of TiO_2 [10–13].

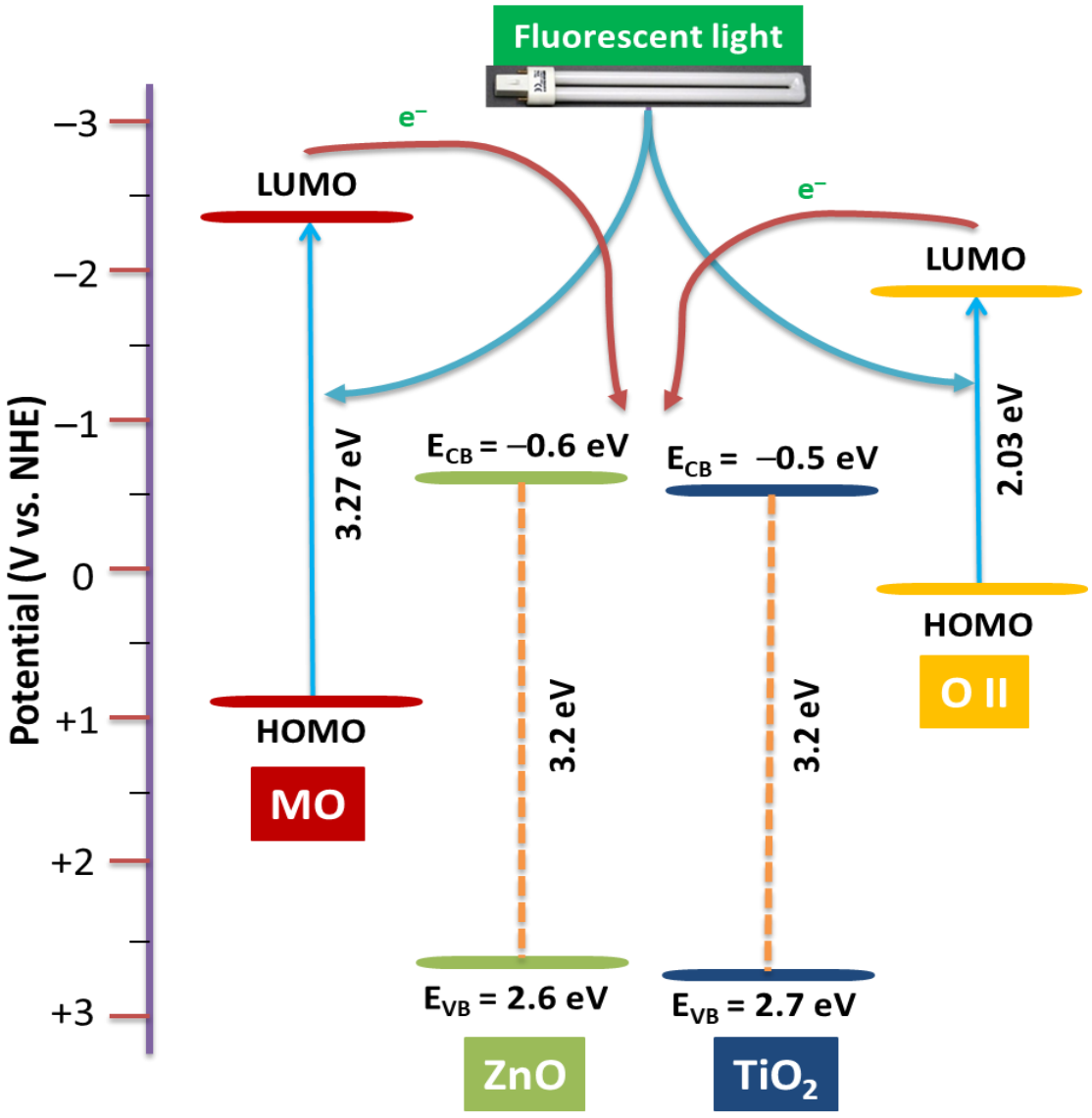

Figure 3.1. Schematic self–dye–sensitization pathway under fluorescent light illumination.

Recently, the self–sensitized degradation of dye under visible light irradiation has been investigated. Park et al. [14] reported the dye–sensitization can be applied for the self–degradation of dyes. Wu et al. [15] studied self–photosensitized oxidative decolorization of rhodamine B under visible light irradiation in TiO_2 dispersions with halogen lamp and cutoff filter. The photosensitized degradation of a textile azo dye with TiO_2 using visible light with fiber optic illuminator was reported by Vinodgopal and Kamat [16]. Xing et al. [17] studied the enhanced self–sensitized degradation of colored pollutants under visible light with mercury lamp and filter. The photocatalytic performance of ZnO for self–sensitized degradation of malachite green under solar light was investigated by Saikia et al. [18]. Shang et al. [19] studied the photocatalytic degradation of rhodamine B by dye–sensitized TiO_2 under visible light irradiation. According to our knowledge, there is little information on the photocatalytic decolorization of dye in water with self–dye–sensitized photocatalysts under room fluorescent light irradiation with very week intensity.

This chapter deals with photocatalytic decolorization of dye in water with self–dye–sensitized TiO_2 and ZnO under room fluorescent light irradiation. The radical scavenger studies are also carried out to investigate the active species involved in the photodegradation of orange II (OII) and rhodamine B (RhB) with self–sensitized TiO_2 under the visible light irradiation ($\lambda > 400$ nm) and the possible mechanism is discussed based on radical trapping experiments.

3.2. MATERIALS AND METHODS

3.2.1. Chemicals and Materials

All reagents were of analytical grade and were used without further purification. Orange II, methyl orange and rhodamine B used in this study were purchased from Nacalai Tesque Inc., Kyoto, Japan (grade>99%). Ascorbic acid (AA), *di*–ammonium oxalate (AO) and *tert*–butyl alcohol (TBA) were obtained from Wako Pure Chemicals. TiO_2 powder (Degussa P25, purity 99.9%) was obtained Wako Pure Chemical Industries, Ltd. Photocatalyst ZnO was purchased from Sigma–Aldrich. Ultrapure water (18 MΩ cm) was prepared by an ultrapure water system (Advantec MFS Inc., Tokyo, Japan). The detailed experimental conditions were shown in Table 3.1.

3.2.2. Characterization of Photocatalyst

In order to record the diffraction patterns of photocatalysts (TiO_2 and ZnO), the powder X–ray diffractometer (XRD, RIGAKU Ultima IV, sample horizontal type) was used in the condition of Cu Kα radiation of wavelength 0.15406 nm with tube current of 50 mA at 40 kV in 2θ angle range from 10° to 80° with a scan speed of 4°/min and a step size of 0.02°. Figure 3.2 shows the X–ray diffraction (XRD) pattern of TiO_2. Because P25 is a mixture of 20% rutile and 80% anatase, XRD pattern shows both anatase and rutile lines [20]. Figure 3.3 illustrates the XRD of ZnO. Three main distinct peaks at 31.76°, 34.42° and 36.26° are observed in the patterns, which are indexed to the (100), (002) and (101) diffractions of the wurtzite ZnO, respectively [21]. The particle size of the TiO_2 and ZnO have been obtained from the full width at half maximum (FWHM) of the most intense peaks of the respective crystals using the Scherrer equation, $D = 0.9\lambda/\beta\cos\theta$, where λ is the X–ray wavelength, D the average crystallite size, θ the Bragg diffraction angle

and β the full width at half–maximum. The crystal size of TiO_2 and ZnO could be estimated as ~21 and ~38 nm, respectively.

Table 3.1

Experimental conditions.

Samples	Orange II (5 mg/L,30 mL)
	Methyl orange (5 mg/L, 30 mL)
	Rhodamine B (5 mg/L, 30 mL)
Photocatalysts	P25 TiO_2 (20 mg)
	Aldrich ZnO (20 mg)
Temperature	Room temperature (25 °C)
pH	~6
Light source	450 nm LED light (5.14 mW/cm^2)
	Fluorescent light (0.034 mW/cm^2)
	LED lamp with cut filter (5.3 mW/cm^2)
λ_{max}	Orange II (485 nm)
	Methyl orange (464 nm)
	Rhodamine B (554 nm)
Illumination time	6 h

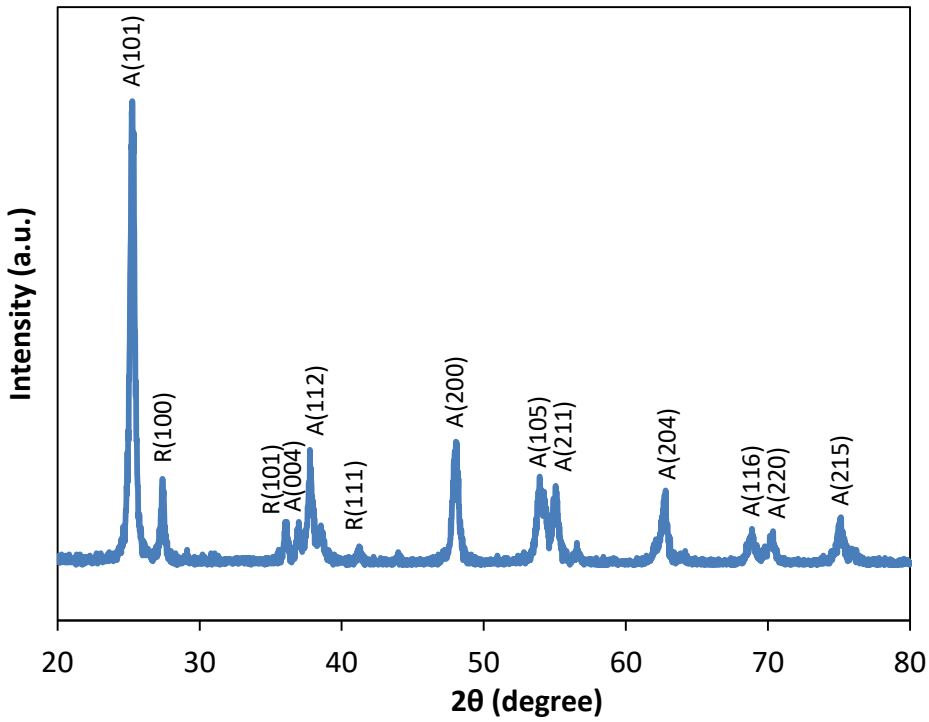

Figure 3.2. XRD patterns of P25 TiO_2.

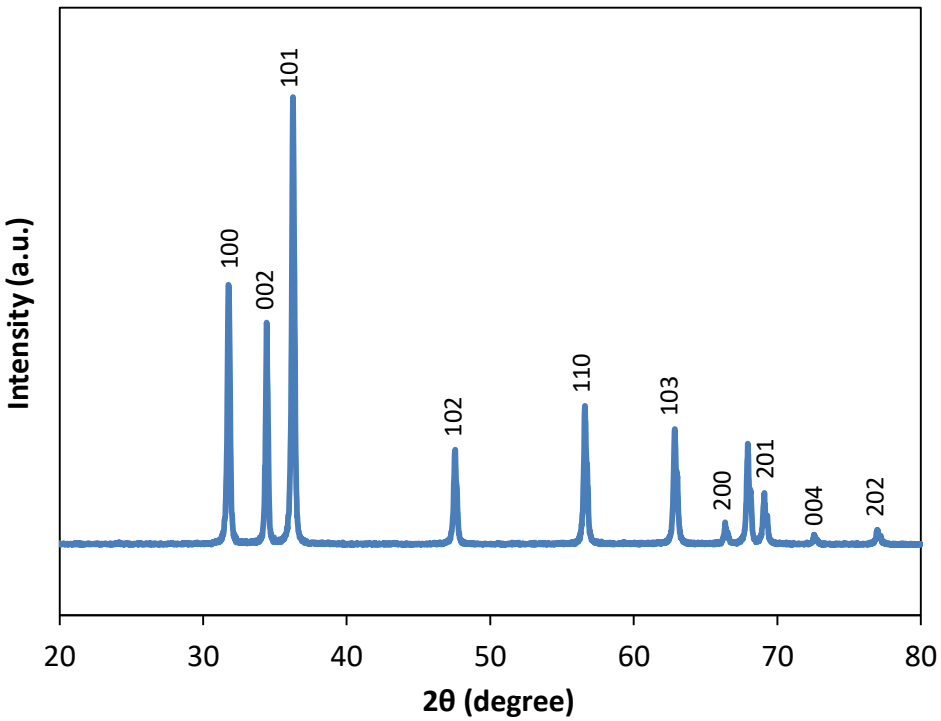

Figure 3.3. XRD patterns of Aldrich ZnO.

The diffuse reflectance spectra (DRS) of photocatalysts were checked over a range of 200–800 nm using a Shimadzu UV–2450 UV/vis system equipped with an integrating sphere diffuse reflectance accessory with the reference material $BaSO_4$. The diffuse reflectance spectra of the TiO_2 and ZnO samples were studied, as shown in Figures 3.4 and 3.5. The reflectance data was converted to Kubelka–Munk equation which is expressed as $F(R) = (1-R)^2/2R$. The optical band gap of TiO_2 was deduced by extrapolating the straight linear portion of the plot of $[F(R)h\nu]^{0.5}$ versus the photon energy ($h\nu$) to the phonon energy axis, which is shown in the interior of Figure 3.3. The band gap of ZnO was estimated from Tauc plot of $[F(R)h\nu]^2$ versus photon energy, which is presented in the interior of Figure 3.4.

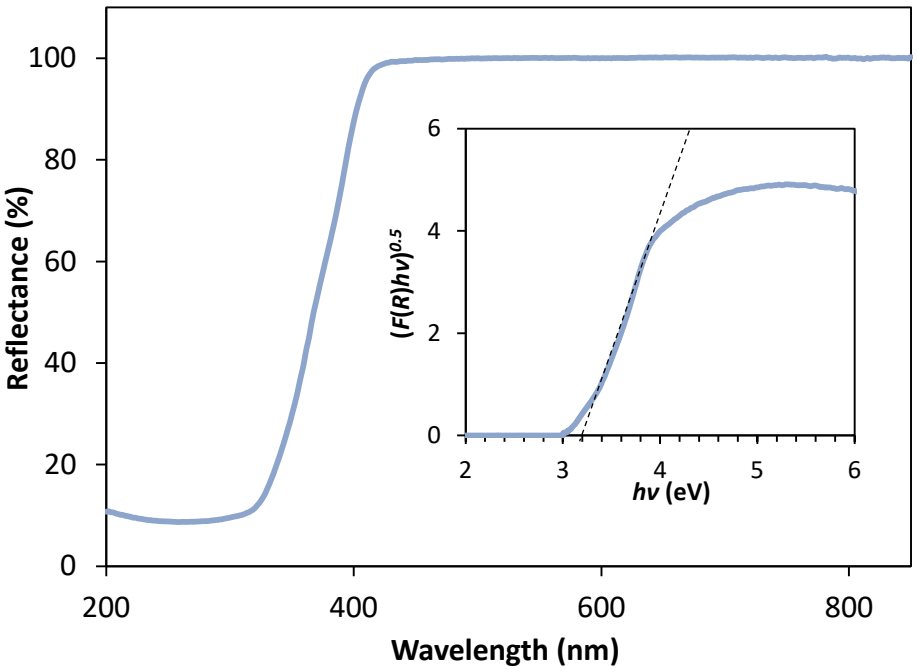

Figure 3.4. UV–Vis DRS patterns of TiO_2. Inset figure: Tauc plot of $[F(R)h\nu]^{0.5}$ versus photon energy.

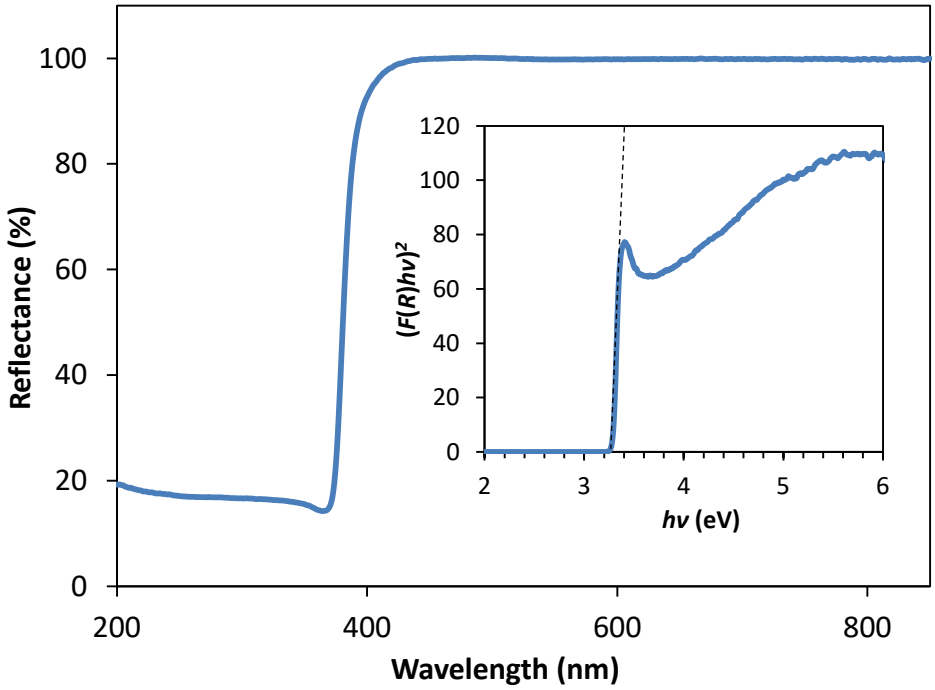

Figure 3.5. UV–Vis DRS patterns of ZnO. Inset figure: Tauc plot of $[F(R)hv]^2$ versus photon energy.

3.2.3. Evaluation of Photocatalytic Activity

The photodegradation system is illustrated in Figure 3.6. The photocatalytic activities of TiO_2 and ZnO were checked by the decolorization of two typical azo dyes, orange II (OII) and methyl orange (MO), under 450 nm LED light and fluorescent light irradiation. The photocatalytic reactions were performed in a Pyrex glass reactor. The catalyst powder (20 mg) was suspended in 30 mL of dye solutions with 5 mg/L without adjustment of pH. The luminous intensities were measured by a LI–COR light sensor (LI–250A), and were 5.1 mW/cm^2 for LED lamp and 0.034 mW/cm^2 for fluorescent light, respectively. The adsorption experiment was conducted with aluminum foil coverage to block the impact of radiation. Prior to light illumination, the catalyst suspension was dispersed by a magnetic stirrer for 30 min in the dark, to achieve adsorption equilibrium. During irradiation, the catalyst was kept in suspension state by a magnetic stirrer.

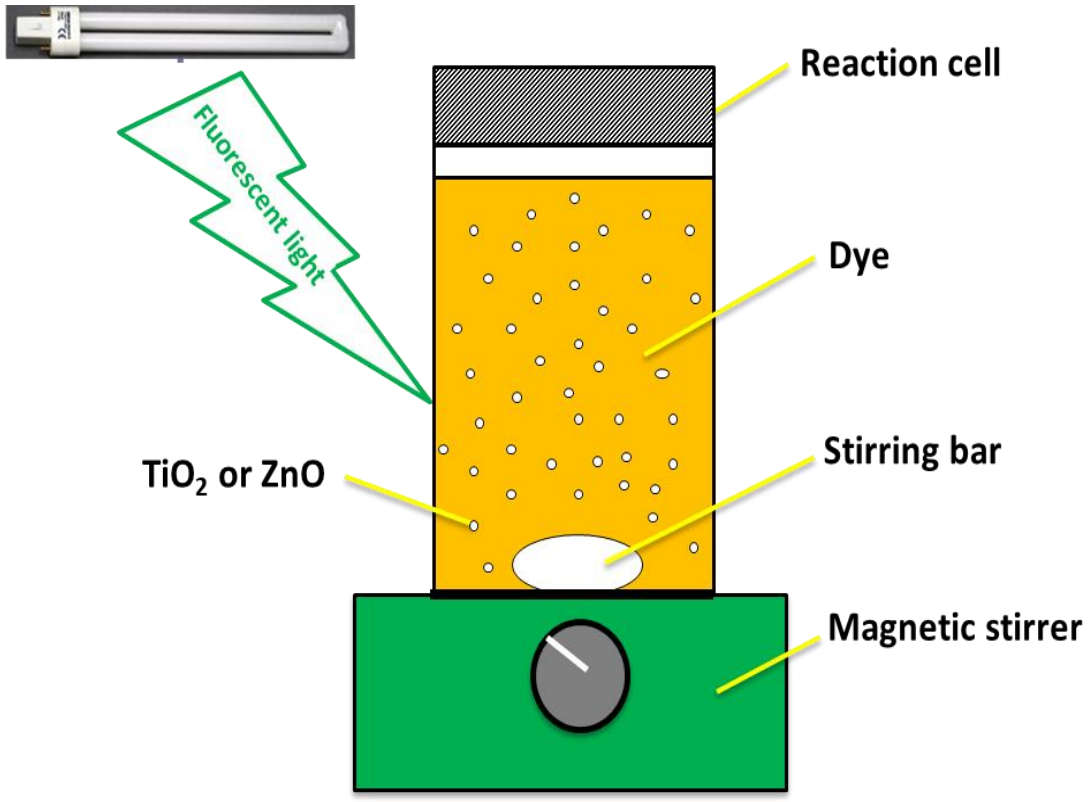

Figure 3.6. Schematic reactor for photocatalytic degradation of dye.

After the illumination, the catalyst was separated through the Advantec membrane filter 0.45 μm. The catalysts could be almost removed by the filtration. The concentration of dye was measured using a UV–visible spectrometry (UV–1650PC, SHIMADZU Co., Tokyo, Japan). According to Beer–Lambert law, the relative concentration (C/C_0) of the OII solution was calculated by the relative absorbance (A/A_0) at 485 nm, where A_0 and A are the absorbance of the OII solution at the beginning time (t_0) of photocatalytic treatment and at time t, respectively. The photodegradation of OII under fluorescent light irradiation was similar to that under visible light irradiation except for the light source. The photodegradation of MO (5 mg/L) was similar to that of OII except that the detection wavelength was 464 nm.

3.2.4. Detection of Reactive Oxygen Species

Radical scavenger studies were carried out to investigate the active species involved in the photodegradation of dye. The scavenging experiments of reactive oxygen species were evaluated by the degradation of OII and RhB with TiO_2 under visible light irradiation at ambient temperature. The sample solution was irradiated with a LED lamp (990 W, Ushio Electronics) in conjunction with a UV cut filter (Y–44, HOYA), which was positioned on the side of the reaction cell. The light intensity of the LED lamp was 5.3 mW/cm^2. Three scavengers were selected, namely, *tert*–butyl alcohol ($^{\bullet}OH$ radical scavenger), *di*–ammonium oxalate monohydrate (hole scavenger) and ascorbic acid ($^{\bullet}O_2^-$ radical scavenger). Different quantity of *tert*–butyl alcohol, *di*–ammonium oxalate monohydrate [22] and ascorbic acid [23] were added into the dye solution prior to addition of catalysts.

3.3. RESULTS AND DISCUSSION

3.3.1. UV–Visible Analysis

The temporal absorption spectral changes during the photocatalytic decolorization of OII and MO with TiO_2 and ZnO under fluorescent and 450 nm light illuminations were investigated, as shown in Figure 3.7 (a, b) and Figure 3.8 (a, b), respectively. As they can be seen, the intensities of the peak at 485 and 464 nm progressively decreased with increasing irradiation time up to 360 min. The well–defined absorption bands decreased after irradiation for 360 min, indicating that OII and MO had been decolored in the presence of TiO_2 and ZnO with fluorescent light and 450 nm LED light irradiation. Therefore, the self–dye–sensitization was very effective for the decolorization of OII and MO under fluorescent and 450 nm light illuminations. The UV–visible spectra of aqueous solutions of OII and MO before and after treatment under fluorescent light and 450 nm LED light are illustrated in Figure 3.8 (a) and (b), respectively.

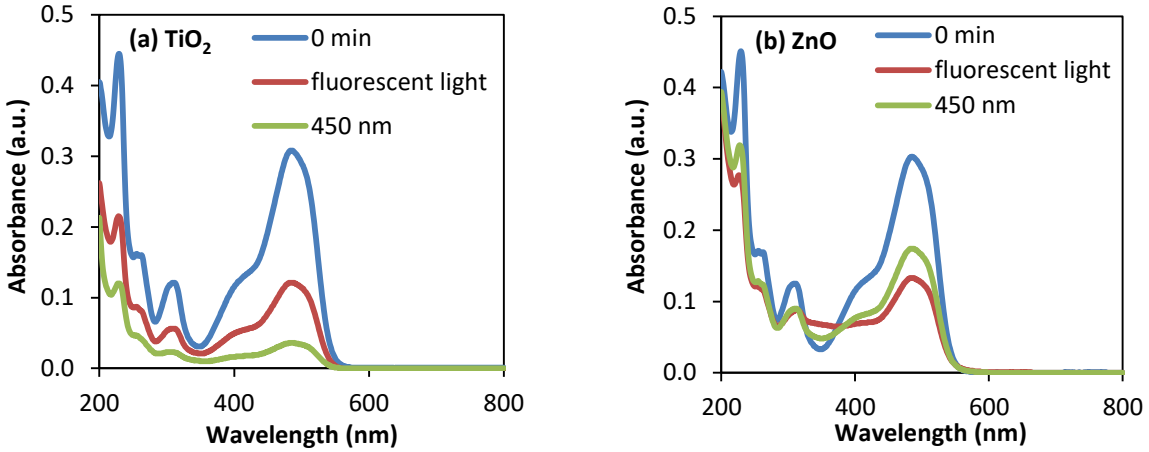

Figure 3.7. UV–visible spectra of aqueous solutions of OII for 0 min and 360 min using (a) TiO_2 and (b) ZnO under fluorescent light and 450 nm LED light, respectively.

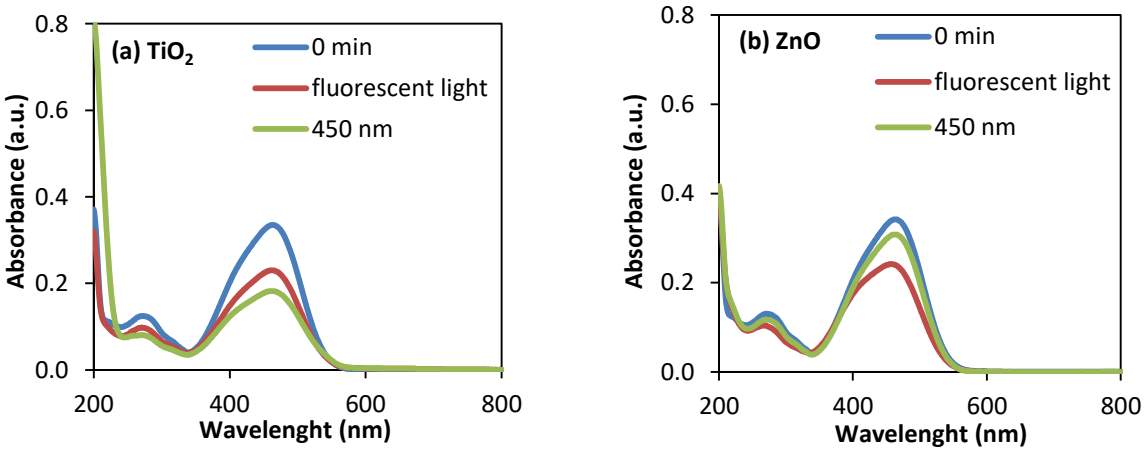

Figure 3.8. UV–visible spectra of aqueous solutions of MO for 0 min and 360 min using (a) TiO_2 and (b) ZnO under fluorescent light and LED light, respectively.

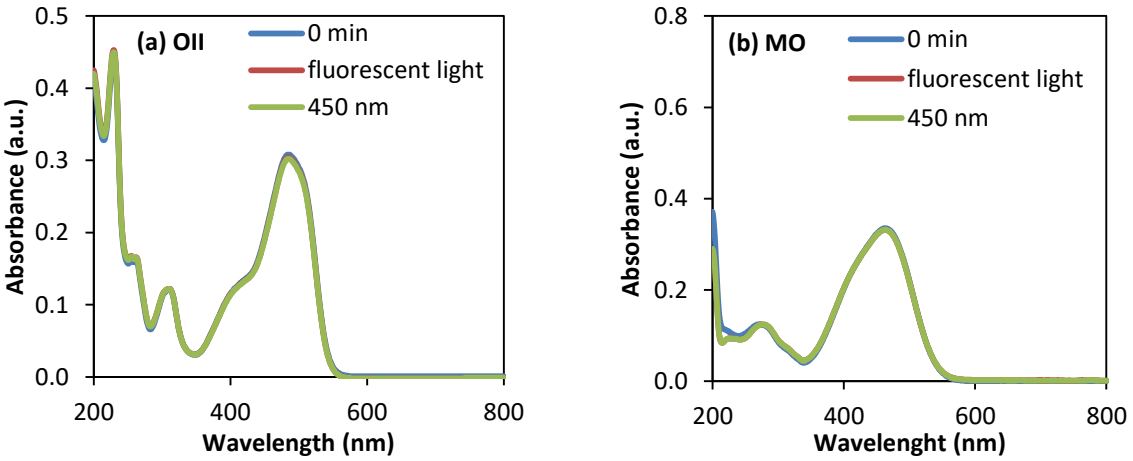

Figure 3.9. UV–visible spectra of aqueous solutions of (a) OII and (b) MO before and after treatment under fluorescent light and 450 nm LED light.

3.3.2. Photocatalytic Decolorization of OII and MO with TiO_2

The effect of irradiation time on photocatalytic decolorization of dye (OII and MO) was performed by measuring the percentage of dye removal at different periods under fluorescent and 450 nm LED lights, as shown in Figure 3.10 (a) and (b), respectively. The percentage of OII and MO removal increased with an increase in irradiation time, and reached up to about 61% and 24% for fluorescent light and about 88% and 41% for LED light after 6 h, respectively. The adsorption (removal) percentage of OII on TiO_2 particles was large up to 30 min, whereas MO adsorption was very little. There was little change in the OII and MO solutions during photolysis. The photocatalytic decolorization processes of both dyes under LED light were more effective compared with those obtained under fluorescent light radiation. These facts may be due to the light intensity, because the amounts of electron–hole pair are dependent on them [24].

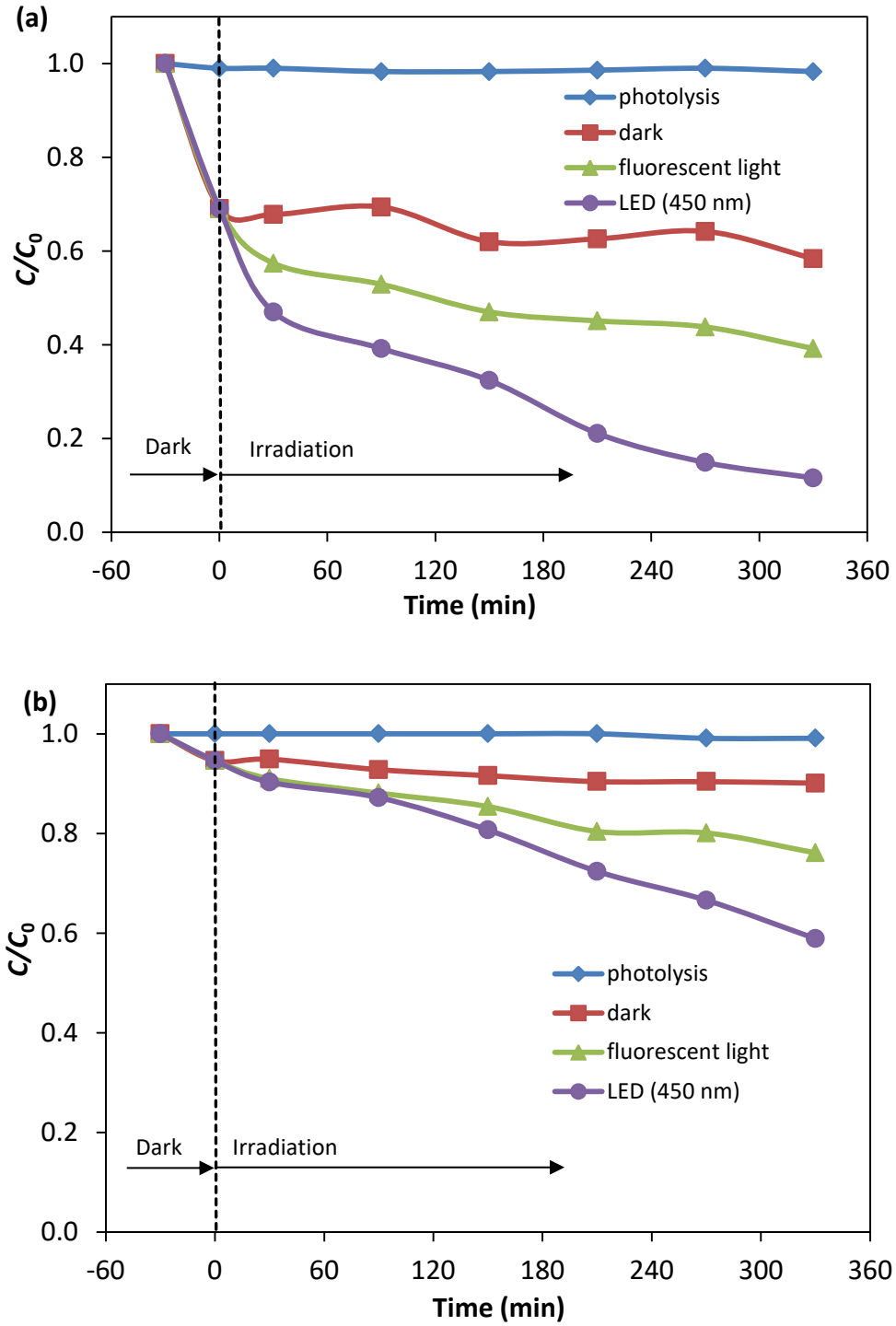

Figure 3.10. Time courses of concentration of orange II (a) and methyl orange (b). Photolysis: ♦, TiO_2 dispersions: under dark ■, under fluorescent light irradiation ▲ and under LED light irradiation ●.

3.3.3. Photocatalytic Decolorization of OII and MO with ZnO

Figure 3.10 (a) and (b) show the percentage of dye (OII and MO) in the presence of ZnO nanopowders under fluorescent light and 450 nm LED light. About 57% and 28% degradation of OII and MO took place at 6 h under fluorescent light, whereas about 43% and 10% was eliminated under 450 nm LED light. Negligible decolorization occurred in the presence of fluorescent light and 450 nm LED light without any catalyst, as shown in Figure 3.9 (a, b). Without the presence of either photocatalysts (TiO_2 and ZnO) or the light (fluorescent and 450 nm) radiation, little change in the absorbance values was observed. The adsorption (removal) percentage of OII on TiO_2 and ZnO particles was large, whereas adsorption of MO on the same photocatalyst was very little in the time range. This weaker adsorption process of methyl orange compared to the OII dye could be due to it that the MO molecule has the only one ($–SO_3$) group while the OII molecule has one ($–SO_3$) and one (–OH) groups. These observations revel that visible light and photocatalyst are needed for effective decolorization of dye.

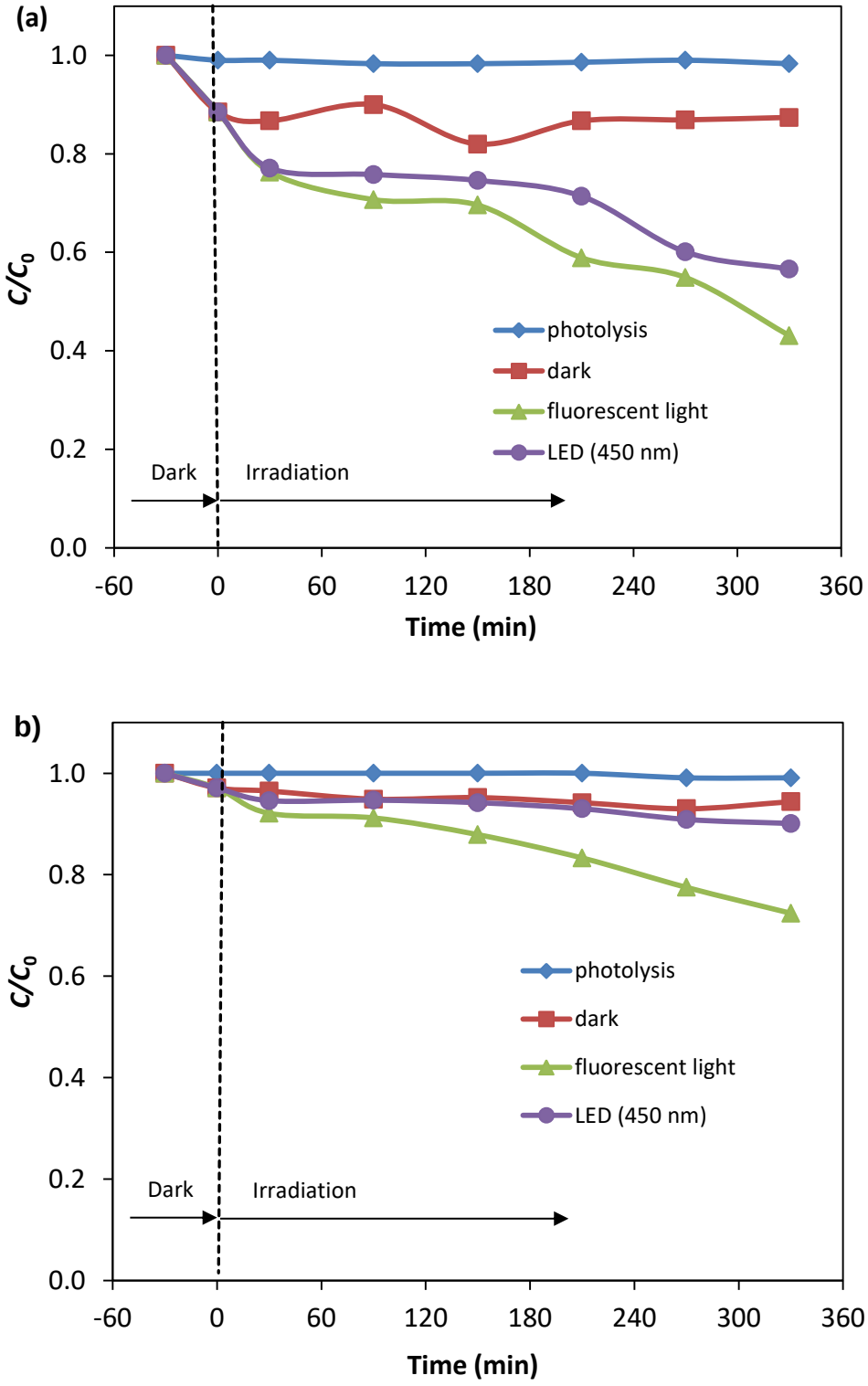

Figure 3.11. Time courses of concentration of orange II (a) and methyl orange (b). Photolysis: ♦, ZnO dispersions: under dark ■, under fluorescent light irradiation ▲ and under LED light irradiation ●.

3.3.4. Kinetic Analysis

The photocatalytic oxidation process for many organic contaminants has often been modeled with the Langmuir–Hinshelwood (L–H) equation, which also covers the adsorption properties of the substrate on the photocatalyst surface. This model was developed by Turchi and Ollis [25] and expressed as Eq. (3.1):

$$\boldsymbol{r_0 = -\frac{dC}{dt} = \frac{kKC}{1+KC}} \quad (3.1)$$

where r_0 is the degradation rate of the reactant, k is the reaction rate constant and K and C are the adsorption equilibrium constant and concentration for the reactant, respectively. If the concentration of reactant is very low, i.e. $KC << 1$, the L–H equation (Eq. (3.1)) simplifies to a pseudo–first–order kinetic law (Eq. (3.2)) where k_{obs} is being the apparent pseudo–first–order rate constant.

$$\boldsymbol{-\frac{dC}{dt} = kKC = k_{obs}C} \quad (3.2)$$

Integration of the above equation with the limit of $C = C_0$ at t = 0 with C_0 gives the following equation:

$$\boldsymbol{-\mathrm{Ln}\frac{C}{C_0} = k_{obs}t} \quad (3.3)$$

The primary degradation reaction is estimated to follow a pseudo–first–order kinetic law, according to Eq. 3.3. In order to confirm the speculation, $\mathrm{Ln}(C/C_0)$ was replotted as a function of illumination time for OII and MO shown in Figure 3.12 and 3.13, respectively. Because the linear plots were observed as expected, the kinetics of OII and MO in the TiO_2 suspension solution followed the first–order degradation curve, which agreed with the L–H model resulting from the low coverage in the experimental concentration range (5 mg/L).

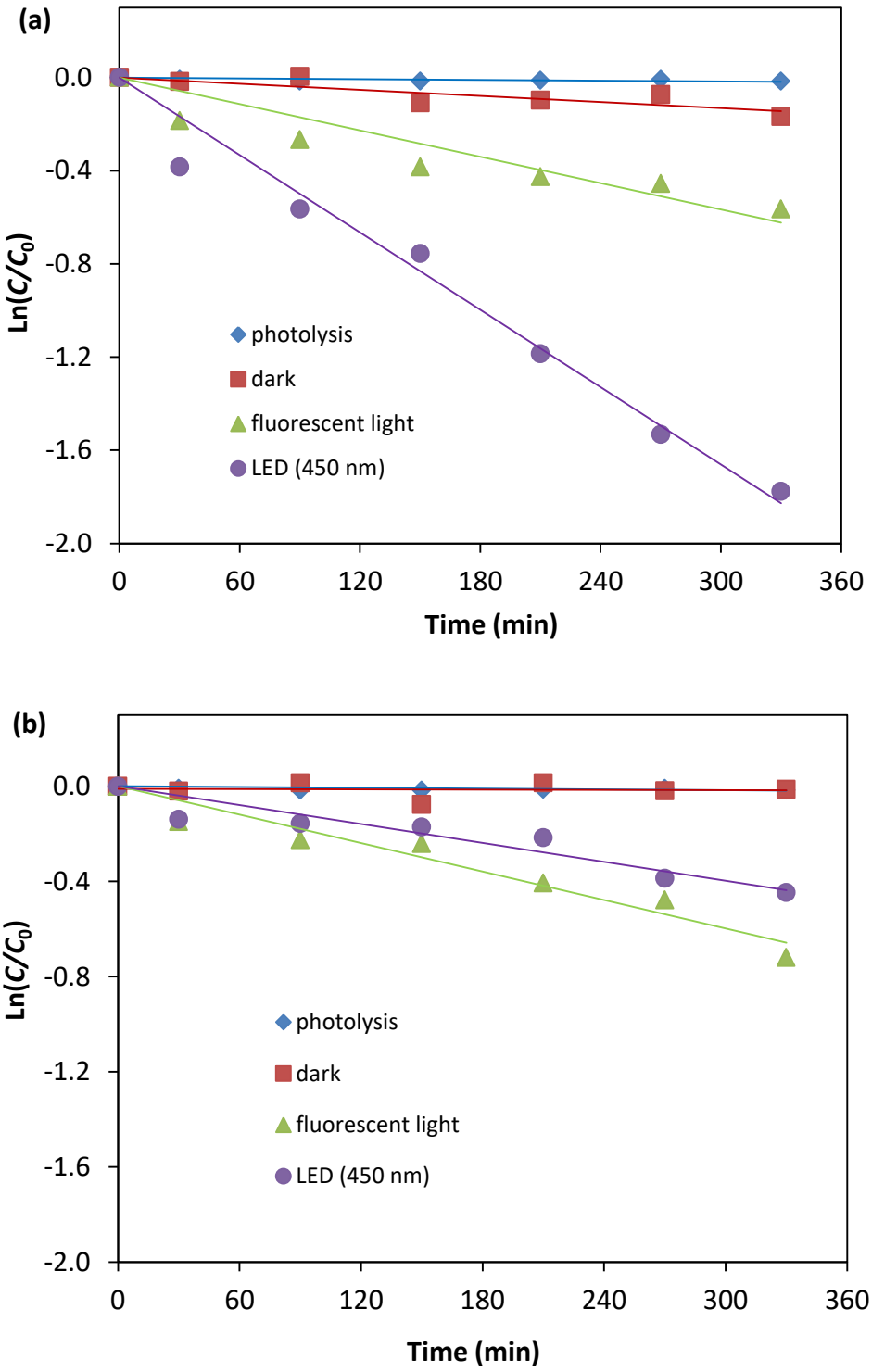

Figure 3.12. Kinetic plot of $\mathrm{Ln}(C/C_0)$ versus irradiation time for the photocatalytic degradation of orange II (a) TiO_2, (b) ZnO.

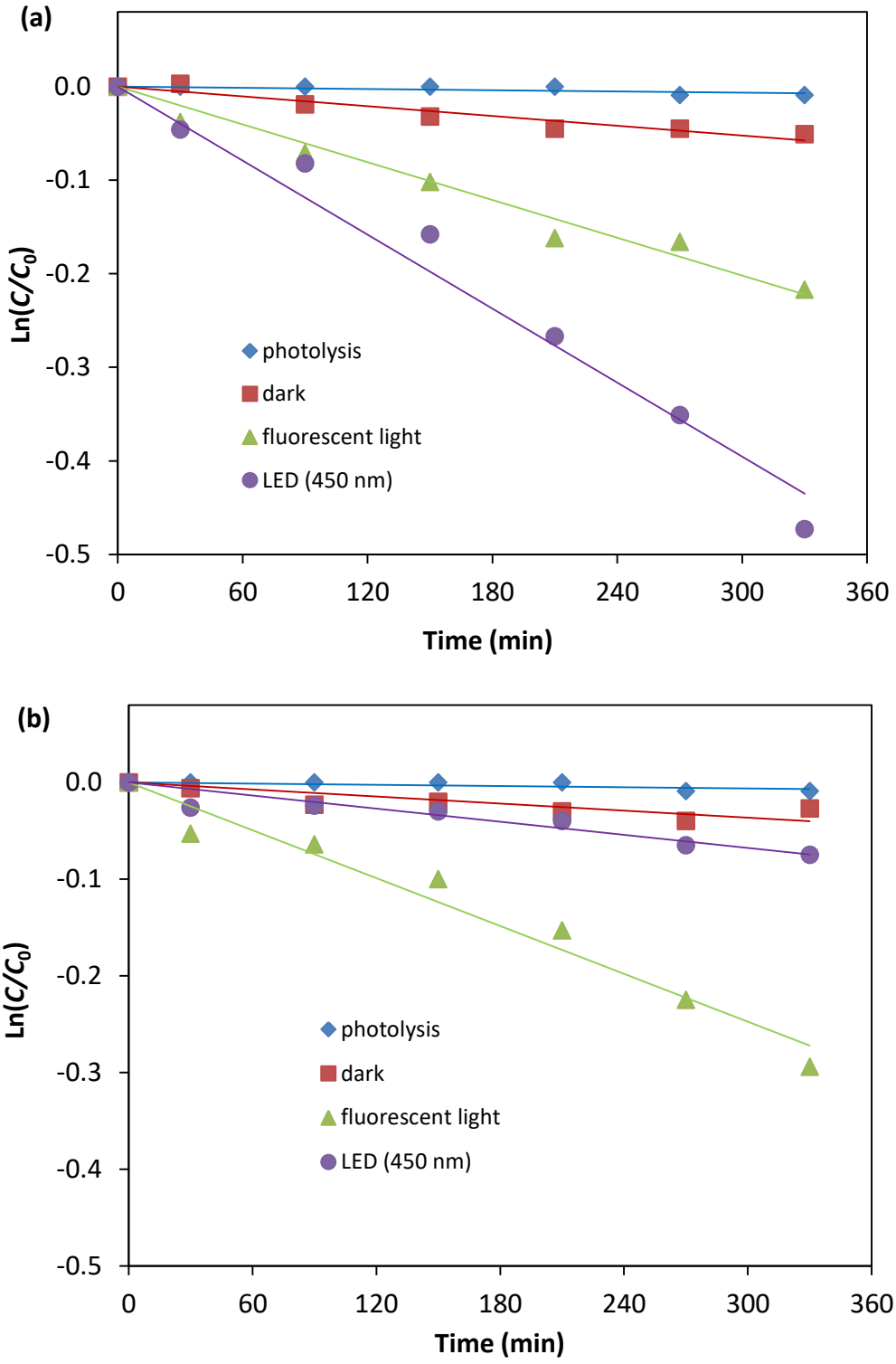

Figure 3.13. Kinetic plot of Ln(C/C_0) versus irradiation time for the photocatalytic degradation of methyl orange (a) TiO_2, (b) ZnO.

The photocatalytic decolorization kinetic parameters such as pseudo–first–order rate constant, correlation coefficient and substrate half–live are shown in Table 3.2. The values of rate constants have been determined from the slope of these plots. As shown in Table 3.2, the rate constant values k_{obs} (min^{-1}) were lower in fluorescent light compared with that under LED light for both dyes.

Table 3.2

Rate constants, correlation coefficient and half–life values of OII and MO dyes using TiO_2 and ZnO.

Light source	**Catalysts**	**Rate constant, k_{obs} (min^{-1})**		**Correlation coefficient, R^2**		**Half–life, $t_{1/2}$ (min)**	
		OII	**MO**	**OII**	**MO**	**OII**	**MO**
Fluorescent light	TiO_2	0.0019	0.00067	0.80	0.97	367	1029
	ZnO	0.0019	0.00083	0.93	0.96	346	866
LED light	TiO_2	0.0055	0.0013	0.97	0.98	125	525
	ZnO	0.0013	0.00023	0.88	0.88	533	3465

3.3.5. Radical Scavenger Studies on TiO_2 Using OII

To determine the possible degradation mechanism of Orange II by TiO_2, different scavengers were introduced to quench the relevant active species. In this study, *tert*–butyl alcohol (TBA), *di*–ammonium oxalate monohydrate (AO) and ascorbic acid (AA) were adopted to be the scavengers of hydroxyl radicals ($^{\bullet}OH$), superoxide radical ($^{\bullet}O_2^-$) and holes (h^+), respectively. As shown in Figure 3.14, the photocatalytic degradation efficiency of OII (5 mg/L) with TiO_2 was about 100% after 6 h under visible light irradiation. The photodegradation of OII over the TiO_2 was affected slightly by the addition of TBA, demonstrating that $^{\bullet}OH$ active species

played a small role in the photocatalytic degradation of OII. However, the photocatalytic degradation efficiency of OII decreases significantly in the presence of AA, which indicates that $^{\bullet}O_2^-$ is an important active species in the process of OII degradation. In addition, the photocatalytic activity of the TiO_2 was completely suppressed by AO, suggesting that h^+ can be also involved in the process of OII degradation.

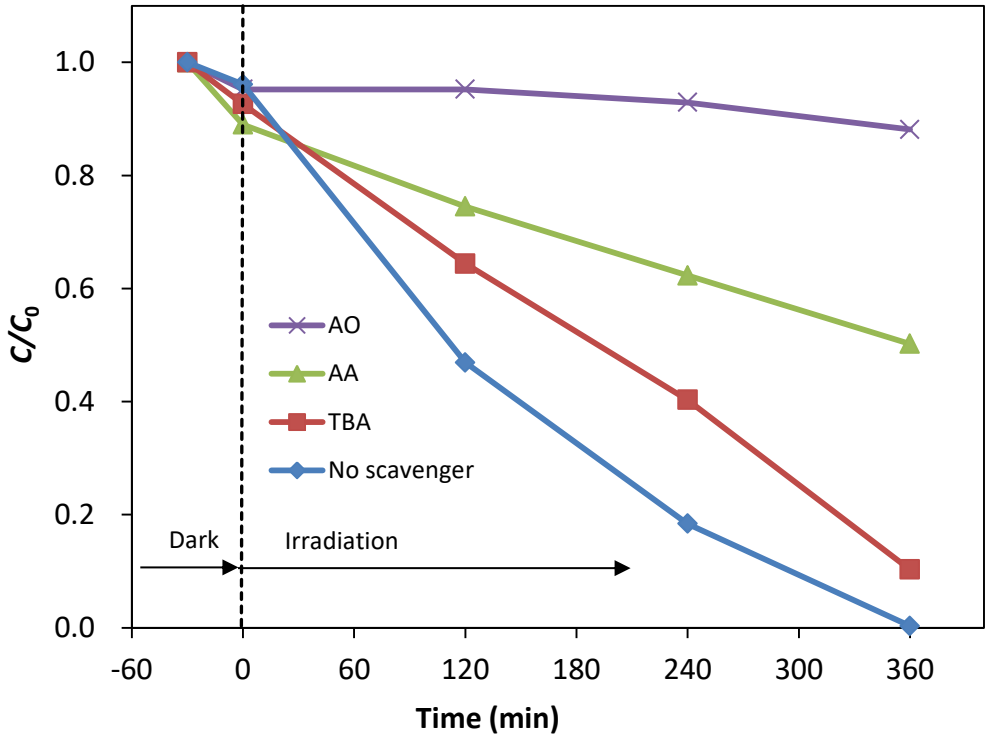

Figure 3.14. Effects of different radical scavengers on OII degradation in presence of TiO_2 under visible light irradiation.

3.3.6. Radical Scavenger Studies on TiO_2 Using RhB

In order to investigate the active species involved in photodegrading RhB, scavenger studies were also carried out on TiO_2. As shown in Fig. 3.15, photocatalytic degradation of RhB over TiO_2 was retarded with the presence of di–ammonium oxalate monohydrate (AO) and ascorbic acid (AA). The results strongly

indicated that h^+ and $^{\bullet}O_2^-$ were the active species involved in the photodegradation of RhB. However, $^{\bullet}O_2^-$ was more dominant in photodegrading RhB, with h^+ as the most important active species. As aforementioned, the enhanced photocatalytic degradation of RhB was contributed by the photosensitizing of RhB toward TiO_2. The electron ejected from HOMO to conduction band of TiO_2 could have been utilized for the reduction of surface adsorbed oxygen to produced $^{\bullet}O_2^-$ [26]. The photocatalytic degradation of RhB was retarded most significantly with the presence of AO, conveying that oxidation reaction occurred mainly via photogenerated holes, not via hydroxyl radical [27]. Therefore, the presence of holes scavenger has decreased the most the photocatalytic degradation of RhB. The presence of TBA had little effect on the decolorization rate, indicating that RhB was almost not degraded by $^{\bullet}OH$.

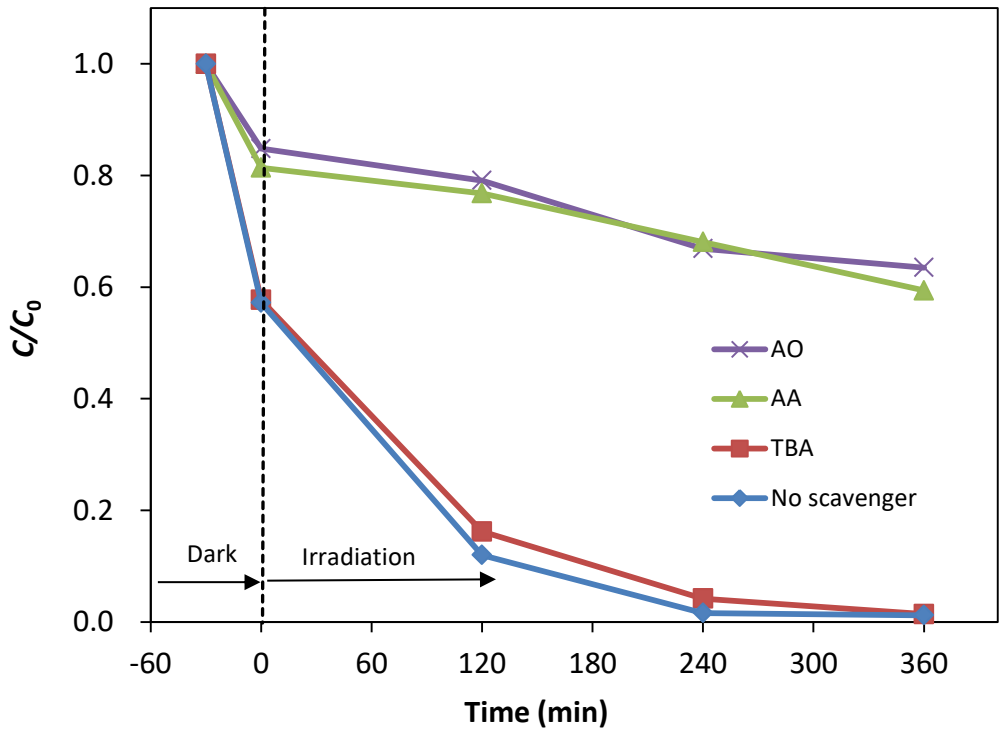

Figure 3.15. Effects of different radical scavengers on RhB degradation in presence of TiO_2 under visible light irradiation.

3.3.7. Reaction Mechanism

TiO_2 and ZnO cannot absorb visible light energy directly due to the band gap 3.2 eV [28] (Figure 3.4 and 3.5). On the contrary, when a colored organic compound is present, a sensitized photocatalytic process is possible. Huang et al. investigated dye sensitized photodegradation which follows the radical mechanism [29]. In dye sensitization, a dye absorbing visible light excites an electron from the HOMO (highest occupied molecular orbital) of a dye to the LUMO (lowest unoccupied molecular orbital) [30]. The HOMO and LUMO levels and band gap energy of OII, MO and RhB were obtained from literatures and the values are presented in Table 3.3.

Table 3.3

HOMO and LUMO levels and energy gaps (eV) of dye molecules and λ_{max} (nm).

Molecules	**HOMO**	**LUMO**	**Energy gaps**	**λ_{max}**	**Ref.**
OII	0.17	–1.86	2.03	485	[31]
MO	0.84	–2.43	3.27	464	[32]
RhB	0.95	–1.42	2.37	554	[33]

Figure 3.15 demonstrates the valence band (VB) and conduction band (CB) levels and the energy gaps of catalyst vs NHE reference electrodes. It is observed that the LUMO levels of OII, MO and RhB are more negative relative to the conduction band edge potential of TiO_2 and ZnO. Otherwise, due to the more negative potential of lowest unoccupied molecular orbital (LUMO) level for dye relative to the conduction band (CB) of catalyst [33], the electron transfer from the LUMO of dyes to the CB of catalyst is feasible. It is reported the redox potential of $O_2/{}^{\bullet}O_2^-$ is –0.33

V vs NHE [34], which is more positive than conduction band potential of TiO_2 and ZnO (–0.5 V vs NHE) [35,36].

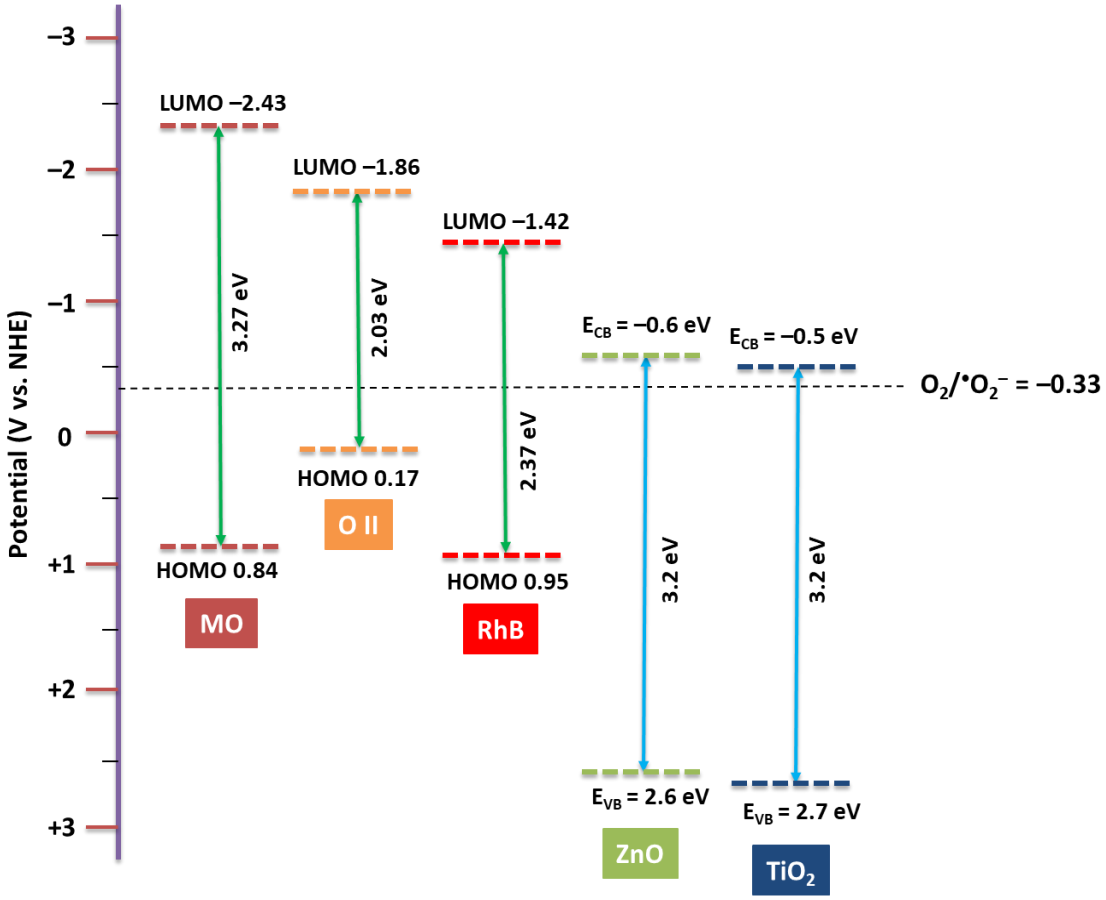

Figure 3.16. Schematic energy level diagram of TiO_2 and ZnO with respect to potential of $O_2/{}^{\bullet}O_2^-$ and the HOMO–LUMO levels of dye.

Under visible light irradiation, a dye–sensitized mechanism has been depicted in Figure 3.17. Upon irradiation of visible light, a dye absorbs the light to create an electron and hole in the conduction and valence bands (LUMO and HOMO) of the dye [37]. The electron in the LUMO then transfers to the CB of TiO_2. The adsorbed molecular oxygen on the catalyst captures electron from the CB of TiO_2 to form ${}^{\bullet}O_2^-$. The oxidant (${}^{\bullet}O_2^-$) radical reacts with adsorbed dye to degrade it. The holes in the HOMO react with adsorbed OH^- species to form ${}^{\bullet}OH$ radical. However, the

formation channel to •OH is minor under visible light [37], which is similar with the result shown in Figures 3.14 and 3.15. According to the results of the radical scavengers, OII and RhB were attacked by the super oxide, $•O_2^-$ and holes, h^+ and finally completed the degradation of dye. A possible degradation reaction mechanism is described below.

$$\text{Dye} + \text{visible light} \rightarrow \text{dye}\ (e_{CB}^- + h_{VB}^+) \quad (3.4)$$

$$\text{Adsorbed dye}\ (e_{CB}^- + h_{VB}^+) + TiO_2 \rightarrow TiO_2\ (e_{CB}^-) + \text{dye}\ (h_{VB}^+) \quad (3.5)$$

$$TiO_2\ (e_{CB}^-) + \text{adsorbed } O_2 \rightarrow TiO_2 + •O_2^- \quad (3.6)$$

$$\text{Adsorbed dye} + \text{dye}\ (h_{VB}^+) \rightarrow \text{degradation} \quad (3.7)$$

$$•O_2^- + \text{adsorbed dye} \rightarrow \text{degraded or mineralized products} \quad (3.8)$$

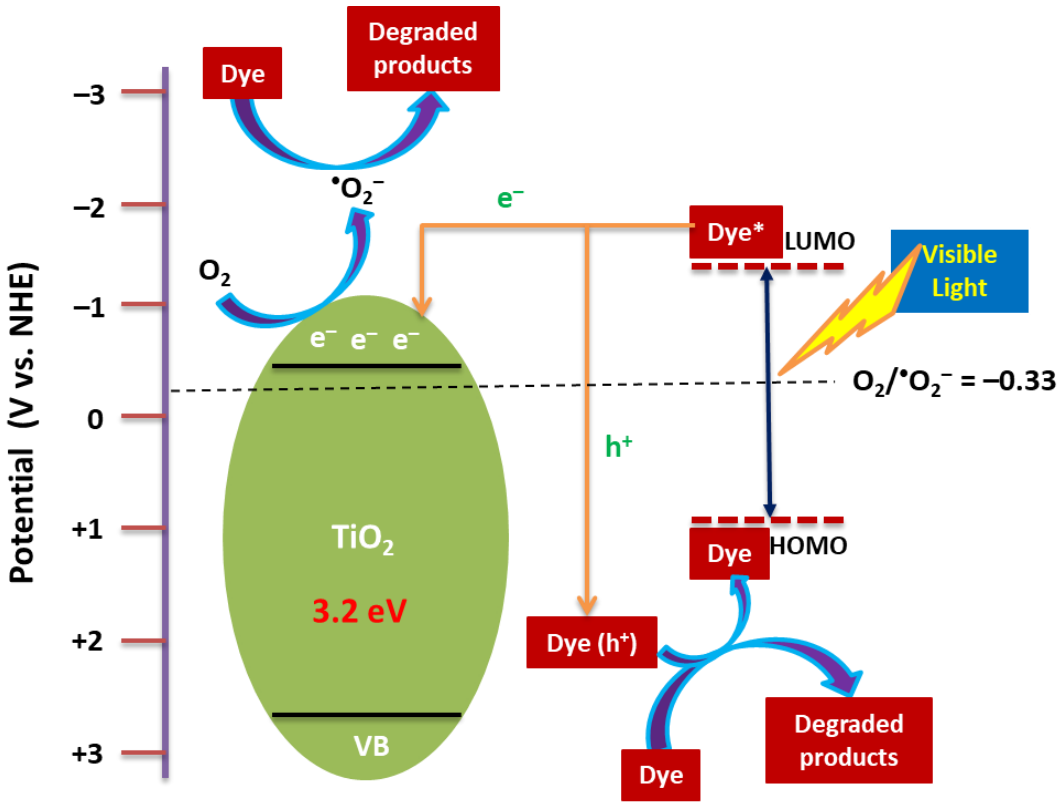

Figure 3.17. Schematic mechanisms of self–sensitized TiO_2 reaction of superoxide radical ($•O_2^-$) and holes (h^+) formation under visible light irradiation (λ > 400 nm).

3.3.8. Proposed Decolorization Pathway of Dye

The peak corresponding to the azo group of dyes decreased after 360 min of irradiation (Figure 3.7 (a), (b) and Figure 3.8 (a), (b)). This may be attributed to the fact that azo bonds are more reactive than the aromatic part of the molecule. They are easily oxidized by the photogenerated $^{\bullet}O_2^-$, h^+ and $^{\bullet}OH$ radicals. The cleavage of the azo (–N=N–) bond leads to decolorization of dyes [38]. According to the previous studies, a possible decolorization pathway of OII [39], MO [40] and RhB [41,42] was proposed in Figure 3.18.

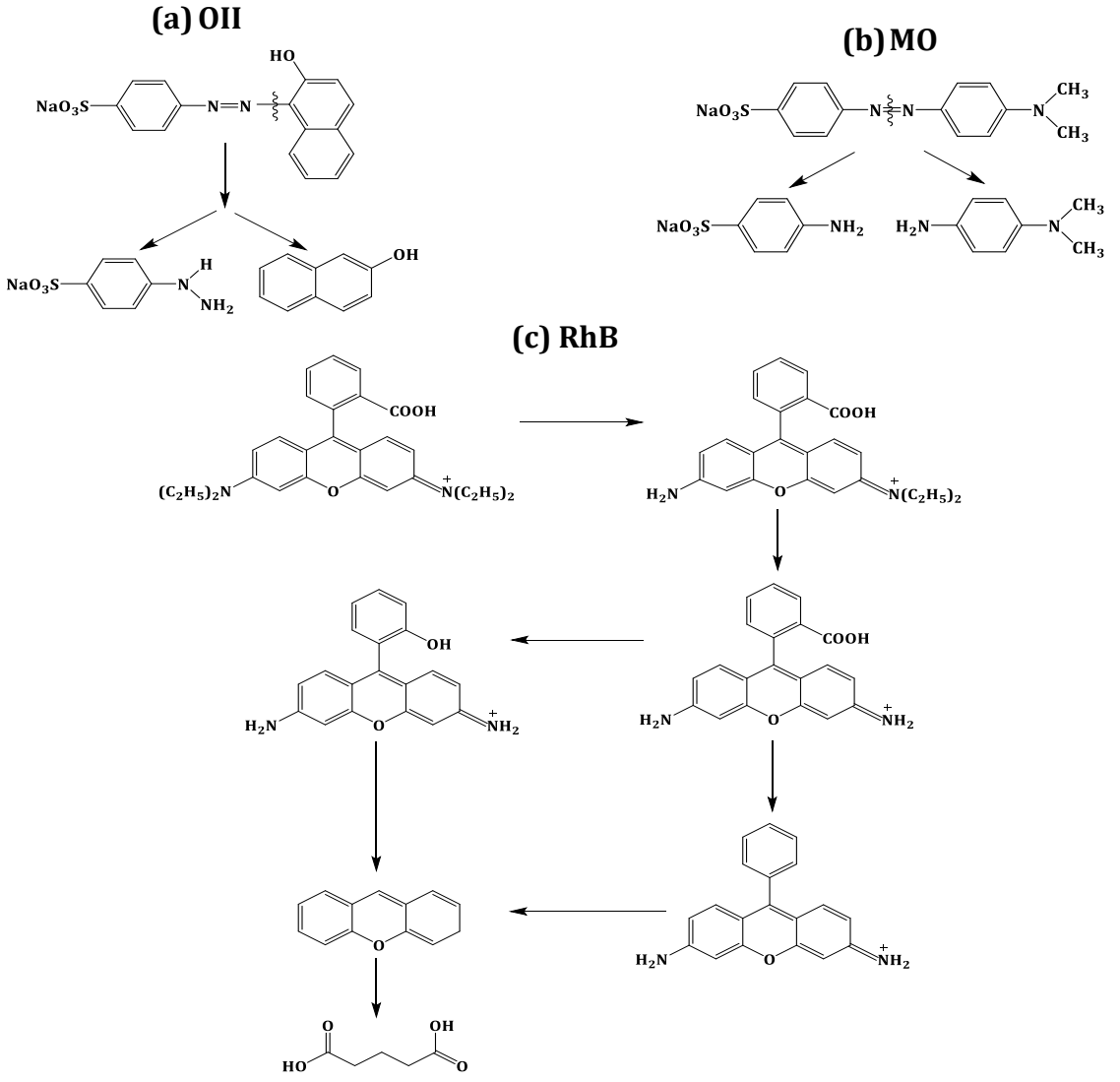

Figure 3.18. Proposed decolorization pathway of (a) OII, (b) MO and (c) RhB under visible light.

3.4. CONCLUSIONS

The photocatalytic activity of self–dye–sensitized TiO_2 and ZnO in the degradation of OII and MO was studied under fluorescent light irradiation. The percentage of degradation of OII and MO increased with an increase in irradiation time under fluorescent light for TiO_2 and ZnO catalyst. The photocatalytic activity of ZnO nanoparticles were better than that of TiO_2 for MO, and were the same activity of ZnO and TiO_2 for OII photodegradation under fluorescent light. The kinetics of OII and MO photodegradation followed the pseudo–first–order rate law, and could be described in terms of Langmuir–Hinshelwood model. The quenching effects of different scavengers displayed that the reactive h^+ and $^{\bullet}O_2^-$ radicals play the major role in the dye decolorization under visible light irradiation, while the $^{\bullet}OH$ radical played a minor role in the oxidization process. The photocatalytic degradation of waste dye in water with self–dye–sensitized TiO_2 and ZnO under fluorescent light irradiation will become a promising technique.

3.5. REFERENCES

[1] W.J. Ong, L.L. Tan, S.P. Chai, S.T. Yong, A.R. Mohamed, Highly reactive {001} facets of TiO_2–based composites: synthesis, formation mechanism and characterization, Nanoscale 6 (2014) 1946–2008.

[2] Q. Zhang, C.S. Dandeneau, X. Zhou, G. Cao, ZnO nanostructures for dye sensitized solar cells, Adv. Mater. 21 (2009) 4087–4108.

[3] M. Ni, M.K.H. Leung, D.Y.C. Leung, K. Sumathy, A review and recent developments in photocatalytic water–splitting using TiO_2 for hydrogen production, Renew. Sustain. Energy Rev. 11 (2007) 401–425.

[4] A. Di Mauroa, M. Cantarella, G. Nicotra, V. Privitera, G. Impellizzeri, Low temperature atomic layer deposition of ZnO: Applications in photocatalysis, Appl. Catal. B: Environ. 196 (2016) 68–76.

[5] G. Impellizzeri, V. Scuderi, L. Romano, E. Napolitani, R. Sanz, R. Carles, V. Privitera, C ion–implanted TiO_2 thin film for photocatalytic applications, J. Appl. Phys. 117 (2015) 105308–6.

[6] W. Kim, T. Tachikawa, T. Majima, W. Choi, Photocatalysis of dye–sensitized TiO_2 nanoparticles with thin overcoat of Al_2O_3: enhanced activity for H_2 production and dechlorination of CCl_4, J. Phys. Chem. C 113 (2009) 10603–10609.

[7] W.R. Duncan, O.V. Prezhdo, Theoretical studies of photoinduced electron transfer in dye–sensitized TiO_2, Anul. Rev. Phys. Chem. 58 (200) 143–184.

[8] M. Ni, M.K.H. Leung, D.Y.C. Leung, K. Samathy, A review and recent developments in photocatalytic water–splitting using TiO_2 for hydrogen production, Renew. Sustain. Energy Rev. 11 (2007) 401–425.

[9] M.R. Narayan, Review: dye sensitized solar cells based on natural photosensitizers, Renew. Sustain. Energy Rev. 16 (2012) 208–215.

[10] M. Gratzel, Photoelectrochemical cells, Nature 414 (2001) 338–344.

[11] R. Vinu, S. Polisetti, G. Madras, Dye sensitized visible light degradation of phenolic compounds, Chem. Eng. J. 165 (2010) 784–797.

[12] P. Chowdhury, J. Moreira, H. Gomaa, A.K. Ray, Visible–solar–light–driven photocatalytic degradation of phenol with dye–sensitized TiO_2: parametric and kinetic study, Ind. Eng. Chem. Res. 51 (2012) 4523–4532.

[13] H. Chang, C.H. Chen, M.J. Kao, S.H. Chien, C.Y. Chou, Photoelectrode thin film of dye–sensitized solar cell fabricated by anodizing method and spin coating and electrochemical impedance properties of DSSC, Appl. Surface Sci. 275 (2013) 252–257.

[14] H. Park, Y. Park, W. Kim, W. Choi, Surface modification of TiO_2 photocatalyst for environmental applications, J. Photochem. Photobiol. C: Photochem. Rev. 15 (2013) 1–20.

[15] T. Wu, G. Liu, J. Zhao, H. Hidaka, N. Serpone, Photoassisted degradation of dye pollutants. V. Self–photosensitized oxidative transformation of rhodamine B under visible light irradiation in aqueous TiO_2 dispersions, J. Phys. Chem. B. 102 (1998) 5845–5851.

[16] D. Vinodgopal, P.V. Kamat, Enhanced rates of photocatalytic degradation of an azo–dye using SnO_2/TiO_2 coupled semiconductor thin–films, Environ. Sci. Technol. 29 (1995) 841–845.

[17] G. Xing, C. Tang, B. Zhang, L. Zhao, Y. Su, X. Wang, A highly uniform $ZnO/NaTaO_3$ nanocomposite: Enhanced self–sensitized degradation of colored pollutants under visible light, J. Alloy Compd. 647 (2015) 287–294.

[18] L. Saikia, D. Bhuyan, M. Saikia, B. Malakar, D.K. Dutta, P. Sengupta, Photocatalytic performance of ZnO nanomaterials for self–sensitized

degradation of malachite green dye under solar light, Appl. Catal. A: Gen. 490 (2015) 42–49.

[19] J. Shang, F.W. Zhao, T. Zhu, J. Li, Photocatalytic degradation of rhodamine B by dye–sensitized TiO_2 under visible–light irradiation, Sci. China Chem. 54 (2011) 167–172.

[20] K. Selvam, M. Swaminathan, Photocatalytic synthesis of 2–methylquinolines with TiO_2 Wackherr and Home Prepared TiO_2–A comparative study, Arabian J. Chem. 10 (2017) S28–S34.

[21] Y. Liang, N. Guo, L. Li, R. Li, G. Ji, S. Gan, Fabrication of porous 3D flower–like Ag/ZnO heterostructure composites with enhanced photocatalytic performance, Appl. Surf. Sci. 332 (2015) 32–39.

[22] H. Katsumata, M. Taniguchi, S. Kaneco, T. Suzuki, Photocatalytic degradation of bisphenol A by Ag_3PO_4 under visible light, Catal. Commun. 34 (2013) 30–34.

[23] J. Su, L. Zhu, P. Geng, G. Chen, Self–assembly graphitic carbon nitride quantum dots anchored on TiO_2 nanotube arrays: An efficient heterojunction for pollutants degradation under solar light, J. Hazard. Mater. 316 (2016) 159–168.

[24] T. Zhang, T. Oyama, A. Aoshima, H. Hidaka, J. Zhao, Serpone, hotooxidative N–demethylation of methylene blue in aqueous TiO_2 dispersions under UV irradiation, J. Photochem. Photobiol. A: Chem. 140 (2001) 163–172.

[25] C.S. Turchi, D.F. Ollis, Photocatalytic degradation of organic water contaminants: mechanisms involving hydroxyl radical attack, J. Catal. 122 (1990) 178–192.

[26] H. Khan, D. Berk, Characterization and mechanistic study of Mo^{+6} and V^{+5} codoped TiO_2 as a photocatalyst, J. Photochem. Photobiol. A: Chem. 294 (2014) 96–109.

[27] K. Ishibashi, A. Fujishima, T. Watanabe, K. Hashimoto, Quantum yields of active oxidative species formed on TiO_2 photocatalyst, J. Photochem. Photobiol. A: Chem. 134 (2000) 139–142.

[28] K.M. Lee, C.W. Lai, K.S. Ngai, J.C. Juan, Recent developments of zinc oxide based photocatalyst in water treatment technology: a review, Water Res. 88 (2016) 428–448.

[29] S.T. Huang, Y.R. Jiang, S.Y. Chou, Y.M. Dai, C.C. Chen, Synthesis, characterization, photocatalytic activity of visible–light–responsive photocatalysts BiO_xCl_y/BiO_mBr_n by controlled hydrothermal method, J. Mol. Catal. A: Chem. 391 (2014) 105–120.

[30] H. Park, Y. Park, W. Kim, W. Choi, Surface modification of TiO_2 photocatalyst for environmental applications, J. Photochem. Photobiol. C: Photochem. Rev. 15 (2013) 1–20.

[31] Y. Bessekhouad, R. Brahimi, F. Hamdini, M. Trari, Cu_2S/TiO_2 heterojunction applied to visible light Orange II degradation, J. Photochem. Photobiol. A: Chem. 248 (2012) 15–23.

[32] O. Prakash, S. Kumar, P. Singh, V. Deckert, S. Chatterjee, A.K. Ghosh, R.K. Singh, Surface–enhanced Raman scattering characteristics of CuO: Mn/Ag heterojunction probed by methyl orange: effect of Mn^{2+} doping, J. Raman Spectrosc. 47 (2016) 813–818.

[33] L. Pan, J. Zou, X. Liu, X. Liu, S. Wang, X. Zhang, L. Wang, Visible–light–induced photodegradation of rhodamine B over hierarchical TiO_2: effects of storage

period and water–mediated adsorption switch, Ind. Eng. Chem. Res. 51 (2012) 12782–12786.

[34] Y. Su, L. Peng, J. Guo, S. Huang, L. Lv, X. Wang, Tunable optical and photocatalytic performance promoted by nonstoichiometric control and site–selective codoping of trivalent ions in $NaTaO_3$, J. Phys. Chem. C 2014, 118, 10728–10739.

[35] A. Fujishima, T.N. Tao, D.A. Tryk, Titanium dioxide photocatalysis, J. Photochem. Photobiol. C: Photochem. Rev. 1 (2000) 1–21.

[36] J. Maa, K. Wang, L. Li, T. Zhang, Y. Kong, S. Komarnenib, Visible–light photocatalytic decolorization of Orange II on Cu_2O/ZnO nanocomposites, Ceram. Int. 41 (2015) 2050–2056.

[37] W.J. Kima, D. Pradhanb, B.–K. Minc, Y. Sohna, Adsorption/photocatalytic activity and fundamental natures of BiOCl and $BiOCl_xI_{1-x}$ prepared in water and ethylene glycol environments, and Ag and Au–doping effects, Appl. Catal. B: Environ. 147 (2014) 711–725.

[38] N. Turkten, Z. Cinar, Photocatalytic decolorization of azo dyes on TiO_2: Prediction of mechanism via conceptual DFT, Catal. Today 287 (2017) 169–175.

[39] I.K. Konstantinou, T.A. Albanis, TiO_2–assisted photocatalytic degradation of azo dyes in aqueous solution: kinetic and mechanistic investigations, a review, Appl. Catal. B: Environ. 49 (2004) 1–14.

[40] S. Xie, P. Huang, J.J. Kruzic, X. Zeng, H. Qian, A highly efficient degradation mechanism of methyl orange using Fe–based metallic glass powders, Sci. Rep. 6 (2016) 21947; doi:10.1038/srep21947.

[41] K.A. Lin, J.T. Lin, Ferrocene–functionalized graphitic carbon nitride as an enhanced heterogeneous catalyst of Fenton reaction for degradation of Rhodamine B under visible light irradiation, Chemosphere 182 (2017) 54–64.

[42] K. Yu, S. Yang, H. He, C. Sun, C. Gu, Y. Ju, Visible light–driven photocatalytic degradation of rhodamine B over $NaBiO_3$: pathways and mechanism, J. Phys. Chem. A 113 (2009) 10024–10032.

CHAPTER 4

PHOTOCATALYTIC REMOVAL OF FAMOTIDINE WITH TiO_2 FROM WATER IN THE PRESENCE OF DYE UNDER VISIBLE LIGHT IRRADIATION

4.1. INTRODUCTION

Pharmaceutical compounds in surface waters are an emerging environmental concern due to their biological activity and consequently provide a new challenge to drinking water and wastewater treatment systems [1]. Most of the pharmaceuticals administered to patients are not entirely metabolized in the human body, and unmetabolized amounts are excreted to water effluents to be treated at wastewater treatment plants. The persistence of their residues in surface waters is of great concern [2]. Numerous studies have documented that both metabolized and non–metabolized pharmaceutical residues are speculated to have adverse effects on human health and the safety of ecosystems [3–5].

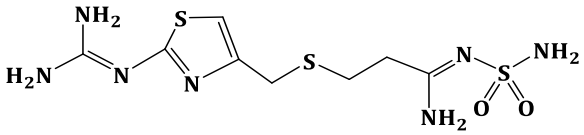

Figure 4.1. Molecular structure of Famotidine.

Famotidine (FMT, M.W. = 337.44 g/mol, Figure 4.1) is chemically 3–[({2–[(diaminomethylidene)–amino]–1,3–thiazol–4–yl}methyl)sulfanyl]–*N'*–sulfam–oylpropanimidamide. This compound is extensively used for treating a variety of stomach and duodenum sicknesses, connected with an excessive secretion of H^+ ions. Its bioavailability is about 40–45%. FMT creates stable complexes with palladium, copper, cobalt and nickel. Previous research reports have proved the stability of FMT in the environment and water bodies [6]. Taking the above–mentioned issues into account, one can argue that FMT should be considered as persistent contaminants in an aqueous environment which are frequently found in wastewater at various detectable concentrations. The frequent presence of these

pharmaceuticals in wastewater underscores the necessity of removing them from water matrices before they are discharged into the environment.

Titanium dioxide (TiO_2) has drawn great attention since they are one group of the most promising photocatalysts in water splitting and the mineralization of toxic organic substances owing its virtue of nontoxicity, highly chemical stability and low cost [7,8]. However, TiO_2 can only be excited by the irradiation of UV light, which merely occupies about 4% of total solar energy [9]. This problem can be solved only by extending the light absorption capacity of those catalysts. Dye sensitization is a simpler method that can extend catalysts activation to wavelengths longer than those corresponding to its band gap. Dye–sensitization begins with electron injection from the excited dye into the conduction band (CB) of TiO_2, followed by interfacial electron transfer [10–14]. Chatterjee et al. [15] investigated the visible light assisted photodegradation of halocarbons on the dye modified TiO_2 surface using visible light with Xe lamp and UV filter. Chowdhury et al. [16] reported the visible solar light driven photocatalytic degradation of phenol with dye sensitized TiO_2 using solar simulator. Xing et al. [17] studied the enhanced self–sensitized degradation of colored pollutants under visible light with mercury lamp and filter. According to our knowledge, there is little information on the photocatalytic degradation of famotidine in water with dye–sensitized photocatalysts under visible light irradiation.

In this chapter, we intended to investigate the photocatalytic degradation of famotidine in water with dye–sensitized TiO_2 under visible light irradiation (λ > 400 nm).

4.2. MATERIALS AND METHODS

4.2.1. Materials

All reagents were of analytical grade and were used without further purification. Famotidine, orange II, bromophenol blue, acid red 88 and rhodamine B used in this study were purchased from Nacalai Tesque. Ascorbic acid (AA), *di*–ammonium oxalate (AO) and *tert*–butyl alcohol (TBA) were obtained from Wako Pure Chemicals. P25 TiO_2 was purchased from Degussa. Ultrapure water (18 MΩ) was prepared by an ultrapure water system (Advantec MFS Inc.).

4.2.2. Characterization

The UV–visible diffuse reflectance spectra of the photocatalysts (TiO_2 and dye adsorbed TiO_2) were recorded using a Shimadzu UV–2450 spectrophotometer equipped with an integral sphere assembly. The analysis range was from 200 to 800 nm, and $BaSO_4$ was used as a reflectance standard.

4.2.3. Photocatalytic Activity and Detection of Reactive Oxygen Species

The photocatalytic activities of dye (Orange II, Bromophenol blue, Acid red and Rhodamine B) sensitized TiO_2 (label as: TiO_2–OII, TiO_2–BPB, TiO_2–AR88 and TiO_2–RhB) were evaluated by the degradation of famotidine under visible light (λ > 400 nm) irradiation at ambient temperature. Typically, 30 mL of famotidine solution, 20 mg of photocatalyst and sensitizer (5 mg/L) were added to a 35–ml Pyrex glass cell. The initial concentration of famotidine in all experiments was 2 mg/L and 5 mg/L and the famotidine solution containing the appropriate quantity of the photocatalyst powder was magnetically stirred before and during irradiation. Before irradiation, the photocatalyst suspension containing famotidine was allowed to equilibrate for 30 min in the dark. The sample solution was irradiated

with a LED lamp (990 W, Ushio Electronics) in conjunction with a UV cut filter (Y–44, HOYA), which was positioned on the side of the reaction cell. The luminous intensity was measured by a UV radio meter (UVR–300, UD–400, 360–490, Iuchi Co., Osaka, Japan). The light intensity of the LED lamp was 5.3 mW/cm^2. The photodegradation system is described in Figure 4.2.

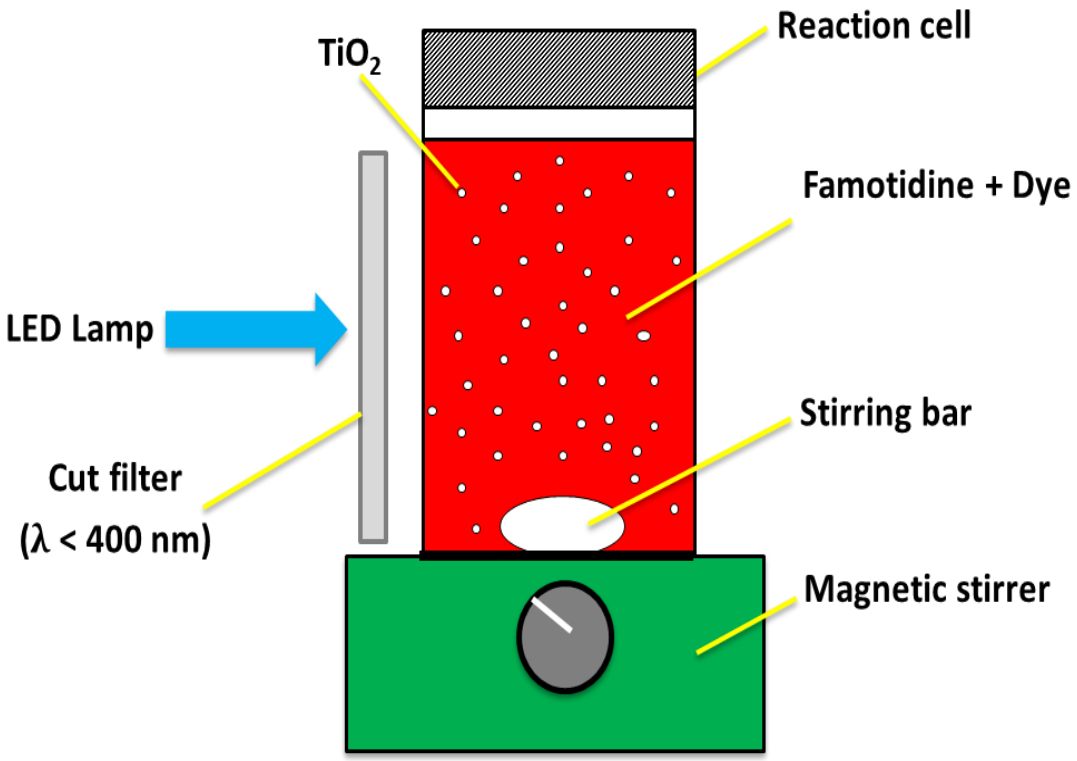

Figure 4.2. Schematic reactor for photocatalytic degradation of Famotidine.

After the desired irradiation time, the photocatalyst was separated by the centrifugation. The amount of the remnant famotidine in the aqueous solution was measured using a high–performance liquid chromatograph (HPLC, GL–7400), equipped with a HITACHI L–3000 optical detector and an Inertsil ODS–3 column (GL Science, Japan). The elution was monitored at 276 nm. The mobile phase was a mixture of acetonitrile and water (1/1, v/v), and was pumped at a flow rate of 1.0

mL/min. The concentration of dye was measured by UV–vis spectrophotometer. Radical scavenger studies were carried out to investigate the active species involved in the photodegradation of FMT. The scavenging experiments of reactive oxygen species were similar to the photodegradation experiments. Three scavengers were selected, namely, *tert*–butyl alcohol (•OH radical scavenger), *di*–ammonium oxalate monohydrate (hole scavenger) and ascorbic acid ($\bullet O_2^-$ radical scavenger). Different quantity of *tert*–butyl alcohol, *di*–ammonium oxalate monohydrate [18] and ascorbic acid [19] were added into the dye solution prior to addition of catalysts.

4.2.4. Calculation of Photocatalytic Efficiency

The degradation efficiency of FMT in the reaction process was calculated using the following formula:

Degradation rate = $\frac{C}{C_0}$ (4.1)

where C is the concentration of famotidine at time t, and C_0 is the initial concentration of famotidine (2 and 5 mg/L) at the start of the reaction.

4.3. RESULTS AND DISCUSSION

4.3.1. UV–Vis DRS Analysis

Figure 4.3 shows the diffuse Reflectance spectra of the dye adsorbed TiO_2 materials in the 200–800 nm range, as %R [20]. The semiconductor photocatalysis with dyes is known largely to occur through dye adsorption on the surface of the photocatalyst, followed by e^-–h^+ generation on photoexcitation and oxidative breakdown of the dye molecule on action of reactive species generated [21]. It is cleared from UV–vis DRS (Figure 4.2) that the dye molecules adsorbed onto TiO_2 semiconductors were excited under visible light irradiation and then injected electrons into the conduction band (CB) of TiO_2 particle. However, the significant adsorption of dye onto the TiO_2 surface decreased with increasing time due to degradation of dye by self–sensitization. The UV–vis DRS for all four dyes adsorbed TiO_2 show absorption edges were not changed.

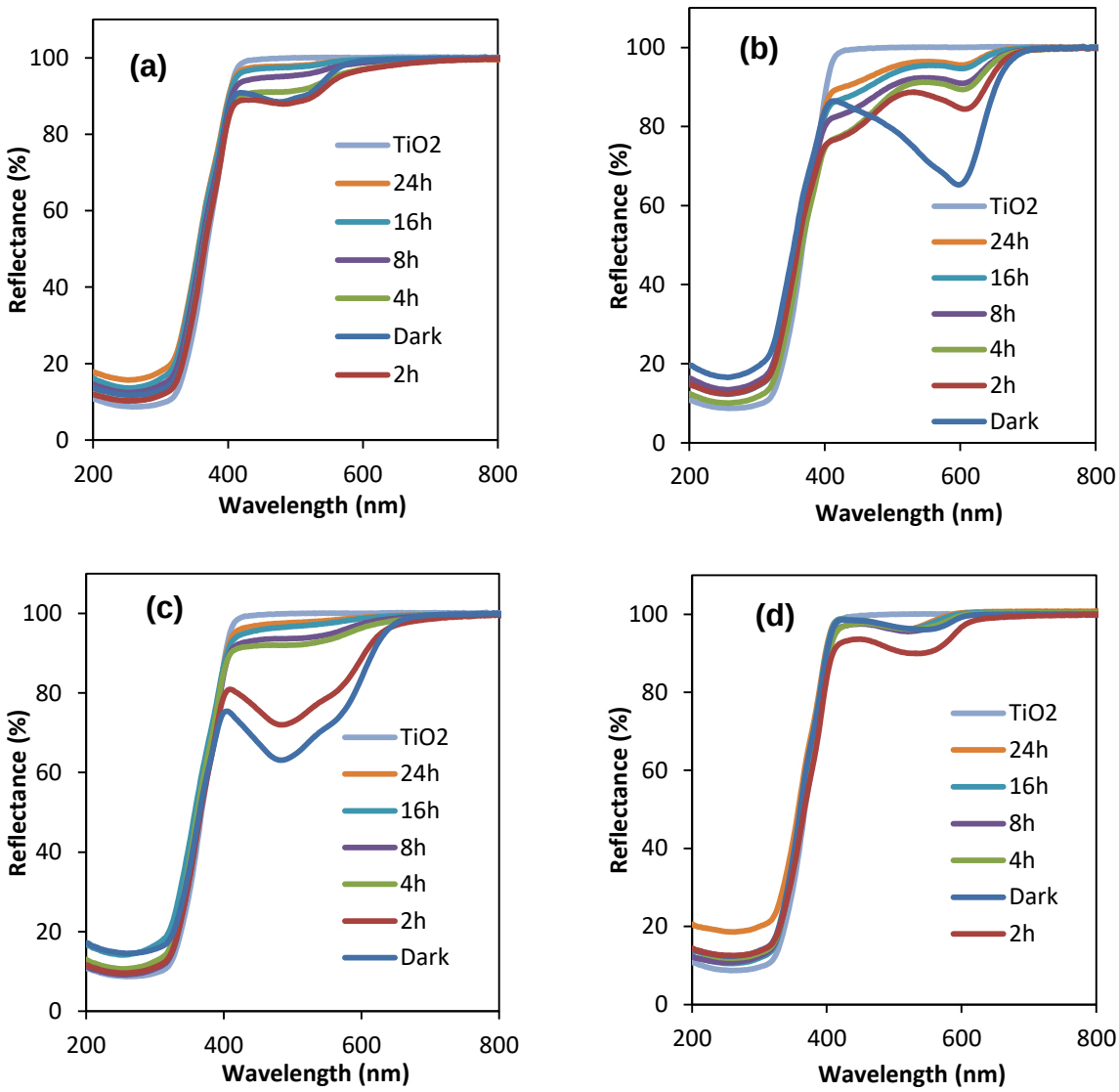

Figure 4.3. UV–Vis DRS patterns of TiO_2 and dye adsorbed TiO_2 (a) TiO_2–OII, (b) TiO_2–BPB, (c) TiO_2–AR88 and (d) TiO_2–RhB at different time irradiation.

4.3.2. Photocatalytic Efficiency of Dye–Sensitized TiO_2 in Famotidine Degradation

Photocatalytic activity of dye–sensitized TiO_2 photocatalysts was evaluated through photocatalytic degradation of Famotidine (2 and 5 mg/L) under visible light irradiation (λ > 400 nm) for 8 and 24 h, respectively. Figure 4.4 shows the degradation efficiency of famotidine (2 mg/L) with reaction time using only bare TiO_2 and TiO_2 in the presence of OII, BPB, AR88 and RhB. The degradation of Famotidine rapidly increased with increasing irradiation times, reaching almost 48%, 67%, 49% and 70% degradation after 8 h in the presence of OII, BPB, AR88 and RhB, respectively. Under the same conditions, the percentage of Famotidine degradation with TiO_2 catalysts was only 33%. This clearly showed it that under visible light the dye–sensitized TiO_2 exhibited higher catalytic activity in the degradation of famotidine compared with those obtained with P25 TiO_2.

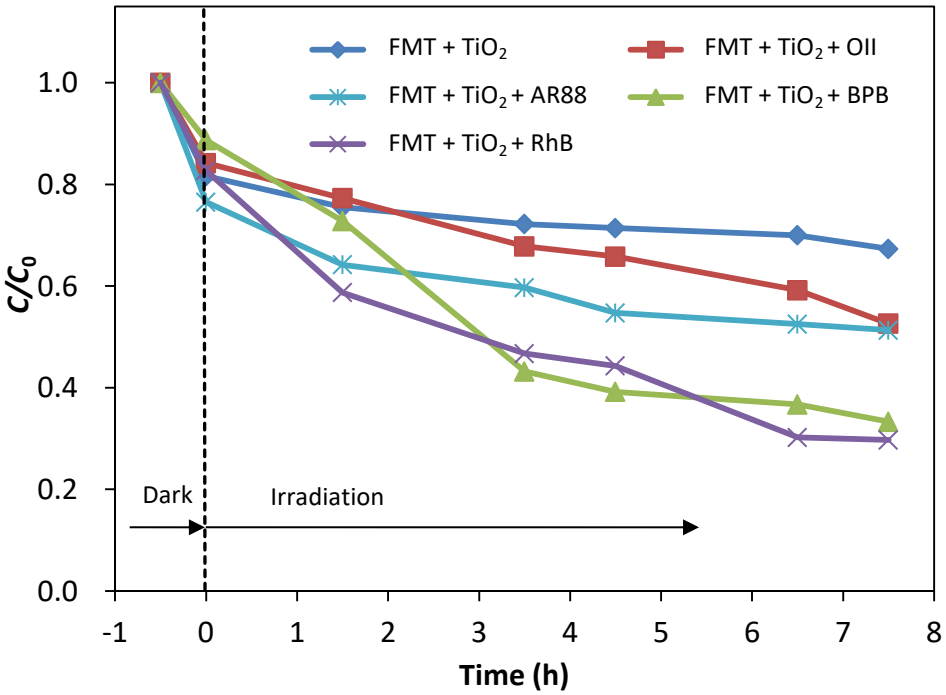

Figure 4.4. Time courses of Famotidine concentration (2 mg/L) in the dispersions containing dye (OII, BPB, AR88 and RhB) sensitized TiO_2 under λ > 400 nm radiation.

In order to compare the photodegradation performance of different concentrations of Famotidine, the TiO_2 in the presence of OII, BPB, AR88 and RhB were applied into 5 mg/L of Famotidine under visible light irradiation (λ > 400 nm) in 24 h. Figure 4.5 shows the photocatalytic degradation of Famotidine (5 mg/L) as a function of irradiation time for the different systems investigated. The photodegradation of FMT with TiO_2 in the presence of OII, BPB, AR88 and RhB catalysts were about 60%, 74%, 75% and 85% after 24 h irradiation under visible light, respectively. The case of only TiO_2 achieved about 36% adsorption of Famotidine after 24 h under the same conditions. Hence, the results for all of dye sensitized TiO_2 samples are significantly better than that observed with TiO_2. The improvement of the catalytic activities may be due to the sensitized TiO_2 in the presence of dye. TiO_2 with RhB exhibited the highest activity of FMT elimination from water.

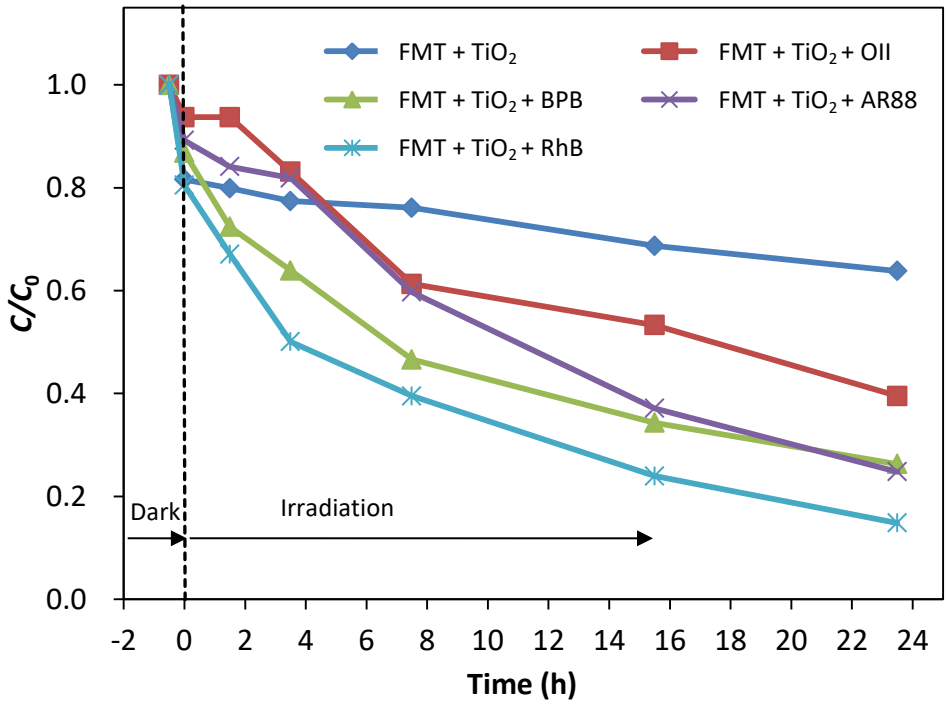

Figure 4.5. Time courses of Famotidine concentration (5 mg/L) in the dispersions containing dye (OII, BPB, AR88 and RhB) sensitized TiO_2 under λ > 400 nm radiation.

4.3.3. Adsorption of Famotidine with TiO_2 in the Presence of Dyes

The adsorption of Famotidine with TiO_2 in the presence of OII, BPB, AR88 and RhB was carried out shown in Figure 4.6. The adsorption (removal) percentage of FMT on TiO_2 particles was found to increase up to 30 min for four dyes, and after the time the appreciable change was not observed until 4.5 h. Photolysis experiment of FMT in absence of photocatalyst under visible light was performed.

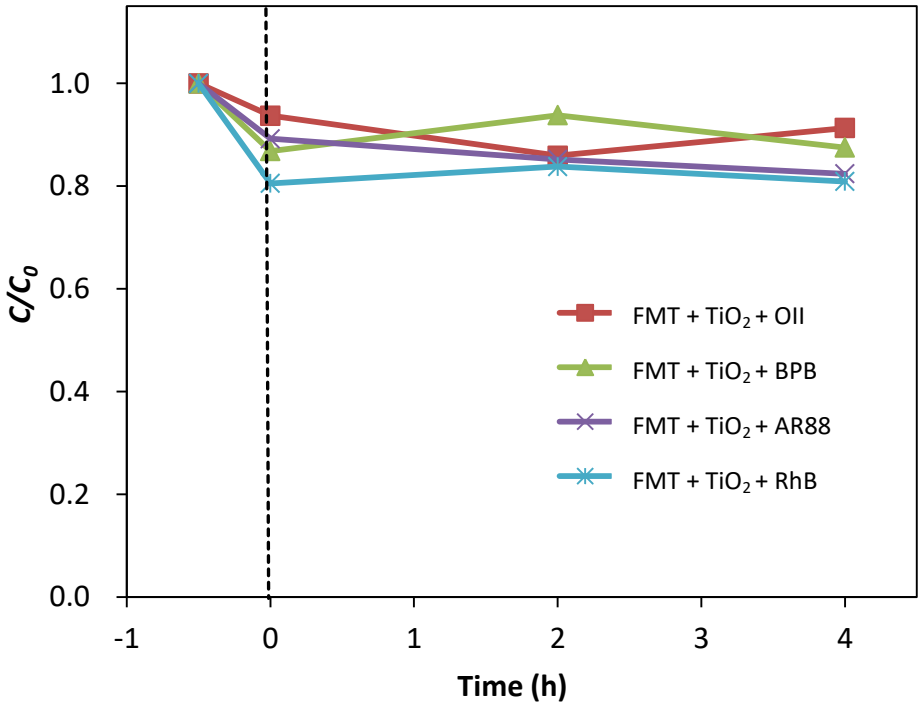

Figure 4.6. Time courses of Famotidine concentration (5 mg/L) in the dispersions containing TiO_2 and dye (OII, BPB, AR88 and RhB) under dark.

4.3.4. Photolysis of Famotidine

As shown in Figure 4.6, the FMT degradation efficiency by photolysis was approximately 5% after 24 h under visible light irradiation. The adsorption of FMT in the presence of bare TiO_2 was carried out under dark (Figure 4.7). The efficiency increased up to 30 min, and then adsorption increased slowly with increasing time.

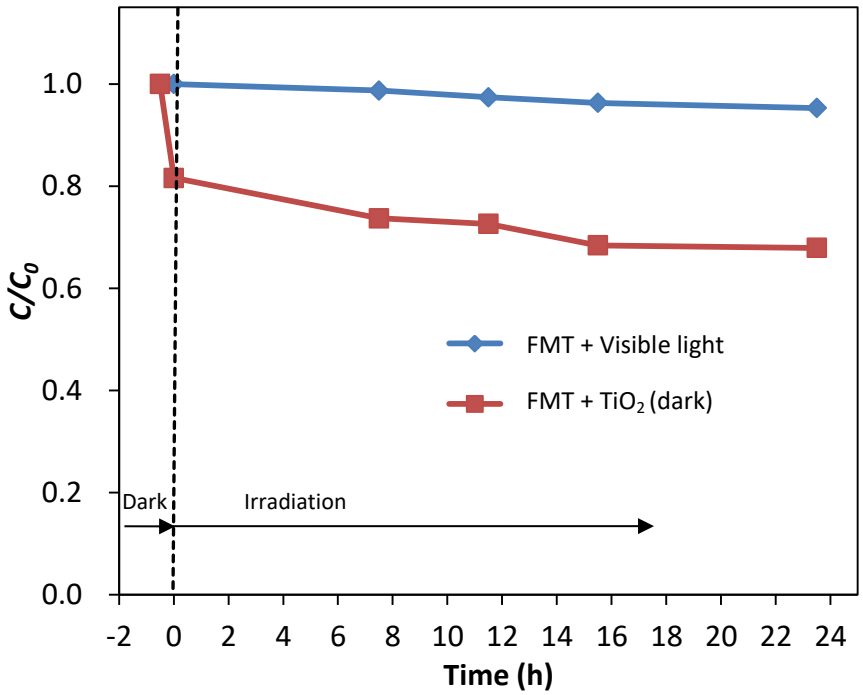

Figure 4.7. Time courses of Famotidine concentration (5 mg/L) in the dispersions containing TiO_2 under dark and visible light photolysis.

4.3.5. Photocatalytic Degradation of Dyes

The degradation efficiency of sensitizer (OII, BPB, AR88 and RhB) was also evaluated under visible light irradiation. The concentration of sensitizer in the treatment decreased with increasing time shown in Figures 4.8–4.11. Thus, the dye may be firstly excited by absorbing visible light, and then degraded through a self–sensitized mechanism.

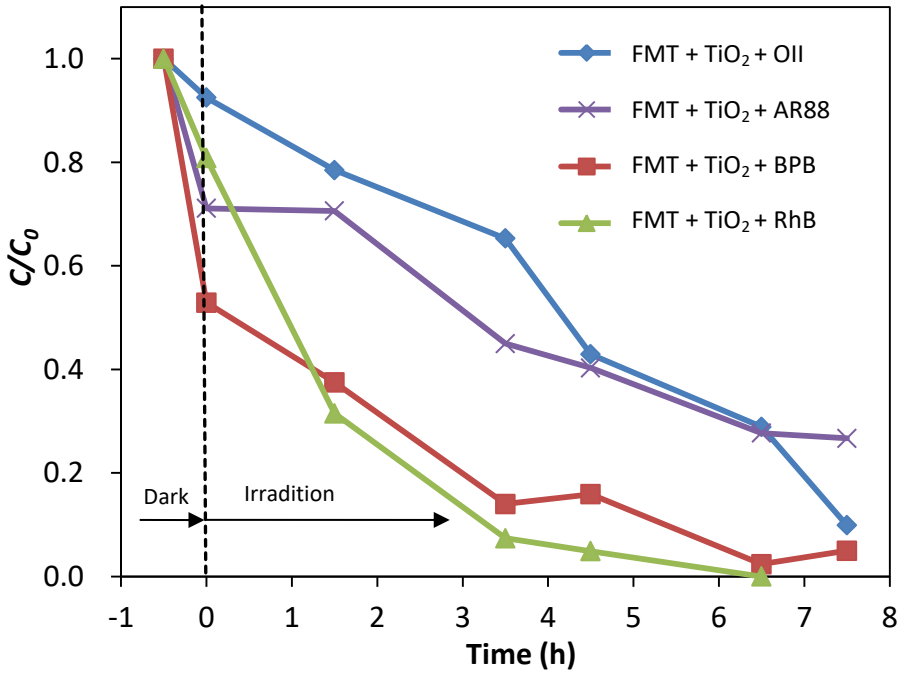

Figure 4.8. Time courses of dye (OII, BPB, AR88 and RhB) concentration in the dispersions containing Famotidine (2 mg/L) with TiO_2 under λ > 400 nm irradiation.

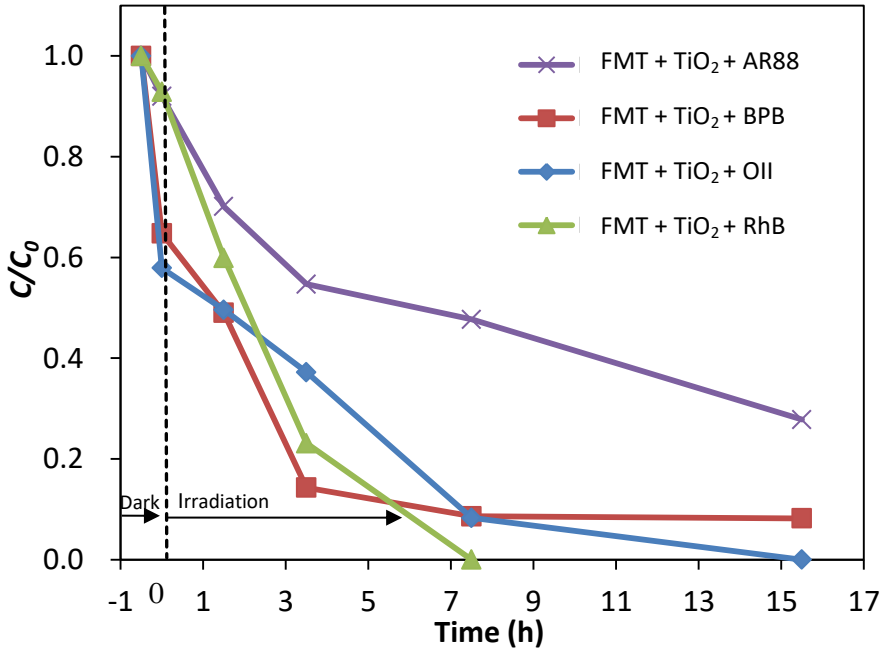

Figure 4.9. Time courses of dye (OII, BPB, AR88 and RhB) concentration in the dispersions containing Famotidine (5 mg/L) with TiO_2 under λ > 400 nm irradiation.

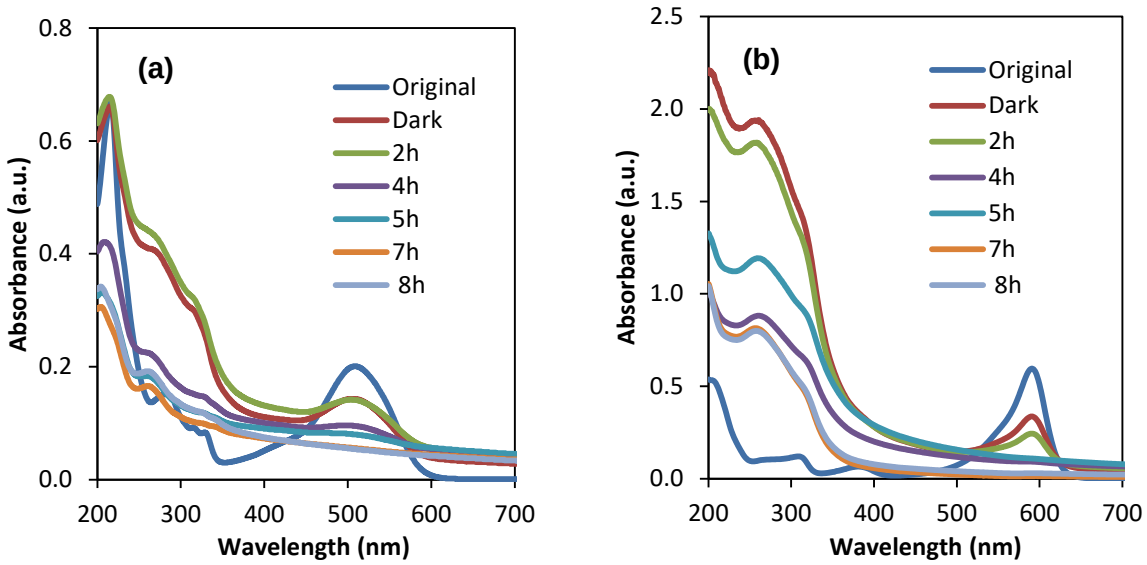

Figure 4.10. Absorption spectra of Famotidine (2 mg/L) in the presence of dye (5 mg/L) of the photocatalytic degradation with TiO_2 under $\lambda > 400$ nm irradiation. (a) AR88 and (b) BPB.

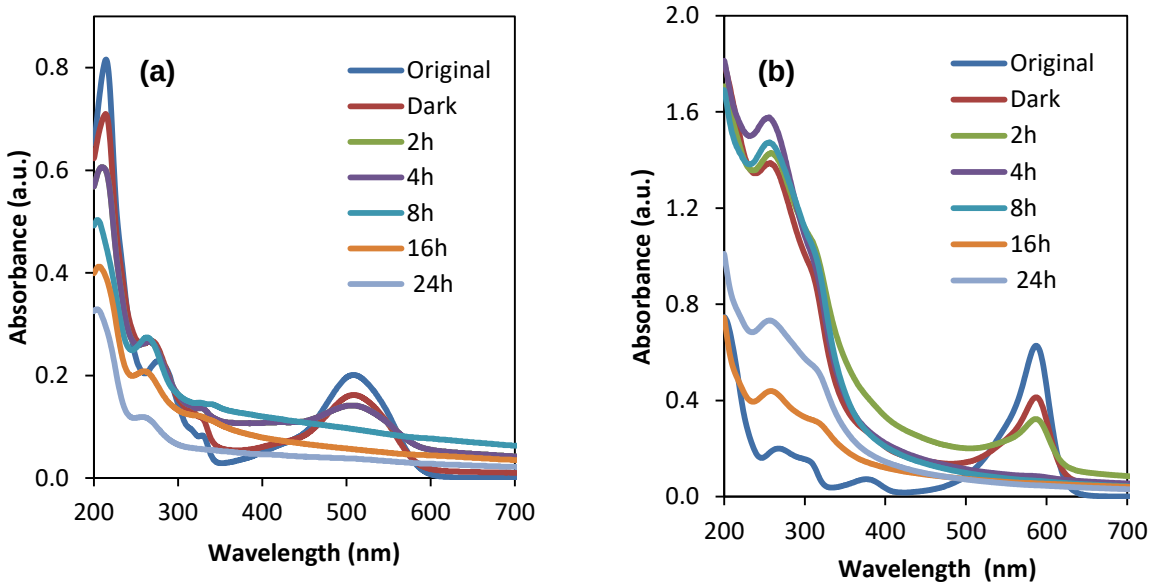

Figure 4.11. Absorption spectra of Famotidine (5 mg/L) in the presence of dye (5 mg/L) of the photocatalytic degradation with TiO_2 under $\lambda > 400$ nm irradiation. (a) AR88 and (b) BPB.

4.3.6. Kinetic Analysis

The photocatalytic oxidation kinetics of many organic compounds has often been modeled with the Langmuir–Hinshelwood (L–H) equation (This information already discussed in Chapter 3).

The primary degradation reaction is estimated to follow a pseudo–first–order kinetic law, according to Eq. (3.3). In order to confirm the speculation, Ln(C/C_0) was plotted as a function of illumination time for famotidine 2 mg/L and 5 mg/L shown in Figure 4.12 (a) and (b), respectively. Since the linear plots were observed as expected, the kinetics of famotidine in the TiO_2 suspension with dye solution followed the first–order degradation curve which was consistent to the L–H model resulting from the low coverage in the experimental concentration range (2 and 5 mg/L). The photocatalytic degradation kinetic parameters such as pseudo–first–order rate constant, correlation coefficient and substrate half–live are shown in Table 4.1. The values of rate constants have been determined from the slope and intercept of these plots. As shown in Table 4.1, the rate constant values k_{obs} (h^{-1}) of FMT (2 and 5 mg/L) were better for dye–sensitized TiO_2 than that observed with bare TiO_2.

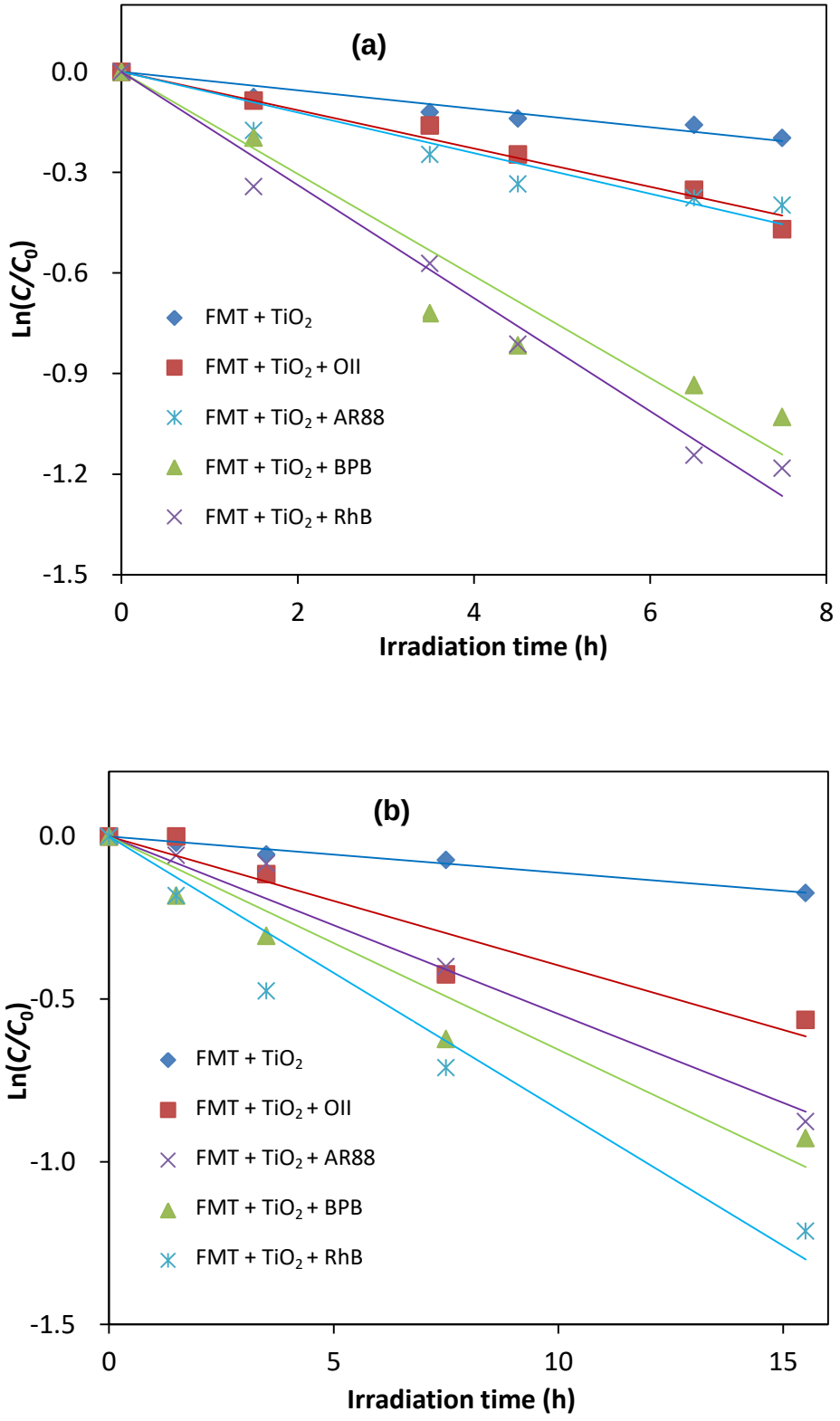

Figure 4.12. Kinetic plot of $\mathrm{Ln}(C/C_0)$ versus irradiation time for Famotidine (a) 2 mg/L and (b) 5 mg/L.

Table 4.1

Rate constants, correlation coefficient and half–life values of FMT (2 and 5 mg/L) using TiO_2 and dye–sensitized TiO_2.

Catalysts	Rate constant, k_{obs} (h^{-1})		Correlation coefficient, R^2		Half–life, $t_{1/2}$ (h)	
	FMT (2 mg/L)	FMT (5 mg/L)	FMT (2 mg/L)	FMT (5 mg/L)	FMT (2 mg/L)	FMT (5 mg/L)
TiO_2	0.0275	0.0112	0.89	0.98	25.2	61.9
TiO_2–OII	0.0572	0.0397	0.98	0.91	12.1	17.5
TiO_2–AR88	0.0606	0.0546	0.86	0.98	11.4	12.7
TiO_2–BPB	0.1522	0.0656	0.92	0.93	4.5	10.6
TiO_2–RhB	0.1687	0.0839	0.98	0.94	4.1	8.3

4.3.7. Detection of Reactive Species

The radical and holes trapping experiments (scavenger tests) with different scavenger molecules were carried out to elucidate the photocatalytic degradation mechanism of FMT under visible light irradiation over dye–sensitized TiO_2. Generally, the reactive species such as, hydroxyl radicals ($^{\bullet}OH$), superoxide radical anions ($^{\bullet}O_2^-$) and holes (h^+) are expected to be involved in the photocatalytic dye degradation processes [22]. In this study, *tert*–butyl alcohol (TBA), *di*–ammonium oxalate monohydrate (AO) and ascorbic acid (AA) were adopted to be the scavengers of hydroxyl radicals ($^{\bullet}OH$), superoxide radical ($^{\bullet}O_2^-$) and holes (h^+), respectively. As shown in Figure 4.13, the photocatalytic degradation of FMT over the RhB sensitized TiO_2 was affected slightly by the addition of TBA, demonstrating that $^{\bullet}OH$ active species played a small role in the photocatalytic degradation of FMT. However, the photocatalytic degradation efficiency of FMT decreases significantly

in the presence of AO. Moreover, the photocatalytic activity of the RhB sensitized TiO_2 was completely suppressed by AA. This indicates that h^+ and $^{\bullet}O_2^-$ are playing a dominant role in the photocatalytic degradation of FMT over RhB sensitized TiO_2 under visible light.

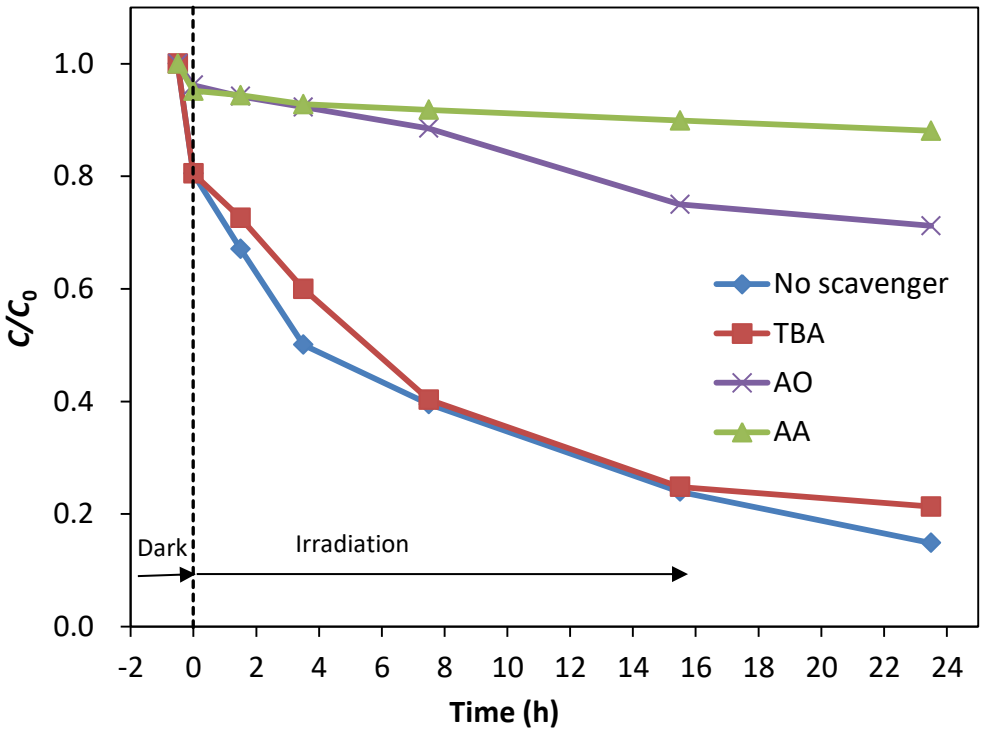

Figure 4.13. Effects of different scavengers on the degradation of Famotidine (5 mg/L) with TiO_2 in the presence of RhB at 24 h under visible light irradiation.

In order to investigate the active species involved in photodegrading FMT, scavenger studies were also carried out on dye–sensitized TiO_2 at 24 h as shown in Figure 4.14. The photocatalytic degradation of FMT over TiO_2 was retarded with the presence of AA and AO. The results strongly indicated that h^+ and $^{\bullet}O_2^-$ were the active species involved in the photodegradation of FMT. However, h^+ was more dominant in photodegrading FMT, with $^{\bullet}O_2^-$ as the most important active species. The presence of TBA had little effect on the decolorization rate, indicating that

FMT was almost not degraded by •OH.

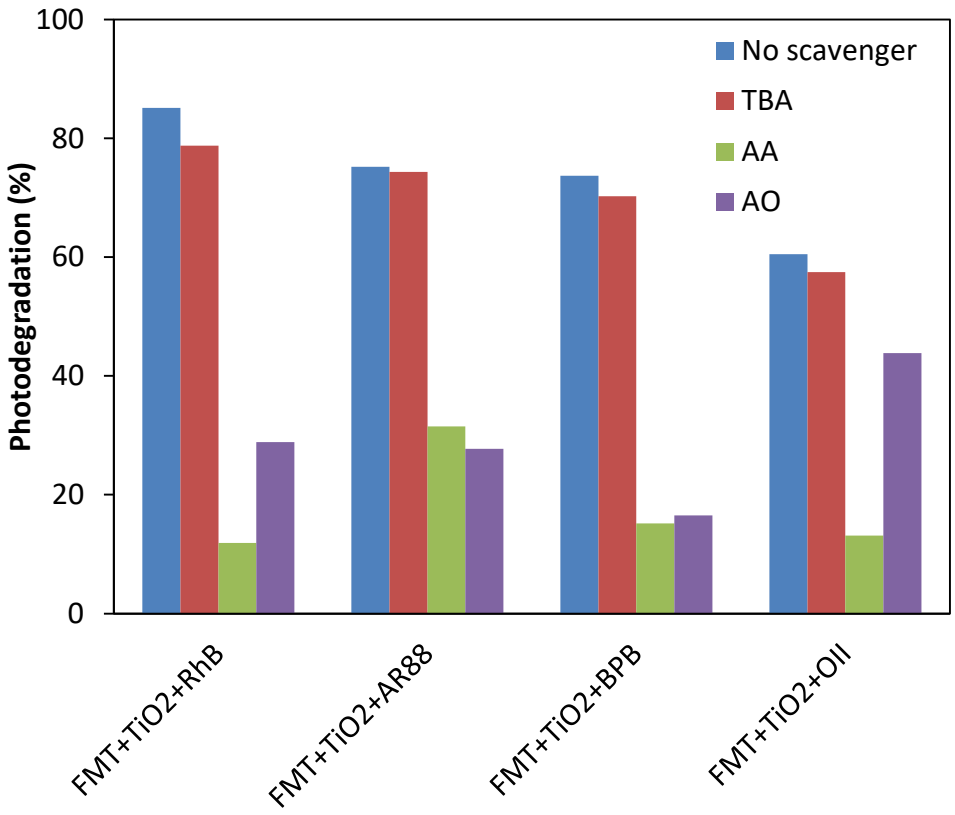

Figure 4.14. Effects of different scavengers on the degradation of Famotidine (5 mg/L) with TiO_2 in the presence of various dyes at 24 h under visible light irradiation.

4.3.8. Reaction Mechanism

TiO_2 cannot absorb visible light directly due to the band gap 3.2 eV [23,24], but when a colored organic compound is present, a sensitized photocatalytic process is able to operate. In dye sensitized photocatalysis, a dye absorbing visible light excites an electron from the HOMO (highest occupied molecular orbital) of a dye to the LUMO (lowest unoccupied molecular orbital). The HOMO and LUMO levels and band gap energy of OII, BPB, AR88 and RhB were obtained from literatures and the values are presented in Table 4.2.

Table 4.2

HOMO and LUMO levels, and energy gaps (eV) of dye molecules and λ_{max} (nm).

Molecules	HOMO	LUMO	Energy gaps	λ_{max} (nm)	Ref.
OII	0.17	–1.86	2.03	485	[25]
BPB	2.13	–2.73	4.86	590	[26]
AR88	–4.34	–4.57	0.23	506	[27]
RhB	0.95	–1.42	2.37	553	[21]

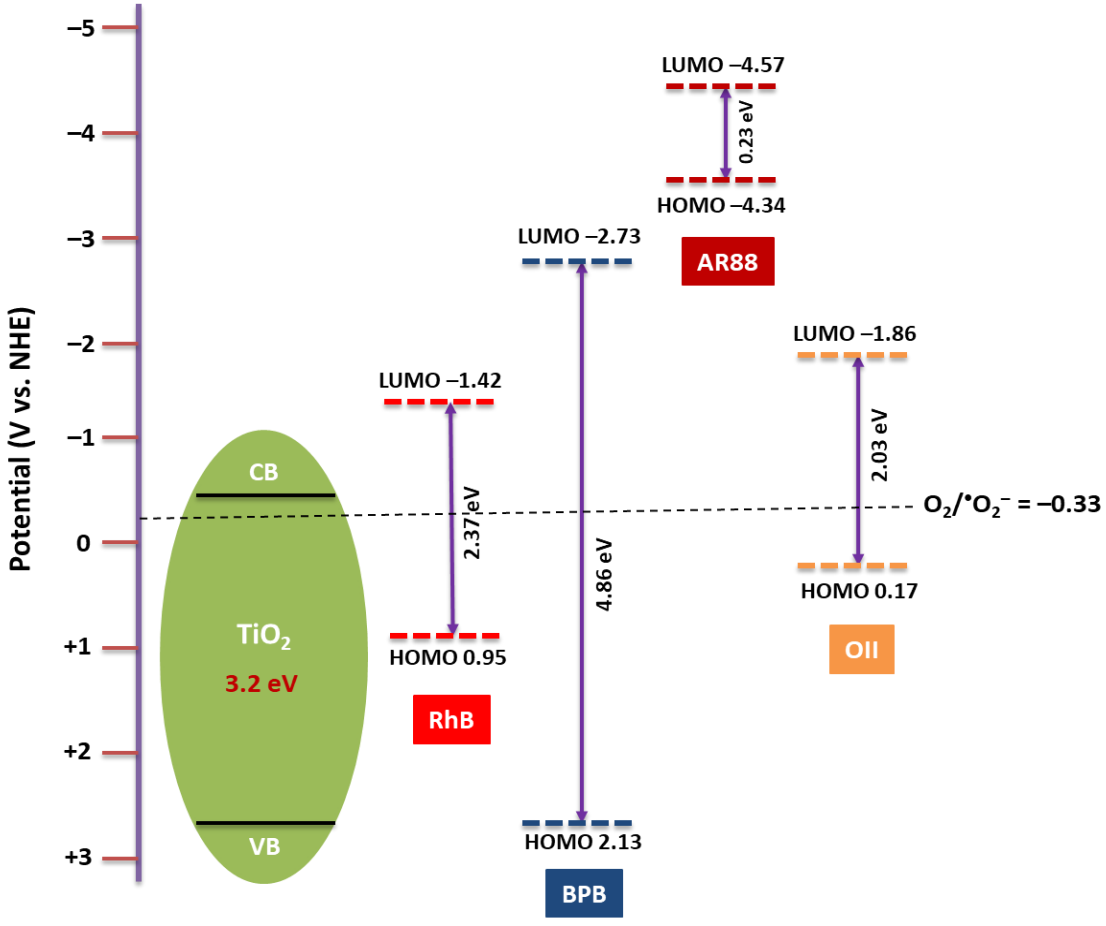

Figure 4.15. Schematic energy level diagram of TiO_2 with respect to potential of $O_2/{}^{\bullet}O_2^-$ and the HOMO–LUMO levels of dye.

Figure 4.15 demonstrates the valence band (VB) and conduction band (CB) levels and the band gap energy of TiO_2 vs NHE reference electrodes. It is observed that the LUMO levels of OII, BPB, AR88 and RhB are more negative than the conduction band edge potential of TiO_2. Otherwise, as the more negative potential of dye of lowest unoccupied molecular orbital (LUMO) level than the conduction band (CB) of TiO_2 [28,29], the electron transfer from the LUMO of dyes to the CB of TiO_2 is feasible. It is reported the redox potential of $O_2/{}^{\bullet}O_2^-$ is –0.33 V vs NHE [30], which is less negative than conduction band potential of TiO_2 (–0.5 V vs NHE) [31].

Under visible light irradiation, a dye sensitized mechanism has been depicted in Figure 4.16. Upon irradiation of visible light, a dye absorbs the light to create an electron and hole in the conduction and valence bands (LUMO and HOMO) of the dye [32]. The electron in the LUMO then transfers to the CB of TiO_2. The adsorbed molecular oxygen on the catalyst captures electron from the CB of TiO_2 to form ${}^{\bullet}O_2^-$. Thus the FMT could be efficiently degraded by the aid of high oxidizing–power of the ${}^{\bullet}O_2^-$ for the formation of S–oxide of Famotidine [33]. The oxidant (${}^{\bullet}O_2^-$) radical also reacts with adsorbed dye to degrade it. The holes in the dye (HOMO) react with adsorbed OH^- species to form ${}^{\bullet}OH$ radical. However, the formation channel to ${}^{\bullet}OH$ is minor under visible light [32], which is similar with the result shown in Figure 4.13 and 4.14. The holes of dye react with adsorbed FMT to form the degraded products and to regenerate of dye molecules for the next dye–sensitization process [16,32]. According to the results of the radical scavengers, FMT was attacked easily by the holes for the degradation of FMT in aqueous solution. Therefore, the TiO_2–dye–sensitized degradation of FMT under visible light irradiation could be mainly attributed to the oxidization by h^+ and ${}^{\bullet}O_2^-$ radicals, while the ${}^{\bullet}OH$ radicals played only a relatively minor role in the

oxidization process. On the basis of the photodegradation results with a scavenger, a possible degradation reaction mechanism is described below.

$$\text{Dye} + \text{visible light} \rightarrow \text{dye}\ (e_{CB}^{-} + h_{VB}^{+}) \quad (4.2)$$

$$\text{Adsorbed dye}\ (e_{CB}^{-} + h_{VB}^{+}) + TiO_2 \rightarrow TiO_2\ (e_{CB}^{-}) + \text{dye}\ (h_{VB}^{+}) \quad (4.3)$$

$$TiO_2\ (e_{CB}^{-}) + O_2 \rightarrow TiO_2 + {}^{\bullet}O_2^{-} \quad (4.4)$$

$${}^{\bullet}O_2^{-} + \text{FMT} \rightarrow \text{S–oxide of FMT} \quad (4.5)$$

$$\text{Dye}\ (h_{VB}^{+}) + \text{FMT} \rightarrow \text{FMT degraded products} + \text{dye} \quad (4.6)$$

$${}^{\bullet}O_2^{-} + \text{dye} \rightarrow \text{dye degraded products} \quad (4.7)$$

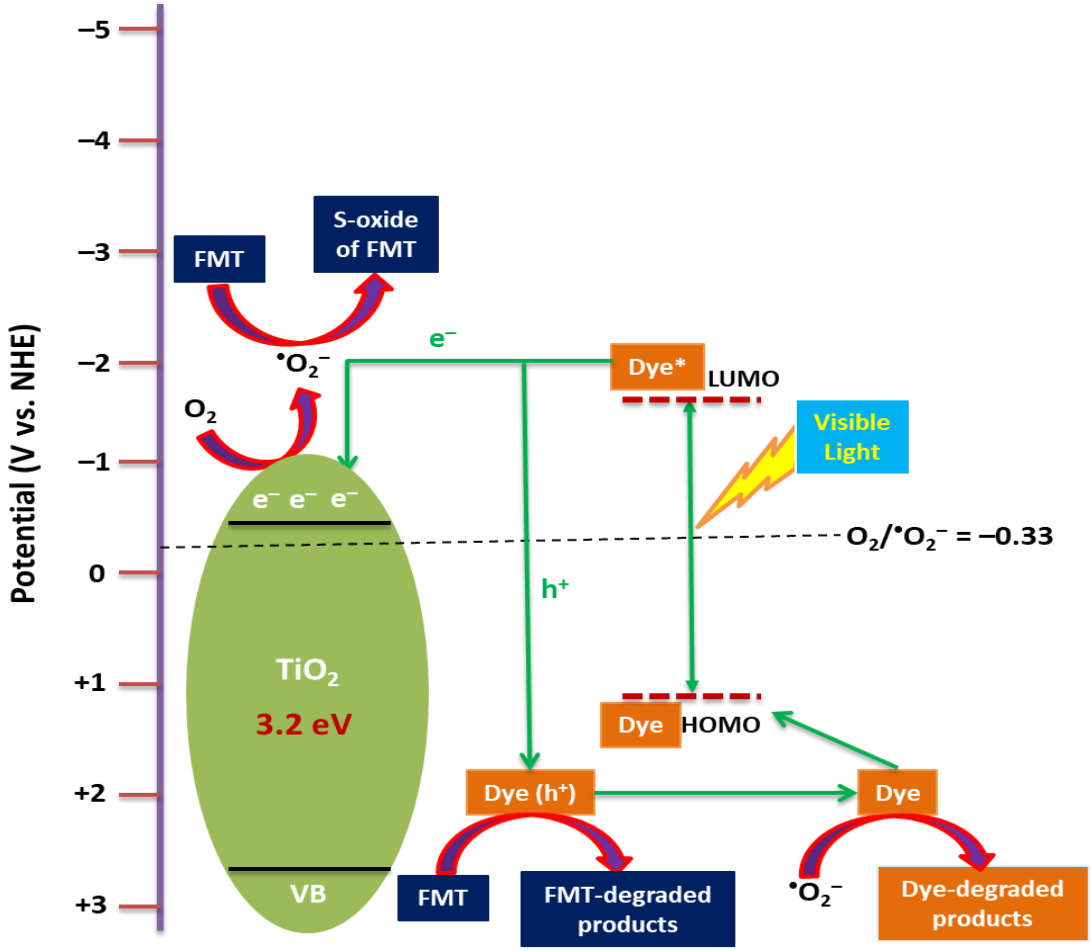

Figure 4.16. Schematic mechanisms of dye–sensitization directed photodegradation of Famotidine with TiO_2 under visible light irradiation.

4.4. CONCLUSIONS

In summary, the photocatalytic activity of dye–sensitized TiO_2 in the degradation of famotidine under visible light irradiation ($\lambda > 400$ nm) was investigated. The TiO_2 in the presence of RhB exhibited excellent photocatalytic performance for famotidine degradation, displaying a considerably higher photocatalytic activity compared with that of TiO_2. Investigation of the photocatalytic mechanism showed that the TiO_2–dye–sensitized degradation of Famotidine under visible light irradiation could be mainly attributed to the direct oxidization by h^+ and $^{\bullet}O_2^-$ radicals, while the $^{\bullet}OH$ radicals played only a relatively minor role in the oxidization process. The kinetics of FMT photodegradation was found to follow the pseudo–first–order rate law and could be described in terms of Langmuir–Hinshelwood model. The present work may provide deep insight into the photosensitization induced photocatalytic mechanism, and also offer new opportunities for their industrial application in the elimination of Famotidine and dye pollutants from wastewater.

4.5. REFERENCES

[1] T.A. Ternes, J. Stuber, N. Hermann, D. Mc Dowell, A. Ried, M. Kampman, B. Teiser, Ozonation: a tool for removal of pharmaceuticals, contrast media and musk fragrances from wastewater, Water Res. 37 (2003) 1976–1982.

[2] K. Ikehata, N.J. Naghashkar, M. G. Ei–Din, Degradation of aqueous pharmaceuticals by ozonation and advanced oxidation processes: A review, Ozone Sci. Eng. 28 (2006) 353–414.

[3] P. Verlicchi, M. Al Aukidy, E. Zambello, Occurrence of pharmaceutical compounds in urban wastewater: removal, mass load and environmental risk after a secondary treatment–a review, Sci. Total Environ. 429 (2012) 123–155.

[4] A.R. Khataee, M. Fathinia, S.W. Joo, Simultaneous monitoring of photocatalysis of three pharmaceuticals by immobilized TiO_2 nanoparticles: chemometric assessment, intermediates identification and ecotoxicological evaluation, Spectrochim. Acta Part A: Mol. Biomol. Spectrosc. 112 (2013) 33–45.

[5] D. Nasuhoglu, A. Rodayan, D. Berk, V. Yargeau, Removal of the antibiotic levofloxacin (levo) in water by ozonation and TiO_2 photocatalysis, Chem. Eng. J. 189–190 (2012) 41–46.

[6] J. Karpin´ska, A. Sokoł, M. Kobeszko, B. Starczewska, U. Czyzewska, M. Hryniewicka, Study on degradation process of famotidine hydrochloride in aqueous samples, Toxicol. Environ. Chem. 92 (2010) 1409–1422.

[7] W.J. Ong, L.L. Tan, S.P. Chai, S.T. Yong, A.R. Mohamed, Highly reactive {001} facets of TiO_2–based composites: synthesis, formation mechanism and characterization, Nanoscale 6 (2014) 1946–2008.

[8] S. Liu, J. Yu, M. Jaroniec, Anatase TiO_2 with dominant high–energy {001}

facets: synthesis, properties, and applications, Chem. Mater. 23 (2011) 4085–4093.

[9] C. Hua, X. Dong, X. Wang, M. Xue, X. Zhang, H. Ma, Enhanced photocatalytic activity of W–doped and W–La–codoped TiO_2 nanomaterials under simulated sunlight, J. Nanomater. 2014 (2014) 943796; http://dx.doi.org/10.1155/2014/943796.

[10] R.J. Ellingson, J.B. Asbury, S. Ferrere, H.N. Ghosh, J.R. Sprague, T. Lian, A.J. Nozik, Dynamics of electron injection in nanocrystalline titanium dioxide films sensitized with [Ru(4,4'–dicarboxy–2,2'–bipyridine)$_2$(NCS)$_2$] by infrared transient absorption, J. Phys. Chem. B 102 (1998) 6455–6458.

[11] G. Elena, Linkers for anchoring sensitizers to semiconductor nanoparticles, Coord. Chem. Rev. 248 (2004) 1283–1297.

[12] M. Gratzel, Solar energy conversion by dye–sensitized photovoltaic cells, Inorg. Chem. 44 (2005) 6841–6851.

[13] W.R. Duncan, O.V. Prezhdo, Theoretical studies of photoinduced electron transfer in dye–sensitized TiO_2, Annu. Rev. Phys. Chem. 58 (2007) 143–184.

[14] W W. Kim, T. Tachikawa, T. Majima, W. Choi, Photocatalysis of dye–sensitized TiO_2 nanoparticles with thin overcoat of Al_2O_3: enhanced activity for H_2 production and dechlorination of CCl_4, J. Phys. Chem. C 113 (2009) 10603–10609.

[15] D. Chatterjee, S. Dasgupta, N.N. Rao, Visible light assisted photodegradation of halocarbons on the dye modified TiO_2 surface using visible light, Sol. Energy Mater. Sol. Cells 90 (2006) 1013–1020.

[16] P. Chowdhury, J. Moreira, H. Gomaa, A.K. Ray, Visible–solar–light–driven photocatalytic degradation of phenol with dye–sensitized TiO_2: parametric and kinetic study, Ind. Eng. Chem. Res. 51 (2012) 4523–4532.

[17] G. Xing, C. Tang, B. Zhang, L. Zhao, Y. Su, X. Wang, A highly uniform ZnO/$NaTaO_3$ nanocomposite: Enhanced self–sensitized degradation of colored pollutants under visible light, J. Alloy Compd. 647 (2015) 287–294.

[18] H. Katsumata, M. Taniguchi, S. Kaneco, T. Suzuki, Photocatalytic degradation of bisphenol A by Ag_3PO_4 under visible light, Catal. Commun. 34 (2013) 30–34.

[19] J. Su, L. Zhu, P. Geng, G. Chen, Self–assembly graphitic carbon nitride quantum dots anchored on TiO_2 nanotube arrays: An efficient heterojunction for pollutants degradation under solar light, J. Hazard. Mater. 316 (2016) 159–168.

[20] P. Kubelka, F. Munk, Ein Beitrag Zur Optik Der Farbanstriche, Z. Techn. Phys. 12 (1931) 593–601.

[21] G. Naresh, T.K. Mandal, Excellent Sun–Light–Driven Photocatalytic Activity by Aurivillius Layered Perovskites, $Bi_{5-x}La_xTi_3FeO_{15}$ (x = 1, 2), ACS Appl. Mater. Interfaces 6 (2014) 21000–21010.

[22] S. Kumar, T. Surendar, A. Baruah, V. Shanker, Synthesis of a Novel and Stable g–C_3N_4–Ag_3PO_4 Hybrid nanocomposite photocatalyst and study of the photocatalytic activity under visible light irradiation, J. Mater. Chem. A 1 (2013) 5333–5340.

[23] H.X. Li, Z.F. Bian, J. Zhu, Y.N. Huo, H. Li, Y.F. Lu, Mesoporous Au/TiO_2 nanocomposites with enhanced photocatalytic activity, J. Am. Chem. Soc. 129 (2007) 4538–4539.

[24] V. Subramanian, E.E. Wolf, P.V. Kamat, Catalysis with TiO_2/gold nanocomposites. Effect of metal particle size on the fermi level equilibration, J. Am. Chem. Soc. 126 (2004) 4943–4950.

[25] S. Bassaid, B. Bellal, M. Trari, Photocatalytic degradation of orange II on the novel hetero–system WS_2/TiO_2 under UV light, Reac. Kinet. Mech. Catal. 115 (2015) 389–400.

[26] P. Ren, Y. Li, Y. Zhang, H. Wang, Q. Wang, Photoelectric properties of DSSCs sensitized by phloxine B and bromophenol blue, Int. J. Photoenergy 2016 (2016) 2135847; http://dx.doi.org/10.1155/2016/2135847.

[27] X.F. Sun, B.B. Guo, L. He, P.F. Xia, S.G. Wang, Electrically accelerated removal of organic pollutants by a three–dimensional graphene aerogel, Am. Int. Chem. Eng. 62 (2016) 2154–2162.

[28] A.J. Nozik, R. Memming, Physical chemistry of semiconductor–liquid interfaces, J. Phys. Chem. 100 (1996) 13061–13078.

[29] L. Pan, J. Zou, X. Liu, X. Liu, S. Wang, X. Zhang, L. Wang, Visible–light–induced photodegradation of rhodamine B over hierarchical TiO_2: effects of storage period and water–mediated adsorption switch, Ind. Eng. Chem. Res. 51 (2012) 12782–12786.

[30] Y. Su, L. Peng, J. Guo, S. Huang, L. Lv, X. Wang, Tunable optical and photocatalytic performance promoted by nonstoichiometric control and site–selective codoping of trivalent ions in $NaTaO_3$, J. Phys. Chem. C 118 (2014) 10728–10739.

[31] A. Fujishima, T.N. Tao, D.A. Tryk, Titanium dioxide photocatalysis, J. Photochem. Photobiol. C: Photochem. Rev. 1 (2000) 1–21.

[32] W.J. Kima, D. Pradhanb, B.–K. Minc, Y. Sohna, Adsorption/photocatalytic activity and fundamental natures of BiOCl and $BiOCl_xI_{1-x}$ prepared in water and ethylene glycol environments, and Ag and Au–doping effects, Appl. Catal. B: Environ. 147 (2014) 711–725.

[33] S. Murphy, C. Saurel, A. Morrissey, J. Tobin, M. Oelgemoller, K. Nolan, Photocatalytic activity of a porphyrin/TiO_2 composite in the degradation of pharmaceuticals, Appl. Catal. B: Environ. 119–120 (2012) 156–165.

CHAPTER 5

FABRICATION OF Ag METAL DECORATED ZnO BY MECHANOCHEMICAL COMBUSTION METHOD AND THEIR APPLICATION INTO PHOTOCATALYTIC FAMOTIDINE DEGRADATION

5.1. INTRODUCTION

Zinc oxide (ZnO) is a wide band–gap (3.2 eV) semiconductor with large exciton binding energy of 60 meV at room temperature. [1]. It is known as one of the important active photocatalysts due to its advantages, including the large initial rates of activity, many active sites with high surface reactivity, low price and environment safety [2]. However, ZnO have several disadvantages such as a rapid recombination of photoexcited electron and hole pairs which inhibits its photocatalytic efficiency. To improve the photocatalytic activity of ZnO, surface charge transfer processes should be enhanced and the recombination rate of electron and hole should be decreased. Several methods have been applie to reduce electron–hole recombination and increase the surface charge transfer [3–8]. One of these methods is to dope transition metal into ZnO photocatalysts. Doping of transition metals into the ZnO lattice can lead to changes in the electrical, optical, and magnetic properties of ZnO. Besides, it reduces band gap energy of ZnO, improves charge separation between electron and hole by forming electron traps and, enhances photocatalytic activity of ZnO [9]. Different transition or noble metals such as Ag, Cu, Fe, Mn, and Ni have been widely used for doping of ZnO. Among them, Ag is the cheapest noble metal and has potentials in industrial productions [10–12]. The wide band gap ZnO semiconductor shows only photo–absorption under UV irradiation whereas silver metal acts as electron sink, which effectively trapped photo–excited electrons from ZnO surface and preventing the recombination of electron–hole [13–15]. The photo–generated holes and metal trapped electrons have effectively produced the hydroxyl radicals and super oxide radicals. The generated hydroxyl and superoxide radicals are strong oxidant species which can degrade the Famotidine molecule.

In this chapter, the various proportions of Ag/ZnO nanocomposites were prepared by mechanochemical combustion method. This method has several advantages such as low–temperature preparation, accurate control of the stoichiometry, easy to handle, one–step reaction and great variety of crystalline metal oxides. The synthesized nanophotocatalysts were characterized by XRD, SEM, EPMA, TEM, BET, XPS, PL and UV–vis spectrophotometer. The target molecule Famotidine (FMT) for degradation is a histamine H2–receptor antagonist, which may induce altered mental status in older adults, especially in those with chronic kidney disease [16]. FMT displays excellent complexing properties and could be considered as a persistent contaminant [17,18]. Hence, it is very important to develop the treatment technology for FMT urgently to complete removal from wastewaters, preventing its hazardous accumulation in future. The photocatalytic activities of ZnO and Ag/ZnO were investigated by degrading FMT in water under UV light irradiation.

5.2. MATERIALS AND METHODS

5.2.1. Chemicals and Materials

Zinc acetate dehydrate ($C_4H_6O_4Zn{\cdot}2H_2O$), oxalic acid dehydrate ($C_2H_2O_4{\cdot}2H_2O$), silver acetate ($C_2H_3O_2Ag$) and pure water (resistivity >18 MΩ cm) were used for the synthesis of the sample. Famotidine ($C_8H_{15}N_7O_2S_3$) was used for photocatalytic studies. Ascorbic acid ($C_6H_8O_6$), *tert*–butyl alcohol ($C_4H_{10}O$) and *di*–ammonium oxalate monohydrate ($C_2H_{10}N_2O_5$) were selected as scavengers. All the reagents are of analytical grade and used without further purification.

5.2.2. Preparation of Photocatalyst

Ag/ZnO was prepared by the mechanochemical combustion technique with controlled combustion method (Figure 5.1). In a typical synthesis, 2.195 g of zinc acetate dihydrate and 2.521 g of oxalic acid dihydrate were taken in agate mortar, and the mixture was ground for 10 min in order to obtain a paste of zinc oxalate dihydrate and acetic acid. The existence of acetic acid was confirmed by its typical smell. The loss of acetic acid byproduct in the form of fumes became a driving force for the reaction. Silver acetate was added to the above paste as a source of silver, and the grinding process was continued for the next 10 min to obtain zinc oxalate–silver oxalate precursor.

The Ag–doped zinc oxide crystallites were obtained by calcination of precursor powders at the temperature of 300–700 °C under an air atmosphere. The undoped ZnO was also synthesized by calcination of a paste of zinc oxalate and acetic acid for the comparison.

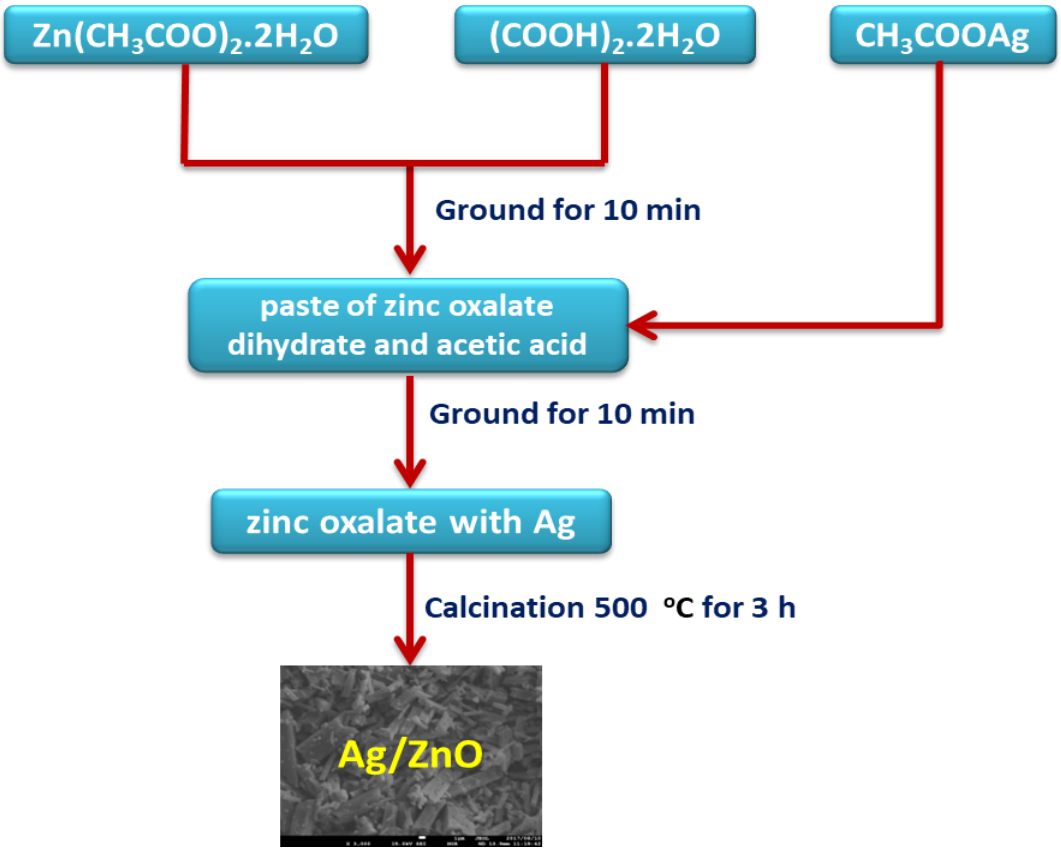

Figure 5.1. Schematic representation of the synthesis process of Ag/ZnO.

5.2.3. Characterization of Photocatalyst

The powder X–ray diffractometer (XRD, RIGAKU Ultima IV, sample horizontal type) was used in order to record the diffraction patterns of photocatalysts employing Cu Kα radiation of wavelength 0.15406 nm with tube current of 50 mA at 40 kV in 2θ angle range from 10° to 80° with a scan speed of 4°/min and a step size of 0.02°. The specific surface areas of catalysts were determined by the three points BET method with N_2 adsorption–desorption isotherms (BELSORP–mini I–MSP–PS, BEL Japan, Inc.). X–ray photoelectron spectroscopy (XPS) measurements were carried out with PHI Quantera SXM photoelectrom spectrometer using Al Kα radiation. A Hitachi S–4000 scanning electron microscope (SEM) was employed to observe the morphologies of oxides. The particle size was observed by Transmission electron microscopy (TEM, JEOL, JEM–1011) working at 100 kV. The

elemental mappings were recorded using electron probe micro–analyzer (EPMA, JEOL, JXA–8530F). The diffuse reflectance spectra (DRS) of photocatalysts were recorded over a range of 200–800 nm with a Shimadzu UV–2450 UV/vis system equipped with an integrating sphere diffuse reflectance accessory using the reference material $BaSO_4$. Photoluminescence (PL) spectra of oxide powders were measured at room temperature using a Shimadzu RF–5300PC system equipped with solid sample holder.

5.2.4. Photocatalytic Activity

The photodegradation system is displayed in Figure 5.2. The photocatalytic activities of Ag/ZnO were investigated by degradation of FMT aqueous solution under UV light irradiation. In the degradation, 10 mg of catalyst was dispersed into 30 mL of 10 mg/L FMT solution. Before irradiation, the suspension was magnetically stirred to equilibrate for 30 min in the dark. A black lamp (TOSHIBA, EFD15BLB–T, 15 W, 365 nm) was used as the light source which was positioned on the side of the reaction cell. Samples were taken at regular intervals and centrifuged to remove the photocatalyst before analysis. The amount of FMT was measured using a high–performance liquid chromatograph (HPLC, GL–7400), equipped with a HITACHI L–3000 optical detector and an Inertsil ODS–3 column (GL Science, Japan). The elution was monitored at 276 nm. The flow rate of the mobile phase (acetonitrile and water (1/1, v/v)) was 1.0 mL/min.

The progress of mineralization of FMT was monitored by measuring the total organic carbon (TOC). The TOC was measured with a Shimadzu TOC analyzer (TOC–V_E) based on CO_2 quantification by non–dispersive infrared analysis after

high–temperature catalytic combustion. Fifty µL of the sample solution was injected into the TOC analyzer.

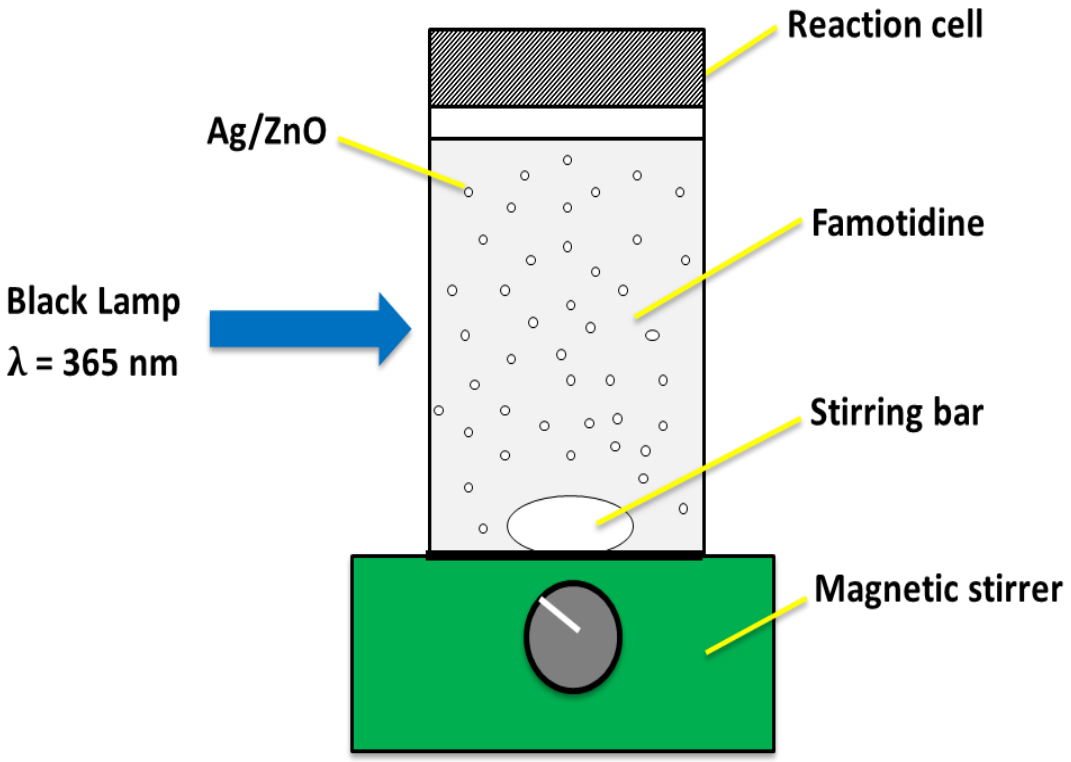

Figure 5.2. Schematic reactor for photocatalytic degradation of Famotidine.

5.2.5. Detection of Reactive Species

To investigate the active species responsible for photodegradation of FMT, various scavenger tests were carried out in the same way as mentioned in the activity experiment. For this purpose, *tert*–butyl alcohol, *di*–ammonium oxalate monohydrate [19] and ascorbic acid [20] were selected as $^{\bullet}OH$, h^{+} and $^{\bullet}O_2^{-}$ radical scavenger, respectively.

5.3. RESULTS AND DISCUSSIONS

5.3.1. Structural Analysis

The structural properties of the synthetic samples were analyzed by X–ray diffraction (XRD). Figure 5.3 shows the XRD patterns for the ZnO and Ag/ZnO composites with different Ag contents. Three main distinct peaks at around 31.82°, 34.50° and 36.32° are observed in above patterns, which are indexed to the (100), (002) and (101) diffractions of the wurtzite ZnO (JCPDS no. 36–1451) [21]. From Figure 5.4, it can be seen that Ag/ZnO composite samples had four major peaks at 38.16°, 44.34°, 64.48° and 77.42°, which were readily assigned to the (111), (200), (220) and (311) planes of face–center–cubic (fcc) structure of Ag (JCPDS card no. 04–783), respectively [22]. In addition, the diffraction intensities and angles of ZnO do not show remarkable change after adding Ag content. The diffraction peak of Ag (111) becomes much stronger and sharper with the increase in the amount of Ag content. This indicates the formation of metallic silver along with ZnO [23]. Additionally, no other peaks and remarkable shifts with increase amount of Ag indicate it that no solid solution of ZnO and Ag is formed or lattice expansion and shrinkage of Ag/ZnO should be negligible.

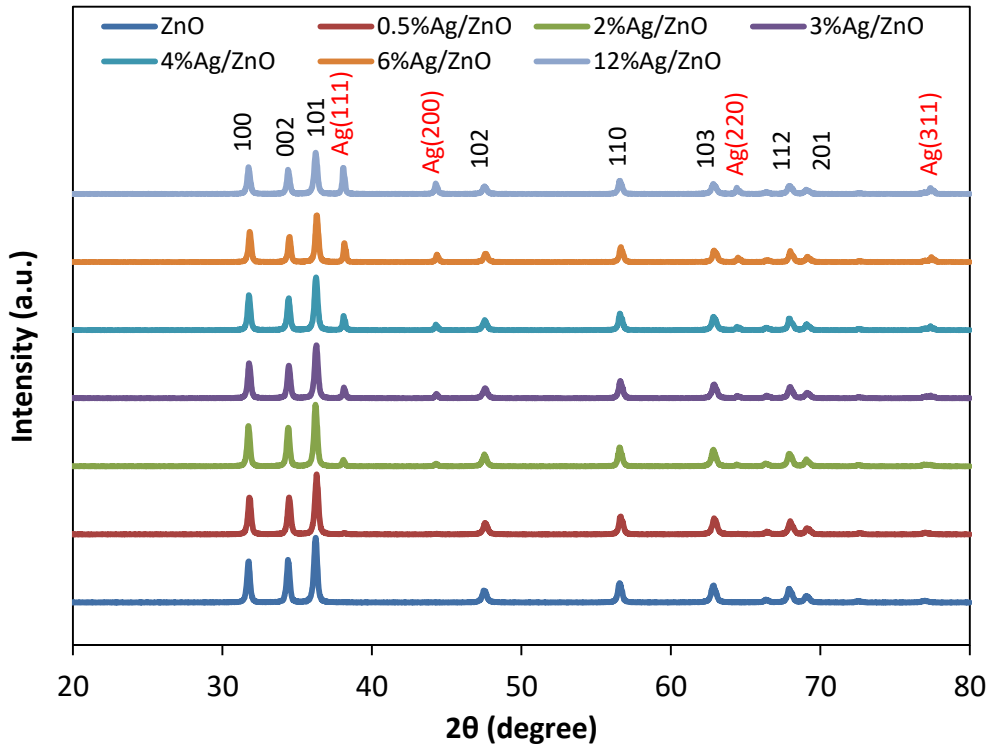

Figure 5.3. XRD patterns of undoped ZnO and Ag/ZnO composites.

The particle size of the oxides has been obtained from the full width at half maximum (FWHM) of the most intense peaks of the respective crystals using the Debye–Scherrer's equation:

$$\boldsymbol{D = \frac{k\lambda}{\beta \cos\theta}} \qquad (5.1)$$

where D is the average crystallite size, λ is the X–ray wavelength, θ is the Bragg diffraction angle, and β is the full width at half–maximum. The crystal size of Ag–doped ZnO was smaller compared with those of the undoped one (Table 5.1).

The lattice parameters for hexagonal ZnO nanoparticles were estimated from the equation:

$$\boldsymbol{\frac{1}{d^2} = \frac{4}{3}\left(\frac{h^2 + hk + k^2}{a^2}\right) + \frac{l^2}{c^2}} \qquad (5.2)$$

where a and c are the lattice parameters and h, k and l are the Miller indices and d_{hkl} is the interplaner spacing for the plane ($h\ k\ l$). This interplaner spacing can be calculated from Bragg's law:

$$\mathbf{2}\boldsymbol{d}\ \mathbf{sin}\,\boldsymbol{\theta} = \boldsymbol{n\lambda} \tag{5.3}$$

The volume (V) of the unit cell for hexagonal system and the number of unit cells (n) in the particle (considering it to be spherical in shape) have been calculated from the following equations:

$$\boldsymbol{V} = \mathbf{0.866}\ \times \boldsymbol{a}^{\mathbf{2}} \times \boldsymbol{c} \tag{5.4}$$

$$\boldsymbol{n} = \frac{\mathbf{4}}{\mathbf{3}\ \boldsymbol{\pi}(\frac{\boldsymbol{D}}{\mathbf{2}\boldsymbol{V}})} \tag{5.5}$$

where D is the average particle size. Significant extent of strains are associated with nanoparticles because they are known to have a number of surface atoms which have unsaturated in co–ordinations. We have estimated and compared the strains in Ag/ZnO nanoparticles using the Williamson–Hall (W–H) equation [24]:

$$\boldsymbol{\beta}\ \mathbf{cos}\,\boldsymbol{\theta} = \frac{\boldsymbol{k\lambda}}{\mathbf{D}} + \mathbf{4}\boldsymbol{\varepsilon}\ \mathbf{sin}\,\boldsymbol{\theta} \tag{5.6}$$

where ε is the strain associated with the nanoparticles. Eq. (5.6) represents a straight line between 4 sin θ (X–axis) and β cos θ (Y–axis). The slope of line gives the strain (ε) and intercept ($k\lambda/D$) of this line on Y–axis gives grain size (D). The lattice parameters and cell volume value calculated from the XRD data are shown in Table 5.1.

Table 5.1

Summary of physical parameters.

Catalysts	2θ for (101)	Crystalline size (nm)	Lattice parameters (Å)		Volume (Å^3)
			a, d_{hkl} (101)	c, d_{hkl} (002)	
ZnO	36.24	32.15	3.250	5.212	47.67
0.5%Ag/ZnO	36.30	30.96	3.245	5.201	47.43
2%Ag/ZnO	36.22	32.15	3.254	5.201	47.69
3%Ag/ZnO	36.28	32.15	3.247	5.201	47.49
4%Ag/ZnO	36.26	33.44	3.249	5.204	47.57
6%Ag/ZnO	36.34	32.16	3.243	5.201	47.37
12%Ag/ZnO	36.24	32.15	3.250	5.212	47.67

The crystal strains of doped ZnO were obtained from the slope (η) of the W–H plot, as shown in Figure 5.4. Positive slopes were observed for ZnO and Ag/ZnO except for 0.5 wt.% Ag/ZnO, suggesting the tensile strain for crystal ZnO. From the Table 5.1, it is found that a slight decrease in the *a* and *c* lattice parameters, which can be explained by the formation of Ag nanocollection and the part substitution of Ag^+ ions at the ZnO lattice, respectively. The substitution did not cause any increase in the lattice parameters via very small percentage of silver doping. Consequently, the Ag–doping influences showed the following rough characteristics: (i) broadening of XRD peaks, (ii) degradation in the crystallinity, (iii) reduction in crystallite size, (iv) smaller particle size and (v) tensile strain.

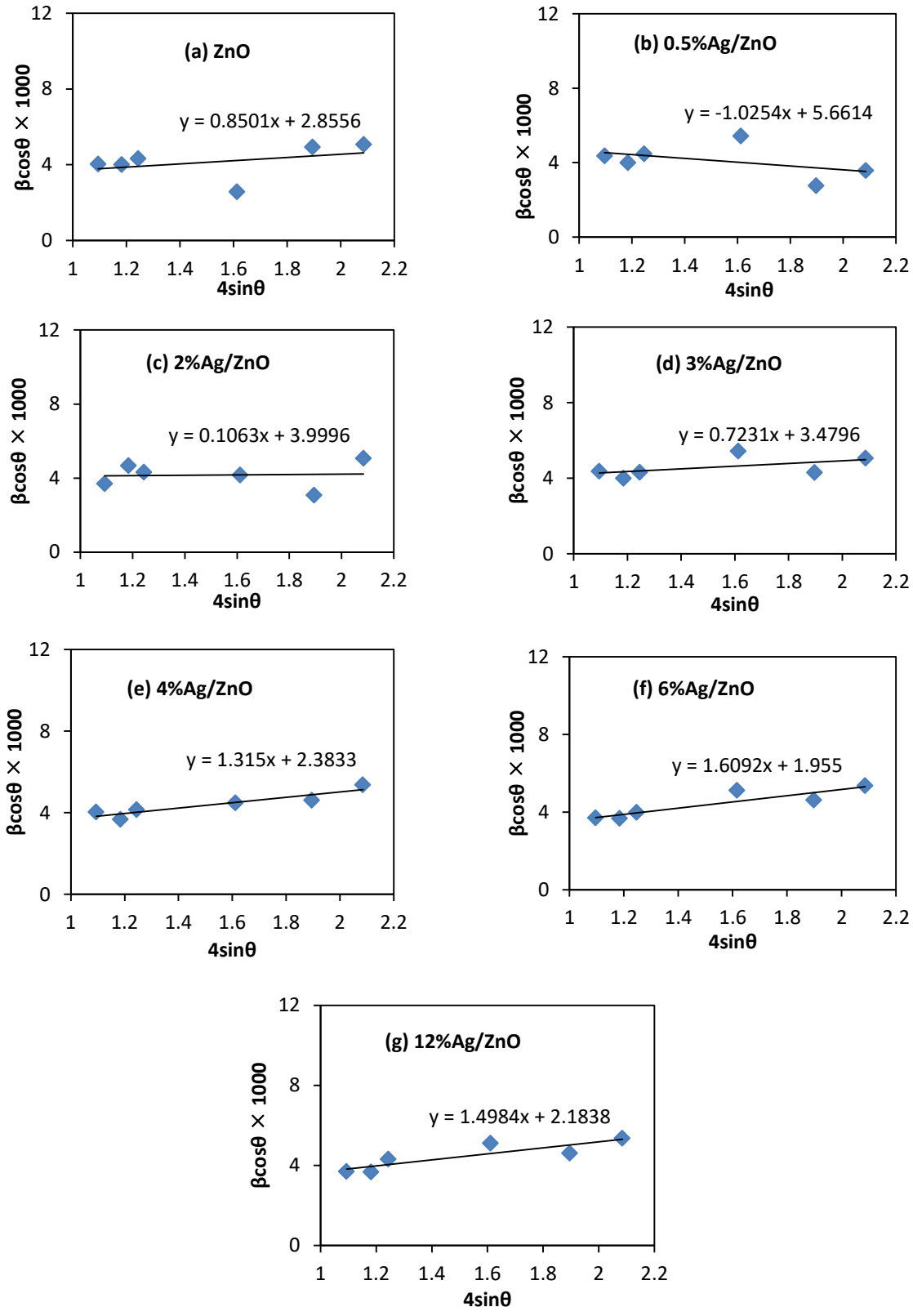

Figure 5.4. Williamson–Hall plots of undoped ZnO and Ag/ZnO composites.

Figure 5.5 displays XRD analysis of 6 wt.% Ag/ZnO composites synthesized at different calcination temperatures from 300 °C to 700 °C. The major peaks of ZnO at 2θ values of 31.7, 34.4, 36.2, and 47.5° could be indexed to (100), (002), (101) and (102) crystal planes and characteristic ZnO peaks become obvious at calcination temperatures above 300 °C. It should be noted that the formation of the crystalline phase of ZnO begins at about 400 °C [25]. From Figure 5.5, it can be seen clearly that the half peak widths of characteristic peaks gradually reduce with increasing calcination temperatures. The fact suggests that ZnO particle sizes increase with calcination temperature. The diffraction intensities and angles of Ag did not any sugnificantly change with increasing calcination temperatures. The average crystallite size (*D*) was found to be 19 and 46 nm at calcination temperature of 400 °C and 700 °C, respectively.

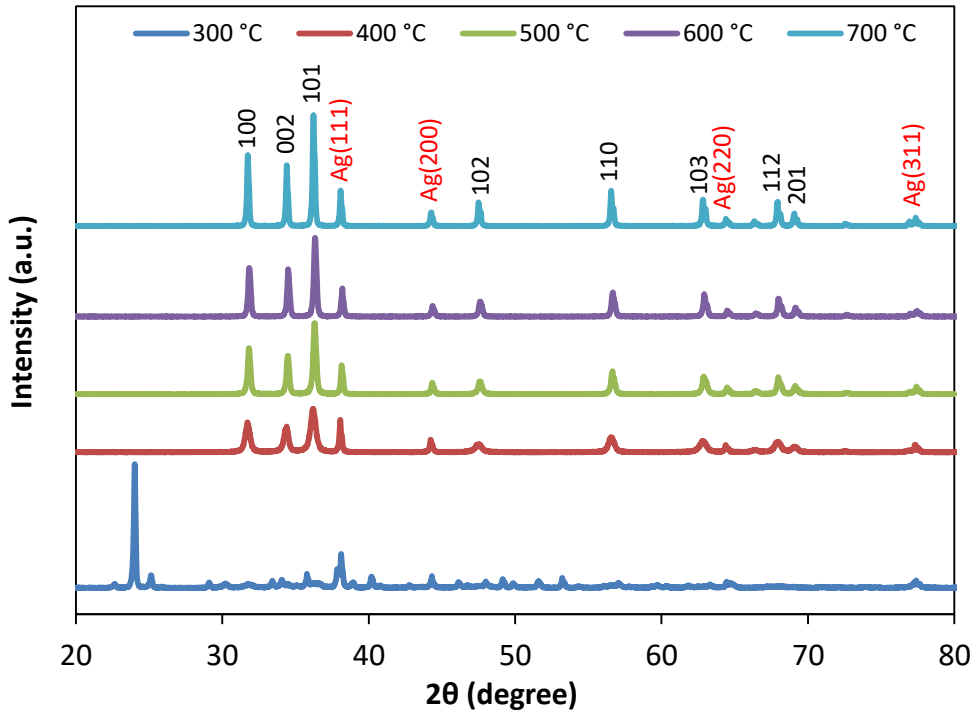

Figure 5.5. XRD patterns of 6 wt.% Ag/ZnO synthesized at different calcination temperatures.

Figure 5.6 illustrates XRD analysis of 6 wt.% Ag/ZnO composites at different calcination times from 0.5 h to 4 h. The diffraction intensities and angles of ZnO and Ag did not remarkable shift with increasing calcination time.

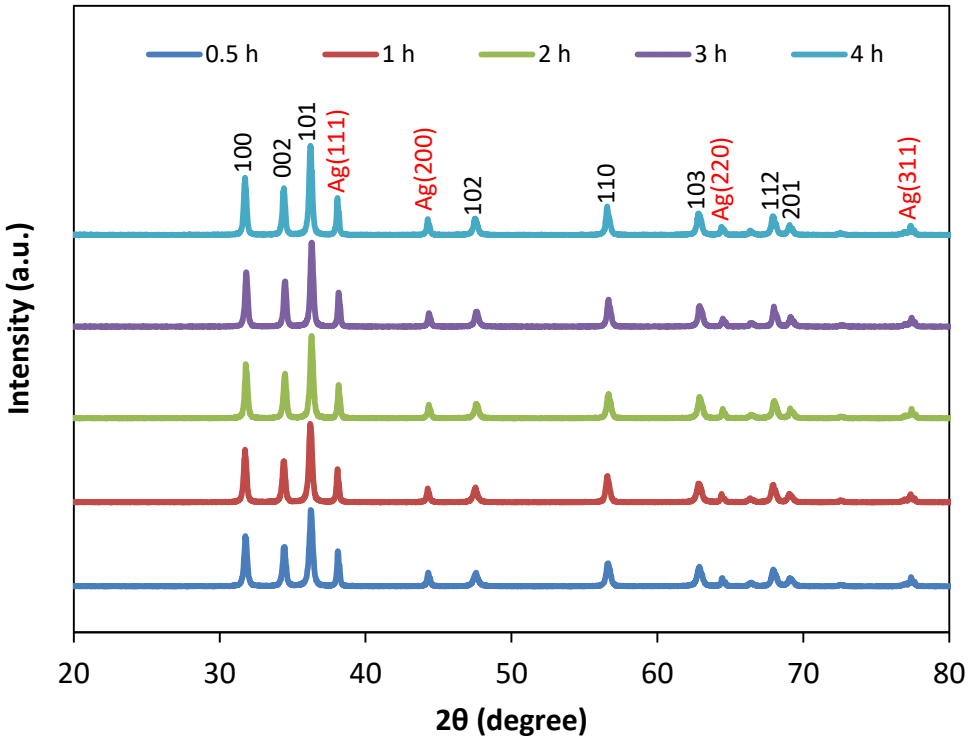

Figure 5.6. XRD patterns of 6 wt.% Ag/ZnO synthesized at different calcination times.

5.3.2. Morphology

Figure 5.7 shows SEM and TEM micrographs of the undoped ZnO and Ag/ZnO nanocomposites. The spherical ZnO particles were in the 100–200 nm size range. SEM characterizations reveal that the microstructures are assembled by spherical multipods with the rod shape branches of building blocks. No appreciable change either in morphology or in size of the ZnO particles could be observed on Ag–doping. The elemental mapping of the Ag/ZnO composites recorded using electron probe micro–analyzer (EPMA), indicates it that Ag are not uniformly distributed on the surface of ZnO. The Ag nanoparticles are distributed locally on the surface of ZnO. In these images, the products are almost exclusively composed of discrete ZnO nanoparticles agglomerated with Ag. The prepared composites showed the microstructure even at high Ag content onto the surface of ZnO.

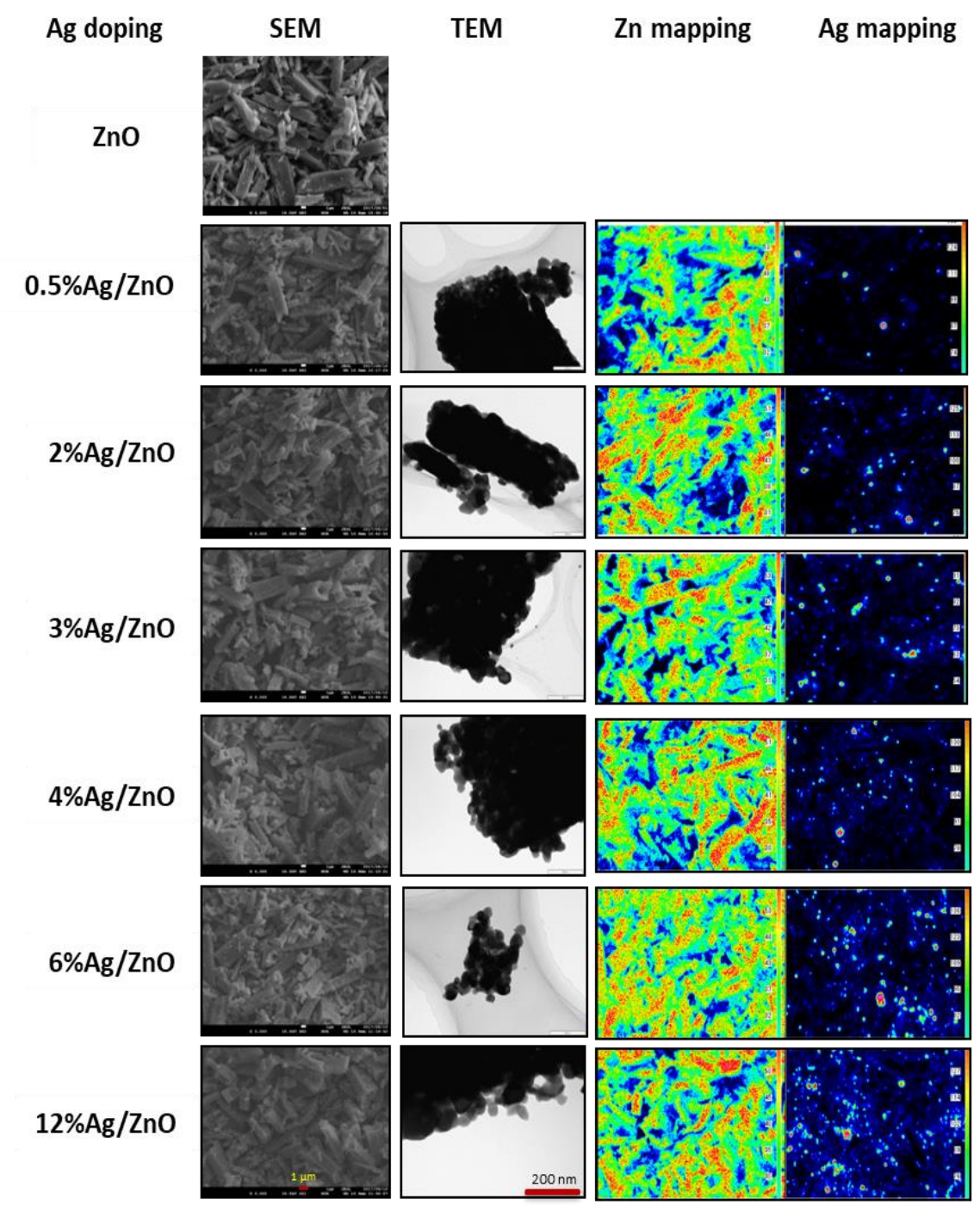

Figure 5.7. SEM and TEM images of undoped ZnO and Ag/ZnO, and Zn and Ag elemental mappings.

Zn and Ag elemental mapping area: The element content increases according to the following orders: (low) black < green < yellow < red (large).

5.3.3. Percentage of Ag from EPMA and Area of Ag from XPS

Figure 5.8 displays the percentage of Ag from EPMA analysis verses percentage of Ag from XPS spectra for Ag/ZnO nanocomposites. From the Figure 5.8, it is found that Ag percentage increase linearly from 0.5–12 wt.% of Ag/ZnO composites. This may be due to the localization of Ag in higher contentment of Ag/ZnO nanocomposites.

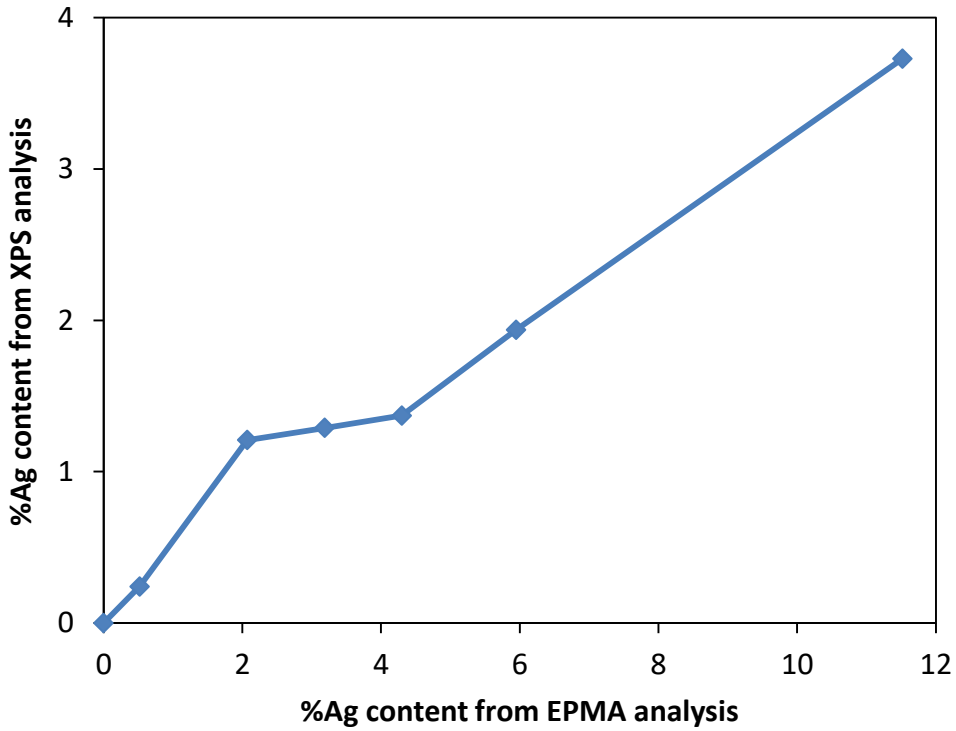

Figure 5.8. Comparison of EPMA analysis with XPS one for Ag contents in the composite.

5.3.4. BET Analysis

Figure 5.9 exhibits N_2 adsorption–desorption isotherms of pure ZnO and various Ag/ZnO samples. All of nanocomposites showed typical type IV isotherm according to the IUPAC classification. Table 5.2 summarizes the BET parameters of ZnO, 4 wt.% Ag/ZnO and 6 wt.% Ag/ZnO composites. The pure ZnO showed a BET surface area of 7.3 m^2/g with a mean pore diameter and a cumulative pore volume of 40.1 nm and 0.0732 cm^3/g, respectively. The surface area, mean pore diameter and total pore volume of 6 wt.% Ag/ZnO were 10.7 m^2/g, 50.4 nm and 0.134 cm^3/g, respectively. Thus, it is found that the introduction of Ag increased the surface area and the pore diameter, which in turn the number of active sites of the catalyst, and is beneficial for the enhancement of the photocatalytic activity.

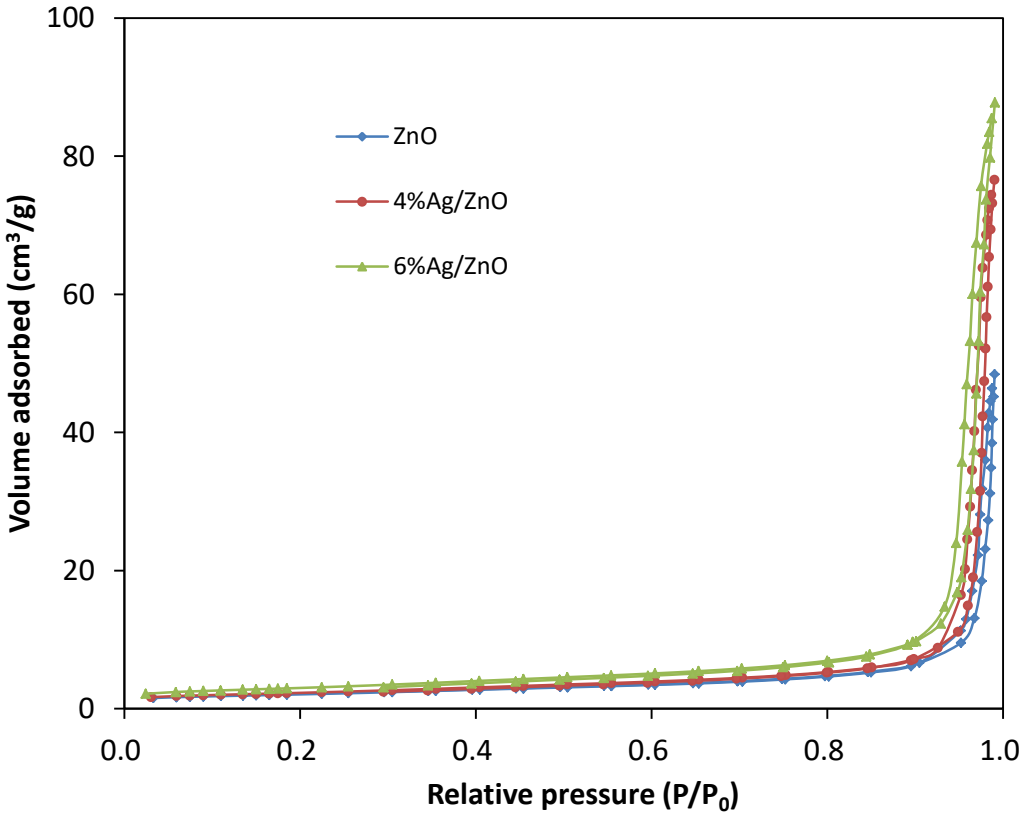

Figure 5.9. N_2 adsorption/desorption isotherms of undoped ZnO, 4 wt.% Ag/ZnO and 6 wt.% Ag/ZnO.

Table 5.2.

BET Parameters of undoped ZnO, 4 wt.% Ag/ZnO and 6 wt.% Ag/ZnO Composites

Catalysts	**BET surface area (m^2/g)**	**Pore diameter (nm)**	**Pore volume (cm^3/g)**
ZnO	7.30	40.1	0.0732
4%Ag/ZnO	8.17	57.8	0.118
6%Ag/ZnO	10.7	50.4	0.134

5.3.5. DRS Spectra

The electronic properties of materials significantly influence their photocatalytic performance. Therefore, the spectra of undoped ZnO and various Ag/ZnO samples were measured by UV–Diffuse reflectance spectroscopy (Figure 5.10). The absorption peaks at UV region corresponds to the absorption of ZnO. The zinc oxide–silver nanocomposite materials display strong absorption in UV region and small absorption in visible region which is related to Ag/ZnO [26]. The absorption band intensity in visible region for Ag nanoparticles was increased with increase in Ag percentage in the composite. The obtained results confirmed that the Ag/ZnO composites effectively absorbed the UV. It can be found that the 6 wt.% Ag/ZnO shows apparently enhanced UV–Vis absorption intensity, demonstrating the presence of Ag^0 nanoparticles on ZnO surface [27]. The reflectance data was converted to Kubelka–Munk equation which is expressed as $F(R) = (1 - R)^2/2R$. The band gap of the oxides was deduced from Tauc plot of $[F(R)h\nu]^2$ versus photon energy (Figure 5.11), and their values are presented in Table 5.4.

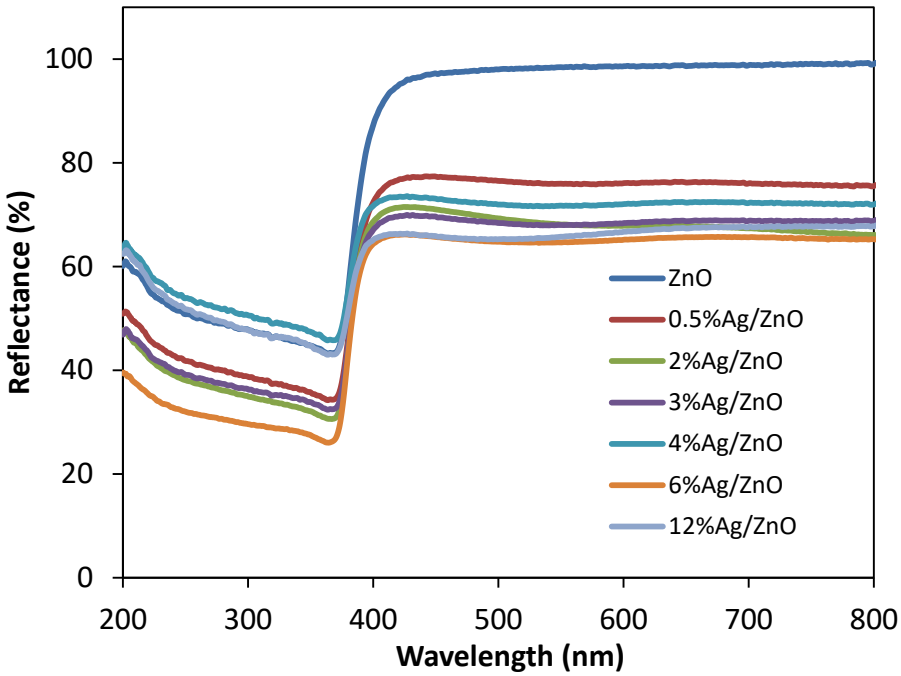

Figure 5.10. UV–Vis DRS patterns of undoped ZnO and (0.5–12) wt.% Ag/ZnO.

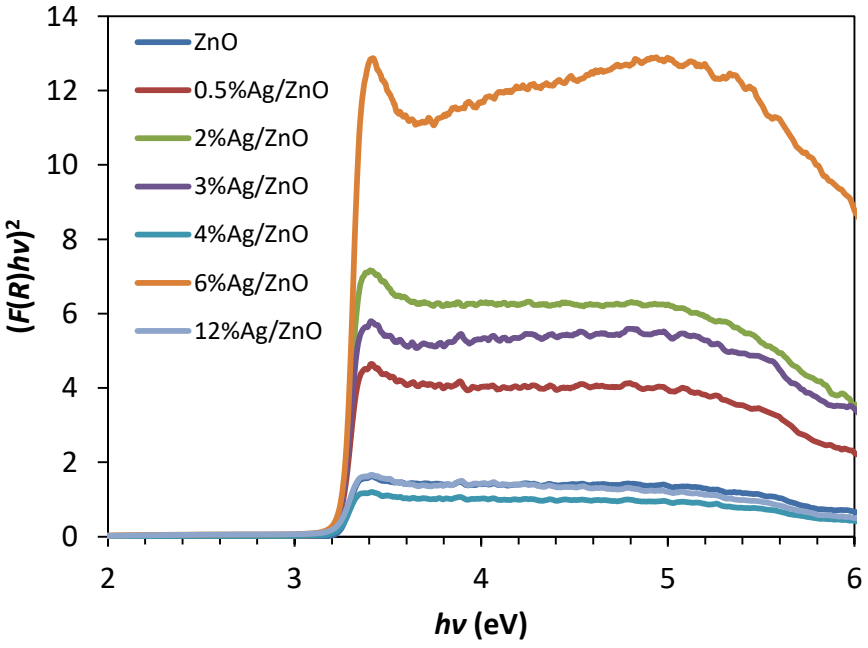

Figure 5.11. Tauc plot of $[F(R)h\nu]^2$ versus photon energy for undoped ZnO and (0.5–12) wt.% Ag/ZnO.

The optical property of the 6 wt.% Ag/ZnO composites synthesized at different calcination temperatures was studied by DRS (Figure 5.12). The maximum absorption intensity for Ag/ZnO composite was obtained at the calcination temperature of 500 °C. The values of the band gap energy were obtained from the Tauc plots (Figure 5.13). A slight decrease in the band gap for Ag/ZnO was obtained at 500 °C calcination temperature, compared with those observed at other temperatures

The effect of different calcination times on the optical property of Ag/ZnO was investigated by DRS (Figure 5.14). The base absorption intensity of Ag/ZnO composite was obtained for 3 h of calcination time. The Tauc plots were shown in Figure 5.15.

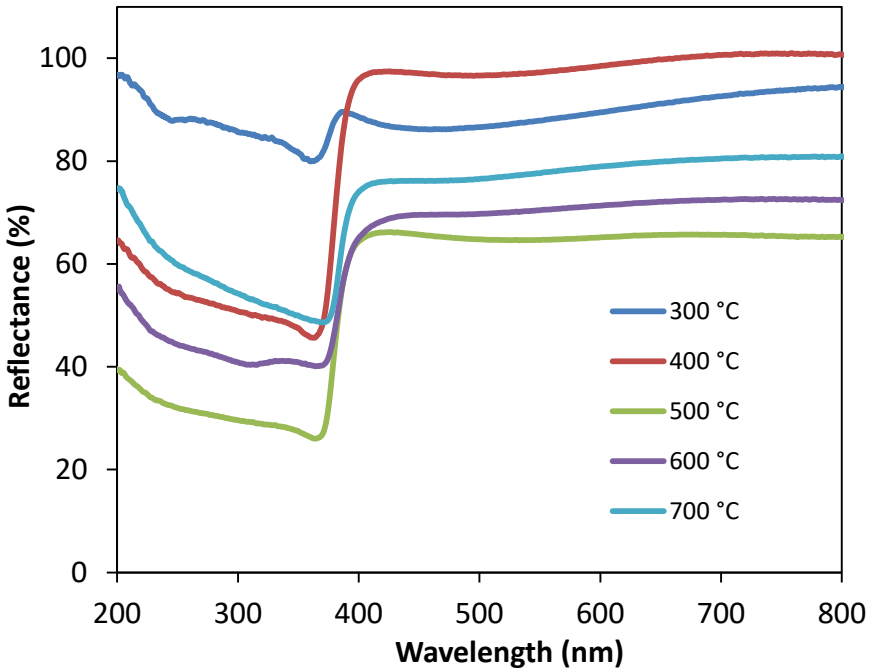

Figure 5.12. UV–Vis DRS patterns of 6 wt.% Ag/ZnO at different calcination temperatures.

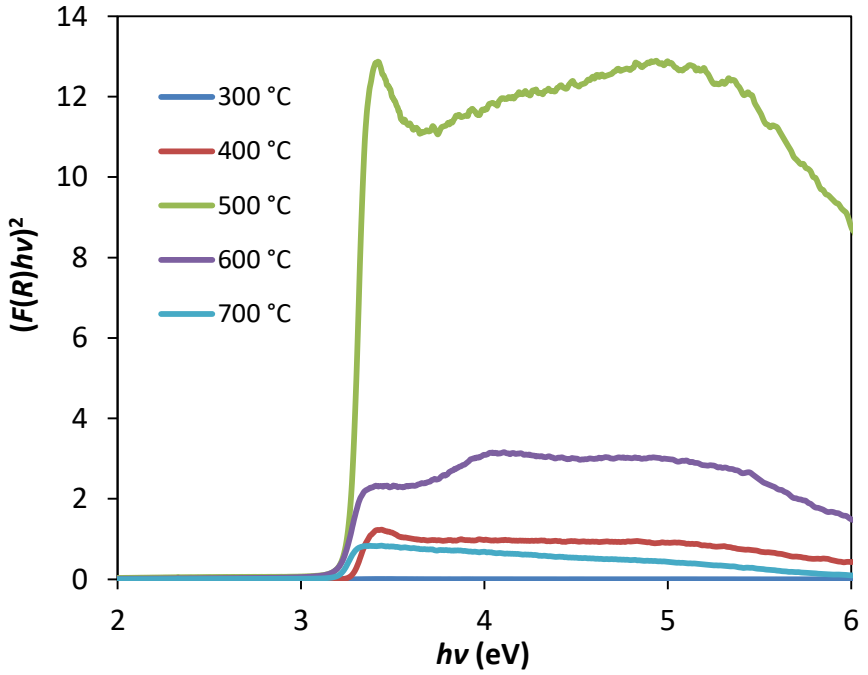

Figure 5.13. Tauc plot of $[F(R)h\nu]^2$ versus photon energy for 6 wt.% Ag/ZnO synthesized at different calcination temperatures.

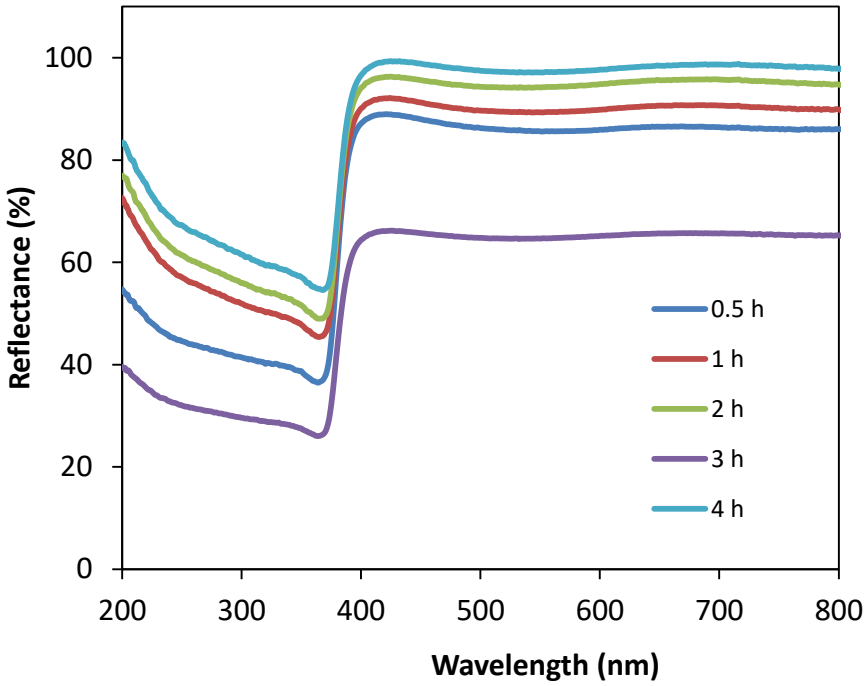

Figure 5.14. UV–Vis DRS patterns of 6 wt.% Ag/ZnO at different calcination times.

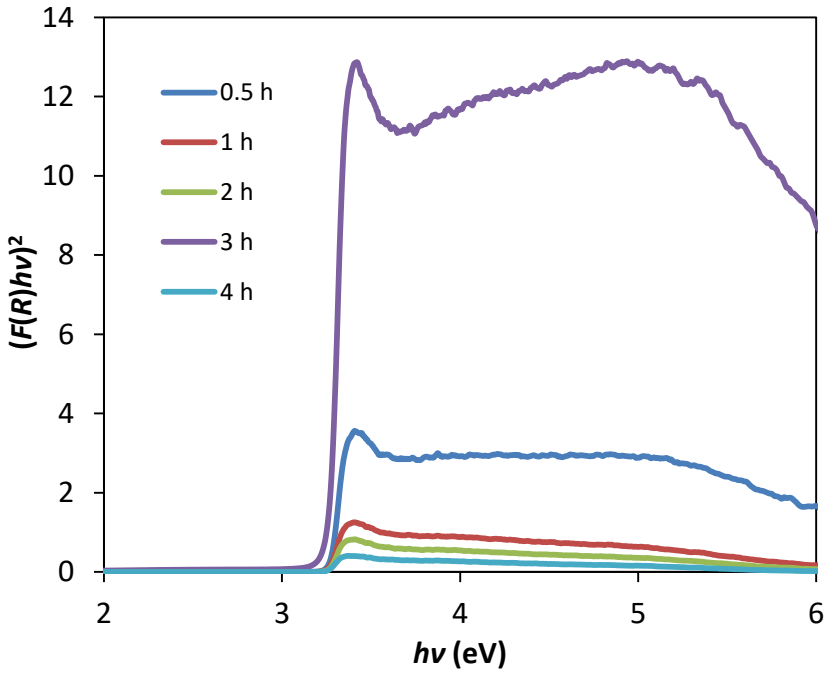

Figure 5.15. Tauc plot of $[F(R)h\nu]^2$ versus photon energy for 6 wt.% Ag/ZnO synthesized at different calcination times.

5.3.6. Photoluminescence Study

The room temperature photoluminescence (PL) spectra of undoped ZnO and Ag/ZnO composites were recorded over the wavelength range 350–600 nm. Figure 5.16 illustrates the PL spectra at excitation wavelengths. In the PL spectra for ZnO, typically there are emission bands in the ultraviolet (UV) and visible (green, yellow, blue and violet) regions [28–30]. The ZnO and Ag/ZnO composites shows strong emission peak at around 389 nm in the UV region which is attributed to near band edge emission and also related with electron–hole charge recombination process [31,32]. The weak emission at 400–600 nm is corresponding to the intrinsic or extrinsic defects in ZnO and oxygen vacancies. It is estimated that the blue band emission is due to the transition from extended interstitial Zn states to the valence band [29]. The usual band–edge emission could not be obtained at the high excitation energy (330 nm) for Ag/ZnO composites. The band–edge and blue band emissions could be observed for the use of low excitation energy at 335~360 nm, respectively.

In Ag/ZnO composite, the Ag metal acts as electron trapper which effectively captures photoexcited electrons from ZnO as well as prevents the rate of electron and hole recombination, hence the emission intensity was quenched [33,34]. The photoluminescence emission intensity is quenched with increase of Ag percentage in the Ag/ZnO composites (Figure 5.16). According to the above analysis, Ag incorporation with ZnO effectively captured electrons from ZnO surface and has attributed to a higher electron–hole charge separation. The photogenerated charge carriers possess a longer lifetime. Thus, the existence of Ag nanoparticles in Ag/ZnO may finally improve its photocatalytic activity significantly [35].

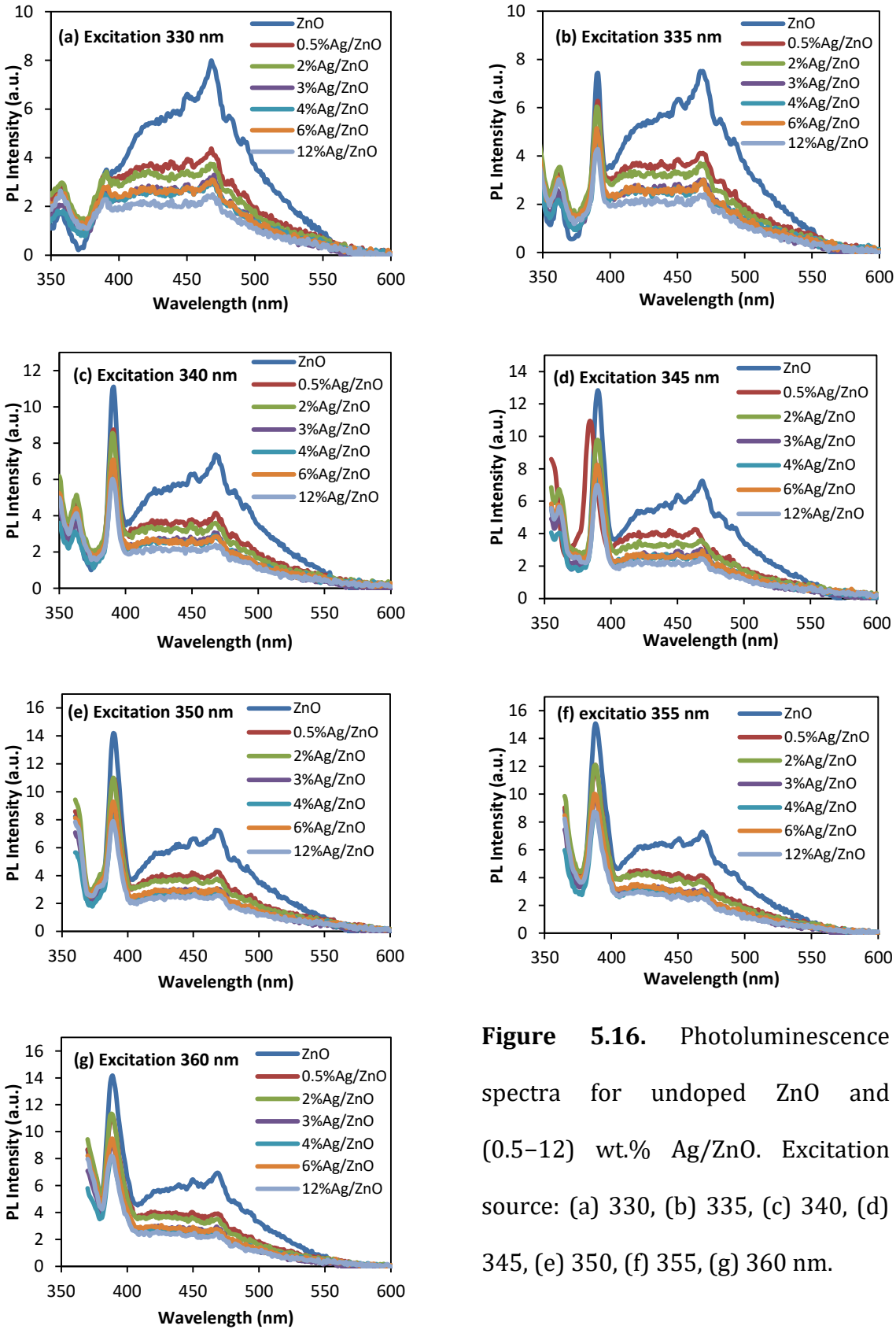

Figure 5.16. Photoluminescence spectra for undoped ZnO and (0.5–12) wt.% Ag/ZnO. Excitation source: (a) 330, (b) 335, (c) 340, (d) 345, (e) 350, (f) 355, (g) 360 nm.

Figures 5.17 and 5.18 present the PL of ZnO and Ag/ZnO synthesized at different calcination temperatures and times. The peak position of the blue emissions was almost the same for the samples obtained at 300–700 °C calcination temperatures, and the usual band–edge emission in the UV could not be obtained at 330 nm excitation (Figure 5.17a). At excitation energies for 335~360 nm, the usual band–edge and deep–level emission in the blue band can be seen, as shown in Figures 5.17 (b–g). The dependence of the intensity of UV and blue emissions on calcination temperatures could be clearly associated in Figure 5.19. The rapid increases of intensity at 390 nm and 467 nm using 340 nm excitation are well demonstrated with increasing calcination temperatures.

The peak positions of the blue emissions were almost the same for the composites obtained for calcination times (Figure 5.18). Figure 5.20 shows the calcination times dependence of the intensity of UV and blue emissions using 340 nm excitation for Ag/ZnO. The blue emissions intensity at 468 nm were almost flat for all of calcination times.

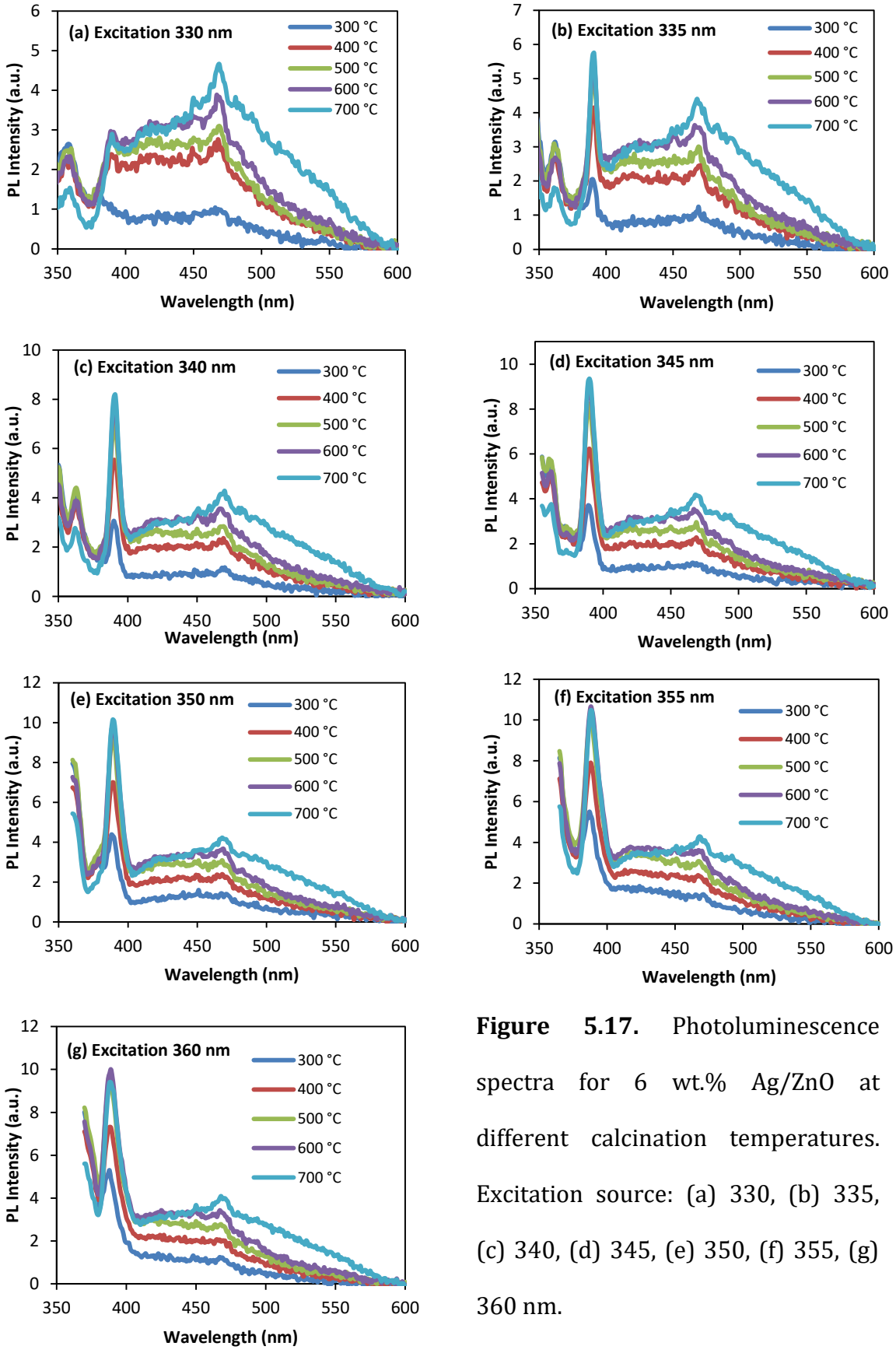

Figure 5.17. Photoluminescence spectra for 6 wt.% Ag/ZnO at different calcination temperatures. Excitation source: (a) 330, (b) 335, (c) 340, (d) 345, (e) 350, (f) 355, (g) 360 nm.

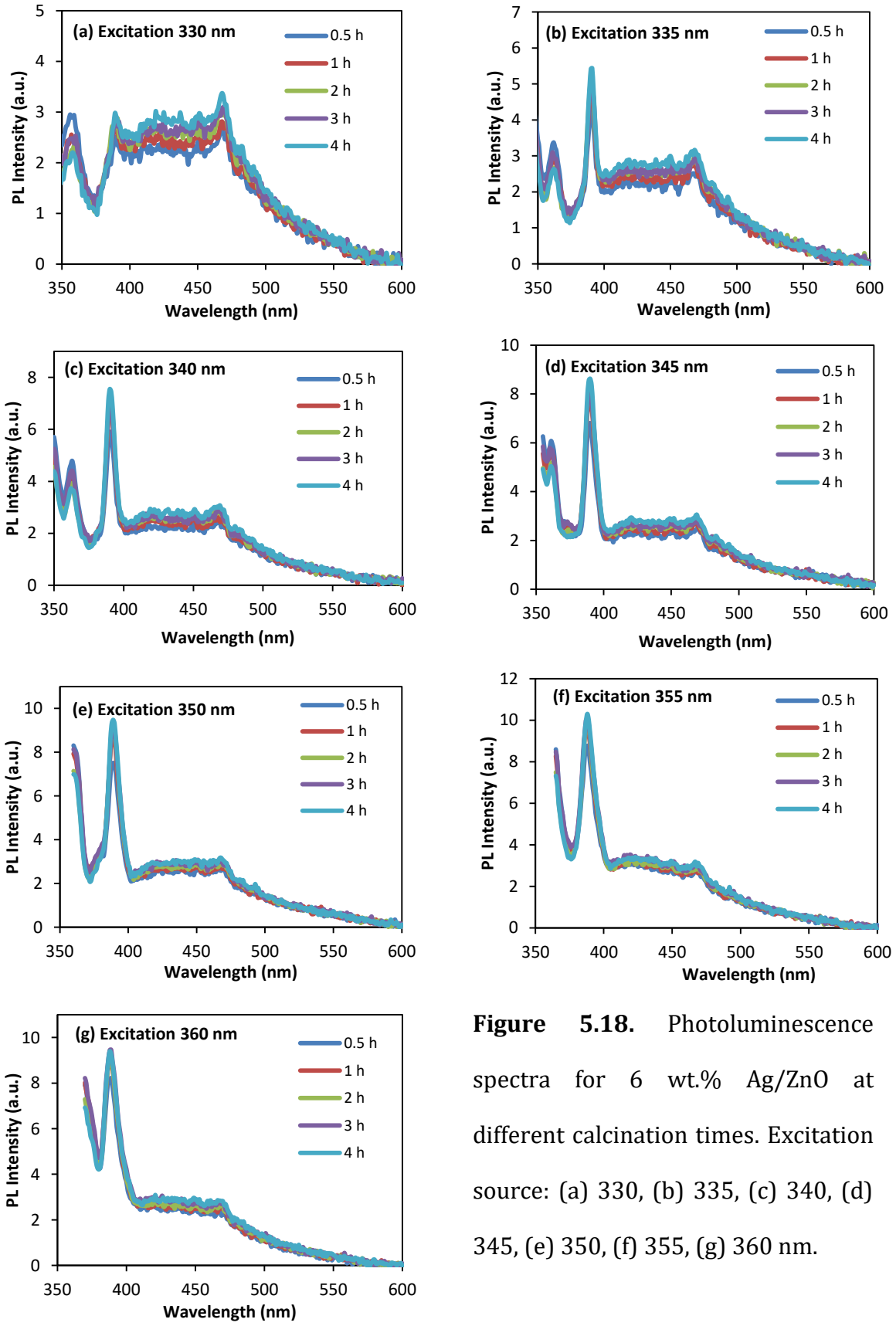

Figure 5.18. Photoluminescence spectra for 6 wt.% Ag/ZnO at different calcination times. Excitation source: (a) 330, (b) 335, (c) 340, (d) 345, (e) 350, (f) 355, (g) 360 nm.

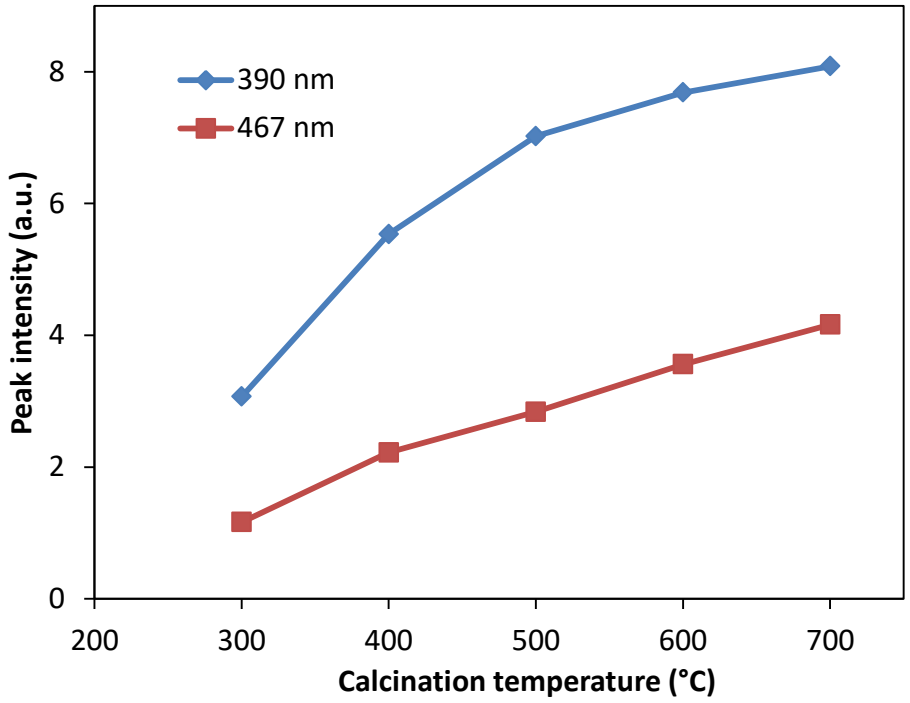

Figure 5.19. Changes of relative intensity of emission at 390 nm and 467 nm with different calcination temperatures.

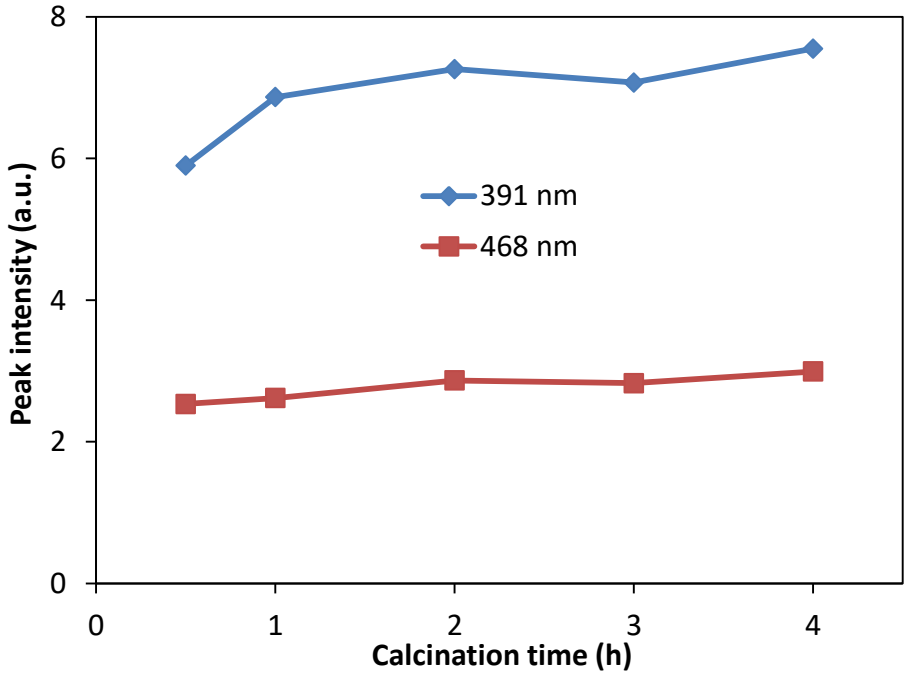

Figure 5.20. Changes of relative intensity of emission at 391 nm and 468 nm with different calcination times.

5.3.7. XPS spectra

XPS is a sensitive technique for investigating the chemical composition of the surface of a material. The surface compositions and chemical states of the pure ZnO were determined with XPS. Figure 5.21a displays the fully scanned spectrum ZnO. In Figure 5.21b, the peak of Zn $2p_{1/2}$ and Zn $2p_{3/2}$, located at 1044.1 and 1021.0 eV, respectively [36]. At 373.6 eV (Ag $3d_{3/2}$) and 367.6 eV (Ag $3d_{5/2}$), the peaks was not detected in undoped ZnO (Figure 5.21c) [37]. The O1s spectra of ZnO are shown in Figure 5.21d. The 529.6 eV peak belongs to the crystal lattice oxygen (O_L) in ZnO, while the 531.2 eV peak can be assigned to the oxygen of surface hydroxyl (O_H) on the catalyst surface [38].

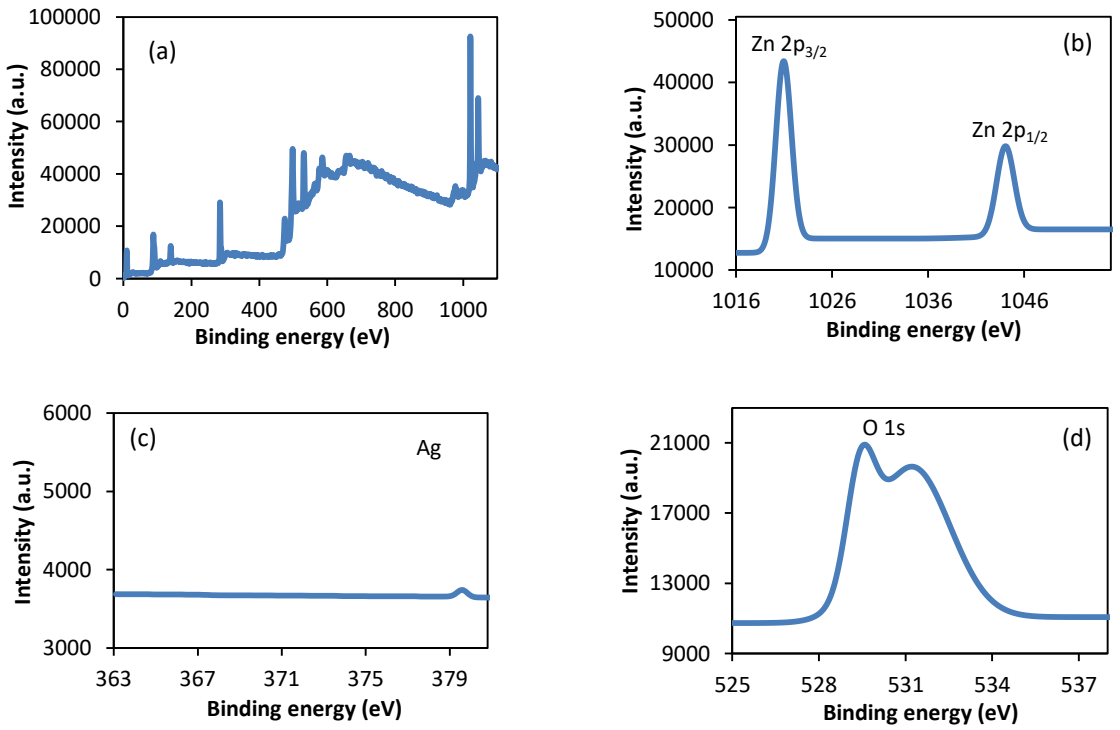

Figure 5.21. (a) Full range XPS spectra of ZnO; (b–d) High resolution XPS spectra of Zn 2P, Ag 3d and O 1s for ZnO.

The surface components and chemical states of Ag/ZnO are investigated by XPS analysis. Figures 5.22a–5.27a show the scan survey spectra for the representative Ag/ZnO composites. All of the peaks on the curve can be ascribed to Ag, Zn, O and C elements and no peaks of other elements were observed (Figure 5.26). The presence of C mainly comes from the hydrocarbon contaminants that commonly exist for XPS [39]. Therefore, it can be concluded that the sample is composed of Ag, Zn and O only. These results are agreement with the XRD patterns.

The positions of Zn $2p_{3/2}$ peak for all Ag/ZnO composites (Figures 5.22b–5.27b) are nearly same value, compared with that of the prepared undoped ZnO nanoparticles (Table 5.3), which confirms that Zn element exists mainly in the form of Zn^{2+} chemical state on the sample surfaces. The difference between the two bonding energies of Zn $2p_{1/2}$ and Zn $2p_{3/2}$ for all Ag/ZnO samples is 23.1 eV, which also suggests that the Zn is in a +2 oxidation state [40].

Figures 5.22c–5.27c illustrate the Ag 3d XPS spectra for all Ag/ZnO samples. Table 5.3 shows that the difference between the peaks of Ag $3d_{5/2}$ and $3d_{3/2}$ for all of the composites is 6.0 eV, indicates the presence of metallic Ag and Ag–Zn–O ternary compounds, respectively [41,42]. It should be noted here that, in general, the binding energy value of zero valence metallic atom is smaller than that of metal cation (Binding energy value of Ag^0 and Ag^+ is about 368.2 and 367.2 eV, respectively. However, Ag is exceptional [43].

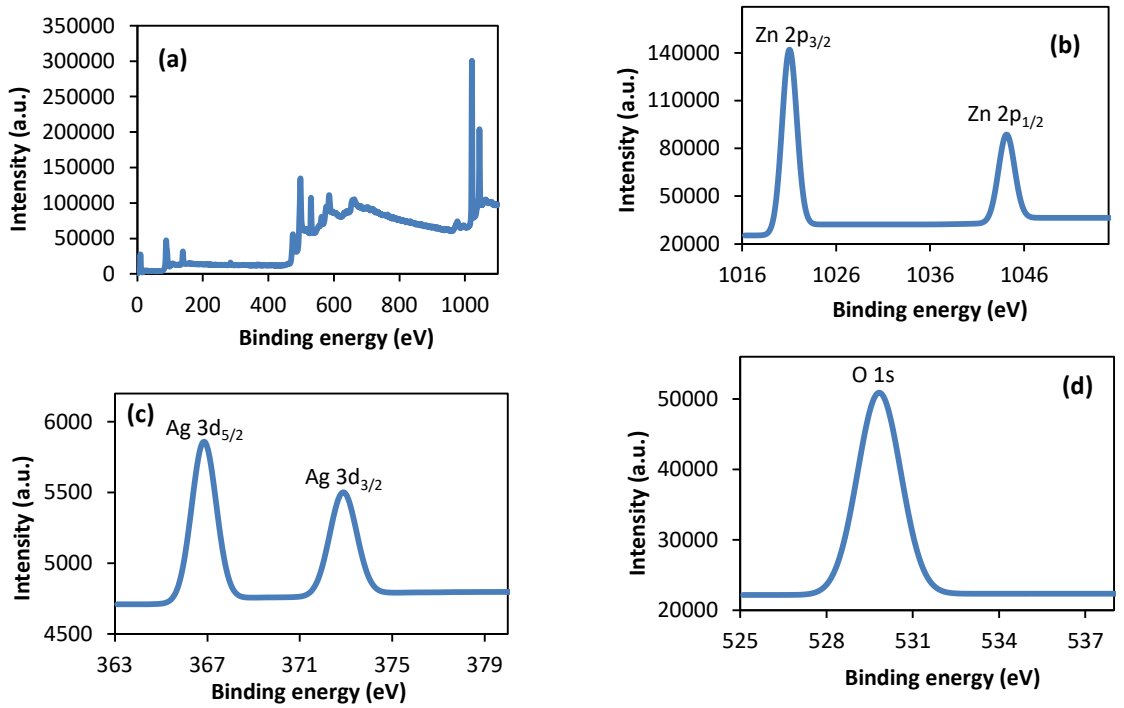

Figure 5.22. (a) Full range XPS spectra of 0.5 wt.% Ag/ZnO; (b–d) High resolution XPS spectra of Zn 2P, Ag 3d and O 1s for 0.5 wt.% ZnO/Ag composite.

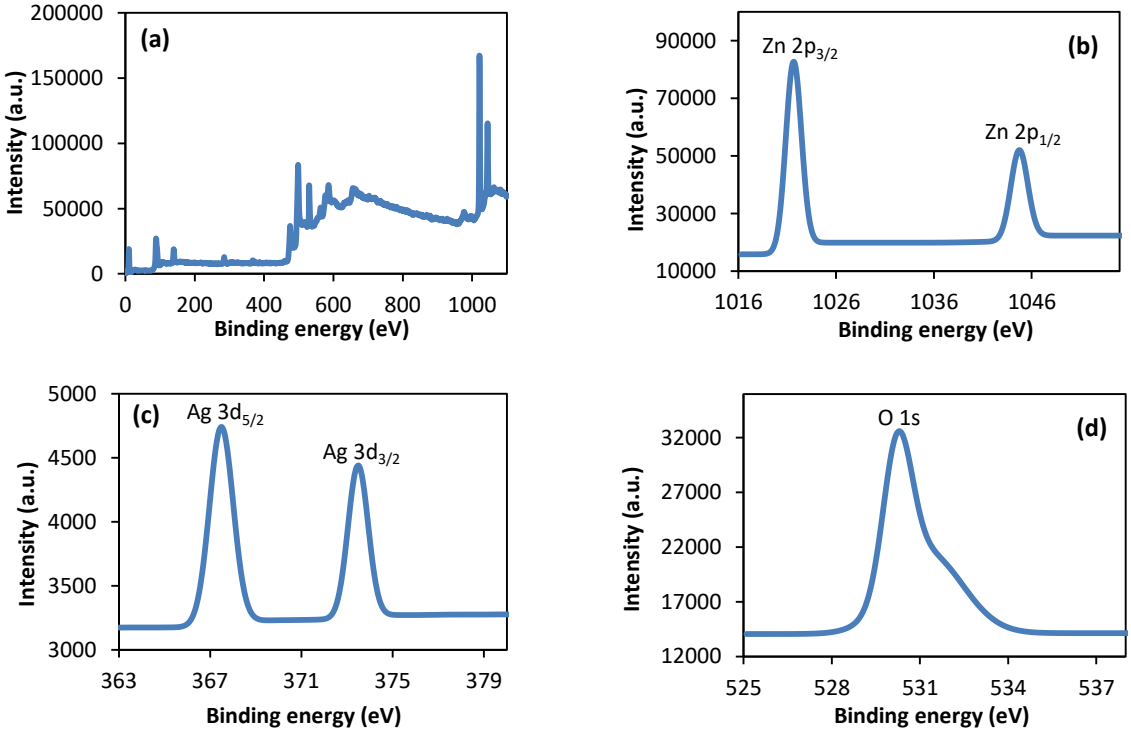

Figure 5.23. (a) Full range XPS spectra of 2 wt.% Ag/ZnO; (b–d) High resolution XPS spectra of Zn 2P, Ag 3d and O 1s for 2 wt.% ZnO/Ag composite.

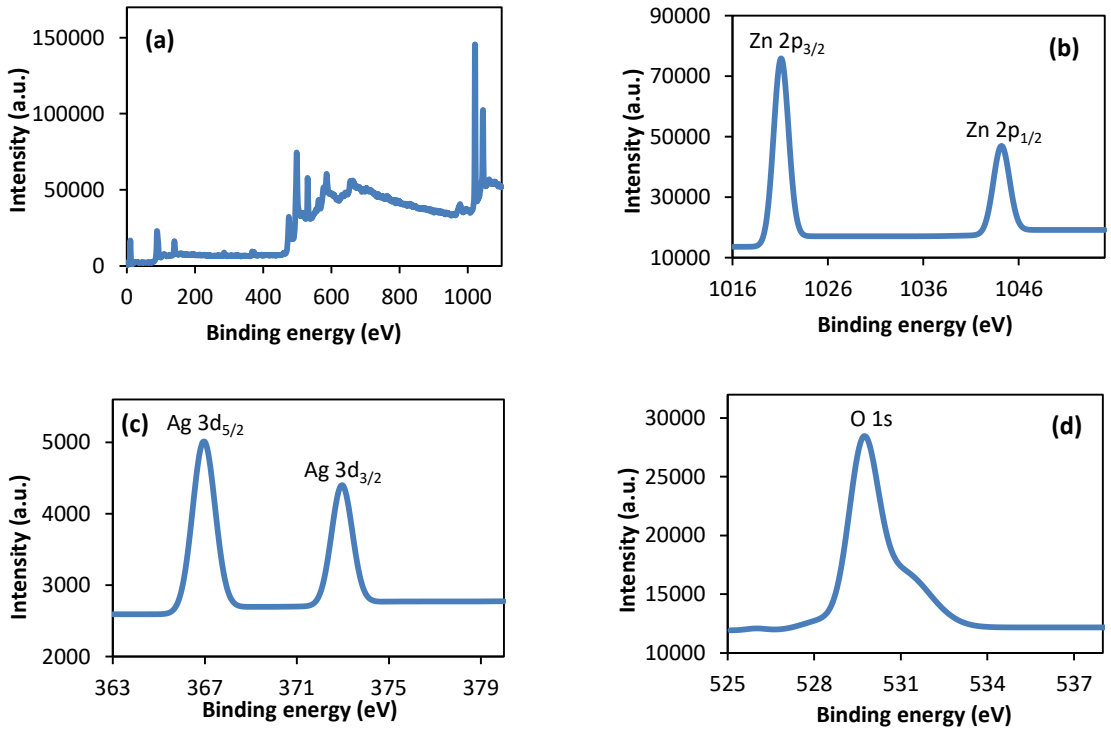

Figure 5.24. (a) Full range XPS spectra of 3 wt.% Ag/ZnO; (b–d) High resolution XPS spectra of Zn 2P, Ag 3d and O 1s for 3 wt.% ZnO/Ag composite.

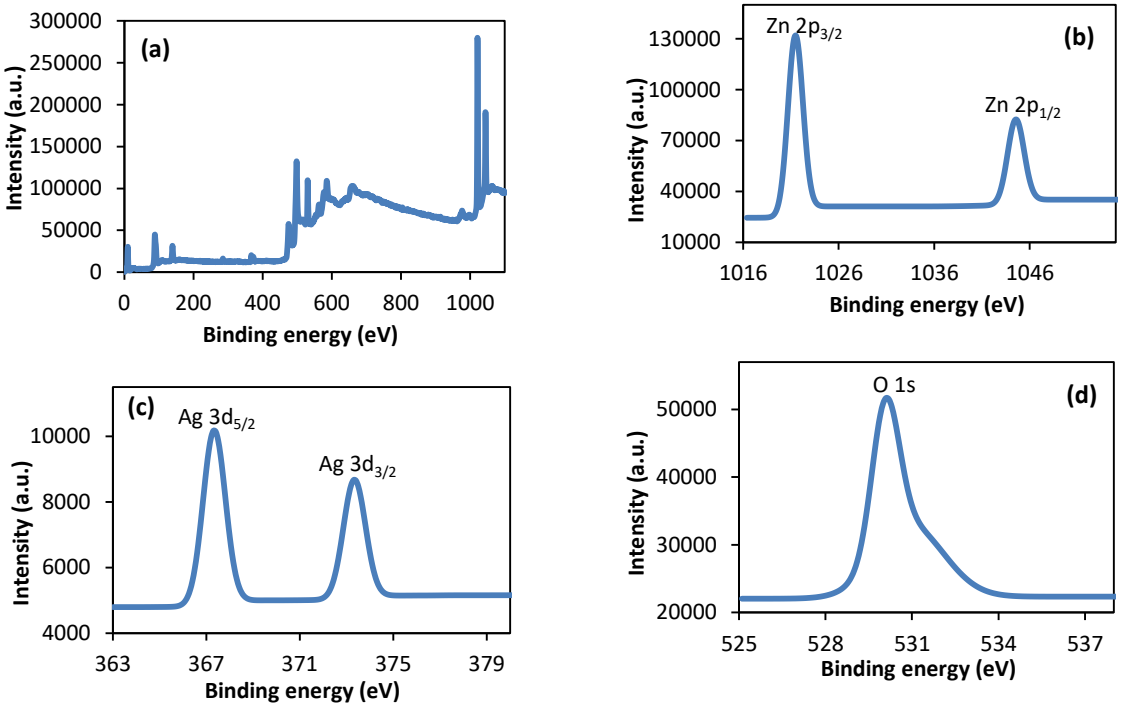

Figure 5.25. (a) Full range XPS spectra of 4 wt.% Ag/ZnO; (b–d) High resolution XPS spectra of Zn 2P, Ag 3d and O 1s for 4 wt.% ZnO/Ag composite.

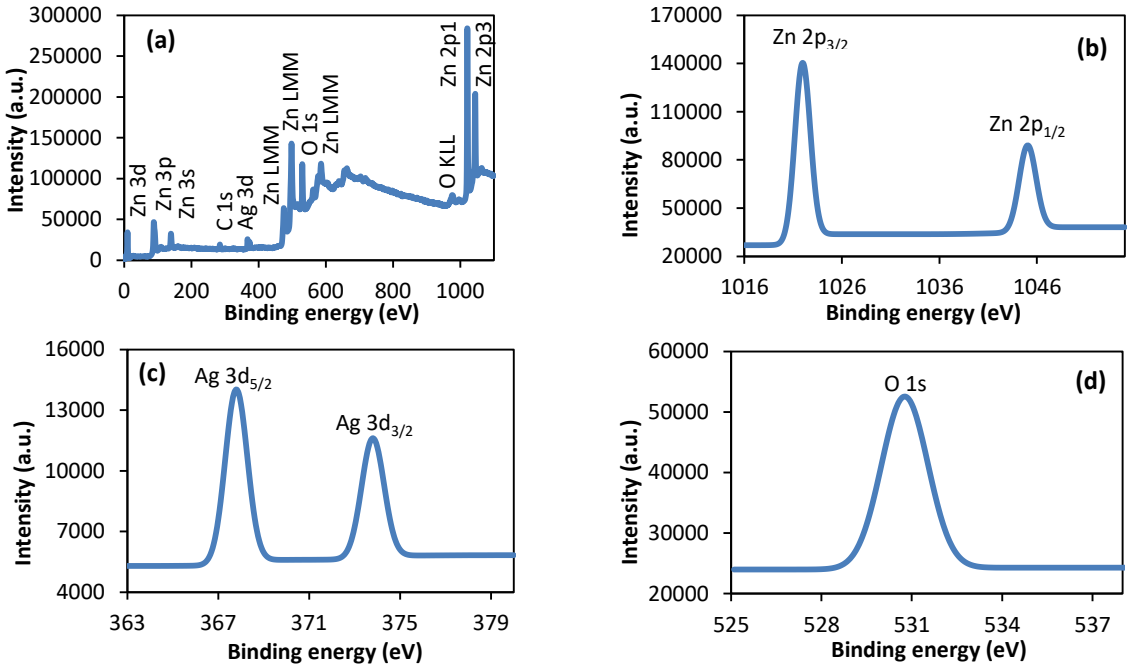

Figure 5.26. (a) Full range XPS spectra of 6 wt.% Ag/ZnO; (b–d) High resolution XPS spectra of Zn 2P, Ag 3d and O 1s for 6 wt.% ZnO/Ag composite.

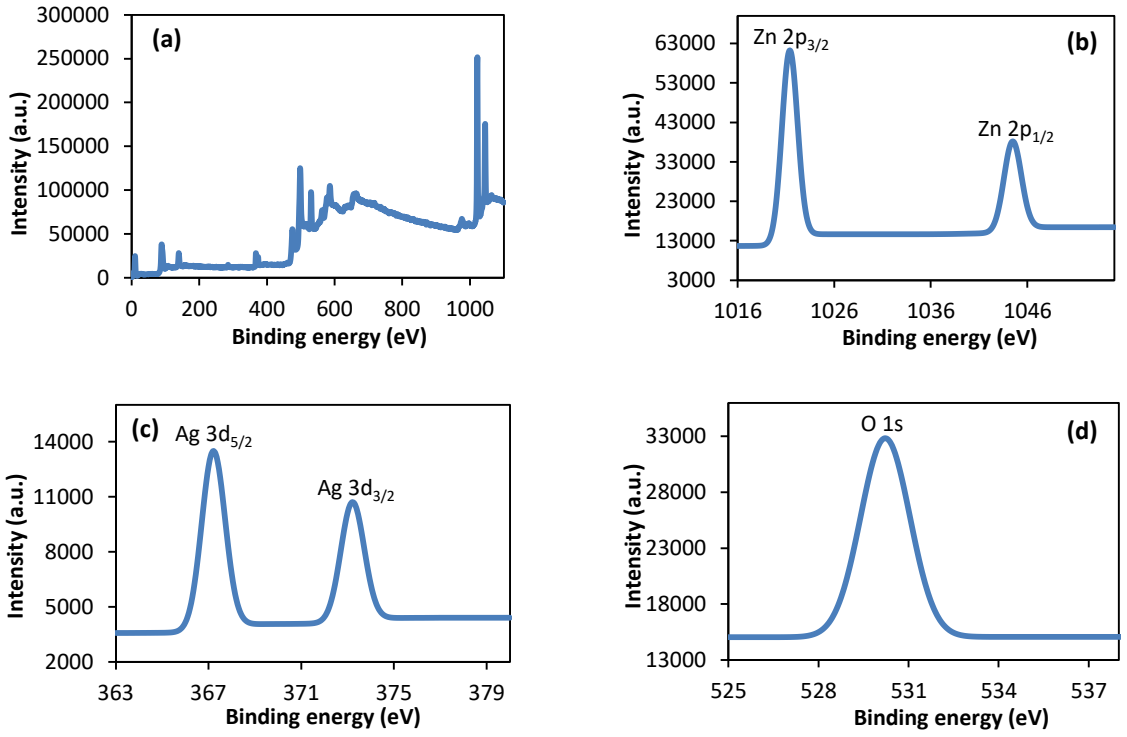

Figure 5.27. (a) Full range XPS spectra of 12 wt.% Ag/ZnO; (b–d) High resolution XPS spectra of Zn 2P, Ag 3d and O 1s for 12 wt.% ZnO/Ag composite.

The high resolution spectra of O 1s are shown in Figures 5.22d–5.27d. The quantitative analysis of O 1s XPS data has been carried out and the results are summarized in Table 5.3. O 1s profile is asymmetric, which can be attributed to the lattice oxygen of ZnO and physical adsorbed oxygen, respectively [39]. Several researchers reported the existence of two different types of O species (O_L and O_H) in ZnO and Ag/ZnO samples [44,45]. However, Patil et al. mentioned only O_L in the O 1s spectrum of the Ag–ZnO sample at a binding energy of 529.75 eV [46]. The data was similar to our synthesized Ag/ZnO composites and no O_H peak is present at the binding energy of about 531.2 eV (Figure S22d–S27d). This suggests that the oxygen presence of surface hydroxyl O_H formation may be depended on the synthesis methods used for the preparation of Ag/ZnO samples.

Table 5.3

Calculation results for Zn 2P, Ag 3d and O1s XPS spectra of Ag/ZnO with different Ag contents.

Catalysts	Peak center (eV)						
	Zn $2p_{1/2}$	**Zn $2p_{3/2}$**	**Difference**	**Ag $3d_{3/2}$**	**Ag $3d_{5/2}$**	**Difference**	**O1s**
ZnO	1044.1	1021.0	23.1	–	–	–	529.6
0.5%Ag/ZnO	1044.1	1021.0	23.1	372.9	366.9	6.0	529.8
2%Ag/ZnO	1044.7	1021.7	23.0	373.5	367.5	6.0	530.3
3%Ag/ZnO	1044.2	1021.1	23.1	373.0	367.0	6.0	529.7
4%Ag/ZnO	1044.6	1021.5	23.1	373.3	367.3	6.0	530.1
6%Ag/ZnO	1045.1	1022.0	23.1	373.8	367.8	6.0	530.8
12%Ag/ZnO	1044.5	1021.4	23.1	373.2	367.2	6.0	530.2

5.3.8. Effect of Ag–doping Amount on the Photodegradation of FMT

The influence of silver doping amounts on the photocatalytic FMT degradation was studied in the aqueous solution. The results are depicted in Figure 5.28. The degradation rate increased with increase in silver percentage upto 6 wt.% in the composite, and exceeding this silver percentage results decreased photocatalytic activity. The possible reason may be attributable to the tradeoff between the decrease in particle size and the deterioration in crystallinity for ZnO [47]. An optimal amount (6%) of silver deposition on ZnO surface is desirable for higher photocatalytic activity, which leads better charge separation at ZnO surface and efficient electron transfer to Ag metal.

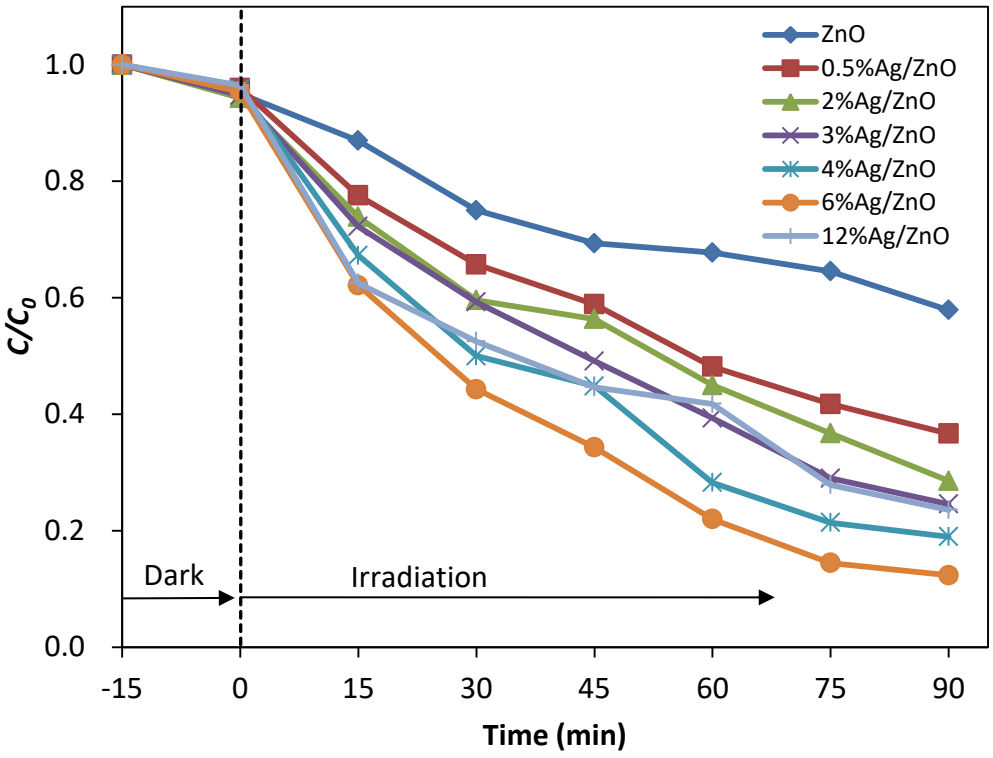

Figure 5.28. Effect of Ag–doping amount on the photocatalytic degradation of Famotidine with Ag/ZnO under UV light irradiation. Calcination temperature 500 °C; calcination time 3 h.

5.3.9. Effect of Calcination Temperature on the Photodegradation of FMT

Figure 5.29 shows the effect of calcination temperature on the photocatalytic FMT degradation with Ag/ZnO for 60 min. The optimum calcination temperature for Ag/ZnO was 500 °C. Above 500 °C, the photocatalytic FMT degradation decreased with the calcination temperatures. It was reported previously that the crystallite size of the oxides increased with increasing the calcination temperatures [48–51]. Therefore, the reason for the decrease in the photocatalytic FMT degradation may be due to the larger particle size of ZnO.

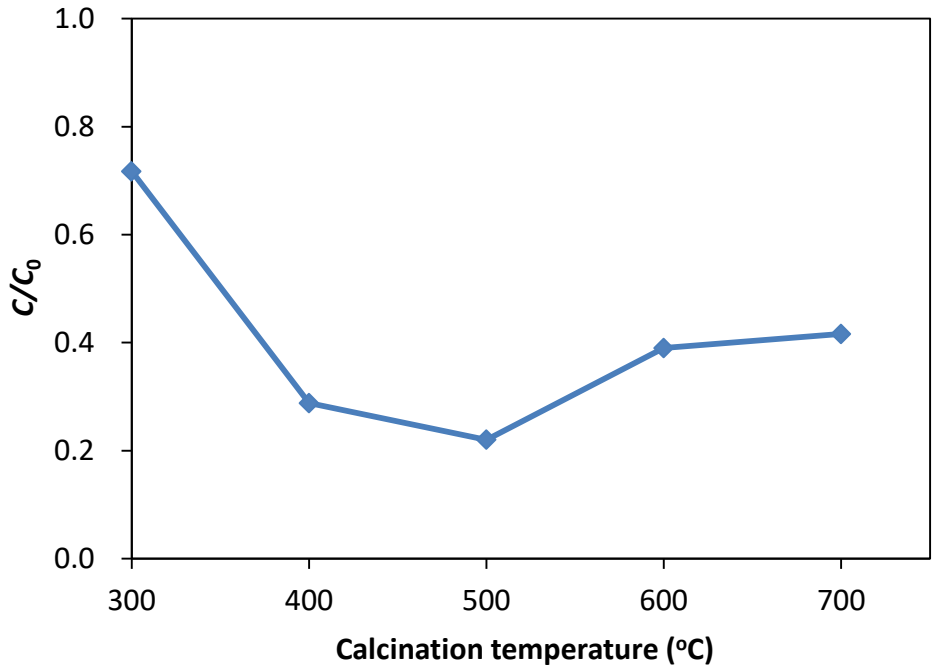

Figure 5.29. Effect of calcination temperature on the photocatalytic degradation of Famotidine with Ag/ZnO under UV light irradiation. Calcination time 3 h; Ag doping 6 wt.%.

5.3.10. Effect of Calcination Time on the Photodegradation of FMT

The effect of calcination time on the photocatalytic FMT degradation was evaluated using Ag/ZnO (Figure 5.30). As the calcination time increased up to 3 h, the FMT degradation with Ag/ZnO increased gradually. Over the calcination time of 3 h, the photocatalytic FMT degradation turned from increase to decrease.

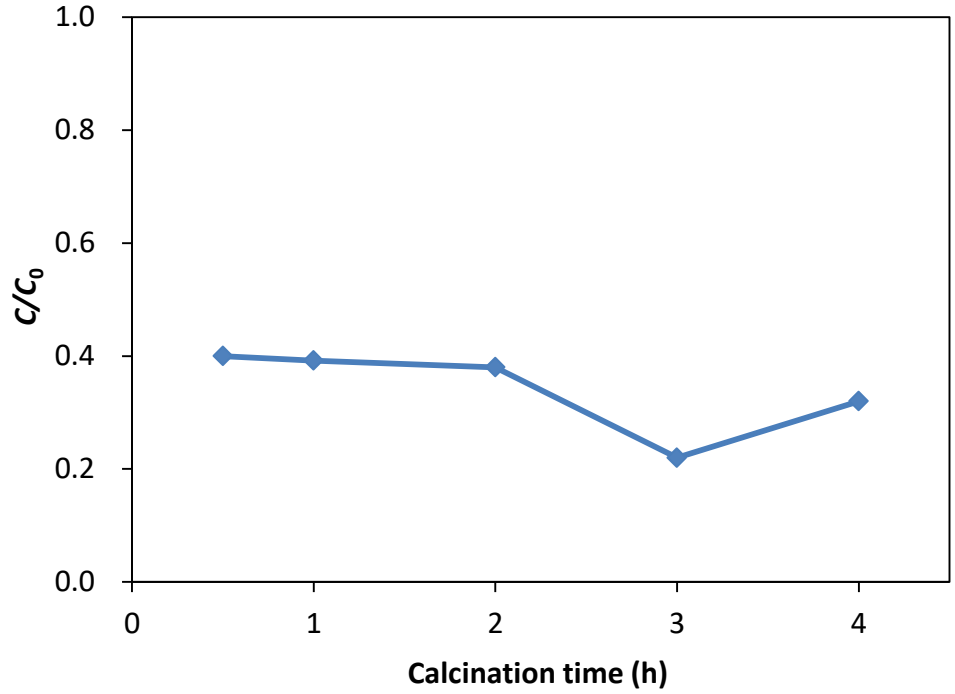

Figure 5.30. Effect of calcination time on the photocatalytic degradation of Famotidine with Ag/ZnO under UV light irradiation. Ag doping 6 wt.%; calcination temperature 500 °C.

5.3.11. Role of the Reactive Species in the Photocatalytic Process

The role of the reactive species in the photocatalytic process was studied by using different quenchers. The quenchers used to scavenge the relevant reactive species were: *tert*–butyl alcohol (TBA), *di*–ammonium oxalate monohydrate (AO) and ascorbic acid (AA). The effect of different scavengers on the FMT degradation over Ag/ZnO heterojunction is presented in Figure 5.31. It was observed that by using AA, TBA and AO as scavenger, the photocatalytic activity significantly reduced from 88% (no scavenger) to 18% (due to $^{\bullet}O_2^-$), 33% (due to $^{\bullet}OH$), and 46% (due to h^+), respectively. Hence, it was concluded that all the reactive species ($^{\bullet}O_2^-$, $^{\bullet}OH$ and h^+) contributed in the photodegradation process. However, $^{\bullet}O_2^-$ was the main reactive species in the photodegradation process as maximum reduction in photocatalytic activity was found by using AA as scavenger.

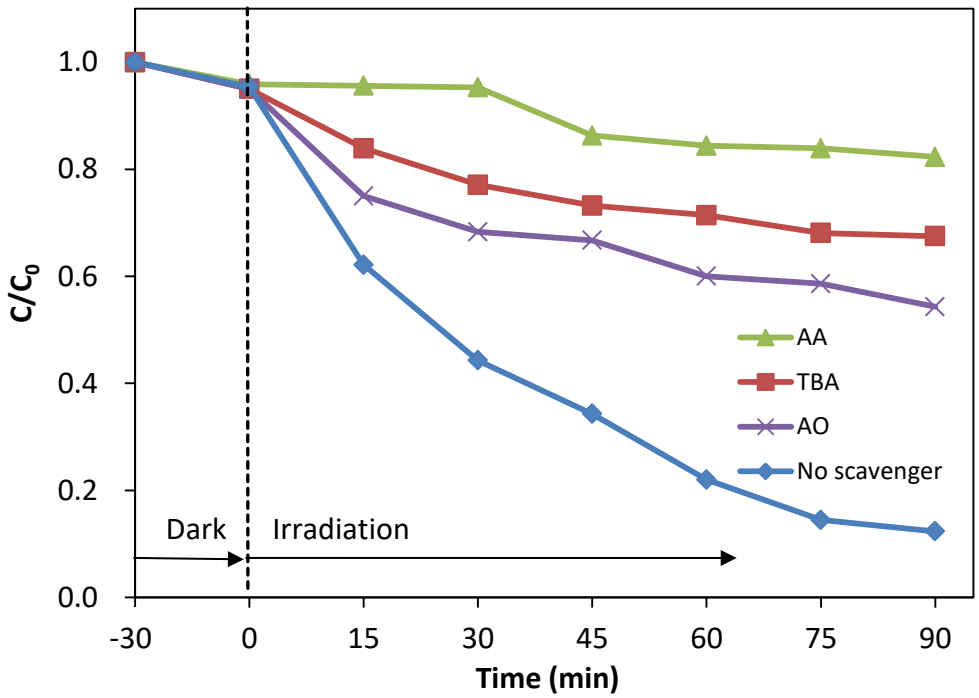

Figure 5.31. Effects of different scavengers on the degradation of Famotidine with 6 wt.% Ag/ZnO under UV light irradiation.

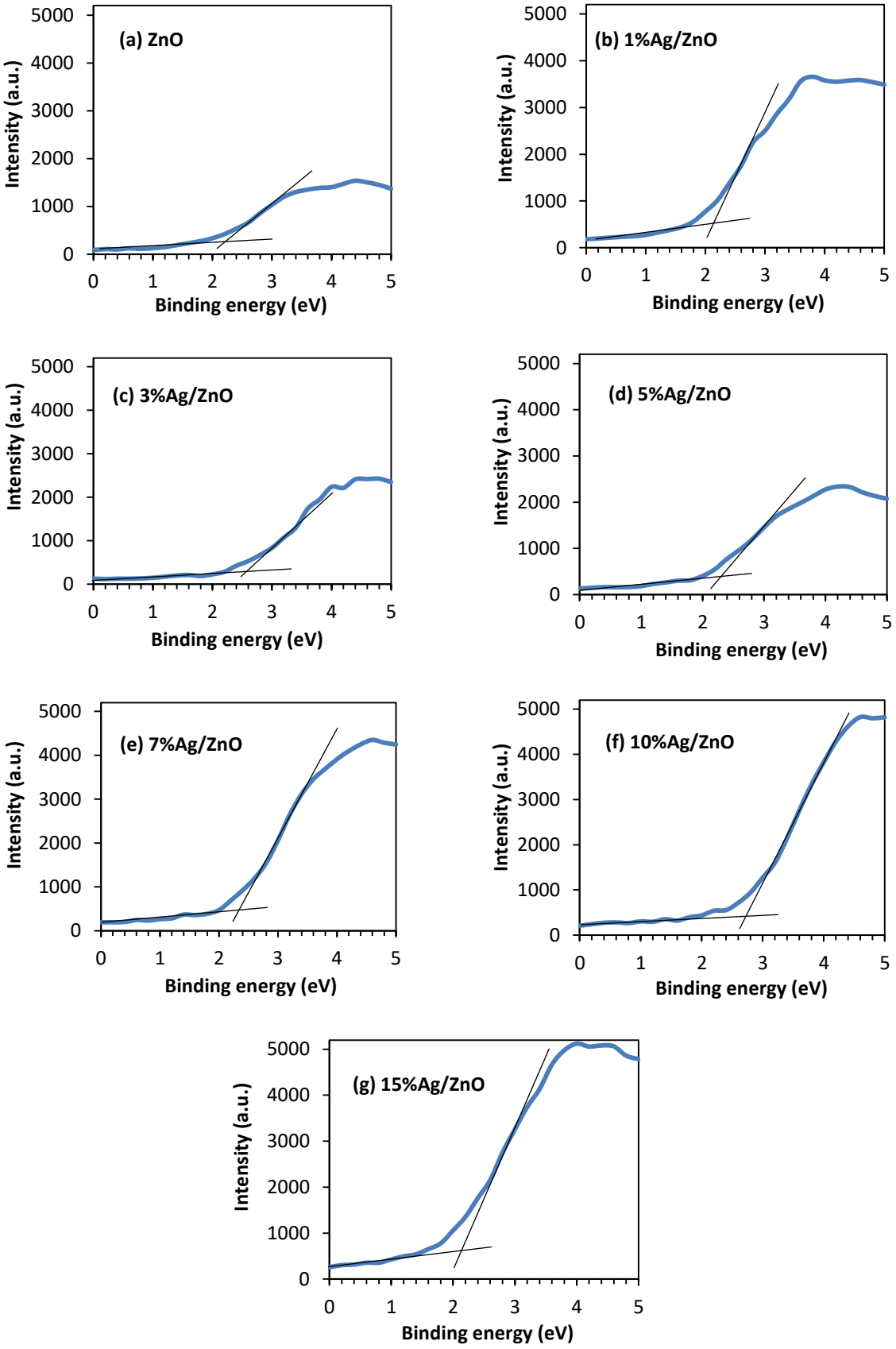

Figure 5.32. Valence band XPS spectra of (a) ZnO and (b–g) Ag/ZnO.

5.3.12. Determination of Energy Levels

The photocatalytic activity of the heterostructure is closely related to its alignment of energy levels, which is determined by the results of UV–vis absorption spectra and valence band XPS. The respective bandgap of ZnO and Ag/ZnO composites were calculated according to the UV–vis absorption spectra (Figure 5.32) and presented in Table 5.4. The binding energy of onset edge in the valence band XPS spectrum reveals energy gap between the valence band maximum and Fermi level (E_f).

Table 5.4

Determined band gaps, valence band XPS and conduction band XPS, and calculated valence band edge and conduction band edge for ZnO and Ag/ZnO.

Catalysts	Determined values (eV)			Calculated values (eV)	
	Energy band gap, E_g	Valence band XPS, E_{VB}	Conduction band, E_{CB}	Valence band edge, E_{VB}	Conduction band edge, E_{CB}
ZnO	3.23	+2.20	–1.03	+2.90	–0.33
0.5%Ag/ZnO	3.27	+2.18	–1.09	+2.92	–0.35
2%Ag/ZnO	3.27	+2.59	–0.68	+2.92	–0.35
3%Ag/ZnO	3.27	+2.36	–0.91	+2.92	–0.35
4%Ag/ZnO	3.25	+2.38	–0.87	+2.91	–0.34
6%Ag/ZnO	3.23	+2.77	–0.46	+2.90	–0.33
12%Ag/ZnO	3.23	+2.14	–1.09	+2.90	–0.33

5.3.13. Calculation of Conduction and Valence Band Positions

The migration direction of the photogenerated charge carrier depends on the band edge positions of the two semiconductors. There are three methods to determine the band edge positions: experiments based on photoelectrochemical techniques, spectroscopic methods and predicting theoretically from the absolute (or Mulliken) electronegativity [52]. The first one is not always easy to handle, and the second one cannot obtain the absolute energy of band edges with respect to vacuum and always has large discrepancies between calculated and measured values. The third one is a simple approach with reasonable results for many oxides photocatalysts [53]. The conduction and valence band positions of the semiconductor at the point of zero charge can be calculated by the following formula [54,55]:

$$\boldsymbol{E_{VB} = \chi - E_e + 0.5E_g} \quad (5.7)$$

$$\boldsymbol{E_{CB} = E_{VB} - E_g} \quad (5.8)$$

Where E_{VB} is the potential of the valence band, χ is the electronegativity of the semiconductor which was the geometric mean of the electronegativity of the constituent atoms. Both of electronegativity values for ZnO and Ag/ZnO were 5.79 eV [53]. The E_e was the energy of free electrons on the hydrogen scale (4.5 eV) and E_g was the band gap energy of the ZnO and Ag/ZnO nanocomposites. The E_{VB} and E_{CB} were calculated as presented in Table 5.4.

5.3.14. Mechanism of Degradation

As shown in Figure 5.33, the work function and the first electron affinity of ZnO is about 5.2 eV and 4.3 eV, respectively, whereas the work function of Ag is about 4.26 eV. Thus, the Fermi energy level of ZnO (E_{fs}) is lower than that of Ag (E_{fm}) because of the larger work function of ZnO. This results in the transfer of electrons from Ag to ZnO until the two systems attain equilibrium and form the new Fermi energy (E_f) [56–58]. Due to it that the equilibrium Fermi energy level (E_f) of Ag nanoparticles is lower than the bottom energy level of the conduction band (CB) of pure ZnO, most photogenerated electrons will transfer from ZnO to Ag nanoparticles driven by the potential energy, while the holes can be remained on ZnO surface because of the Schottky barrier formed at the interface between Ag and ZnO particles [59]. After UV irradiation of Ag/ZnO nanocomposite, the electrons are excited from valence band to the conduction band (CB) and the holes are generated at valence band (VB) of ZnO (Figure 5.33). Then the photo–excited electrons are transferred from ZnO to Ag metal nanoparticle because Ag metal act as electron sink. The trapped electrons react with surface adsorbed O_2 and produce superoxide radical [60]. Moreover, the photo–induced holes can also readily react H_2O to generate hydroxyl radical. The generated hydroxyl and superoxide radicals are strong oxidant species which can degrade the FMT molecule. The Ag metal incorporated in ZnO is responsible for reducing photo–induced electron–hole charge recombination and prolongs the lifetime of photoexcited electrons. On the other hand, the better separation of electrons and holes in the Ag/ZnO heterostructure is confirmed by PL emission spectra, since it is found that Ag/ZnO exhibits much lower fluorescence emission intensity than ZnO, indicating that the recombination of photogenerated electron and hole is

inhibited greatly. The possible mechanistic pathway of Ag/ZnO nanocomposites for degradation of FMT can be proposed as follows [17]:

$$ZnO + h\nu\ (UV) \rightarrow ZnO\ (e_{CB}^{-} + h_{VB}^{+}) \quad (5.9)$$

$$e_{CB}^{-} + O_2 \rightarrow {}^{\bullet}O_2^{-} \quad (5.10)$$

$$h_{VB}^{+} + OH^{-} \rightarrow {}^{\bullet}OH \quad (5.11)$$

$${}^{\bullet}O_2^{-} + FMT \rightarrow \text{S–oxide of FMT} \quad (5.12)$$

$$h_{VB}^{+} + FMT \rightarrow \text{degraded products} \quad (5.13)$$

$${}^{\bullet}OH + FMT \rightarrow \text{degraded products} \quad (5.14)$$

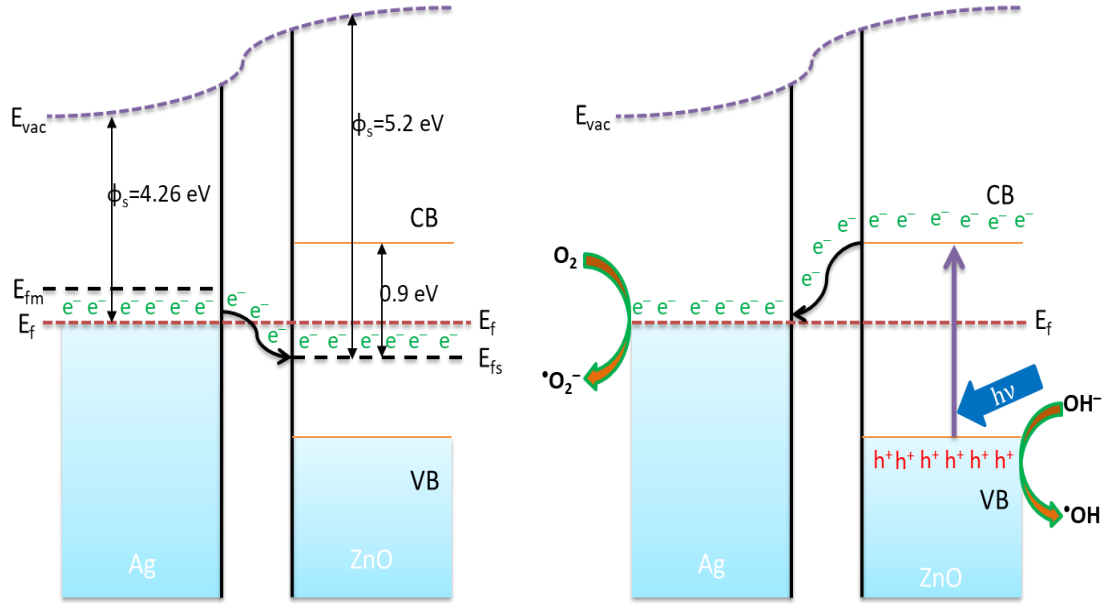

Figure 5.33. (a) Band structures of Ag and ZnO junction and the Fermi energy level equilibrium without UV irradiation, and (b) proposed charge separation process and the photocatalytic mechanism of Ag/ZnO nanocomposites under UV irradiation.

5.3.15. Stability of the Ag/ZnO

The stability of 6 wt.% Ag/ZnO was evaluated by recycled degradations. During the first run, the suspension of the Ag/ZnO and FMT in water was irradiated with UV light 90 min. The composites were naturally dried and then analyzed using X–rays diffractometry. The XRD patterns of Ag/ZnO before and after treatment are illustrated in Figure 5.34. It can be seen that both of them show similar X–ray diffraction patterns, demonstrating that the photocatalyst was stable and metal Ag was not change into oxides.

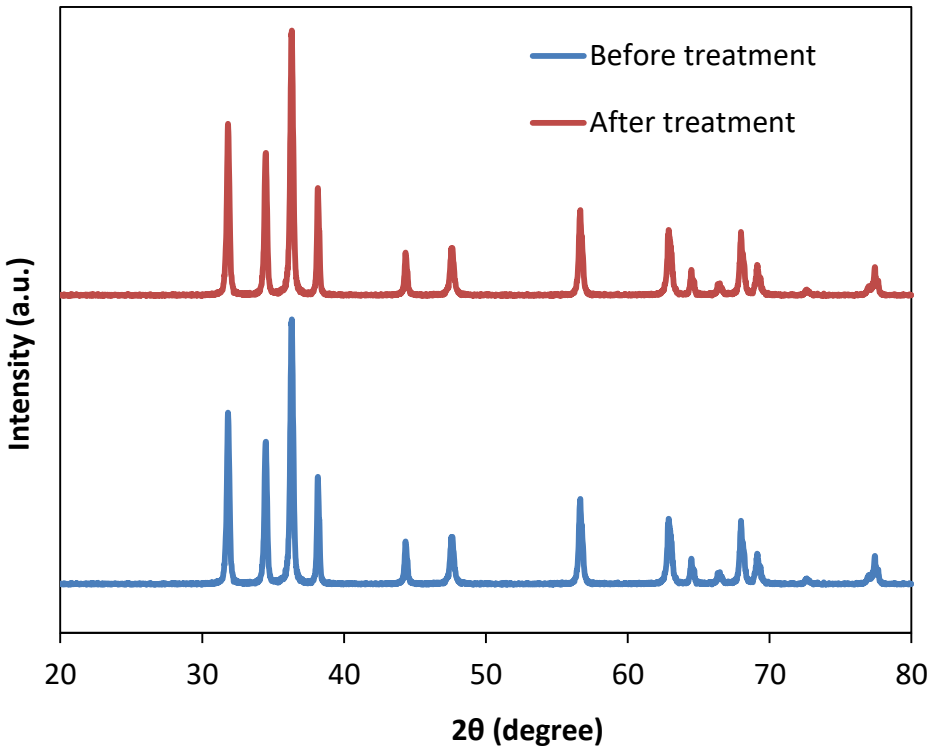

Figure 5.34. XRD patterns of 6 wt.% Ag/ZnO before and after treatment of FMT under UV light for 90 min.

5.3.16. Reusability of the Ag/ZnO

The reusability of Ag/ZnO was tested by utilizing the same composite for 3 cycles of FMT degradation reactions. The results of the reactions were shown in Figure 5.35. The graph clearly illustrates that, up to 3rd cycle the photocatalytic activity of the Ag/ZnO remains almost consistent, highlighting the stability and reusability of Ag/ZnO.

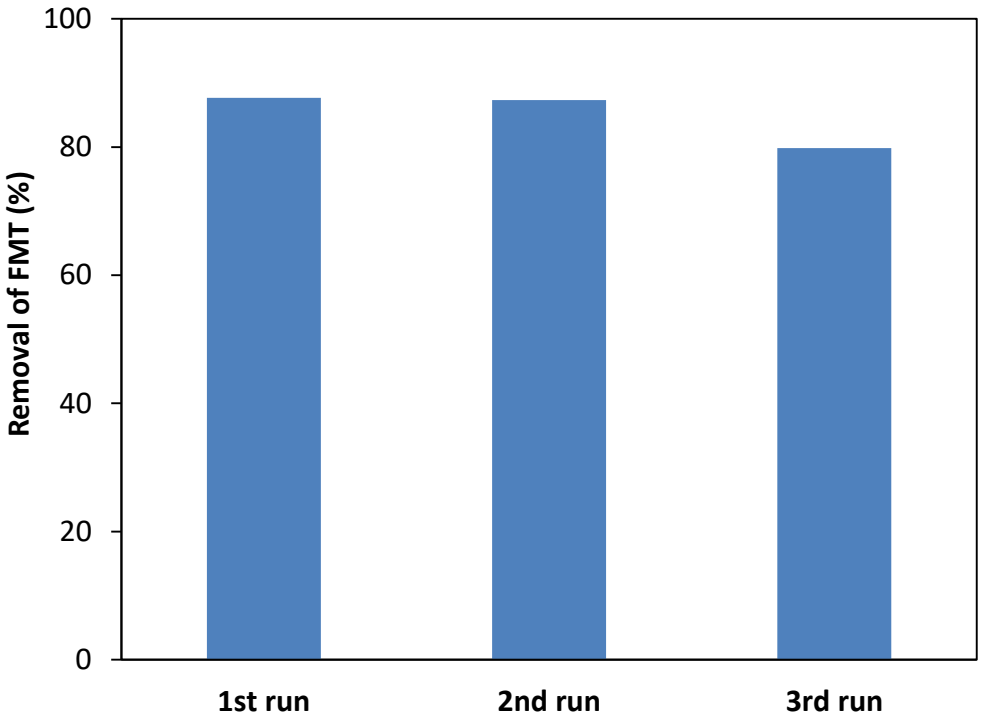

Figure 5.35. Photocatalytic degradation of FMT using recycled 6 wt.% Ag/ZnO under UV irradiation for 90 min.

5.3.17. TOC Analysis

The total organic carbon (TOC) was measured because of the evaluation of mineralization in the FMT degradation. The TOC removal in the FMT solution under UV irradiation is shown in Figure 5.36. The TOC decreased slowly with the irradiation time. After 24 h irradiation with Ag/ZnO, 24% reduction of TOC is observed for the mineralization of FMT. Murphy has reported the photocatalytic degradation of FMT, in which the reaction intermediate (mass number: 311) released diaminomethylideneamino function from FMT molecule was formed [61]. The facts for reported intermediate product and the remaining 76% carbon indicate it that the bond cleavage in FMT molecule may occur either at both **a** and **c** positions or at **b** position (Figure 5.37).

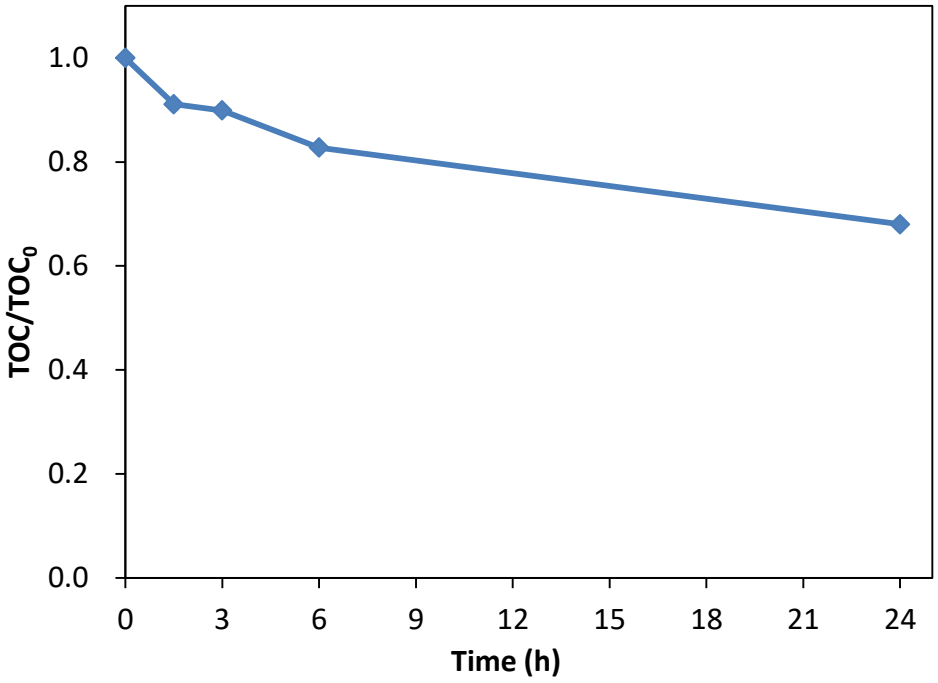

Figure 5.36. Photocatalytic degradation of FMT using 6 wt.% Ag/ZnO under UV irradiation over time, express as TOC removal.

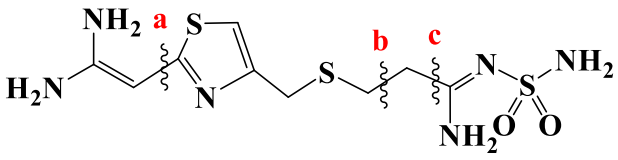

Figure 5.37. Proposed cleavage of the FMT molecule during photocatalysis.

5.4. CONCLUSIONS

Ag–doped ZnO photocatalysts were successfully synthesized at different Ag contents (0–12 wt.%) through simple, effective, high yield and low cost mechanochemical combustion technique, with addition of silver acetate to a zinc acetate and oxalic acid mixture. The synthesized materials were characterized by XRD, EPMA, XPS, SEM, TEM, BET surface area analysis, UV–DRS and PL. It was shown that all samples were composed of metallic Ag and wurtzite ZnO. The Ag–doped ZnO was applied into the photocatalytic degradation of FMT in aqueous medium under UV irradiation. The optimum calcination temperature and time were 500 °C and 3 h, respectively. The best Ag–doping amount was 6 wt.%. The maximum photocatalytic activity for FMT degradation on Ag/ZnO was more than two times better compared with undoped ZnO. The developed system may provide a strategy for the design of stable and inexpensive technologies for highly efficient photocatalytic FMT degradation. The effect of different scavengers on the FMT degradation over Ag/ZnO means it that all the reactive species ($^{\bullet}O_2^-$, $^{\bullet}OH$ and h^+) contributed in the photocatalytic degradation process. However, $^{\bullet}O_2^-$ was the main reactive species in the photodegradation system.

5.5. REFERENCES

[1] K.M. Lee, C.W. Lai, K.S. Ngai, J.C. Juan, Recent developments of zinc oxide based photocatalyst in water treatment technology: a review, Water Res. 88 (2016) 428–448.

[2] S.M. Lam, J.C. Sin, A.Z. Abdullah, A.R. Mohamed, Degradation of wastewaters containing, organic dyes photocatalysed by zinc oxide: a review, Desalin. Water Treat. 41 (2012) 131–169.

[3] K.S. Siddhapara, D.V. Shah, Study of photocatalytic activity and properties of transition metal ions doped nanocrystalline TiO_2 prepared by sol–gel method, Adv. Mater. Sci. Eng. 2014 (2014) 4462198; http://dx.doi.org/10.1155/2014/462198.

[4] R. Saleh, N.F. Djaja, UV light photocatalytic degradation of organic dyes with Fe–doped ZnO nanoparticles, Superlattices Microstruct. 74 (2014) 217–233.

[5] R. Saleh, N.F. Djaja, Transition–metal–doped ZnO nanoparticles: synthesis, characterization and photocatalytic activity under UV light, Spectrochim. Acta Part A: Mol. Biomol. Spectrosc. 130 (2014) 581–590.

[6] K. Kumar, M. Chitkara, I.S. Sandhu, D. Mehta, S. Kumar, Photocatalytic, optical and magnetic properties of Fe–doped ZnO nanoparticles prepared by chemical route, J. Alloys Compd. 588 (2014) 681–689.

[7] S. Deka, P.A. Joy, Synthesis and magnetic properties of Mn doped ZnO nanowires, Solid State Commun. 142 (2007) 190–194.

[8] R. Viswanatha, S. Sapra, S.S. Gupta, B. Satpati, P.V. Satyam, B.N. Dev, D.D. Sarma, Synthesis and characterization of Mn–doped ZnO nanocrystals, J. Phys. Chem. B 108 (2004) 6303–6310.

[9] Ş.Ş. Türkyılmaza, N. Güya, M. Özacar, Photocatalytic efficiencies of Ni, Mn, Fe and Ag doped ZnO nanostructures synthesized by hydrothermal method: The

synergistic/antagonistic effect between ZnO and metals, J. Photochem. Photobiol. A: Chem. 341 (2017) 39–50.

[10] X.M. Hou, ZnO/Ag heterostructured nanoassemblies: wet–chemical preparation and improved visible–light photocatalytic performance, Mater. Lett. 139 (2015) 201–204.

[11] C.L. Yu, W.Q. Zhou, L.H. Zhu, G. Li, K. Yang, R.C. Jin, Integrating plasmonic Au nanorods with dendritic like alpha–Bi_2O_3/$Bi_2O_2CO_3$ heterostructures for superior visible–light–driven photocatalysis, Appl. Catal. B 184 (2016) 1–11.

[12] W.H. Feng, B. Wang, Z.Y. Zheng, Z.B. Fang, Z.F. Wang, S.Y. Zhang, Y.H. Li, P. Liu, Predictive model for optimizing the near–field electromagnetic energy transfer in plasmonic nanostructure–involved photocatalysts, Appl. Catal. B 186 (2016) 143–150.

[13] Y. Zheng, C. Chen, Y. Zhan, X. Lin, Q. Zheng, K. Wei, J. Zhu, Photocatalytic activity of Ag/ZnO heterostructure nanocatalyst: correlation between structure and property, J. Phys. Chem. C 112 (2008) 10773–10777.

[14] W. Xie, Y. Li, W. Sun, J. Huang, H. Xie, X. Zhao, Surface modification of ZnO with Ag improves its photocatalytic efficiency and photostability, J. Photochem. Photobiol. A 216 (2010) 149–155.

[15] M.–K. Lee, T.G. Kim, W. Kim, Y.–M. Sung, Surface plasmon resonance (SPR) electron and energy transfer in noble metal–zinc oxide composite nanocrystals, J. Phys. Chem. C 112 (2008) 10079–10082.

[16] D. Tawadrous, S. Dixon, S.Z. Shariff, J. Fleet, S. Gandhi, A. K. Jain, M.A. Weir, T. Gomes, A.X. Garg, Altered mental status in older adults with histamine2–receptor antagonists: A population–based study, Eur. J. Intern. Med. 25 (2014) 701–709.

[17] S. Murphy, C. Saurel, A. Morrissey, J. Tobin, M. Oelgemoller, K. Nolan, Photocatalytic activity of a porphyrin/TiO_2 composite in the degradation of pharmaceuticals, Appl. Catal. B: Environ. 119–120 (2012) 156–165.

[18] J. Karpin´ska, A. Soko´l, M. Kobeszko, B. Starczewska, U. Czyzewska, M. Hryniewicka, Study on degradation process of famotidine hydrochloride in aqueous samples, Toxicol. Environ. Chem. 92 (2010) 1409–1422.

[19] H. Katsumata, M. Taniguchi, S. Kaneco, T. Suzuki, Photocatalytic degradation of bisphenol A by Ag_3PO_4 under visible light, Catal. Commun. 34 (2013) 30–34.

[20] J. Su, L. Zhu, P. Geng, G. Chen, Self–assembly graphitic carbon nitride quantum dots anchored on TiO_2 nanotube arrays: An efficient heterojunction for pollutants degradation under solar light, J. Hazard. Mater. 316 (2016) 159–168.

[21] R. Lamba, A. Umar, S.K. Mehta, S.K. Kansal, Sb_2O_3–ZnO nanospindles: a potential material for photocatalytic and sensing applications, Ceram. Inter. 41 (2015) 5429–5438.

[22] Y. Liang, N. Guo, L. Li, R. Li, G. Ji, S. Gan, Fabrication of porous 3D flower–like Ag/ZnO heterostructure composites with enhanced photocatalytic performance, Appl. Surf. Sci. 332 (2015) 32–39.

[23] R. Saravanan, N. Karthikeyan, V.K. Gupta, E. Thirumal, P. Thangadurai, ZnO/Ag nanocomposite: An efficient catalyst for degradation studies of textile effluents under visible light, Mater. Sci. Eng. C 33 (2013) 2235–2244.

[24] G.K. Willamson, W.H. Hall, X–ray line broadening from filed aluminium and wolfram, Acta Metall. 1 (1953) 22–31.

[25] R. Georgekutty, M.K. Seery, S.C. Pillai, A highly efficient Ag–ZnO photocatalyst: synthesis, properties, and mechanism, J. Phys. Chem. C 112 (2008) 13563–13570.

[26] Y. Zheng, C. Chen, Y. Zhan, X. Lin, Q. Zheng, K. Wei, J. Zhu, Photocatalytic activity of Ag/ZnO heterostructure nanocatalyst: correlation between structure and property, J. Phys. Chem. C 112 (2008) 10773–10777.

[27] O. Bechambia, M. Chalbib, W. Najjara, S. Sayadi, Photocatalytic activity of ZnO doped with Ag on the degradation of endocrine disrupting under UV irradiation and the investigation of its antibacterial activity, Appl. Surf. Sci. 347 (2015) 414–420.

[28] H. Zeng, G. Duan, Y. Li, S. Yang, X. Xu, W. Cai, Blue luminescence of ZnO nanoparticles based on non–equilibrium processes: Defect origins and emission controls, Adv. Funct. Mater. 20 (2010) 561–572.

[29] D.H. Zhang, Q.P. Wang, Z.Y. Xue, Photoluminescence of ZnO films excited with light of different wavelength, Appl. Surf. Sci. 207 (2003) 20–25.

[30] X.D. Gao, X.M. Li, W.D. Yu, Rapid preparation, characterization, and photoluminescence of ZnO films by a novel chemical method, Mater. Res. Bull. 40 (2005) 1104–1111.

[31] K. Rokesh, A. Pandikumar, K. Jothivenkatachalam, Zinc oxide nanopillar: preparation, characterization and its photoelectrocatalytic activity, Mater. Focus 3 (2014) 345–349.

[32] J. Liu, X. Huang, Y. Li, Q. Zhong, L. Ren, Preparation and photoluminescence of ZnO complex structures with, controlled morphology, Mater. Lett. 60 (2006) 1354–1359.

[33] R. Georgekutty, M.K. Seery, S.C. Pillai, A highly efficient Ag–ZnO photocatalyst: synthesis, properties, and mechanism, J. Phys. Chem. C 112 (2008) 13563–13570.

[34] W. Lu, G. Liu, S. Gao, S. Xing, J. Wang, Tyrosine–assisted preparation of Ag/ZnO nanocomposites with enhanced photocatalytic performance and synergistic antibacterial activities, Nanotechnology 19 (2008) 445711; https://doi.org/10.1088/0957–4484/19/44/445711.

[35] M.K. Lee, T.G. Kim, W. Kim, Y.M. Sung, Surface plasmon resonance (SPR) electron and energy transfer in noble metal–zinc oxide composite nanocrystals, J. Phys. Chem. C 112 (2008) 10079–10082.

[36] J. Zhai, L. Wang, D. Wang, Y. Lin, D. He, T. Xie, UV–illumination room–temperature gas sensing activity of carbon–doped ZnO microspheres, Sens. Actuators B: Chem. 161 (2012) 292–297.

[37] S.A. Ansari, M.M. Khan, M.O. Ansari, J. Lee, M.H. Cho, Biogenic synthesis, photocatalytic, and photoelectrochemical performance of Ag–ZnO nanocomposite, J. Phys. Chem. C 117 (2013) 27023–27030.

[38] H.W. Bai, Z.Y. Liu, D.D. Sun, Hierarchical ZnO/Cu corn–like materials with high photodegradation and antibacterial capability under visible light, Phys. Chem. Chem. Phys. 13 (2011) 6205–6210.

[39] W.W. Lu, S.Y. Gao, J.J. Wang, One–pot synthesis of Ag/ZnO self–assembled 3D hollow microspheres with enhanced photocatalytic performance, J. Phys. Chem. C 112 (2008) 16792–16800.

[40] J. Das, S. Pradhan, D. Sahu, D. Mishra, S. Sarangi, B. Nayak, S. Verma, B. Roul, Micro–Raman and XPS studies of pure ZnO ceramics, Physica B: Condens. Matter 405 (2010) 2492–2497.

[41] S. Khosravi–Gandomani, R. Yousefi, F. Jamali–Sheini, N.M. Huang, Optical and electrical properties of p–type Ag–doped ZnO nanostructures, Ceram. Int. 40 (2014) 7957–7963.

[42] R. Dhabbe, A. Kadam, M. Suwarnkar, M. Kokate, K. Garadkar, Enhancement in the photocatalytic activity of Ag loaded N–doped TiO_2 nanocomposite under sunlight, J. Mater. Sci. Mater. Electron. 25 (2014) 3179–3189.

[43] J.F. Moulder, W.F. Stickle, P.E. Sobol, K.D. Bomben, Handbook of X–Ray Photoelectron Spectroscopy: A Reference Book of Standard Spectra for Identification and Interpretation of Xps Data, Reissue ed., Physical Electronics, Boston, 1995.

[44] X. Zhang, Y. Wang, F. Hou, H. Li, Y. Yang, X. Zhang, Y. Yang, Y. Wang, Effects of Ag loading on structural and photocatalytic properties of flower–like ZnO microspheres, Appl. Sur. Sci. 391 (2017) 476–483.

[45] J. Xu, Y. Chang, Y. Zhang, S. Ma, Y. Qu, C. Xu, Effect of silver ions on the structure of ZnO and photocatalytic performance of Ag/ZnO composites, Appl. Sur. Sci. 255 (2008) 1996–1999.

[46] S.S. Patil, M.G. Mali, M.S. Tamboli, D.R. Patil, M.V. Kulkarni, H. Yoon, H. Kim, S.S. Al–Deyab, S.S. Yoon, S.S. Kolekar, B.B. Kale, Green approach for hierarchical nanostructured Ag–ZnO and their photocatalytic performance under sunlight, Catal. Today 260 (2016) 126–134.

[47] B. Chai, X. Wang, S. Cheng, H. Zhou, F. Zhang, One–pot triethanolamine–assisted hydrothermal synthesis of Ag/ZnO heterostructure microspheres with enhanced photocatalytic activity, Ceram. Int. 40 (2014) 429–435.

[48] P.R. Potti, V.C. Srivastava, Comparative studies on structural, optical, and textural properties of combustion derived ZnO prepared using various fuels and their photocatalytic activity, Ind. Eng. Chem. Res. 51 (2012) 7948–7956.

[49] J. Lu, Q. Zhang, J. Wang, F. Saito, M. Uchida, Synthesis of N doped ZnO by grinding and subsequent heating ZnO–urea mixture, Powder Technol. 162 (2006) 33–37.

[50] P. Praserthdam, P.L. Silveston, O. Mekasuwandumrong, V. Pavarajarn, J. Phungphadung, P. Somrang, A new correlation for the effects of the crystallite size and calcination temperature on the single metal oxides and spinel oxide nanocrystal, Cryst. Growth Des. 4 (2004) 39–43.

[51] Y. Li, G. Ma, S. Peng, G. Lu, S. Li, Boron and nitrogen co–doped titania with enhanced visible–light photocatalytic activity for hydrogen evolution, Appl. Surf. Sci. 254 (2008) 6831–6836.

[52] Y.I. Kim, S.J. Atherton, E.S. Brigham, T.E. Mallouk, Sensitized layered metal oxide semiconductor particles for photochemical hydrogen evolution from nonsacrificial electron donors, J. Phys. Chem. 97 (1993) 11802–11810.

[53] Y. Xu, M.A.A. Schoonen, The absolute energy positions of conduction and valence bands of selected semiconducting minerals, Am. Mineral. 85 (2000) 543–556.

[54] Sh. Sohrabnezhad, A. Pourahmad, T. Salavatiyan, CuO–MMT nanocomposite: effective photocatalyst for the discoloration of methylene blue in the absence of H_2O_2, Appl. Phys. A 122 (2016) 111–117.

[55] X. Lin, J. Xing, W. Wang, Z. Shan, F. Xu, F. Huang, Photocatalytic activities of heterojunction semiconductors $Bi_2O_3/BaTiO_3$: a strategy for the design of efficient combined photocatalysts, J. Phys. Chem. C 111 (2007) 18288–18293.

[56] A. Wood, M. Giersig, P. Mulvaney, Fermi level equilibration in quantum dot–metal nanojunctions, J. Phys. Chem. B 105 (2001) 8810–8815.

[57] X. Wang, C.J. Summers, Z.L. Wang, Self–attraction among aligned Au/ZnO nanorods under electron beam, Appl. Phys. Lett. 86 (2005) 013111;

https://doi.org/10.1063/1.1847713.

[58] D.A. Neamen, Semiconductor Physics and Devices: Basic Principles, 3rd ed.; McGraw–Hill Professional: New York, 2003.

[59] S.Y. Gao, X.X. Jia, S.X. Yang, Z.D. Li, K. Jiang, Hierarchical Ag/ZnO micro/nanostructure: Green synthesis and enhanced photocatalytic performance, J. Solid State Chem. 184 (2011) 764–769.

[60] Y. Zheng, L. Zheng, Y. Zhan, X. Lin, Q. Zheng, K. Wei, Ag/ZnO heterostructure nanocrystals: synthesis, characterization, and photocatalysis, Inorg. Chem. 46 (2007) 6980–6986.

[61] S. Murphy, Photocatalytic degradation of pharmaceuticals in aqueous solutions and development of new dye sensitised photocatalytic materials, Ph.D. Dissertation, Dublin City University, Dublin, Ireland, 2012.

CHAPTER 6

SUMMARY

6.1. THESIS CONCLUSIONS

The presence of organic pollutants in humans has become subject of intense research for human exposure and health risk assessment. One of the main current worldwide concerns is the growth of water pollution by organic compounds arising from many industrial, agricultural and urban human activities. Organic pollutants have been detected in rivers, lakes, sea and even drinking water in Bangladesh. Although continued efforts for their remediation have been made, an effective and efficient organic pollutants removal method has not been developed yet. This work was devoted to explore the highly efficient and cost effective organic pollutants removal techniques. Organic pollutants removal was evaluated by the heterogeneous photocatalytic treatment with TiO_2, the dye–sensitized TiO_2 and ZnO, and Ag–doped ZnO.

In chapter 1, the organic pollutants sources and the effect of organic pollutants on human health and on environment, and the photocatalytic degradation mechanism were discussed. A few hundred organic pollutants have been found to contaminate water resources. These contaminations are very dangerous due to embryotoxicity, mutagenicity, teratogenicity and carcinogenicity as well as health disorders to human beings, such as the dysfunction of kidney, reproductive system, liver, brain and central nervous system. Various techniques such as coagulation–flocculation, biological treatment, membrane technologies, adsorption, advanced oxidation processes and combined methods etc. have been reported for organic pollutants removal. Among various organic pollutants removal methods, photocatalytic treatments have become the promising techniques.

In second chapter, the optimization of solar photocatalytic degradation conditions of amitrole in water using titanium dioxide was investigated. Typical optimum degradation conditions were as follows: photocatalyst loading: 6.7 g/L, temperature: 25 °C and pH 9. The photocatalytic degradation under sunlight irradiation was very effective for amitrole solution. The primary photocatalytic decomposition reaction followed a pseudo–first–order kinetic law. The activation energy (E_a) was estimated to become 6.73 kJ/mol. Nitrate (NO_3^-) and ammonium (NH_4^+) ions were detected as the end products. Triazole was identified as the intermediate products. The solar photocatalytic degradation treatment for the wastewater including amitrole is simple, easy handling and low cost.

In third chapter, the dye–sensitization technique was applied to effective catalysts, TiO_2 and ZnO, under fluorescent light irradiation for orange II and methyl orange degradations. The percentage of degradation of orange II and methyl orange increased with an increase in irradiation time under fluorescent light for TiO_2 and ZnO catalyst. The photocatalytic activity of ZnO nanoparticles were better than that of TiO_2 for methyl orange, and were the same activity of ZnO and TiO_2 for orange II photodegradation under fluorescent light. The quenching effects of different scavengers displayed that the reactive h^+ and $^{\bullet}O_2^-$ radicals play the major role in the dye decolorization under visible light irradiation, while the $^{\bullet}OH$ radical played a minor role in the oxidization process.

In fourth chapter, the photocatalytic activities of dye (orange II, bromophenol blue, acid red 88 and rhodamine B) sensitized TiO_2 were evaluated by the degradation of famotidine under visible light irradiation ($\lambda > 400$ nm) at ambient temperature. The TiO_2 in the presence of rhodamine B exhibited excellent photocatalytic

performance for famotidine degradation, displaying a considerably higher photocatalytic activity compared with that of TiO_2. Investigation of the photocatalytic mechanism showed that the TiO_2–dye–sensitized degradation of famotidine under visible light irradiation could be mainly attributed to the direct oxidization by h^+ and $\bullet O_2^-$ radicals, while the $\bullet OH$ radicals played only a relatively minor role in the oxidization process. The present work may offer new opportunities for their industrial application in the elimination of Famotidine and dye pollutants from wastewater.

In fifth chapter, Ag–doped ZnO photocatalysts were successfully synthesized at different Ag contents (0–12 wt.%) through simple, effective, high yield and low cost mechanochemical combustion technique, with addition of silver acetate to a zinc acetate and oxalic acid mixture. The synthesized materials were characterized by XRD, EPMA, XPS, SEM, TEM, BET surface area analysis, UV–DRS and PL. It was shown that all samples were composed of metallic Ag and wurtzite ZnO. The Ag–doped ZnO was applied into the photocatalytic degradation of Famotidine in aqueous medium under UV light irradiation. The optimum calcination temperature and time were 500 °C and 3 h, respectively. The best Ag–doping amount was 6 wt.%. The maximum photocatalytic activity for famotidine degradation on Ag/ZnO was more than two times better compared with undoped ZnO. The effect of different scavengers on the Famotidine degradation over Ag/ZnO is presented that all the reactive species ($\bullet O_2^-$, $\bullet OH$ and h^+) contributed in the photocatalytic degradation process. However, $\bullet O_2^-$ was the main reactive species in this oxidation process.

LIST OF PRESENTATIONS IN INTERNATIONAL/LOCAL CONFERENCES

1. **M.A.I. Molla**, H. Katsumata, T. Suzuki, S. Kaneco, Visible–Light–Driven Photocatalytic Degradation of Orange II and Methyl Orange with Dye–Sensitized TiO_2, The 5th International Symposium for Sustainability by Engineering at MIU, Japan, September 29, 2015.
2. **M.A.I. Molla**, H. Katsumata, T. Suzuki, S. Kaneco, Visible–Light–Driven Photocatalytic Degradation of Dye with Dye–Sensitized TiO_2, 46th Annual Meeting of Chemistry–Related Societies in Chubu Area, Japan, November 7–8, 2015.
3. **M.A.I. Molla**, H. Katsumata, T. Suzuki, S. Kaneco, Visible Weak Fluorescent Light Photocatalytic Degradation of Orange II and Methyl Orange with Dye–Sensitized TiO_2, The First International Conference on Science, Engineering & Environment, Mie, Japan, November 19–21, 2015.
4. **M.A.I. Molla**, H. Katsumata, T. Suzuki, S. Kaneco, Photocatalytic Degradation of Famotidine with Dye–Sensitized TiO_2 under Visible–Light–Irradiation, The 6th International Symposium for Sustainability by Engineering at MIU, Japan, September 27–28, 2016.
5. **M.A.I. Molla**, H. Katsumata, T. Suzuki, S. Kaneco, Visible–Light–Induced Photocatalytic Degradation of Famotidine with Dye–Sensitized TiO_2, 47th Annual Meeting of Chemistry–Related Societies in Chubu Area, Japan, November 5–6, 2016.
6. **M.A.I. Molla**, H. Katsumata, T. Suzuki, S. Kaneco, Photocatalytic Degradation of Famotidine with Dye–Sensitized TiO_2 under Visible Light, The Second International Conference on Science, Engineering & Environment, Osaka City, Japan, November 21–23, 2016.

7. **M.A.I. Molla**, M. Furukawa, H. Katsumata, T. Suzuki, S. Kaneco, Photocatalytic Activity of Ag–doped ZnO for the Degradation of Famotidine in Water under UV Irradiation, 36th Summer Seminar of Analytical Chemistry in Chubu Area, Japan, August 29–30, 2017.
8. **M.A.I. Molla**, M. Furukawa, H. Katsumata, T. Suzuki, S. Kaneco, Photocatalytic Activity of ZnO Doped with Ag for Degradation of Famotidine in Aqueous Solutions, The 7th International Symposium for Sustainability by Engineering at MIU, Japan, September 29, 2017.
9. **M.A.I. Molla**, M. Furukawa, H. Katsumata, T. Suzuki, S. Kaneco, Degradation of Famotidine with Ag–doped ZnO in Water under UV Irradiation, 48th Annual Meeting of Chemistry–Related Societies in Chubu Area, Japan, November 11–12, 2017.
10. **M.A.I. Molla**, M. Furukawa, H. Katsumata, T. Suzuki, S. Kaneco, Degradation of Famotidine in Water with Ag–ZnO under UV Light Irradiation, Seventh International Conference on Geotechnique, Construction Materials and Environment, Mie, Japan, November 21–23, 2017.

LIST OF SCIENTIFIC PAPERS PUBLISHED/IN SUBMISSION

1. **M.A.I. Molla**, I. Tateishi, M. Furukawa, H. Katsumata, T. Suzuki, S. Kaneco, Evaluation of Reaction Mechanism for Photocatalytic Degradation of Dye with Self–Sensitized TiO_2 under Visible Light Irradiation, *Open Journal of Inorganic Non–metallic Materials* 7 (2017) 1–7.

2. **M.A.I. Molla**, M. Furukawa, I. Tateishi, H. Katsumata, T. Suzuki, S. Kaneco, Photocatalytic Decolorization of Dye with Self–Dye–Sensitization under Fluorescent Light Irradiation, *ChemEngineering* 1 (2017) 8; doi: 10.3390/chemengineering1020008.

3. **M.A.I. Molla**, I. Tateishi, M. Furukawa, H. Katsumata, T. Suzuki, S. Kaneco, Photocatalytic Removal of Famotidine with TiO_2 from Water in the Presence of Dye under Visible Light Irradiation, *Desalination and Water Treatment* 87 (2017) 338–347.

4. **M.A.I. Molla**, S. Ahsan I. Tateishi, M. Furukawa, H. Katsumata, T. Suzuki, S. Kaneco, Degradation, Kinetics, and Mineralization in the Solar Photocatalytic Treatment of Aqueous Amitrole Solution with Titanium Dioxide, *Environmental Engineering Science* (2017); https://doi.org/10.1089/ees.2017.0138.

5. **M.A.I. Molla**, M. Furukawa, I. Tateishi, H. Katsumata, T. Suzuki, S. Kaneco, Fabrication of Ag Metal Decorated ZnO by Mechanochemical Combustion Method and Their Application into Photocatalytic Famotidine Degradation, (2018) – (Submitted).